PHD

Active integrated optic waveguide / laser structures

Pennington, Philip Nigel

Award date:
1989

Awarding institution:
University of Bath

ACTIVE INTEGRATED OPTIC WAVEGUIDE / LASER STRUCTURES

Submitted by Philip Nigel Pennington
for the degree of Ph.D. of the University of Bath
1989.

ProQuest LLC
789 East Eisenhower Parkway
P.O. Box 1346
Ann Arbor, MI 48106-1346

This thesis is dedicated to my wife and parents
with thanks for their love and devotion.

Nigel Pennington, April 1990.

SUMMARY

One solution to the problem of routing optical signals between monolithically integrated active devices is to use a uniform active layer over the entire substrate. Waveguide sections then share a common cross-sectional geometry with the active sources, detectors, and modulators. The waveguide sections are electrically pumped in order to overcome the inherent losses at practical source wavelengths, to provide an active integrated-optic waveguide (AIOW) which is transparent to light from an integrated source.

In this thesis, the behaviour of the pumped AIOW in a variety of situations is considered in detail. The input optical coupling and source detuning for an integrated laser coupled to an AIOW are also examined. To fully model the waveguide behaviour, three new computer numerical models are presented: a Steady State Model, a Small Signal Dynamic Model, and a Large Signal Dynamic Model. In each case a travelling flux model which takes into account longitudinal variations in the flux and carrier density is developed. These models may be applied to a variety of geometries and conditions and are not restricted to the case of an AIOW

Throughout the thesis an engineering perspective is taken and the behaviour is examined from a systems point of view. Thus the inputs under direct control, optical input power, input wavelength and drive current, are considered. The thesis considers the affect of these inputs on key systems parameters such as: port to port gain, signal to noise ratio, harmonic distortion, and dynamic cross talk.

The results presented demonstrate the viability of using active waveguides to route signals in optical integrated circuits. The electrical pumping requirements are not excessive and near-linear operation can be achieved for a range of optical input powers and modulation frequencies.

CONTENTS :

1 SYMBOLS

α	=	absorption coefficient
$\bar{\alpha}$	=	modal absorption coefficient
α_{int}, α_c, α_{scat}	=	internal, cladding layer, scattering loss coefficient
δ	=	spontaneous emission coupling factor
γ	=	effective gain compression term
ε_o	=	permittivity of free space
ε	=	dielectric constant
Γ, Γ_T, Γ_L	=	combined, transverse, lateral optical confinement factor
ψ, ϕ	=	lateral, transverse field distribution
λ	=	wavelength
$\delta\lambda$	=	spacing between laser modes
μ_o	=	permeability of free space
η	=	Kane band tailing parameter
$\rho_c(E_c)$, $\rho_v(E_v)$	=	conduction, valence band density of states
ρ_f	=	charge density
σ	=	conductivity
ζ_1, ζ_2	=	facet reflectance damping factors
τ	=	decay time constant
τ_p	=	photon lifetime
τ_{sp}	=	spontaneous carrier lifetime
ω_l,ω_u	=	lower, upper break frequency
ω_m	=	angular modulation frequency of the optical input
ω_n	=	natural frequency of carrier density variations
χ	=	susceptibility
β, β_{eff}	=	modal, effective propagation constant
ΔP, ΔQ, ΔN	=	small perturbation values for flux and carrier density
Δt	=	large signal model time step

$\mathcal{E}_y(r,\phi)$	=	laser far field
c	=	velocity of light in a vacuum
d	=	active layer / waveguide thickness
d	=	gap width
e	=	electron charge
$\hat{e}$	=	unit electric field vector
f_1, f_2	=	conduction, valence band electron occupation probability
f_{cc}	=	free carrier absorption coefficient
f_m	=	Hertzian modulation frequency of the optical input
f_1, f_2	=	complimentary arbitrary functions
$g(N,\lambda)$	=	gross optical gain
h	=	Planck's constant
$h\upsilon$	=	photon energy
i	=	wavelength slot index
k	=	Boltzmann's constant
k	=	crystal momentum wavevector
k_o	=	free space wave number
$k_{1,2}$	=	coupling coefficient
l_m	=	length of the m^{th} pumped region
m	=	guide longitudinal region index
m	=	index of optical input modulation
m_e, m_{lh}, m_{hh}	=	effective electron, light hole and heavy hole mass
n_1, n_2, n_{eff}	=	cladding, core, effective refractive index
$\bar{n}, n_g$	=	modal, group refractive index
p, q	=	transverse, lateral waveguide mode number
p, q, n	=	small signal magnitudes of flux and carrier density
p_o	=	active layer doping density
p	=	crystal momentum
r	=	3-D spatial vector

r_{eff}, t_{eff}	=	effective reflectivity, transmittivity
t	=	time
v	=	group velocity of light in GaAs active layer
w	=	width of the buried channel active layer
z	=	longitudinal direction
A_{nr}	=	non-radiative recombination rate
A_{21}, B_{21},B_{12}	=	Einstein coefficients for transition probabilities
A_n,	=	polynomial coefficients for quasi-static analysis
ASE	=	amplified spontaneous emission
B_n	=	harmonic output power magnitude
B_r	=	bimolecular recombination rate
BW	=	spectral bandwidth
D, *B*	=	electric and magnetic flux densities
D, W	=	normalised waveguide thickness, width
D_n	=	harmonic distortion coefficient
E_g	=	forbidden band gap energy
E_1, E_2	=	ground, excited state energy
E, *H*	=	electric, magnetic field vector
F_c, F_v	=	non-equilibrium quasi-Fermi levels conduction, valence band
F_i	=	forward pass gain
G(ø)	=	Huygen's obliquity factor
G(N,λ)	=	net effective gain, after taking into account confinement factor and free carrier absorption $G(N,\lambda) = \Gamma \cdot g(N,\lambda) + f_{cc} \cdot (2N + p_o)$
I_{th}, (J_{th})	=	threshold current (density)
J	=	current density
J(z)	=	injected current density
L	=	device length
$M_{m,i}$	=	coherent gain for the m^{th} region and the i^{th} slot

$\overline{M_i}$	=	overall coherent single pass gain
$N(z,t)$	=	large signal carrier density
N_t	=	carrier density required for transparency
N_1, N_2	=	ground, excited state density of population
$N_s(\lambda)$, N_{bb}	=	noise spectral density function, broadband noise power
$N_{s,i}$	=	noise power in the i^{th} wavelength slot
N, P	=	total electron, hole density
P	=	induced electric polarisation
$P(E)$	=	energy density of photons (of energy, E)
$P(z,t,\lambda)$	=	time dependent forward travelling flux
$\hat{P}$, $\hat{Q}$, $\hat{N}$	=	steady state flux and carrier density
$\overline{P}$, $\overline{Q}$	=	spatially averaged flux
$\tilde{P}$, $\tilde{Q}$	=	temporally and spatially averaged flux
$Q(z,t,\lambda)$	=	time dependent backward travelling flux
R_1, R_2	=	reflectances of input and output ports respectively
R_{sp}	=	spontaneous emission rate
R_{12}, R_{21}	=	transition rates
S_m, X_m	=	self, cross coupling coefficient
SNR	=	signal to noise ratio
$S(N,\lambda)$	=	spontaneous emission factor : $\int_0^\infty S(N,\lambda)\, d\lambda = B_r \cdot N \cdot (N + p_o)$
T	=	Kelvin temperature
THD	=	total harmonic distortion
X_i^*	=	spatially averaged flux
$Z(h\upsilon_{21})$	=	$(8\pi n^2 \cdot h\upsilon_{2,21}/c^3)$ = ratio of spontaneous to stimulated emission probabilities

2 INTRODUCTION

2.1 General

In 1969 Stewart Miller presented the seminal paper entitled 'Integrated Optics : an introduction' [1], where he outlined a proposal for using dielectric waveguides as 'laser circuitry' to route optical signals. The paper proposed the integration of distributed feedback lasers, modulators, detectors, couplers, splitters, filters and waveguides.

In figure 2.1, an optical communications systems of the type conceived by Miller is shown. In the transmitter portion, two distributed feedback integrated laser sources are shown, emitting at different optical wavelengths λ_1 and λ_2. The modulated output from the lasers is coupled into a common dielectric waveguide. As the light emitted by each laser is at a different wavelength, the signals may be multiplexed - ie many channels can be transported in the waveguide simultaneously. In the receiver portion, local oscillator distributed feedback lasers provide heterodyne detection of the multiplexed signals.

In the conclusion to [1] Miller writes "Work is just beginning in the directions indicated, and we have identified goals rather than accomplishments. We recognise these are difficult goals; but we believe they are worth the serious effort required to achieve them". To date Miller's goals have still to be fully accomplished. One of the major stumbling blocks to achieving the goal of the monolithic integration of optical components is the integration of the waveguiding sections with other devices in a planar geometry. In this thesis, the concept of using a pumped active waveguide as a solution to this problem is examined in detail.

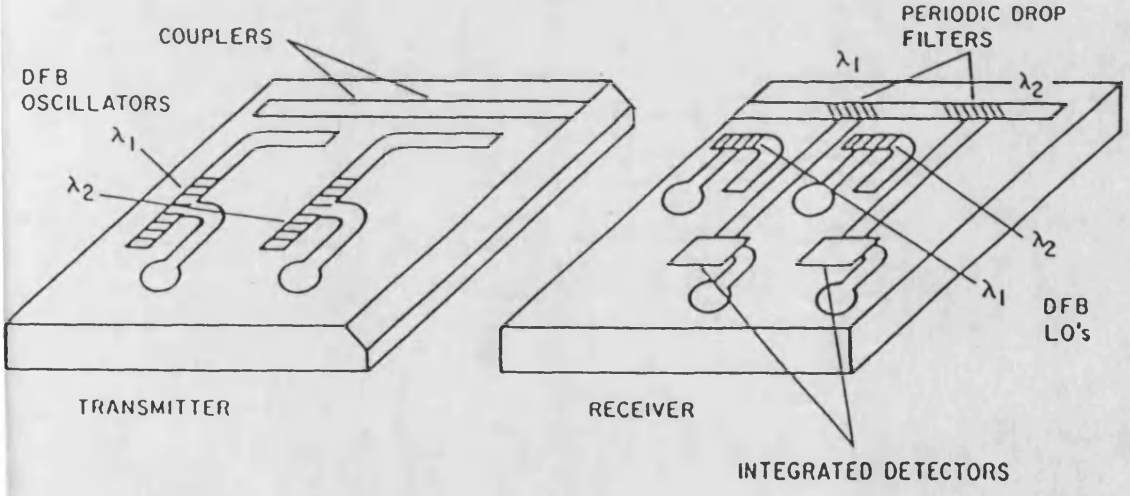

Figure 2.1 : Optical Communications systems using monolithic integratic optic components, as conceived by Miller (3).

2.1.1 Integrated Optics

Since the advent of modern optical technology in the early 1960s with the proposal and subsequent development of the solid-state laser [2], the prospect of integrated optics systems has been recognised [1,3,4]. In such systems, the transmission and processing of information is performed using optical signals, rather than electrical currents. This has led to the development of the optical integrated circuit (OIC), where several optical components are fabricated on a common substrate. In comparison with the electrical integrated circuit, the OIC has a significantly increased bandwidth and the ability to support muliplexing in both (optical) wavelength and (modulation or carrier) frequency.

There are two major branches of integrated optics technology; passive and active. Passive materials such as quartz and Lithium Niobate ($LiNbO_3$), in general, are incapable of light generation, and rely on electro-optic and acousto-optic effects for signal processing. Active materials such as Gallium Arsenide (GaAs) and other direct bandgap semiconductors are capable of light generation. To date, a hybrid approach has been most profitable in developing practical integrated optics systems [2-4] where active devices are used as optical sources and detectors, but passive devices are used in the intermediate signal processing sections.

The rationalé behind the hybrid approach is that it is possible to optimise the performance of a particular integrated circuit element by choice of material. In addition, using passive materials it is relatively straight forward to manufacture low-loss waveguide sections to route the optical signals between the circuit elements. However this approach requires that the various circuit elements must somehow be mechanically aligned and bonded to optical tolerances. Although several sophisticated systems have been developed using the hybrid approach, it is generally seen as a stop gap towards the ultimate goal of monolithic optical integrated circuits.

In order to achieve the objective of monolithic optical integrated circuits where all the devices are fabricated on a single substrate, an active material must be used. To date, devices fabricated from GaAs have dominated the research effort in this area.

Recently devices based on Indium (Gallium Arsenide) Phosphide (InP/InGaAsP) have become of increasing significance because of their application to long haul optical fibre communications. The work in this thesis is concentrated on a proposed building block of GaAs monolithic optical integrated circuits, described below.

2.1.2 Scope of the thesis

One solution to the problem of routing optical signals between monolithically integrated active devices is to use a uniform active layer over the entire substrate. Waveguide sections then share a common cross-sectional geometry with the active sources, detectors, and modulators. Such a method has clear fabrication advantages over the hybrid approach discussed above. However, the waveguide sections must be electrically pumped in order to overcome the inherent losses at practical source wavelengths, to provide an active integrated-optic waveguide (AIOW) which is transparent to light from an integrated source.

For high efficiency operation, it is assumed that a ridge guide or buried heterostructure geometry is used, as shown in figures 2.2(a) and 2.2(b) respectively. With such structures good optical and electrical confinement is achieved, with the primary optical guiding mechanism being index guiding. The three basic integrated laser/waveguide structures considered are shown in figure 2.3. In all of these structures, the source and waveguide share a common geometry in the lateral and transverse directions. Thus the guiding mechanism and the optical guide modes supported by the source and waveguide modes will be virtually identical.

In figure 2.3(a) a conventional Fabry-Perot laser is coupled to a pumped AIOW across an etched or milled gap. This type of structure has the immediate attraction of ease of fabrication but the performance of Fabry-Perot lasers with etched or milled facets is poor. An improved solution is to use either a distributed Bragg reflector (DBR) to replace the laser facets, or to integrated a distributed feedback (DFB) laser with the AIOW, as shown in figures 2.3(b) and 2.3(c) respectively. DBR and DFB lasers are

Figure 2.2 : Schematic cross-sectional structure of integrated laser/waveguide

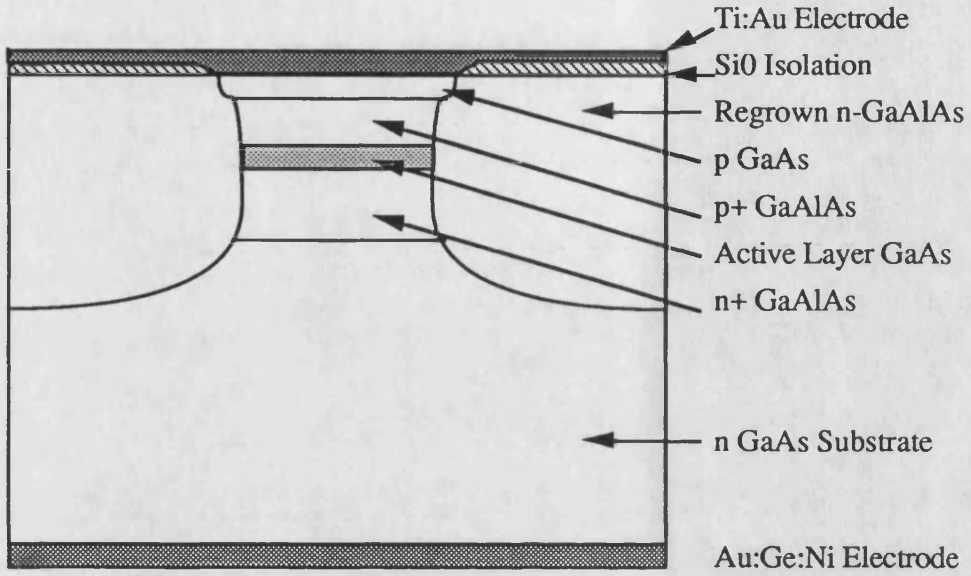

(a) : Buried Heterostructure for integrated laser/waveguide structures.

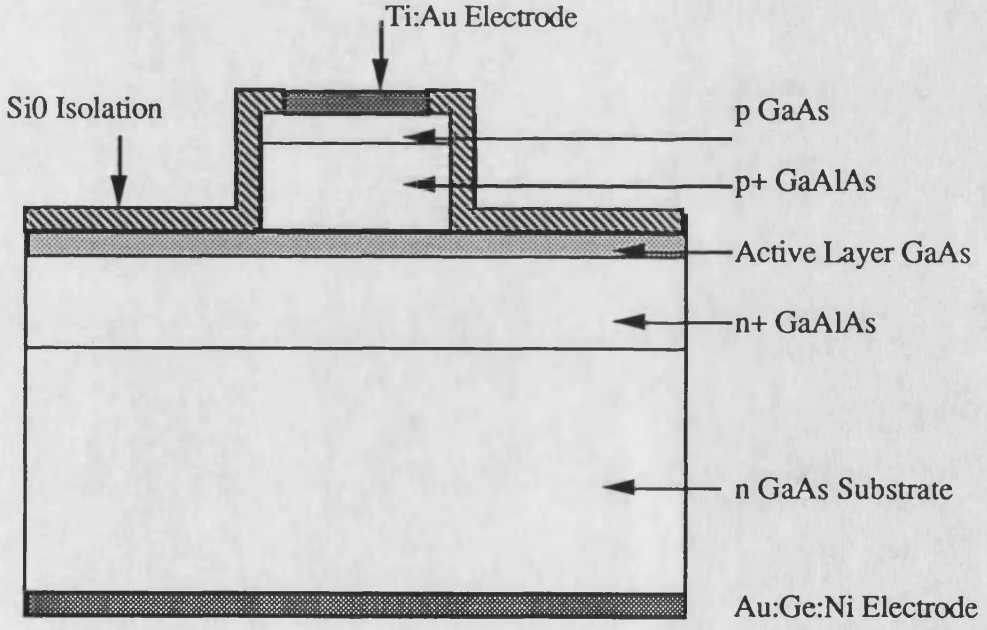

(b) : Ridge guide for integrated laser/waveguide structures.

Figure 2.3 : Schematic representation of an active integrated optic waveguide (AIOW) and integrated laser sources.

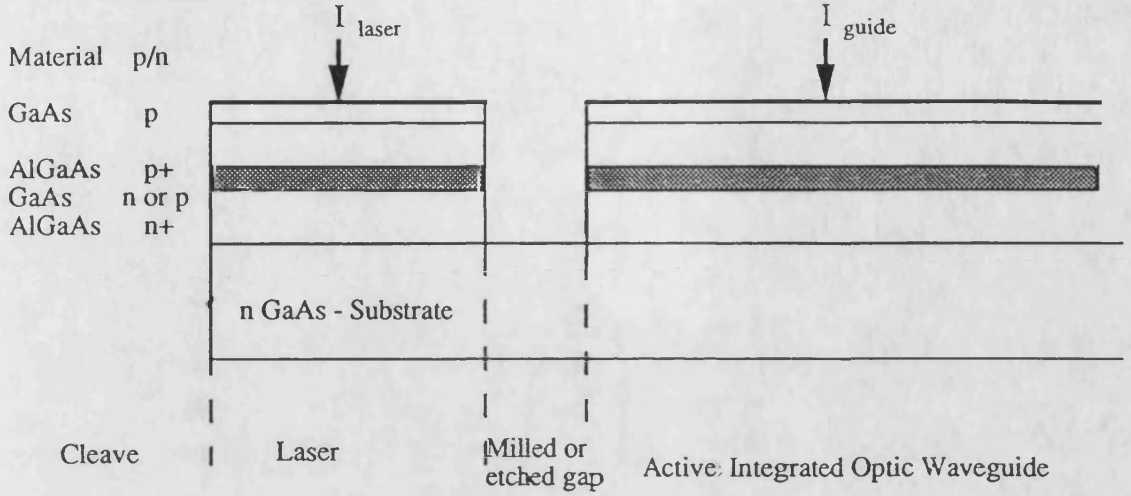

(a) Fabry–Perot laser coupled by etched or milled gap,

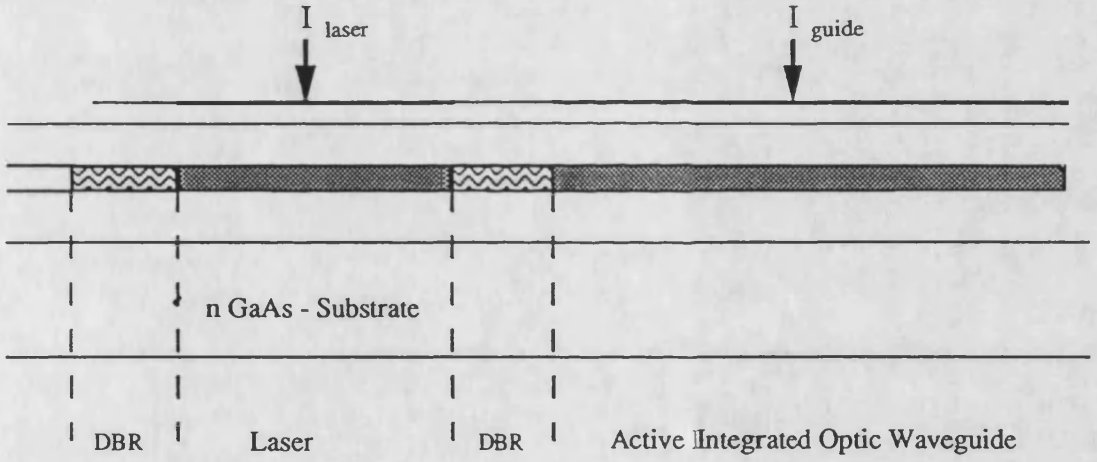

(b) Directly coupled DBR Laser,

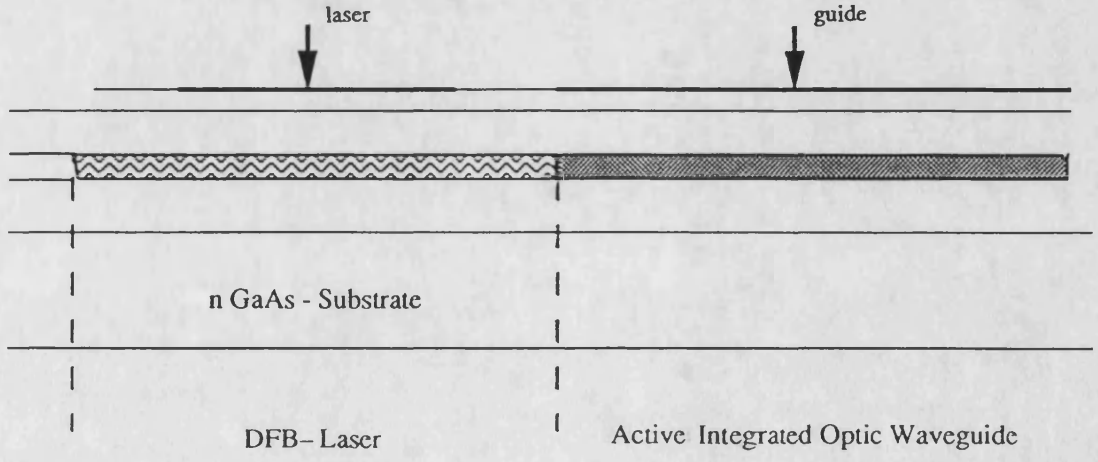

(c) Directly coupled DFB Laser.

ideal sources for monolithic AIOCs because they do not require the formation of 90° facets to provide the necessary optical feedback for laser action.

2.1.3 Objectives of the thesis

It is the intention of this thesis to describe in depth the behaviour of the laser/ waveguide systems described above, fabricated from GaAs. The use of a pumped AIOW presents significant problems however, not least of which is amplified spontaneous emission (ASE) generated and amplified by the guide which gives rise to an unwanted optical noise signal. Further, the coupling between the photon flux and carrier density gives rise to a non-linear variation of guide characteristics with optical input power. This inevitably leads to distortion of optical signals.

The majority of the thesis is concentrated on the behaviour of a pumped AIOW in response to an ideal laser source, and examines its suitability as a circuit element for routing optical signals. The feasibility of coupling the light from the Fabry-Perot laser source into a pumped AIOW across an etched or milled gap is also considered, including the efficiency of the coupling and the detuning effect on the laser source.

Throughout the thesis an engineering perspective is taken and the behaviour is examined from a systems point of view. Thus the inputs under direct control, optical input power, input wavelength and drive current, are considered. The thesis considers the affect of these inputs on key systems parameters such as: port to port gain, signal to noise ratio, harmonic distortion, and dynamic cross talk.

2.2 Historical Perspective

The early developments of integrated optics as a general topic, including both passive and active components, are described in great detail in two excellent review books edited by Tamir [3], and Hunsperger [4]. These review books cover the major aspects of integrated optics, it's development and applications over the period from 1969-1979.

The first practical advances towards monolithic AIOCs began in the early and mid 1970s after the successful room temperature operation of the heterostructure laser in 1969 [5]. The devices fabricated by Reinhart et al [6], Suematsu et al [7] and Campbell et al [8] are typical of the first monolithic integrated laser/waveguide structures. In each case, the laser light is coupled into a low loss 'passive' GaAlAs waveguide, either directly [6] or by mode coupling [7,8]. The waveguide is said to be passive as the aluminium content is varied in the waveguiding layer such that its band gap is greater than that of the laser active layer. Thus the absorption losses of the waveguiding layer are reduced to a level which is acceptable for very short guides. Such a passive waveguide is incapable of providing optical gain at the laser source wavelength.

There are three major drawbacks associated with the laser/waveguide structures presented in [6–8]. First, the structures are technically complex to fabricate as they require multi-heterostructures [7,8], or selective etching and regrowth [6]. Such complexity inevitably leads to reduced yield, device defects and makes consistent manufacture difficult. Secondly, where a traditional Fabry-Perot laser is used [7,8], the efficiency for coupling of light into the waveguide is poor (<5% [8]) as the majority of the light is coupled out of the laser facets. Thirdly, the use of a lossy passive waveguide implies that optical power will be lost, requiring eventual regeneration of optical signals

As the active devices presented in [6–8] are integrated with passive GaAlAs waveguides they are not regarded as true monolithic AIOCs. The first reported

examples of the monolithic integration of more than one active device fabricated from GaAs were presented by Aiki et al [9] in 1976 and Merz et al [10] in 1977. In [9] Aiki et al report the integration of 6 DFB lasers multiplexed into a single low loss passive waveguide. Each laser is separately driven (from an off-chip source) and there is a 2 nm spacing between the operating wavelength of each laser, allowing wavelength division multiplexing (WDM) of signals. The lasers have a separate confinement heterostructure (SCH) whereby light is coupled directly into the passive waveguide, as shown in figure 2.4.

In [10] Merz et al. report the first case of the monolithic integration of the basic communications system of a laser, passive waveguide and detector. The AIOC was fabricated by wet chemical etching and is shown schematically in figure 2.5. Rather than use the then immature DFB technology adopted by Aiki et al, the integrated laser source has a conventional Fabry–Perot cavity. One facet is formed by the traditional cleaving method whilst the other is formed by wet chemical etching.

Although these two devices demonstrated the overall feasibility of monolithic AIOCs they had a poor overall quantum efficiency (<7% for [9] and <10% for [10]) due in part to the passive waveguide losses, and immature fabrication technology. The period from 1977 through to the mid 1980s saw the continued development of these original monolithic AIOCs [11–13], the improvement of low loss waveguides [14, 15], and the maturation of fabrication techniques (such as molecular beam epitaxy (MBE) [16], and metal-organic chemical vapour deposition (MOCVD) [17]).

At the same time, integrated *optoelectronics* circuits emerged, where advantage is taken of the fact that GaAs has good electronic properties, to integrate the required electronic driving circuits for the optical components on the same monolithic substrate [18]. The main body of work on optoelectronics has concentrated on the production of stable laser sources [19], repeaters [20] and detectors [21] for optical fibre communications. In [19] Matsueda et al present an integrated laser, detector and driving circuit, where the laser and detector are defined by etching a gap perpendicular to the heterolayers. The differentiation between source and detector is simply determined by

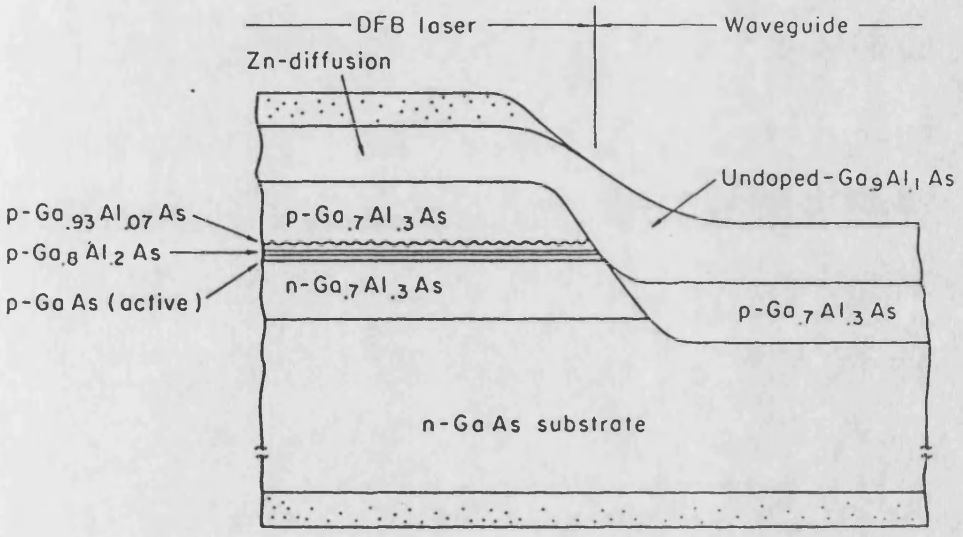

Figure 2.4 : Distributed Feedback (DFB) laser with integrated passive waveguide with separate confinement heterostructure (SCH), after [9].

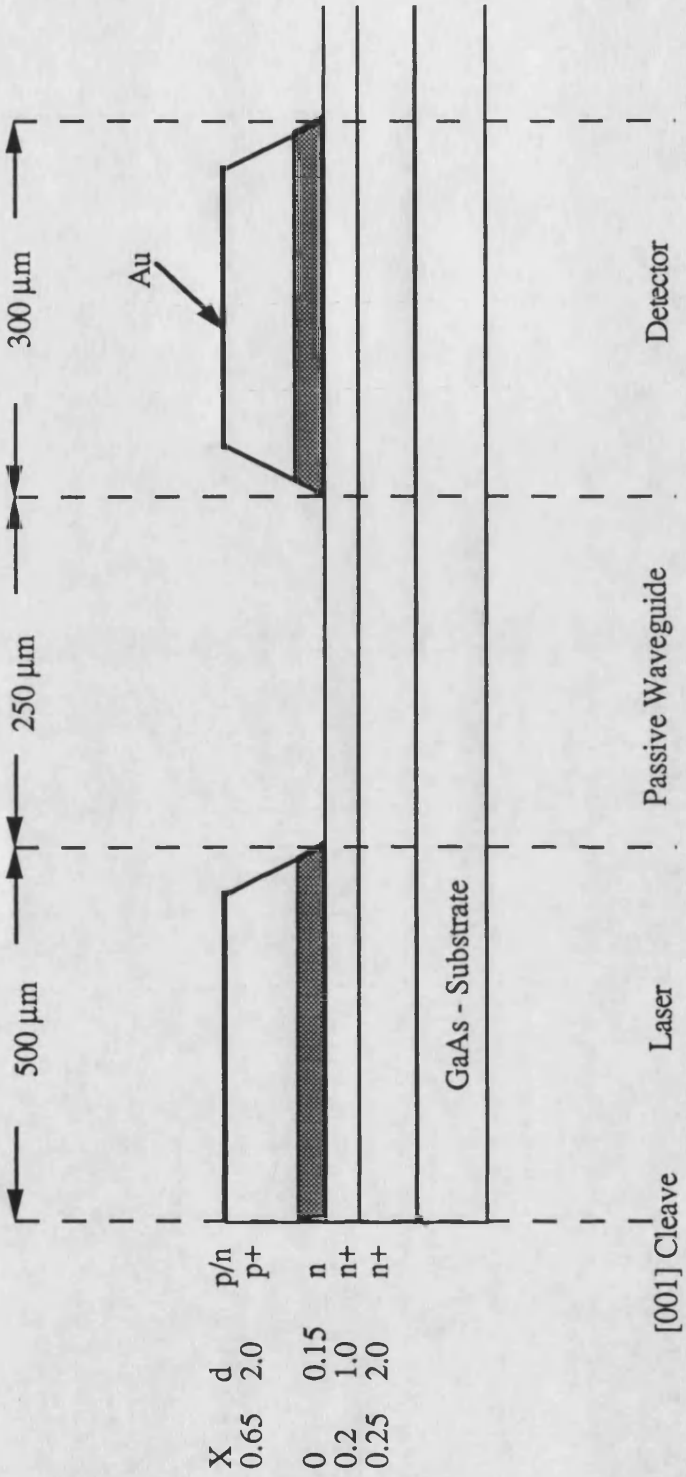

Figure 2.5 : Schematic representation of an integrated Fabry-Perot laser, passive waveguide and detector, after [10].

the bias applied to the device. Ultimately, it is desirable that any AIOC will have the required electronic driving circuits integrated on the same substrate. However, the marrying of the disparate technologies of optic and electronic components presents significant fabrication difficulties which leads to high incidence of material defects [18, 21] and consequently low device lifetimes [19].

One device which is of interest as an antecedent of the AIOW is the travelling wave laser amplifier (TWLA). The motivation for developing the TWLA is to provide an all optical amplifier for long and short haul communications systems to regenerate signals which have decayed due to propagation losses [22]. However, it is clear that TWLAs will have integrated optic applications [24]. The properties of the TWLA have been studied in considerable detail both practically [22, 23] and theoretically [24–27] as a discrete element, and these studies are used to verify the models developed in this thesis for the AIOW.

A schematic diagram of a TWLA is shown in figure 2.6. Light is injected into a pumped cavity which has high forward pass gain (typically 20–30 dB) but is prevented from oscillating due to very low end reflectances (< 1%). Input signals are optical amplified by the process of stimulated emission in the TWLA (see section 2.4.3). The AIOW in contrast has unity gain (0 dB) and the input signal is sustained rather amplified.

To date most authors have accepted the received wisdom that passive waveguides must be used in an AIOC. Indeed only a few papers have been presented using a pumped active waveguide [see for example 28, 30]. In [28] Kambasyshi and Sarma discuss the possibility of using gain-guiding in the lateral direction (ie in the plane of the heterolayers) to route signals in a heterolayer substrate. In their proposal, the waveguide is defined purely by the presence of gain in the active layer underneath a stripe contact. However, gain-guiding is particularly unstable especially if the guide is just transparent or has loss [29]. To ensure a stable waveguide, index guiding is assumed throughout this thesis in both the lateral and transverse directions.

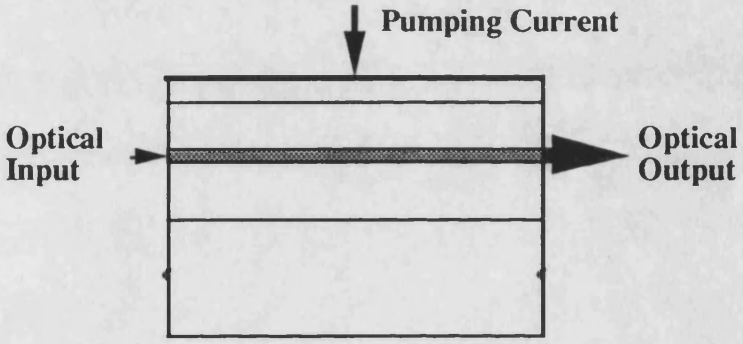

Figure 2.6 : Schematic representation of a Travelling Wave Laser Amplifier (TWLA).

A recent example of an integrated laser/waveguide structure with an active waveguide was presented by Garratt et al [30], where two DFB lasers are integrated with a pumped 'Y'-rib guide coupling section. Clearly, this structure owes a great deal to that presented by Aiki et al., but a uniform heterolayer structure is used over the entire substrate rather than the SCH in [9].

2.3 Structure

In this chapter an introduction to the subject of Active Integrated Optics has been presented. In the main body of the thesis, mathematical models are developed to examine the behaviour of a laser/waveguide system. In chapters 3 and 4 a discussion of the basic theoretical aspects of the behaviour of light in GaAs devices is presented, with particular emphasis placed on the GaAs AIOW. The models presented in chapters 5 through to 9 are all based on the theory presented in chapters 3 and 4.

The major difference between active and passive systems is that light is emitted in an active element. Therefore, in order to predict the behaviour of an active laser/ waveguide system, it is necessary to characterise the behaviour of spontaneous emission and stimulated gain with both carrier density and wavelength. Chapter 3 begins with the derivation of the basic expressions for a two-level atomic system in thermal equilibrium. This analysis is then extended to a multi-level system, such as that found in GaAs and expressions for stimulated and spontaneous emission rates are determined. The effect of semiconductor bandstructure, band tails and **k** selection on these expression is considered. Finally, the stimulated gain and spontaneous emission model used in the rest of the thesis is presented with a discussion of the aspects of that model.

The behaviour of light in the guiding geometry proposed (either a buried heterostructure or an etched ridge guide) is considered in chapter 4. Starting from Maxwell's equations for a dielectric, non-magnetic medium, the optical behaviour of the guide is analysed. The wave equation which describes the propagation of light in the lateral, x, transverse, y, and longitudinal, z, dimensions is derived from Maxwell's equations. Using the effective dielectric constant (EDC) method, the lateral and transverse properties are reduced to two convenient parameters, the effective dielectric constant and the confinement factor.

Incorporating the results from chapter 3 and the behaviour of a heterostructure junction discussed above, the photon and carrier conservation rate equations are

developed. The final element of chapter 4 is the discretisation of the rate equations in wavelength to make their solution more tractable to numerical modelling. These discretised rate equations underpin the models developed in subsequent chapters.

In chapter 5 two aspects of coupling light from a source device into a waveguide are examined. Firstly, the optical field coupled into the waveguide and secondly, the detuning effect on the source. In this chapter, the originally proposed case of a semiconductor laser coupled to a pumped waveguide, across an etched or milled gap is considered. The propagation of light in the gap is modelled by considering the far field from a heterostructure laser to be a modified Fourier transform of the near field.

To determine the detuning effects on a laser source the standard, spatially averaged laser rate equations are used. Rather than quoting these equations in their standard form, they are derived from the full spatial rate equations developed in chapter 4. This is to show the range of validity of the two sets of commonly used rate equations and to establish some key concepts.

From chapter 6 onwards, the work is concentrated on the examination of the behaviour of the AIOW as part of an integrated-optic communications system. Three new, travelling flux models of an active waveguide are presented: in chapter 6 a steady state model is developed, whilst small signal and large signal dynamic models are developed in chapters 7 and 8 respectively. In each case, the development of the model starts from the discretised rate equations derived in chapter 4.

In chapter 6 the static characteristics of an AIOW are examined in depth. The main purpose of the chapter is to determine the feasibility of using a pumped waveguide as a circuit element. Thus several key systems parameters are examined, such as:

- The electrical power required to achieve transparency
- The effect of optical input power on the transparency
- The nature of noise in an active waveguide

- The behaviour of the fundamental transmission properties of the guide as a function of optical input power, guide dimensions and electrical pumping
- The harmonic distortion that would be experienced by low frequency, modulated optical input.

In addition the basic modelling techniques which apply to all three travelling flux models are discussed, together with any assumptions required to model the highly non-linear behaviour of an active waveguide.

The small signal dynamic model introduced in chapter 7 uses the fairly conventional small signal analysis (SSA) technique. However, in this case the technique is applied to the case of a modulated optical, rather than electrical, input. In the SSA technique, the device parameters are assumed to be separable into two parts, steady state and time varying. The steady state solution is obtained using a modified version of the model presented in chapter 6. Although the scope of a small signal model is limited, it does provide an excellent description of the underlying dynamic behaviour of the carrier and flux densities. In chapters 8 and 9, where the large signal model is used, the small signal analysis is often invoked to explain the observed results.

The final model of the three is the large signal dynamic model and is detailed in chapter 8. An analytic solution to the variation of the time dependent optical flux in the guide is determined, whilst a finite difference technique is employed to solve the carrier continuity equation. Using the steady state solution as the starting point, the temporal fluxes are allowed to propagate along the waveguide over discrete steps in time.

In chapter 8, in the main, the model is used to determine the response of the waveguide to single tone, sinusoidally modulated optical inputs. The response of the waveguide characteristics to variations in optical input power, modulation depth and modulation frequency is examined in considerable detail. In conjunction with the small signal expressions developed from chapter 7, the results obtained are used to determine the dynamic behaviour of an active waveguide. The relationship between the modulation inputs listed above and the harmonic distortion caused by the non-linear

behaviour of the guide is analytically determined, and compared with the obtained results.

One of the main advantages of the active waveguide is that it is possible to use a wavelength division multiplexing (WDM) scheme; where signals with separate optical wavelengths can be processed in one circuit element and still be kept separate. In chapter 9, the most basic WDM system is considered where two sinusoidal inputs are applied to the waveguide at separate wavelengths. Due to the non-linear coupling between the photon flux and carrier density, two such input signals interact, giving rise to intermodulation distortion and cross talk. Using the flexibility of the large signal model the effect of optical input power, modulation depth and interaction length upon the intermodulation and cross talk is examined.

The final part of the thesis is a discussion of the overall conclusions which may be drawn from the work, together with some recommendations for further aspects which may be pursued.

2.4 Publications and Conference Papers

To date two journal papers and three conference papers have been presented on the basis of the period of research and the work contained in this thesis.

2.4.1 Journal Papers

- ORMONDROYD, R.F., PENNINGTON, P.N., and PERKINS, M.C.J., 'Nonlinear static characteristics of monolithic active integrated-optic waveguides',
  IEE Proc. J, 1989, 136, (1), pp59-71.

Gives a comprehensive description of the Steady State Model and summarises the key results from Chapter 6.

- PENNINGTON, P.N. and ORMONDROYD, R.F., 'Large-Signal modulation response of active integrated-optic waveguides',
  IEE Proc. J, 1990, 137, (1), pp11-20.

Gives a comprehensive description of the Large Signal Dynamic Model and summarises the key results from Chapter 8. The Small Signal Analysis is described in the Appendix to this paper.

2.4.2 Conference Papers

- PENNINGTON, P.N. and ORMONDROYD, R.F., 'The modulation response of active integrated-optic waveguides',
  Presented at SIOE '89, Paper No.33, Cardiff 20-21 March 1989.

Gives a brief introduction to the Small Signal Model and summarises the key results from Chapter 7.

- ORMONDROYD, R.F., and PENNINGTON, P.N., 'Monolithic Active Integrated Optics',
  Presented at IEE Colloquium on "Integrated Optics", Digest No.1989/93, pp10/1-10/6, London 6 June 1989.

Gives a general summary of the modelling procedure adopted for the Static and Large-Signal Dynamic Models, with key results from Chapters 6 and 9.

- ORMONDROYD, R.F., and PENNINGTON, P.N., 'Non-Linear Static and Dynamic Characteristics of Monolithic Active Integrated-Optic Waveguide (AIOWs)',
  Presented at ISSSE '89 (Invited Late Paper), Erlangen West Germany, 18-20 September 1989.

Gives a general summary of the modelling procedure adopted for the Static and Large-Signal Dynamic Models, with key results from Chapters 6 and 8.

References, Chapter 2

1 MILLER, S.E., 'Integrated Optics : An Introduction',

Bell Syst. Tech. J., 1969, 48, pp2059-2069.

2 MAIMAN, T.H., 'Stimulated optical modulation in ruby masers',

Nature, 1960, 187, p463

3 TAMIR, T., 'Integrated Optics' 2nd ed- Topics in Applied Physics Vol 7,

Springer Verlang, Heidelberg, 1979.

4 HUNSPERGER, 'Integrated Optics : Theory and Practice' 2nd ed.

Springer Verlang, Heidelberg, 1982.

5 ALFREROV, Z.I., ANDRREEV, V.M., KOROL'KOV, V.I., PORTNOI, E.L., and TRETYAKOV, 'Injection properties of n-$Al_xGa_{1-x}As$ p-GaAs Heterojunctions',

Sov. Phys. Semicond., 1969, 2, p843.

6 REINHART, F.K., LOGAN, R.A., and SHANK, C.V., 'GaAs–$Al_xGa_{1-x}As$ injection lasers with distributed Bragg reflectors',

Appl. Phys. Lett, 1975, 27, (2), pp241-243.

7 SUEMATSU, Y., YAMADA, M., and HAYASHI, K., 'A Multi-Heterostructure AlGaAs laser with integrated twin guide',

IEEE Proc., 1975, 63,(1), p208.

8 CAMPBELL, J.C., BELLAVANCE, D.W., 'Monolithic laser/waveguide coupling by evanescent fields',

IEEE J. Quantum Electron, 1977, QE-13, (4), pp253-255.

9 AIKI, K., NAKAMURA, M., and UMEDA, J., ' Frequency multiplexing light source with monolithically integrated distributed feedback diode lasers',

Appl. Phys. Lett, 1976, 29, pp506-508.

10 MERZ, J.L., LOGAN, R.A., and SERGENT, A.M., 'Integrated GaAs–AlGaAs injection laser and detectors with etched reflectors',

Appl. Phys. Lett, 1977, 30, pp530-533.

11 MERZ, J.L., LOGAN, R.A., and SERGENT, A.M., 'GaAs integrated optical circuits by wet chemical etching',

*IEEE J. Quantum Electron, 1979, **QE-15**, (2), pp72-82.*

12 KISHNO, K., SUEMATSU, Y., UTAKA, K., KAWANISHI, 'Monolithic integration of laser and amplifier/detector by twin–guide structure',

*Japan J. Appl. Phys., 1978, **17**, (3), pp589-590.*

13 SHAMS, M.K., NAMIZAKI, H., and WANG, S., 'p–n junction detector directly integrated with $(Ga_{1-x}Al_x)As$ LOC–DBR laser',

*Appl. Phys. Lett, 1978, **32**, pp179-181.*

14 ERMAN, M., VODJDANI, N., THEETEN, J.B., and CABANIE, J.P., 'Low loss waveguides formed by anodization of epitaxial GaAs on $Al_xGa_{1-x}As$ layers',

*15 Appl. Phys., 1975, **57**, (3), pp740-754.*

16. TSANG, W.T., 'Recent progress in growing reliable (AlGa)As DH-lasers by molecular beam epitaxy for optical communications systems',

*J. Cryst. Growth., 1982, **56**, (2), pp464-74.*

17 ZAVADA, J.M., JENKINSION, H.A., COMAS, J., and SCHMIDT, R., 'Optical waveguiding properties of molecular-beam epitaxy multilayer structures',

*18 Opt. Soc Am, 1982, **72**, p1821.*

19 WALKER, R.G., and GOODFELLOW, R.C., 'Attenuation measurements on MOCVD–grown GaAs/GaAlAs optical waveguides',

*Electron. Letts, 1983, **19**, (7), pp590-592.*

20 BAR-CHAIM, N., MARGALIT, S., YARIV, A. and URY, I., 'GaAs Integrated Optoelectronics',

*IEEE Trans Electron Devices, **ED-29**, (9), 1372-1381,*

21 MATSUEDA, H., SASAKI, S. and NAKAMURA, M., 'GaAs Optoelectronic Integrated Light Sources',

*IEEE J. Lightwave Tech., 1982, **LT-1**, (1), pp261-269.*

20 CARTER, A.C., FORBES, N., and GOODFELLOW, R.C., 'Monolithic integration of optoelectronic, electronic and passive components in GaAlAs/GaAs multilayers',

Electron. Letts, 1982, 18, (2), pp72-74.

21 FORREST, G., 'Monolithic optoelectronic integration : a new component technology for lightwave communications'

IEEE J. Lightwave Tech., 1985, LT-3, (6), pp1248–1263.

22 YAMAMOTO, Y., 'Noise and error rate performance of semiconductor laser amplifiers in PCM–IM optical transmission systems',

IEEE J. Quantum Electron, 1980, QE-16, (10), pp1073-1081.

23 MUKAI, T. and YAMAMOTO, Y. : 'Gain, frequency bandwidth and saturation output power of AlGaAs DH laser amplifiers',

IEEE J. Quantum Electron., 1981, VOL QE-17, pp1028-1034.

24 SIMON, J.C., 'Semiconductor laser amplifier for single mode optical fibre communications',

J. Opt. Commun, 1983, 4, (1), pp51-62.

25 MARCUSE, D., 'Computer model of an injection laser amplifier',

IEEE J. Quantum Electron, 1983, QE-19,(1),pp63-73.

26 ADAMS, M.J., COLLINS, J.V. and HENNINGS, I.D., 'Analysis of semiconductor laser optical amplifiers',

IEE Proc. Part J, 1985, 132, (1), pp58-63.

27 LOWERY, A.J. : 'New inline wideband dynamic semiconductor laser amplifier model',

IEE Proc. J, 1988, VOL 135, pp242-250.

28 KAMBAYASHI, T., and SARMA. J., 'Spontaneous emission noise distribution from a gain–guided multimode waveguide',

IEEE J. Quantum Electron, 1983, QE-19, (6), pp1084-1091.

29 ADAMS, M.J., 'An Introduction to Optical Waveguides',

Wiley, New York, 1981.

30 GARRETT, B., MOULE, D.J., ARMISTEAD, C.J., BOURNE, W.O., CHAMPELOVIER, J., BAULCOMB, R.S., and COLLAR, A.J. : 'A monolithically integrated two wavelength DFB laser source for WDM optical communications systems',

Presented at SIOE'89, Cardiff 20-21 March 1989.

3 STIMULATED GAIN AND SPONTANEOUS EMISSION IN SEMICONDUCTOR MEDIA.

3.1 Introduction.

In order to understand the characteristics of a pumped waveguide, it is necessary to have an understanding of the electron-photon interactions in the active region of the guide. In the double heterostructure waveguides described in chapter 2, the active layer is formed from lightly doped p- or n-type GaAs surrounded by heavily doped GaAlAs cladding layers.

The energy diagram for a double heterolayer junction when no bias is applied is shown is figure 3.1(a). The difference in the quasi-Fermi levels causes diffusion of carriers across the junction to restore equilibrium and give the energy distribution shown. In this unpumped state, a GaAs active layer has net loss to light with photon energies, $h\upsilon$, greater than or equal to the forbidden band gap energy, E_g, between the conduction and valence bands. It should be noted that E_g, is greater in the cladding layers than in the active layer.

When a forward bias is applied to the junction, a step in the quasi-Fermi level occurs, causing extra carriers to flow into the active region, as shown in figure 3.1(b). However, the greater band gap of the cladding layers causes a potential barrier, preventing the carriers diffusing through to the cladding layers. The electrons and holes are confined to the active layer.

In materials such as GaAs, electrons and holes confined to the active layer may recombine either non-radiatively or radiatively. For radiative recombinations, the energy associated with an electron-hole pair can be approximated to the forbidden band gap energy E_g. This energy is released by the formation of a photon of frequency υ, or wavelength λ, satisfies the energy conservation equation $E_g = h\upsilon = hc/\lambda$ (h is Planck's constant). Radiative recombination occurs through either spontaneous emission, or stimulated emission. In the case of spontaneous emission, the emitted photon has a

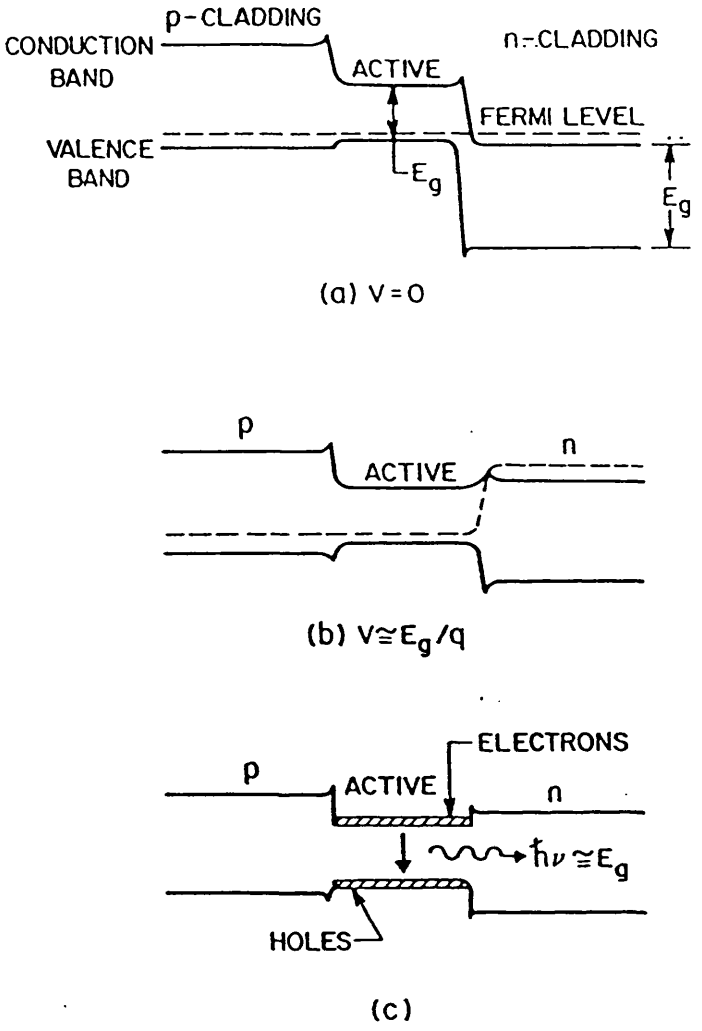

Figure 3.1 : Energy–band diagram of a double-heterostructure laser.

(a) With zero bias.

(b) With forward bias, V.

(c) Showing the confinement of carriers to the active layer.

random phase and direction. Stimulated emission, by contrast, is triggered by the presence of an existing photon in the active layer. The emitted photon has an identical phase, energy and direction of propagation as the existing photon.

The intention of this chapter is to give an introduction to the subject of stimulated gain and spontaneous emission, for the particular case of a pumped GaAs waveguide. Radiative recombination in semiconductor material has been the subject of extensive research effort over a considerable period of time. Therefore, the reader is referred to standard textbooks and the references therein [1-3], for a complete picture of active semiconductor device physics.

The chapter begins with the derivation of the basic expressions for a two-level atomic system in thermal equilibrium interacting with the radiation from an ideal blackbody. This analysis is then extended to a multi-level system, such as that found in GaAs and the condition for net stimulated emission is obtained, along with the basic transition probabilities. In section 3.4 the effect of crystal momentum **k** is included by incorporating all energy levels in the form of the electron density if states. Expressions for stimulated and spontaneous emission rates are determined in section 3.5. These expressions require evaluation of the conduction and valence band density of states, as well as the calculation of basic transition probabilities. Finally, the stimulated gain and spontaneous emission model used throughout this thesis is presented in section 3.6.

3.2 Optical Gain in a Two Level Atomic System.

3.2.1 Introduction : Two-Level Atomic System.

In this section a two-level atomic system in thermal equilibrium will be considered. The atoms are distributed between the ground state, 1 with energy E_1 and the excited state, 2 with energy E_2. The density of population in the ground and excited states is given by N_1 and N_2 respectively. It is possible to examine this system using the basic treatment conceived by Einstein [4], as an introduction to more complex lasing media.

3.2.2 Absorption, Spontaneous Emission and Stimulated Emission.

There are three processes which must be considered. If a photon of energy, $h\upsilon_{21} = E_2 - E_1$ is incident on the system, it may be **absorbed** by promoting an electron to the upper energy level from the lower, figure 3.2(a). The system is now out of thermal equilibrium and the electron may fall back to the ground state with the *spontaneous emission* of a photon of energy $h\upsilon_{21}$, figure 3.2(b). This occurs in a mean time τ_{sp}, the spontaneous carrier lifetime.

Alternatively, a photon of energy $h\upsilon_{21}$ may be incident on the excited system, causing an electron to make the downward transition with the *stimulated emission* of a second photon. This second photon has not only the same energy as the incident photon but also the same direction, phase and polarisation.

The rate of these three key processes are determined by the populations N_1 and N_2, the energy density of photons of energy $h\upsilon_{21}$, $P(E_{21})$ and the transition probabilities, A_{21}, B_{21} and B_{12}. The total rate of upward transitions from ground state to excited state is defined as,

$$R_{12} = B_{12} \cdot N_1 \cdot P(E_{12}) , \qquad (3.1)$$

(a) Absorption

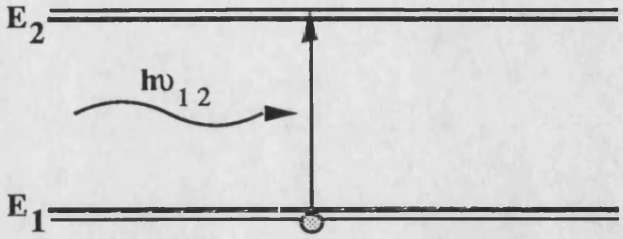

(b) Spontaneous Emission

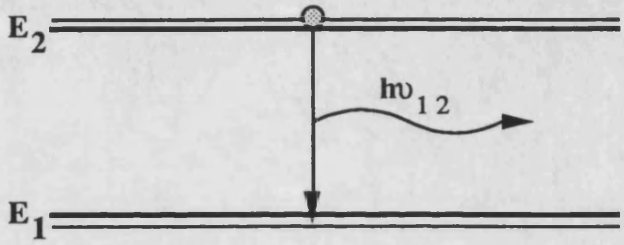

(c) Stimulated Emission

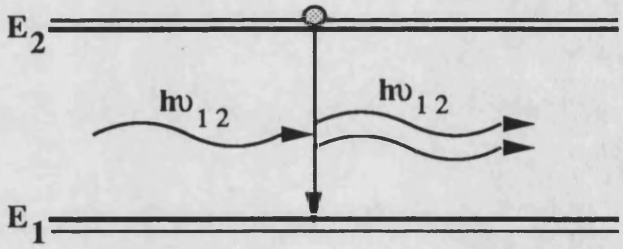

Figure 3.2 : Radiative Processes in the Two-Level Atomic System ,

(a) Absorption, (b) Spontaneous Emission, (c) Simulated Emission.

where B_{12} is referred to as the absorption transition probability. The total rate of downward transitions is given by the sum of spontaneous and stimulated transitions,

$$R_{21} = A_{21} \cdot N_2 + B_{21} \cdot N_2 \cdot P(E_{21}) , \qquad (3.2)$$

A_{21} is the spontaneous transition probability, $1/\tau_{sp}$ and B_{21} is the stimulated transition probability. A_{21}, B_{12} and B_{21} are referred to as the Einstein coefficients. If the system is in thermal equilibrium, then the upward and downward transition rates must be equal,

$$R_{12} = R_{21} . \qquad (3.3)$$

In addition, for a two level system in thermal equilibrium, it may be assumed that the ground and excited state are populated according to Boltzmann statistics,

$$\frac{N_2}{N_1} = \exp\left[\frac{-(E_2 - E_1)}{k \cdot T}\right] , \qquad (3.4)$$

where k is Boltzmann's constant and T is the Kelvin temperature. Combining equations (3.1) – (3.4), the energy density, $P(E_{21})$, can be written as,

$$P(E_{21}) = \frac{A_{21}}{B_{21} \cdot \exp\left[-(E_2 - E_1) / k \cdot T\right] - B_{21}} . \qquad (3.5)$$

Since the system considered is in thermal equilibrium it must give rise to radiation which is identical to that of the blackbody radiation distribution. The energy density of which at an energy $h\upsilon$, is described by Planck's law for blackbody radiation [7],

$$P(h\upsilon) = \left(\frac{8\pi n^2 n_g \cdot (h\upsilon)^2}{(hc)^3}\right) \frac{1}{\left(\exp\left[\frac{h\upsilon}{kT}\right] - 1\right)} , \qquad (3.6)$$

where n is the refractive index of the medium, n_g is the group refractive index, h is Planck's constant and c is the velocity of light in a vacuum. Comparing equations (3.6) and (3.7) for energy density $P(h\upsilon = E_{21})$ it is seen that,

$$B_{12} = B_{21} \qquad (3.7)$$

and

$$\frac{A_{21}}{B_{21}} = Z_{21}(h\upsilon_{21}) = \frac{8\pi n^2 n_g \cdot (h\upsilon_{21})^2}{(hc)^3} . \qquad (3.8)$$

In conclusion, the absorption and stimulated emission transition probabilities are seen to be equal, and related to the spontaneous transition probability by equation (3.8). From equation (3.8), it is seen that, for a particular photon energy there is a fixed ratio between the stimulated and spontaneous transition probabilities. Although these relationships have been derived for a simple two-level system, they can be shown to hold for any material system, such as a direct band gap semiconductor.

3.3 Radiative Processes in Semiconductors.

3.3.1 Band to Band Transitions.

In semiconductors the radiative processes are associated with the recombination (or creation) of an electron in the conduction band and an empty state (hole) in the valence band. The concept of a hole is unnecessary in the two-level system as the excited state is vacant, by definition, when the ground state is occupied. In thermal equilibrium, a direct band gap semiconductor such as GaAs has few electrons in the conduction band and few holes in the valence band. Thus a photon has a high probability of being absorbed, by giving its energy to an electron in the valence band, thereby raising the electron to the conduction band. Conversely the probability of the stimulated emission of a photon by an electron in the conduction band recombining with a hole in the valence band is negligible.

However, as shown in section 3.1, the number of electrons in the conduction band and holes in the valence band can be significantly increased by using a forward biased double heterostructure junction. This increase can be sufficient to make the probability of stimulated emission greater than the probability of absorption. This is the necessary condition for optical gain and corresponds to population inversion in a laser medium. When a semiconductor is externally excited in this way it is no longer in thermal equilibrium.

3.3.2 Transition Rates.

In a simplified case, the available states in a semiconductor can be represented as a continuous band of states within the partially filled conduction and valence bands, as shown in figure 3.3. The energy levels in figure 3.3 are measured from some arbitrary zero point, in this case the bottom of the valence band. In contrast to the idealised two level system, electrons in a solid obey the Pauli exclusion principle that

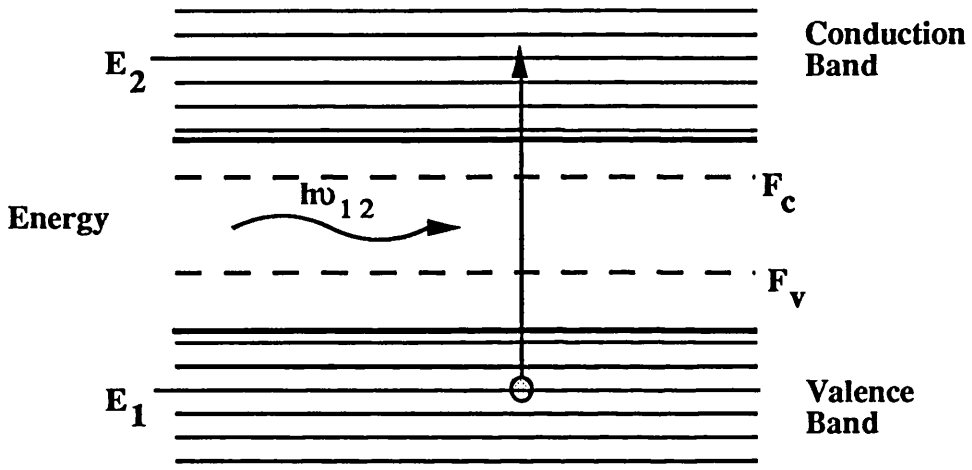

Figure 3.3 : Transition of an electron from E_2 to E_1, by the absorption of a photon of energy $h\nu = E_{21}$, where the states are represented by a continuous Band of States. The quasi-Fermi levels for the valence and conduction bands are represented by Fc and Fv respectively.

two electrons with the same spin may not occupy the same state. The occupation probability is therefore given by Fermi-Dirac statistics, rather than Boltzmann statistics.

At a given temperature, the occupation probability, f_2 of an electron with energy E_2 in the conduction band is given by Fermi-Dirac statistics as,

$$f_2(E_2) = \frac{1}{\exp[(E_2 - F_c)/kT] + 1} \quad . \tag{3.9}$$

Similarly, for the valence band,

$$f_1(E_1) = \frac{1}{\exp[(E_1 - F_v)/kT] + 1} \quad . \tag{3.10}$$

F_c and F_v are the non-equilibrium quasi-Fermi levels for the conduction and valence bands respectively, which give the energy for a 50% probability of occupation in that band. The probability of finding a vacant state (hole) is simply $(1 - f_2)$ in the conduction band, and $(1 - f_1)$ in the valence band.

Using equations (3.9) and (3.10), it is now possible to rewrite the upward and downward transition rates R_{12} and R_{21} in equations (3.1) and (3.2),

$$R_{12}(E) = B_{21}(E) \cdot f_1 \cdot (1 - f_2) \cdot P(E) , \tag{3.11}$$

$$R_{21}(E) = A_{21}(E) \cdot (1 - f_1) \cdot f_2 + B_{21}(E) \cdot (1 - f_1) \cdot f_2 \cdot P(E) . \tag{3.12}$$

It should be noted that (3.11) and (3.12) are valid only for transitions between E_1 and E_2 and that $E = E_2 - E_1 = h\upsilon_{21}$.

3.3.3 Net Stimulated Emission.

In order to achieve net gain or transparency the stimulated emission rate must be greater than or equal to the absorption rate. The necessary condition to achieve this net stimulated emission was first derived by Bernard and Duraffourg [6]. If it is required that,

$$R_{21} - R_{sp} \geq R_{12} , \tag{3.13}$$

where R_{sp} is simply the spontaneous emission rate, $A_{21} \cdot f_1 \cdot (1 - f_2)$, then

$$(1 - f_1) \cdot f_2 \geq f_1 \cdot (1 - f_2) . \tag{3.14}$$

Using equations (3.9) and (3.10), (3.14) reduces to,

$$\exp[(E_1 - F_v)/kT] \geq \exp[(E_2 - F_c)/kT] , \tag{3.15}$$

or more simply,

$$(F_c - F_v) \geq (E_2 - E_1) . \tag{3.16}$$

As $E_2 - E_1 = h\upsilon_{21}$, the separation of the quasi-Fermi levels must exceed the photon energy for net stimulated emission, at that energy. Equation (3.16) shows why an unpumped semiconductor in thermal equilibrium cannot exhibit gain, as there is no separation between the quasi-Fermi levels. The quasi-Fermi levels only become separated when external pumping is applied, as shown in figure 3.1. In addition, equation (3.16) dictates that either one or both of the quasi-Fermi levels must lie *within* the band to which they apply to achieve the required separation.

3.3.4 Absorption Coefficient.

The concept of net stimulated emission or absorption is useful as it allows the development of an expression for an absorption coefficient, α or gross optical gain, g, macroscopic quantities that can be used in a rate equation analysis of the waveguide. The net absorption rate is given by,

$$R_{abs}(E) = B_{21}(E) \cdot P(E) \cdot (f_1 - f_2) \quad . \qquad (3.16)$$

The net absorption rate is the product of the net absorption coefficient, $\alpha(E)$ and the incident photon flux, Q(E). The photon flux is defined as,

$$Q(E) = P(E) \cdot v \, , \qquad (3.17)$$

where, v is the group velocity c / n_g. By substituting $\alpha(E) \cdot Q(E)$ for $R_{abs}(E)$ in equation (3.16), $\alpha(E)$ can be written as,

$$\alpha_{21}(E) = \frac{B_{21}(E)}{v} (f_1 - f_2) \quad . \qquad (3.18)$$

The gross optical gain, g(E), used extensively in this thesis is simply $-\alpha(E)$, ie.,

$$g_{21}(E) = -\alpha_{21}(E) = \frac{B_{21}(E)}{v} (f_2 - f_1) \quad . \qquad (3.19)$$

and is used in preference to the absorption coefficient.

The spontaneous emission rate is also related to the absorption coefficient or gross optical gain. From equations (3.8) and (3.12) it is known that,

$$R_{sp}(E) = A_{21}(E)\cdot f_2(1 - f_1)$$

$$= Z_{21}(E)\cdot B_{21}(E)\cdot f_2(1 - f_1)\,. \qquad (3.20)$$

Combined with equation (3.18), (3.20) yields,

$$R_{sp}(E) = \frac{Z_{21}(E)\cdot v\cdot g_{21}(E)}{1 - \exp\left[\frac{(E_{21} - (F_c - F_v))}{kT}\right]}\,. \qquad (3.21)$$

Thus the spontaneous emission rate, net stimulated emission rate and the gross optical gain are seen to be linked. A knowledge of one of these quantities will yield the other two. In practice, either the transition probabilities $A_{21}(E)$ and $B_{21}(E)$ are calculated theoretically or the gross optical gain is experimentally determined and the other quantities calculated from it. This allows a convenient cross check between theoretical models and an experimentally measured $g(E)$.

3.4 Crystallography and the Radiative Process.

3.4.1 Introduction : Four Band Parabolic Model.

The analysis in the previous section assumes, for simplicity, that there are continuous bands of states available in the conduction and valence bands. This analysis is now extended to include the various available states with the same energy but with different crystal momenta (or wavevector **k**). The transition rates are affected by the *density* of these states at a particular energy value.

An accurate description of the band structure for GaAs would involve sophisticated numerical techniques and can be found in texts such as Long [8]. The major features of the energy band structure of GaAs are shown in figure 3.4. This is plot of electron energy as a function of crystal momentum wavevector **k**. For GaAs, a direct band gap material, the minimum in the conduction band and the maximum in the valence band occur for the same value of **k**, namely $\mathbf{k} = 0$.

In practice a four-band parabolic model is a sufficient approximation to the behaviour of pure GaAs [9]. The modified $E - \mathbf{k}$ diagram for this model is shown in figure 3.5. In this model the valence band is divided into three sub-bands, the heavy hole band; the light hole band; and the split-off band. Usually, the split-off energy Δ is large compared to the thermal energy, kT, hence the split-off band will be full of electrons at standard operating temperatures and can be ignored.

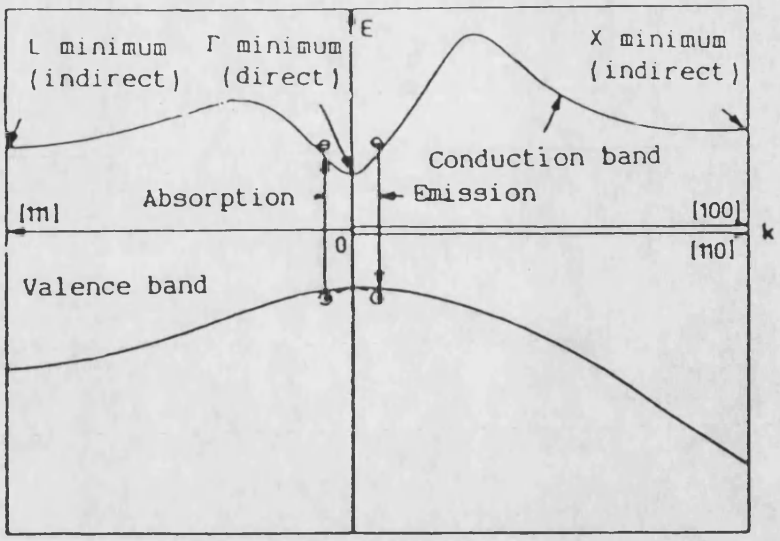

Figure 3.4 : Energy, **E**, versus crystal wavevector, **k**, Band Structure of GaAs

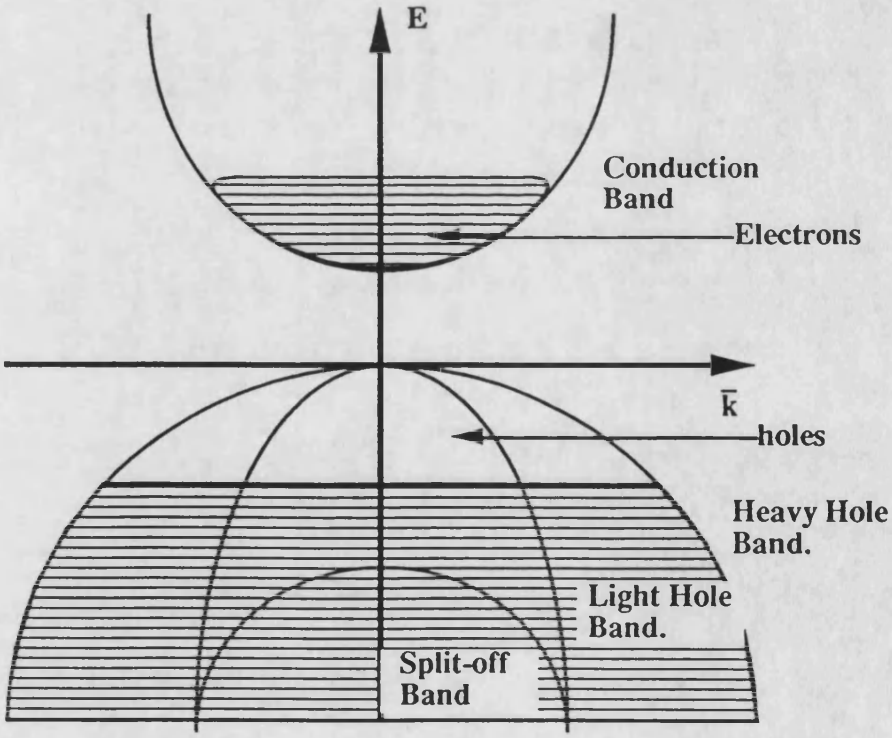

Figure 3.5 : E – **k** for the Four-Band Parabolic Model.

The relationship between E and **k** is the remaining bands is given by,

$$E_c = \frac{\hbar^2 k^2}{2m_e} \quad , \qquad \text{in the conduction band} \qquad (3.23\ a)$$

$$E_{lh} = \frac{\hbar^2 k^2}{2m_{lh}} \quad , \qquad \text{in the light hole sub-band} \qquad (3.23\ b)$$

$$E_{hh} = \frac{\hbar^2 k^2}{2m_{hh}} \quad , \qquad \text{in the heavy hole sub-band} \qquad (3.23\ c)$$

where m_e, m_{lh}, m_{hh} are the effective masses of electrons, light holes and heavy holes respectively, and k is the modulus of the wavevector.

3.4.2 Parabolic Density of States.

The derivation of the (energy) density of states for a parabolic model can be found in most standard texts on semiconductor lasers [1-3]. The energy density of states is found by equating it to the momentum density of states, ie

$$\rho(E)\,\delta E = \rho(k)\,\delta k = (2)\cdot \frac{4\pi k^2}{(2\pi)^3}\,\delta k \quad , \qquad (5.24)$$

$$\text{or,} \quad \rho(E) = \frac{k^2}{\pi^2}\frac{dk}{dE} \quad . \qquad (5.25)$$

The factor $4\pi k^2 \cdot \delta k / (2\pi)^3$ represents the number of states per unit volume of a spherical shell of radius k and thickness δk. : The two is included to take account of electron spin.

The conduction band density of states can now be written as,

$$\rho_c(E_c) = 4\pi \cdot \left(\frac{2m_e}{h^2}\right)^{3/2} \cdot E_c^{1/2}, \tag{3.26}$$

and for the valence band

$$\rho_v(E_v) = 4\pi \cdot \left(\frac{2}{h^2}\right)^{3/2} \left(m_{lh}^{3/2} + m_{hh}^{3/2}\right) E_v^{1/2}, \tag{3.27}$$

ie, the sum of the light and heavy hole density of states. When using equation (3.27) some authors ignore the effect of light holes on the density of states, on the rationale that their effective mass is much less than that of heavy holes. This assumption is not made in the model used in this thesis.

3.4.3 Band Tail Effects in Doped GaAs.

The density of states in equations (3.26) and (3.27) and the parabolic band structure in equation (3.23) relate to pure GaAs. However, as the level of impurity increases (ie, if the material is heavily doped), the impurity states begin to merge with the conduction and valence bands. This leads to the formation of 'band tails' where the bound and free carriers are virtually indistinguishable [9]. These band tails have a significant effect on the emission wavelength characteristics.

There are a number of models of the intrusion of these band tails into the band gap. Two notable examples are those of Kane [10], and Halperin and Lax [11]. Hwang [12] has compared these two models and his results are repeated in figure 3.6. In general, the Kane model tends to overestimate the penetration of the tail into the band gap, particularly that of the conduction band. However, the Halperin and Lax model is of limited use in this case, as it is discontinuous near the band edge. As an alternative to

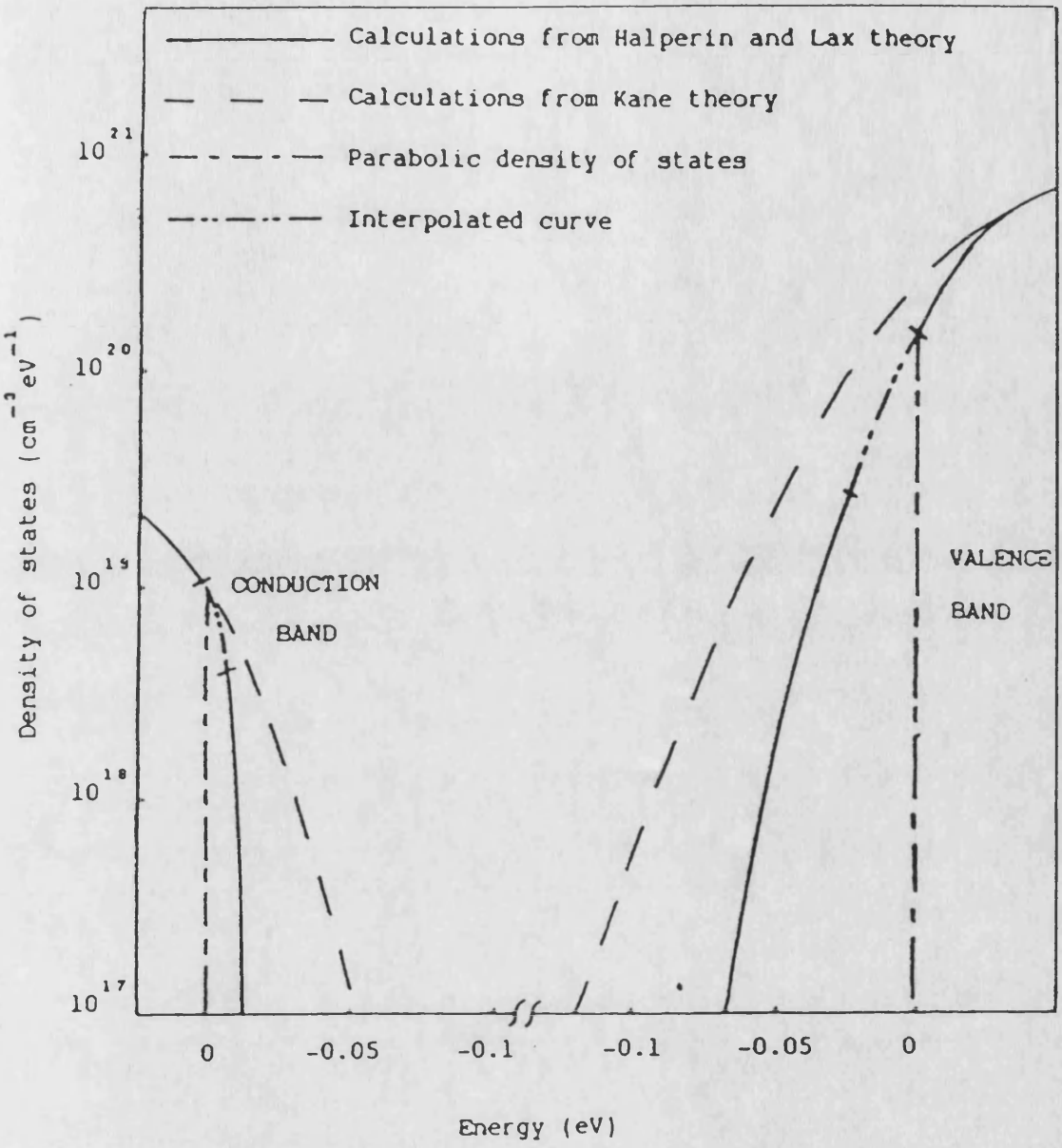

Figure 3.6 : Comparison of the density of states in the bandtails of GaAs obtained from the Kane model and the Halperin and Lax model. Curves apply for a doping density $p_o = 6 \times 10^{18}$ cm^{-3} at 300 K, with and injection level required to give a gain of 100 cm^{-1} [12].

these two methods, Stern [13] calculated the band tail using the Halperin and Lax model and fitted a Kane band tail shape to it. Kane band tails are given by,

$$y(x) = \frac{1}{\pi^{1/2}} \int_{-\infty}^{x} (x - z)^{1/2} \exp\left[-z^2\right] dz \quad , \qquad (3.28)$$

$$(x < \eta)$$

where z is a convenient dummy variable, $x = E / \eta$, and η is the Kane band tailing parameter which is dependent on the doping density.

3.4.4 k-Selection Rule.

In pure GaAs, when a photon is absorbed or emitted, the (crystal) momentum of the carriers must be conserved. As the crystal momentum is given by,

$$\mathbf{p} = h \cdot \mathbf{k}, \qquad (3.29)$$

then is follows that the wavevectors of the initial and final states of the electron must be separated by the wavevector of the interacting photon, $\mathbf{k_p}$,

$$\mathbf{k_c} - \mathbf{k_v} \pm \mathbf{k_p} = 0 \qquad (3.30)$$

where $\mathbf{k_c}$ and $\mathbf{k_v}$ are the wavevectors associated with the energy states E_c and E_v. The wavevector of a photon is generally considered to be negligible when compared to that of an electron. Hence, equation (3.30) becomes the so called k-selection rule, that the wavevector of the initial and final states must be the same,

$$\mathbf{k_c} = \mathbf{k_v} \, . \qquad (3.31)$$

The allowed transitions between initial and final states are sometimes referred to as vertical transitions, as the carriers move in energy (vertically) but not in wavevector

(horizontally) on the E - **k** diagrams shown in figures 3.4 and 3.5. Transitions where the wavevectors are not the same must involve the interaction of a fourth 'particle', a phonon, so that momentum is conserved. The phonon is an energy packet associated with crystal vibrations.

Clearly, the interaction of four quanta (photon, electron, hole and phonon) is much less likely to occur than that of three (photon, electron and hole). Hence this type of interaction can generally be ignored in pure direct band gap semiconductors. This also explains why lasing action does not occur in indirect band gap materials, such as silicon, as they would have to rely on phonon interaction for lasing.

In heavily doped GaAs the situation is different. For transitions well into the bands the k-selection rule still applies as they occur between free electrons and holes with a definite momentum. However, transitions between states in the band tails do not satisfy momentum conservation, as the states are not states of definite momentum. Therefore, the k-selection rule does not apply for band tail transitions [14]. Thus, for pure GaAs, a model using parabolic density of states and strict k-selection would be employed, whilst for heavily doped GaAs, band tail effects must be incorporated with relaxed k-selection in the vicinity of the band tail.

3.5 Calculation of Emission Rates.

The basic expression for radiative transitions given in sections (3.3.2) and (3.3.4) can now be extended to show the effect of density of states and k-selection. When the k-selection rule is applied, all the possible transitions are not considered, and the rates become dependent on the degree of k-selection involved. For pure GaAs (ie, strict k-selection) the conductance and valence bands are considered simultaneously. The expressions obtained for rigourous k-selection are, for the spontaneous emission rate,

$$R_{sp}(h\upsilon) = Z(h\upsilon) \int_{-\infty}^{+\infty} B_{12}(E_c,h\upsilon)\cdot \rho_c(E_c)\cdot \rho_v(E_c - h\upsilon)\cdot f_c(1 - f_v)\left(\frac{\rho_c(E_c)}{\rho_c(E_c) + \rho_v(E_c - h\upsilon)}\right) dE_c \qquad (3.32)$$

and for the stimulated emission rate,

$$R_{st}(h\upsilon) = P(h\upsilon) \int_{-\infty}^{+\infty} B_{12}(E_c,h\upsilon)\cdot \rho_c(E_c)\cdot \rho_v(E_c - h\upsilon)\cdot (f_c - f_v)\left(\frac{\rho_c(E_c)}{\rho_c(E_c) + \rho_v(E_c - h\upsilon)}\right) dE_c \qquad (3.33)$$

where $B_{12}(E_c,h\upsilon)$ is the transition probability from an initial state of E_c (or $E_c - h\upsilon$) to a final state of $E_c - h\upsilon$ (or E_c). The integration over all possible values of E_c gives the total emission rate of photons of energy $h\upsilon$.

The case where k-selection does not apply shall now be considered. Under these conditions it is possible to integrate over the conduction and valence bands independently. The spontaneous and stimulated emission rates may be written as,

$$R_{sp}(h\upsilon) = Z_{21}(h\upsilon) \int_{-\infty}^{+\infty} B_{12}(E_c,h\upsilon)\, \rho_c(E_c)\, \rho_v(E_c - h\upsilon)\, f_c(1 - f_v)\, dE_c \quad , \quad (3.34)$$

$$R_{st}(h\upsilon) = P(h\upsilon) \int_{-\infty}^{+\infty} B_{12}(E_c,h\upsilon)\, \rho_c(E_c)\, \rho_v(E_c - h\upsilon)\, (f_c - f_v)\, dE_c \qquad (3.35)$$

It is possible to obtain a total spontaneous emission rate by integrating (3.34) over all possible photon energies,

$$R_{sp(total)} = \int_{a}^{+\infty} Z_{21}(h\upsilon) \left\{ \int_{-b}^{+\infty} B_{12}(E_c,h\upsilon)\, \rho_c(E_c)\, \rho_v(E_c - h\upsilon) \right. \qquad (3.36)$$

$$\left. \cdot\, f_c(1 - f_v)\, dE_c \right\} d(h\upsilon)$$

where the limits a and b are chosen so that the integrations terminate within the forbidden band. Changing the variable of integration yields,

$$R_{sp(total)} = \int_{+\infty}^{-b-a} \int_{-b}^{+\infty} Z_{21}(E_c - E_v)\, B_{12}(E_c,E_v)\, \rho_c(E_c)\, \rho_v(E_v)\, f_c(1 - f_v)\, dE_c\, d(h\upsilon)$$

(3.37)

If it is assumed that $Z_{21}(E_c - E_v)$ and $B_{12}(E_c,E_v)$ are constant over the limits of integration, then from the definition of the density of states, the resulting integration yields,

$$R_{sp(total)} = B_r N \cdot P \qquad (3.38)$$

where B_r is a constant and N and P are the total electron and hole densities. This is the well known result for bimolecular recombination, hence B_r is usually referred to as the bimolecular recombination rate, $\approx Z_{21}(E) \cdot B_{21}(E)$. Taking into account active layer doping to n_o and p_o, then equations (3.38) can be rewritten as,

$$R_{sp(total)} = B_r (N + n_o) \cdot (P + p_o) \; . \qquad (3.39)$$

A further simplification can be made if $n_o \gg p_o$ and by assuming high injection. Under high rates of injection, $N \approx P$, and $N \gg p_o$ hence equation (3.39) reduces to,

$$R_{sp(total)} = B_r N \cdot \left(N + n_o\right) \quad . \qquad (3.40)$$

The value for total spontaneous emission is useful in the calculation of the carrier continuity equations used throughout the body of this thesis.

3.6 Model Used in this Thesis.

The model used in this thesis is that presented by Liddell [15] and assumes Kane band tail states and k-selection rules. This choice is most appropriate for use with moderately doped waveguides, as it combines the characteristics of both pure and heavily doped materials. The stimulated gain and spontaneous emission curves were fitted to a group of devices by Liddell [15] and Middlemast [16].

In [14] it is assumed that B_{12} and Z are constant over the range of probable transitions, allowing control over the magnitude of the rates by altering the bimolecular recombination rate. The shape of the curves is determined by the Kane band tail parameter, η, as described in section 3.4.3.

The curve for gross optical gain and net spontaneous emission are shown in figures 3.7 and 3.8, on a wavelength scale. A bimolecular recombination rate of 10^{-16} m^3s^{-1} is used, which is consistent with that used by other authors [1,2,3], and a value of 0.25 was used for η.

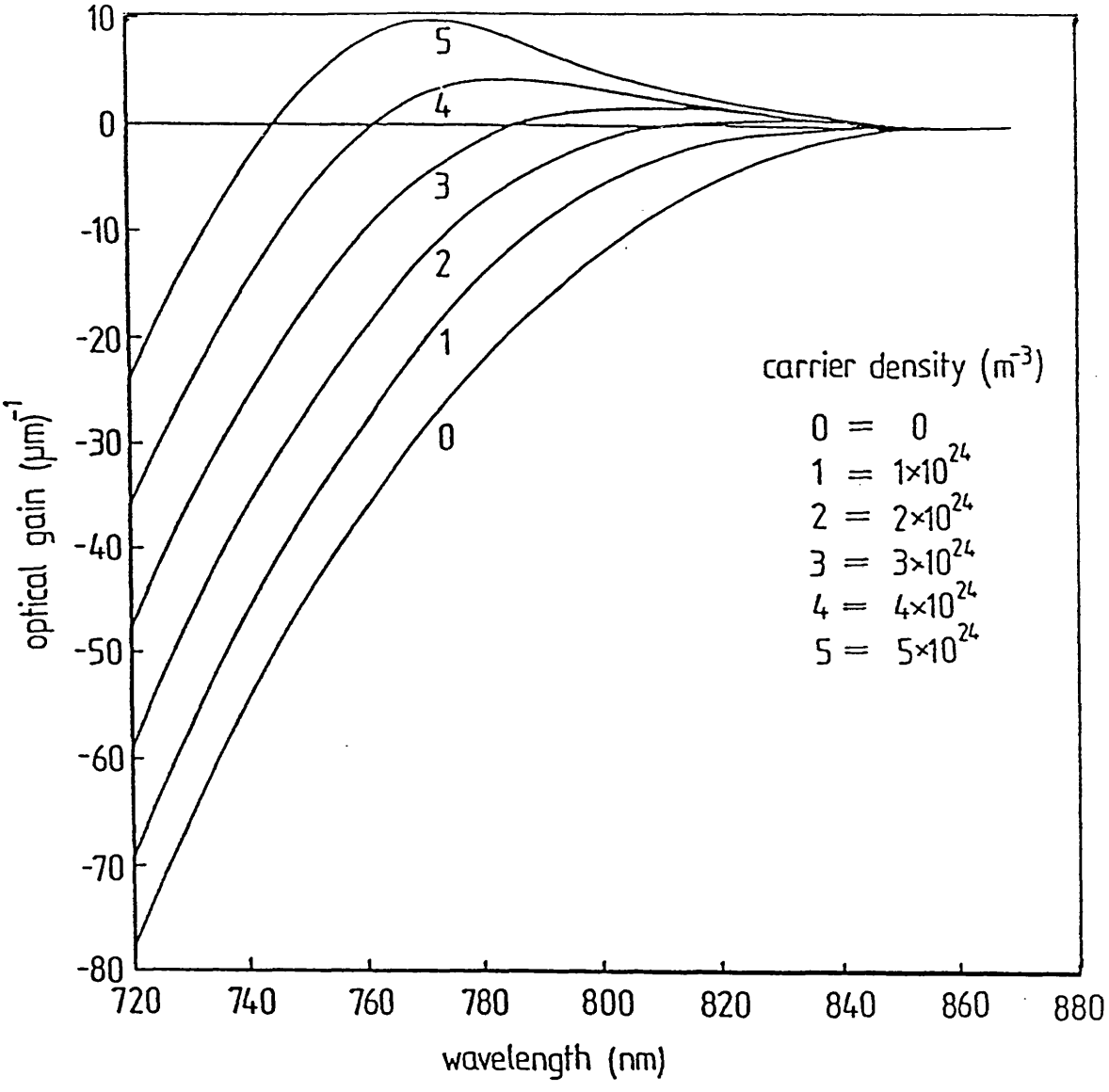

Figure 3.7 : Wavelength dependence of net stimulated optical gain in GaAs.

$B_r = 10^{-16}$, $\eta = 0.25$, T = 300 K, $p_o = 4 \times 10^{23}$ m^{-3}.

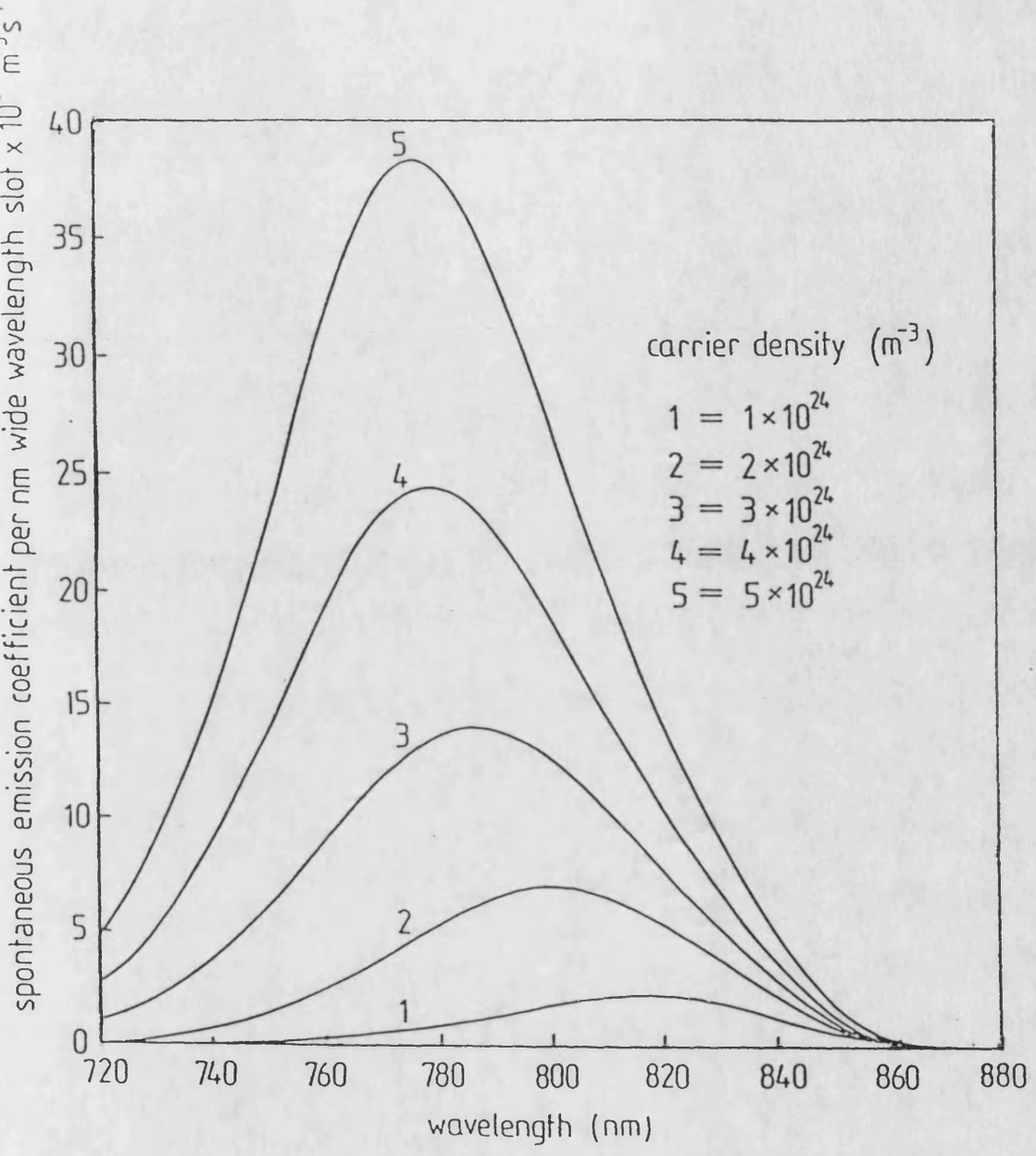

Figure 3.8 : Wavelength dependence of spontaneous emission in GaAs.

$B_r = 10^{-16}$, $\eta = 0.25$, T = 300 K, $p_o = 4 \times 10^{23}$ m^{-3}.

References, Chapter 3

1. CASEY, H.C. Jr and PANISH, M.B., 'Heterostructure Lasers, Part A : Fundamental Principles',

Academic Press, New York, 1978.

2. THOMPSON, G.H.B, 'Physics of Semiconductor Devices',

Wiley, Chichester, 1980.

3. KRESSEL, K. and BUTLER, J.K., 'Semiconductor Lasers and Heterojunction LEDs'

Academic Press, New York, 1977.

4. EINSTEIN, A., 'Zur Quantentheorie de Strahlung',

Phys. Z., 1917,18,pp121

5. WHITE, R.L., 'Basic Quantum Mechanics',

McGraw-Hill, New York, 1970.

6. BERNARD, M.G.A., and DURAFFOURG, G., 'Laser Condition in Semiconductors'

Phys. Status Solidi, 1961, 1, pp699.

7. SCHIFF, L.I., 'Quantum Mechanics' 3rd Edition,

McGraw-Hill, New York, 1968.

8. LONG, D., 'Energy Bands in Semiconductors',

Wiley, New York, 1968.

9. KANE, E.O., 'Band Structure of Indium Antimonide',

J. Phys. Chem. Solids, 1957, 1, pp249-261.

10. KANE, E.O., 'Thomas-Fermi approach to Impure Semiconductor Band Structure',

Phys. Rev., 1963, 131, (1), pp79-88.

11. HALPERIN, B.I., and LAX, M., 'Impurity-Band Tails in the High Density Limit. 1 : Minimum Counting Methods',

Phys. Rev., 1966, 148, (2), pp722-740.

12. HWANG, C.J., 'Properties of Spontaneous and Simulated Emission in GaAs Junction Lasers',

Phys. Rev.(B), 1970, 2, (10), pp4117-4134.

13. STERN, F., 'Gain Current Relation for GaAs Lasers with n-type and Undoped Active Layers',

IEEE J Quantum Electron, 1973, QE-9, p290- .

14. LIDDELL, W.J., 'Polarisation and Spectral Characteristics of Spontaneous Emission in Active Optical Waveguides',

Ph.D Thesis, University of Bath, 1986.

15. MIDDLEMAST, I., 'A Comprehensive Model of the Superluminescent Diode',

Ph.D Thesis, University of Bath, 1986.

4 LIGHT PROPAGATION IN THE ACTIVE WAVEGUIDE

4.1 Introduction

In this chapter the behaviour of light in the buried heterostructure active waveguide is considered. Once again the reader is referred to standard texts for a complete picture of this extensively studied area [1,2,8,10]. Starting from Maxwell's equations for a dielectric, non-magnetic medium, the optical behaviour of the guide is analysed. The key parameters used to characterise the medium, such as dielectric constant, refractive index, propagation constants and susceptibility are introduced in section 4.2. The propagation of light in the lateral, x, transverse, y, and longitudinal, z, dimensions is then described by the wave equation derived from Maxwell's equations.

Unfortunately, it is not possible to determine exact solutions to the wave equation in the active region [4]. Here, the effective dielectric constant (EDC) method [5] is used to give approximate solutions for the transverse and lateral modes of the buried heterostructure waveguide, by approximating the cross-section of the guide to a dielectric box, surrounded by an infinite medium of lower dielectric constant. When considering the longitudinal and time variation, the lateral and transverse behaviour is condensed to an effective dielectric constant, which describes the gain in the guide and the confinement of light to the active region. The solution to the wave equation yields the photon conservation rate equations, for the propagation of a travelling photon flux in the z-dimension and time.

The derivation of the rate equations is completed by the phenomenological derivation of the carrier conservation equation, by treating the active region of the guide as a 'black-box' which converts injected charge carriers (electrons and holes) into photons. Finally, the spectral behaviour of the photon and carrier conservation equations is discretised into a number of wavelength 'slots' to make their solution more tractable to numerical methods. These discretised rate equations are used as the basis of the analysis presented in the remainder of the thesis.

4.2 Maxwell's Equations

As the mathematical description of all optical phenomena is based on Maxwell's equations, it is appropriate to consider these equations in some detail. In SI units, the field equations take the form [2]

$$\nabla \times E = -\frac{\partial B}{\partial t} \quad , \tag{4.1}$$

$$\nabla \times H = J + \frac{\partial D}{\partial t} \quad , \tag{4.2}$$

$$\nabla \cdot D = -\rho_f \quad , \tag{4.3}$$

$$\nabla \cdot B = 0 \quad , \tag{4.4}$$

where E and H are the electric and magnetic field vectors, respectively, and D and B are the corresponding electric and magnetic flux densities. The current density J and the charge density ρ_f represent the sources for the electromagnetic field.

The flux densities D and B arise in response to the electric and magnetic fields E and H propagating in the medium. For a non-magnetic medium, the relationship between flux densities and fields can be expressed through the constitutive relations,

$$D = \varepsilon_o E + P \quad , \tag{4.5}$$

$$B = \mu_o H \quad , \tag{4.6}$$

$$J = \sigma E \quad , \tag{4.7}$$

where ε_o is the permittivity of free space, μ_o is the permeability of free space and σ is the conductivity of the medium. The induced electric polarisation P is calculated

quantum mechanically, for a semiconductor medium this requires a knowledge of the Bloch wave functions and the density of states in the conduction and valence bands described in chapter 3 [1].

Equations (4.1) to (4.7) can now be used to obtain the wave equation to describe the propagation of an optical field inside the medium. It is the wave equation that must be solved, given the boundary conditions in the active waveguide. Taking the curl of (4.1) in conjunction with (4.6) gives,

$$\nabla \times \nabla \times E = -\frac{\partial}{\partial t}(\nabla \times H) \quad . \tag{4.8}$$

Using equations (4.2), (4.5) and (4.7), H, J and D can be eliminated in favour of E and P to obtain,

$$\nabla \times \nabla \times E = -\mu_o \sigma \frac{\partial E}{\partial t} - \mu_o \varepsilon_o \frac{\partial^2 E}{\partial t^2} - \mu_o \frac{\partial^2 P}{\partial t^2} \quad . \tag{4.9}$$

The left hand side of (4.9) can be simplified by using the vector identity,

$$\nabla \times \nabla \times E = \nabla(\nabla \cdot E) - \nabla^2 E \quad . \tag{4.10}$$

In addition, in the absence of free charges, $\rho_f = 0$ and from (4.3) and (4.5),

$$\nabla \cdot D = \varepsilon_o \nabla \cdot E + \nabla \cdot P = 0 . \tag{4.11}$$

The term $\nabla \cdot P$ is negligible in most cases of practical interest, hence $\nabla \cdot E = 0$, to a good approximation. Equation (4.9) now becomes,

$$\nabla^2 E = -\frac{\sigma}{\varepsilon_o c^2}\frac{\partial E}{\partial t} - \frac{1}{c^2}\frac{\partial^2 E}{\partial t^2} = \frac{1}{\varepsilon_o c^2}\frac{\partial^2 P}{\partial t^2} , \tag{4.12}$$

using the familiar relation,

$$\mu_o \varepsilon_o = \frac{1}{c^2} \tag{4.13}$$

where c is the velocity of light in free space. The wave equation (4.12) is valid for arbitrary time-varying fields. However, the solution of the wave equation for simple harmonic time variations is of particular interest, since any field may be decomposed into its Fourier components. Using the complex notation,

$$E(\mathbf{r},t) = \mathrm{Re}\left\{\mathbf{E}(\mathbf{r}) \cdot \exp[-j\omega t]\right\} \tag{4.14}$$

$$P(\mathbf{r},t) = \mathrm{Re}\left\{\mathbf{P}(\mathbf{r}) \cdot \exp[-j\omega t]\right\} \tag{4.15}$$

where **r** is the spatial vector, $\omega = 2\pi\upsilon$ is the angular frequency ($\upsilon = c/\lambda$) at the free space wavelength λ. Re indicates that the real part of the bracketed expression is considered. In general **E** and **P** will be complex as they contain phase information. Substituting (4.14) and (4.15) into (4.12) gives,

$$\nabla^2\mathbf{E} + k_o^2\left[1 + \frac{j\sigma}{(\varepsilon_o\omega)}\right]\mathbf{E} = -\frac{k_o^2}{\varepsilon_o}\mathbf{P}\ , \tag{4.16}$$

where $k_o = \omega/c = 2\pi/\lambda$ is the free space wave number.

In the steady-state, the response of the medium to an electric field is governed by the susceptibility χ defined by,

$$\mathbf{P} = \varepsilon_o \chi \mathbf{E}\ . \tag{4.17}$$

It is useful to decompose χ into two parts,

$$\chi = \chi_o + \chi_p \ , \tag{4.18}$$

where χ_o is the susceptibility of the medium in the absence of external pumping and χ_p is the additional contribution relating to external pumping. This additional contribution is dependent on the charge concentration of carriers in the active waveguide. It should be noted that both χ_o and χ_p are generally complex and (optical) frequency dependent.

The definition of susceptibility (4.17) can be used to eliminate the electric polarisation P in equation (4.16) to give the familiar time-independent wave equation,

$$\nabla^2 \mathbf{E} + \varepsilon k_o^2 \mathbf{E} = 0 \ , \tag{4.19}$$

---

where the complex dielectric constant is introduced,

$$\begin{aligned} \varepsilon &= \varepsilon' + j\varepsilon'' \\ &= \varepsilon_b + j\,\mathrm{Im}\{\chi_o\} + \chi_p + j\frac{\sigma}{\varepsilon_o \omega} \ , \end{aligned} \tag{4.20}$$

and $\varepsilon_b = 1 + \mathrm{Re}\{\chi_o\}$ is the background dielectric constant of the unpumped material and is real, as defined. Re and Im indicate real and imaginary parts, respectively.

4.3 Modes in a Buried Heterostructure Waveguide

4.3.1 Dielectric Box Approximation

An exact analytic solution to the time independent wave equation (4.19) for a pumped buried heterostructure waveguide is not possible [8, 9]. For a complete solution of the wave equation, all the layers of the heterostructure should be considered. One method is to use a transmission line approach to provide numerical solutions of the wave equation for multi-layer guides [3]. However, for this thesis it is sufficient to consider the cross section of the guide to be a rectangular core of refractive index n_2, surrounded by an infinite dielectric cladding of index n_1, as shown in figure 4.1. This approximation is based on the assumption that the cladding layers of the heterostructure, which surround the active guiding layer, are sufficiently thick to prevent the evanescent tails of the field penetrating into the other heterostructure layers.

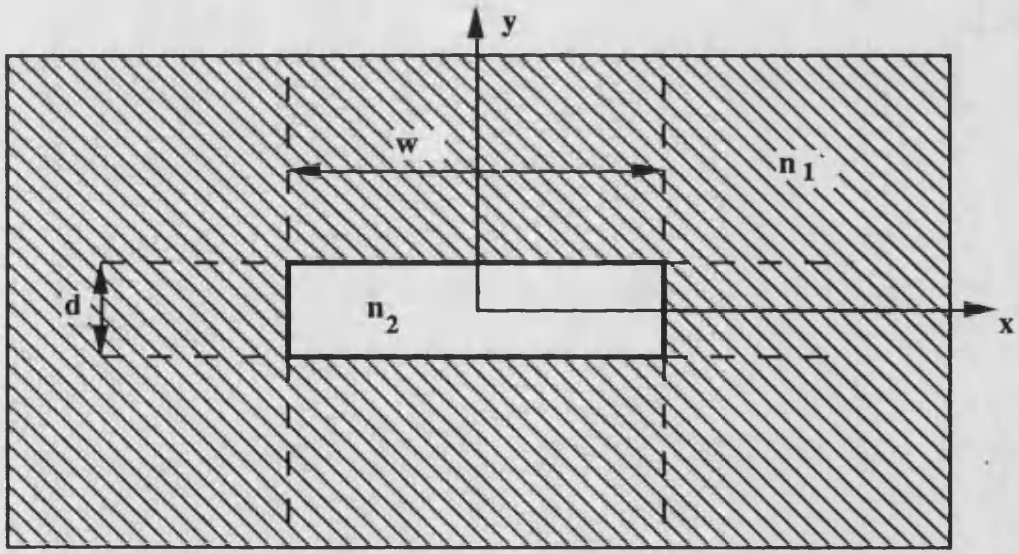

Figure 4.1 : The Dielectric Box Approximation to the Buried Heterostructure Waveguide.

If the refractive index of the core is greater than that of the cladding, then the light will be confined to the core by total internal reflection, under certain conditions. It is then possible to find good approximate solutions to this type of structure. Two

notable examples are the approximate analytic solution presented by Marcatili [4] and the effective index or dielectric constant (EDC) method [5 and 6], both of which compare favourably with the circular harmonic numerical analysis of Goell [7].

4.3.2 The Effective Index Approximation

In contrast to Goell [7] and Marcatili [4] who consider the complete two dimensional problem, the EDC method splits the problem into two one-dimensional parts [5,6,9]. For the one-dimensional three layer dielectric slab it is possible to obtain a closed form analytic solution to the wave equation. As the width of the active region is often an order of magnitude greater than the depth it is assumed that the dielectric constant, ε varies slowly in the lateral x-direction compared with its variation in the transverse y-direction. It is further assumed that the propagation in the longitudinal z-direction can be described by a plane wave with a complex propagation constant β, and that the dielectric constant does not vary in z.

The time independent wave equation can now be rewritten as,

$$\nabla^2 E(x,y,z) + \varepsilon(x,y).k_o^2 E(x,y,z) = 0 \ , \qquad (4.21)$$

where,

$$\varepsilon(x,y) = n_1^2 \ , \qquad \begin{matrix} |x| > w/2 \\ |y| > d/2 \end{matrix} \qquad (4.22)$$

$$\varepsilon(x,y) = n_2^2 \ , \qquad \text{otherwise} \quad . \qquad (4.23)$$

Both ε and n may be complex.

If the variation in the lateral and transverse fields is assumed to be $\psi(x)$ and $\phi(y:x)$ respectively, then the electric field can be approximated to,

$$E \approx \hat{e}\,\phi(y:x)\,\psi(x)\exp[j\beta z] \quad , \tag{4.24}$$

where $\hat{e}$ is the unit vector in the direction that the mode is polarised, and the notation $\phi(y:x)$ indicates that ϕ is solved for each x.

Substituting (4.24) into (4.21) yields,

$$\frac{1}{\psi}\frac{\partial^2\psi}{\partial x^2} + \frac{1}{\phi}\frac{\partial^2\phi}{\partial y^2} + \left[\varepsilon(x,y)k_o^2 - \beta^2\right] = 0 \quad . \tag{4.25}$$

In the effective index approximation, the transverse field distribution, $\phi(y:x)$ is obtained by first solving,

$$\frac{\partial^2\phi}{\partial y^2} + \left[\varepsilon(x,y)k_o^2 - \beta_{eff}^2(x)\right]\phi = 0 \, , \tag{4.26}$$

where $\beta_{eff}(x)$ is the effective propagation constant for a fixed value of x. The lateral field distribution, $\psi(x)$ and is then obtained by solving

$$\frac{\partial^2\psi}{\partial x^2} + \left[\beta_{eff}^2(x) - \beta^2\right]\psi = 0 \quad . \tag{4.27}$$

Both equations (4.26) and (4.27) are one dimensional eigenvalue equations which can be easily solved using the methods developed for the three layer dielectric slab waveguide [8,9,10]. In the case of the buried heterostructure the method of solution is to calculate an effective index for the active layer in the transverse direction. The lateral modes can then be calculated by considering the three layer problem with n_2 replaced by n_{eff}, as shown in figure 4.2.

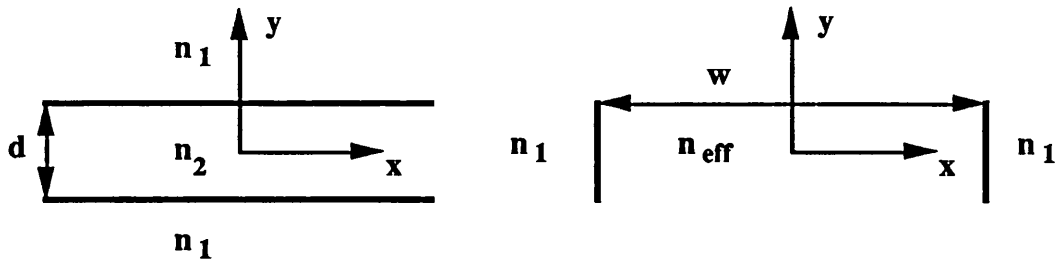

(a) Transverse Guide **(b) Lateral Guide**

Figure 4.2 : The Effective Index Approximation to the Box Dielectric Waveguide.

Although is is possible to include the effect of loss and gain in the solution of (4.26) and (4.27) it is generally cumbersome to do so. A simpler approach is to consider the effect of loss or gain as a small perturbation to the eigenvalue problem. The dielectric constant can now be written as,

$$\varepsilon = n_{b,i}^2 + \Delta\varepsilon_i(x) \ , \qquad (4.28)$$

where i indicates the transverse heterostructure layer, and $n_{b,i}$ is the (real) background refractive index of the unperturbed guide. The perturbation, $|\Delta\varepsilon_i| << n_{b,i}^2$ includes the loss and any contribution from external pumping. In the case of the buried heterostructure waveguide, the major guiding mechanism is real index guiding, due to the refractive index step between the GaAs active region and AlGaAs cladding. The contribution of loss or gain to the guiding problem is negligible and is only considered in the context of calculating the longitudinal propagation constant. The lateral and transverse modes can therefore be calculated from the solution of two real eigenvalue equations.

The effective refractive index, n_{eff} of the active region is given by the solution to,

$$\frac{\partial^2\phi}{\partial y^2} + k_o^2\left[n_b^2 - n_{eff}^2(x)\right]\phi = 0 \quad . \tag{4.29}$$

ie, the unperturbed value of equation (4.26).

4.3.3 Transverse Modes

As was stated in the previous section the transverse modes of the guide may be approximated to those of a three-layer loss-less dielectric slab, shown in figure 4.3, as the effect of loss or gain in the active region of the guide has a negligible effect on the guiding problem. This problem has been extensively studied by many authors, see for instance Marcuse [8], Adams [9], and Kapany and Burke [10], and it is not intended to give a complete analysis here.

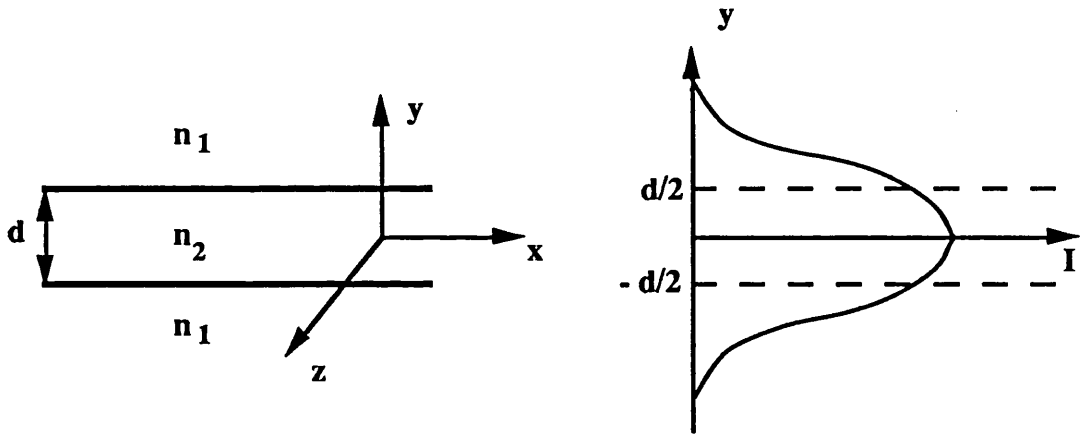

Figure 4.3 : The Three-Layer Dielectric slab waveguide.

Starting from Maxwell's equations, the slab waveguide is seen to support two sets of guided modes, transverse electric (TE) and transverse magnetic (TM), and many unguided modes which are not considered. For TE modes the electric field is polarised in the x-direction, whilst for TM modes the magnetic field is polarised in the

x-direction. The three layer slab is considered infinite in x, hence any derivatives with respect to x will be zero.

For TE modes, $E_y = 0$ (by definition) and, as $\partial/\partial x = 0$, equations (4.1) and (4.2) in conjunction with the constitutive relations (4.5) - (4.7) give $H_x = E_z = 0$, ie TE modes have three non-zero components E_x, H_y and H_z.

Equations of the form (4.29) yield either exponential or sinusoidal solutions. As the waveguide is symmetrical, the solutions must also be symmetrical and the analysis is considerably simplified if odd and even solutions are considered separately. For bound modes, it is required that the solutions are sinusoidal in the central layer with exponentially decaying tails in the cladding layers.

For even TE modes, a general solution of equation (4.29), is of the form,

$$\phi(y) = \begin{cases} A\cos[\kappa y] & |y| \le d/2 \\ B\exp[-\gamma \cdot (|y| - d/2)] & |y| > d/2 \end{cases} \qquad (4.30)$$

where,

$$\kappa = k_o\left(n_2^2 - n_{eff}^2\right)^{1/2} \qquad (4.31)$$

$$\gamma = k_o\left(n_{eff}^2 - n_1^2\right)^{1/2} \qquad (4.32)$$

and n_2 and n_1 are the material refractive indices of the active and cladding layers respectively, with $n_2 > n_1$. Both ϕ and $d\phi/dy$ must be continuous over the layer boundaries at $|y| = d/2$, requiring that,

$$B = A\cos\left[\kappa d/2\right] , \qquad (4.33)$$

$$\gamma B = \kappa A \sin\left[\kappa d/2\right] . \qquad (4.34)$$

Dividing these two equations gives the eigenvalue equation,

$$\gamma = \kappa \tan\left[\kappa d/2\right] \quad , \tag{4.35}$$

where solutions yield the mode effective index, n_{eff} as defined. Clearly, multiple solutions are possible to equation (4.35), corresponding to different even TE modes.

The analysis of odd TE modes is similar to that for even modes, except that the $\cos\left[\kappa y\right]$ term in equation (4.30) is replaced by $\sin\left[\kappa y\right]$. The boundary conditions now yield the eigenvalue equation,

$$\gamma = \kappa \cot\left[\kappa d/2\right] \quad , \tag{4.36}$$

giving the mode effective index, n_{eff} for the odd TE modes. For all guided modes, the inequality $n_2 > n_{eff} > n_1$ is satisfied.

The TE modes eigenvalues are obtained using equations (4.35) and (4.36) together the with the relation,

$$\kappa^2 + \gamma^2 = k_o^2\left(n_2^2 - n_1^2\right) \quad , \tag{4.37}$$

obtained by squaring and adding (4.31) and (4.32). Equation (4.37) describes a circle in the κ - γ plane, and its intersection with the curves obtained using (4.35) and (4.36) yield the κ_p and γ_p values for the p^{th} TE modes, as shown in figure 4.4. Multiple solutions occur because of the periodic nature of the trigonometric functions in (4.35) and (4.36). The number of allowed waveguide modes can be determined by noting that a solution is no longer bound if $\gamma < 0$, as this leads to exponentially growing fields in the cladding layers.

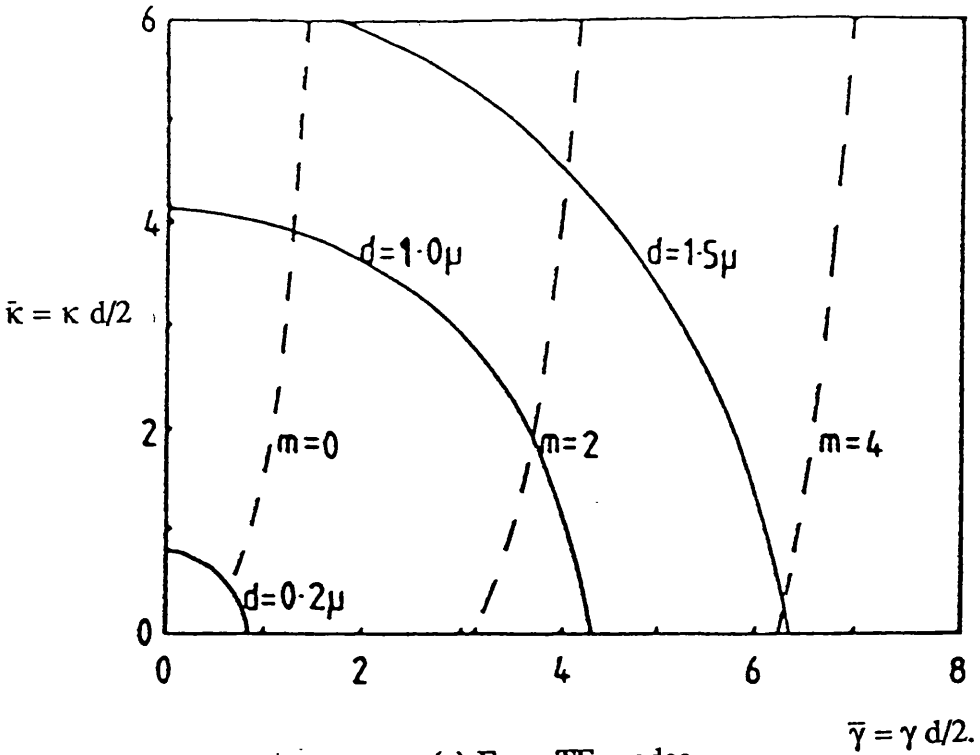

(a) Even TE modes,

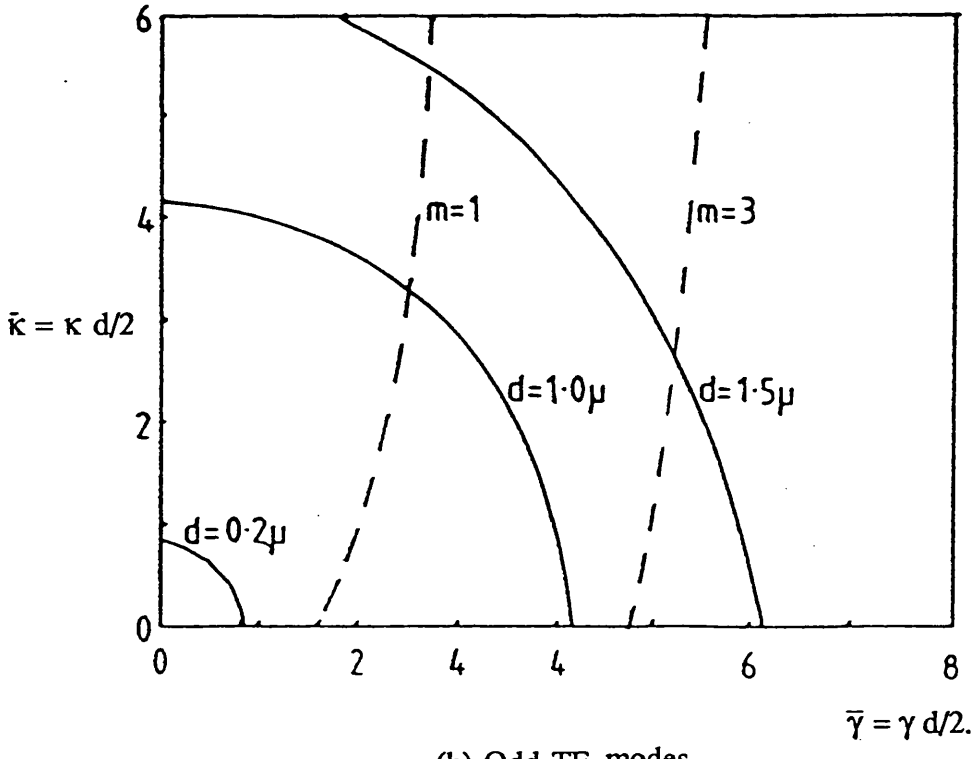

(b) Odd TE modes.

Figure 4.4 : Graphical solution of the eigenvalue equation for the symmetrical slab waveguide, the quantities κ and γ are normalised to the guide thickness, $\bar{\kappa} = \kappa\ d/2$ and $\bar{\gamma} = \gamma\ d/2$.

The cut-off condition is therefore $\gamma = 0$ and occurs when,

$$\kappa d = p\pi , \tag{4.38}$$

where p is the odd or even mode number starting from zero. Equation (4.38) can be simplified if the quantities considered are normalised with respect to κ, giving,

$$D = p\pi, \tag{4.39}$$

where,

$$D = k_o d\left(n_2^2 - n_1^2\right)^{1/2} \tag{4.40}$$

is the normalised waveguide thickness. This parameter plays a crucial part in the design of slab waveguides. It is clear from (4.38) - (4.40) that the lowest even modes, p = 0, will always propagate for any thickness of guide, and for $D < \pi$ this is the only guide mode that will propagate. For a typical GaAs / AlGaAs double heterostructure waveguide, n_1 and n_2 take values of 3.38 and 3.59 respectively. Thus for an emission spectrum with a minimum (free space) wavelength of λ_o = 780 nm, the condition $D < \pi$ becomes

$$d < 0.34\ \mu m , \tag{4.41}$$

to achieve single fundamental mode operation.

Similar solutions can be found for TM modes and it is found that the conditions (4.38) - (4.41) also apply to these modes. In the case of TM modes, $H_y = 0$, by definition, and $E_x = H_y = 0$, ie TM modes have non-zero components H_x, H_y and E_z.

There is another important quantity which must be considered, the transverse confinement factor Γ_T, which represents the fraction of the mode energy that is available for interaction with injected carriers. The confinement factor is defined as the ratio of the mode energy within the active region to the total mode energy. Using $\phi(y)$ from (4.30) the confinement factor is calculated as,

$$\Gamma_T = \frac{\int_{-d/2}^{d/2} \phi^2(y)\, dy}{\int_{-\infty}^{\infty} \phi^2(y)\, dy} \qquad (4.42)$$

Equation (4.42) yield the solutions for TE modes,

$$\Gamma_{T(TE)} = \frac{1 + 2\gamma d/D^2}{1 + 2/\gamma d} \quad . \qquad (4.43)$$

The solution of Γ_T requires the knowledge of κ and γ, and in general it is necessary to solve the eigenvalue equations (4.35) and (4.36) numerically. For the fundamental transverse mode, however, the following expression is obtained,

$$\Gamma_{T(TE)} \approx \frac{D^2}{\left(2 + D^2\right)} \qquad (4.44) \quad .$$

which is accurate to within 1.5%, [11] and can be used to obtain Γ_T for any slab waveguide in conjunction with equation (4.41). Figure 4.5 shows the confinement factor for both fundamental and first order TE modes against the normalised thickness, D. It is found that the confinement factor for TE modes is higher than that for TM modes, hence TE modes are generally favoured in practical laser sources.

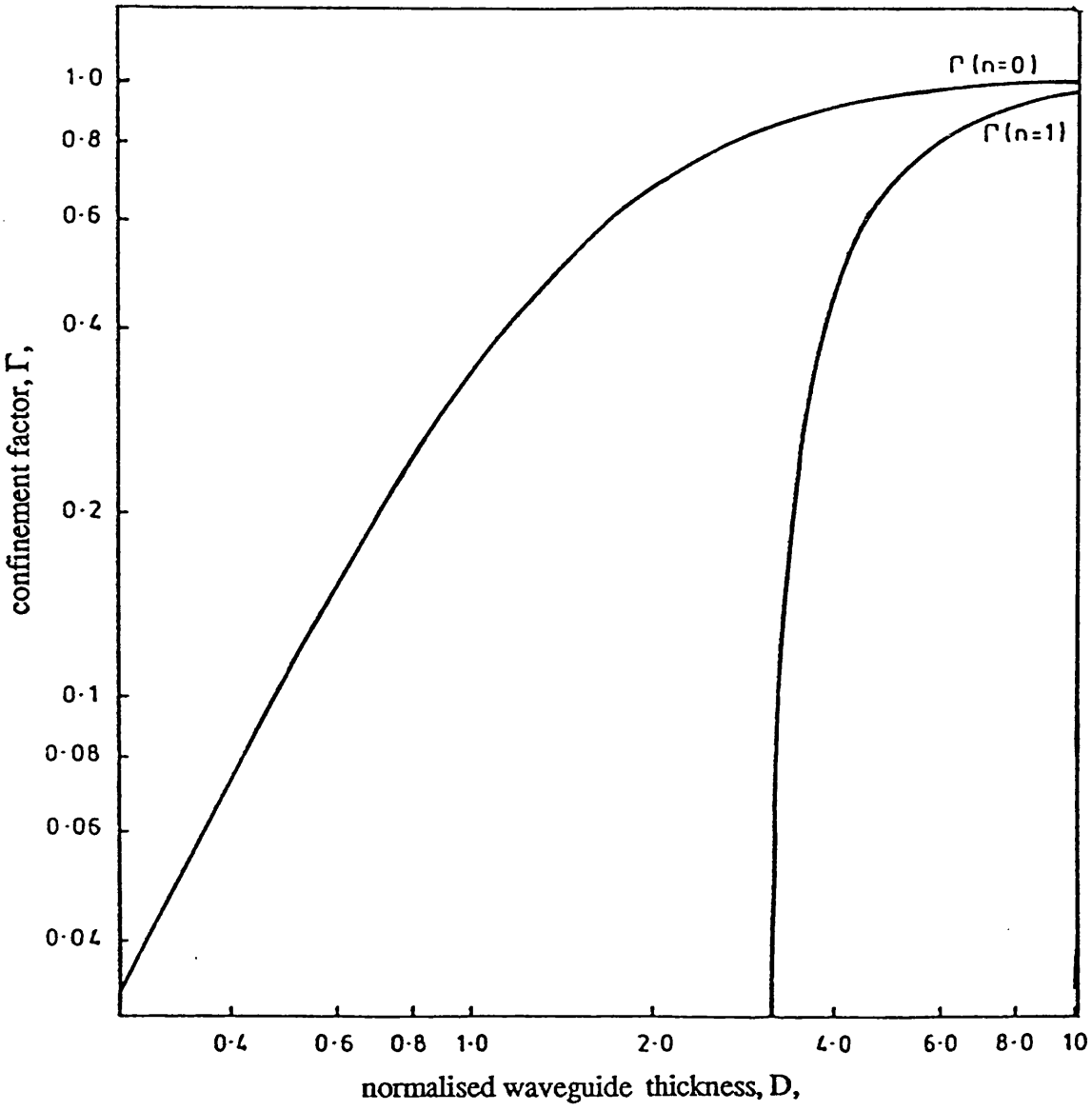

Figure 4.5 : Fundamental confinement factor, Γ, against normalised waveguide thickness, D, for a three-layer, lossless dielectric slab waveguide.

Finally, the effective index of the fundamental TE mode can be approximated by [11],

$$n_{eff}^2 \approx n_1^2 + \Gamma_T\left(n_2^2 - n_1^2\right) \quad . \tag{4.45}$$

Both Γ_T and n_{eff} are used to determine the lateral modes.

4.3.4 Lateral Modes

The lateral modes are obtained by solving equation (4.27). Taking into account the small perturbation in the effective index due to pumping, Δn,(4.27) becomes,

$$\frac{\partial^2\psi}{\partial x^2} + \left\{k_o^2\left[n_{eff}(x) + \Delta n\right]^2 - \beta^2\right\}\psi = 0 \quad . \tag{4.46}$$

In the case of the buried heterostructure guide the effective index, $n_{eff}(x)$ is given by,

$$n_{eff}(x) = \begin{cases} n_{eff} & |x| \le w/2 \\ n_1 & \text{otherwise} \end{cases} , \tag{4.47}$$

where n_{eff} is calculated from the transverse three-layer slab analysis. It should be noted that although, $n_2 > n_{eff} > n_1$ the real refractive index step between n_{eff} and n_1 is sufficient to give rise to strong index guiding. In this case the effect of gain on the propagation in the z-direction can be reduced to a small perturbation on the solution of the passive slab. The propagation constant is divided into real and imaginary parts,

$$\beta = k_o\bar{n} + j\frac{\bar{\alpha}}{2} \tag{4.48}$$

where $\bar{n}$ is the modal refractive index and $\bar{\alpha}$ is the modal absorption coefficient. The factor of 2 is included to take account of wave propagating in the forward and

backward z directions. The modal refractive index, $\bar{n}$ is determined from the solution of,

$$\frac{\partial^2\psi}{\partial x^2} + k_o^2\left[n_{eff}^2(x) - \bar{n}^2\right]\psi = 0 \quad . \tag{4.49}$$

and the mode absorption coefficient is obtained from chapter 3.

Equation (4.49) is solved in the same manner as that used for the transverse modes, with n_2, d and D replaced with the effective index n_{eff}, the guide width w, and the normalised width W, respectively. The normalised width is given by,

$$W = k_o w\left(n_{eff}^2 - n_1^2\right)^{1/2} \tag{4.50}$$

and the mode cut-off condition then becomes,

$$W = q\pi \tag{4.51}$$

where q is the lateral mode number. The lateral confinement factor, Γ_L is determined by equation (4.43) with appropriate substitutions.

It should be noted that for guides with an effective width $W > \pi$ more than one lateral mode may propagate. This will be the case for the choice of active layer widths considered in the thesis (1 - 10 μm), as the choice of width is determined by considerations other than the lateral modes. Although many modes may propagate it is debatable whether such modes will be stimulated or will have sufficient modal gain to be significant.

In this case, it is assumed that all the lateral and transverse effects can be reduced to a single confinement factor,

$$\Gamma = \Gamma_T \Gamma_L , \qquad (4.52)$$

For the materials chosen, and d = 0.3 μm, w = 5μm, equations (4.40, 4.50 and 4.44) give the value for the single confinement factor, $\Gamma \approx 0.75$.

The final part of this section is a discussion of the imaginary part of the propagation constant. For the buried heterostructure waveguide certain assumptions follow from the physical structure. Good carrier confinement means that only the active region is considered to be externally pumped. If the dimensions of the active region are small or of the order of the diffusion length (3 - 5 μm) then the carrier density, and hence the gain, will be independent of position. Thus within the active region the loss is given by,

$$\alpha = -g + \alpha_{int} \quad , \qquad (4.53)$$

whilst in the cladding the loss is,

$$\alpha = \alpha_c \quad , \qquad (4.54)$$

where α_{int} and α_c represent the losses in the active region and cladding region respectively. The main losses are due to free carrier absorption and scattering caused by crystal imperfections in the active and cladding layers

Using the combined confinement factor, Γ gives an overall absorption coefficient,

$$\bar{\alpha} = -\Gamma g + \Gamma \alpha_{int} + (1 - \Gamma) \alpha_c + \alpha_{scat} , \qquad (4.55)$$

where α_{scat} includes the scattering losses due to lattice mismatch at the heterolayer boundaries.

As has been shown in chapter 3 the gain coefficient is both wavelength and carrier density dependent, as are the losses. Free carrier absorption results from the direct interaction between the light and free carriers, in a region. The density of free carriers is directly proportional to the total carrier density. Thus, in the active region (using the approximation of section 3.5, that $N \approx P$ and $p_o \gg n_o$) the free carrier density will be proportional to the $2N + p_o$, whilst in the cladding layers the free carrier density will be proportional to p_c – the cladding layer doping density. As Γ is relatively high and $N \gg p_c$, the term $\Gamma \alpha_{int}$ will dominate the other loss terms in equation (4.55), if the scattering losses are small. Therefore, the total loss can be approximated to the free carrier losses in the active layer,

$$\alpha_{tot} \approx f_{cc} \cdot (2N + p_o) \quad , \tag{4.56}$$

where f_{cc} is the free carrier absorption coefficient. Thus equation (4.55) becomes,

$$\bar{\alpha} = -\Gamma g(N,\lambda) + f_{cc} \cdot (2N + p_o) \ ,$$

or

$$\bar{G}(N,\lambda) = \Gamma g(N,\lambda) - f_{cc} \cdot (2N + p_o) \ , \tag{4.57}$$

where $\bar{G}$ is referred to as the net modal gain, $\bar{G} = -\bar{\alpha}$. Clearly this net gain is a function of carrier density and wavelength.

4.4 Conservation Equations

4.4.1 Photon Conservation Equations

The propagation of light in the z-dimension is also determined by the wave equation (4.12). In general, the dynamic behaviour of the guide should be taken into account to determine the induced polarisation *P*. However, the intraband scattering time which governs the material response is small (≈100 fs) compared with the variation of the magnitude of the electrical field and the other time scales considered (>100 ps). This enables a considerable simplification of the analysis, as the material response can be considered to be instantaneous, and the equation for susceptibility (4.17) then holds for all cases. The time dependent wave equation (4.12) can now be written as,

$$\nabla^2 E - \frac{1}{c^2}\frac{\partial^2}{\partial t^2}(\varepsilon E) = 0 \qquad (4.58)$$

where all the loss terms have been collected into the modified dielectric constant, ε.

The general optical field, *E* may contain many modes which propagate both in the forward and backward z-directions, as well as in time. In this analysis, it is assumed that a plane wave approximation can be made to the longitudinal propagation. The propagation of the plane wave, *E(z,t)*, in time and forward z-direction is assumed to be governed by the radian optical frequency, $\omega = 2\pi\upsilon$ and the complex propagation constant, β,

$$E(z,t) = \frac{1}{2}\,\mathrm{E}\,(z,t)\cdot \exp\left[j(\beta z - \omega t)\right] , \qquad (4.59)$$

there is also a wave propagating in the backward z-direction, the variation of which is determined by (4.59) with z replaced by -z. In the plane wave approximation it is assumed that there is a single mode in the y–dimension, as the guide has an effective thickness $D < \pi$. In the x–dimension, it is assumed that sufficient modes propagate to

give a single, plane wavefront in x. The behaviour in the transverse and lateral dimension is reduced to the group refective index, n_g and average confinement factor, Γ_g. These properties can be determined by the effective index approximation to the waveguide detailed in section 4.3.

If equation (4.59) is substituted into equation (4.58), and assuming that ε is constant for all t, the following is obtained,

$$\left\{\frac{\partial^2 E}{\partial z^2} - \frac{\varepsilon}{c^2}\cdot\frac{\partial^2 E}{\partial t^2}\right\} + 2j\beta\frac{\partial E}{\partial z} + 2j\frac{\omega\varepsilon}{c^2}\cdot\frac{\partial E}{\partial t} = \left(\beta^2 - \frac{\omega^2\varepsilon}{c^2}\right)E \qquad (4.60)$$

where $E = E(z,t)$. In the case of a plane wave, the propagation constant, β, is given by a modified version of equation (4.48) where the group quantities replace the modal ones, ie,

$$\beta = k_o n_g - j\frac{G}{2} \quad . \qquad (4.61)$$

The net gain, G, is now given by a modified version of equation (4.57),

$$G = \Gamma \cdot g(N,\lambda) - f_{cc}\cdot(\wp N + p_o) \quad . \qquad (4.62)$$

Equation (4.60) is reduced by substituting equation (4.61) for β, negecting small terms, and noting that as E(z,t) is also a solution to the wave equation, hence the leading term in eqn. (4.60) is equal to zero. Hence equation (4.60) becomes,

$$\frac{1}{v_g}\frac{\partial E}{\partial t} + \frac{\partial E}{\partial z} = \frac{G}{2}E + j\frac{G^2}{4k_o n_g}E \quad , \qquad (4.63)$$

where v_g is the group velocity, c/n_g.

It is convenient to separate equation (4.63) into real and imaginary parts by equating,

$$E = A\cos\left[-j\theta\right]. \tag{4.64}$$

The forward travelling magnitude and phase equations are then obtained,

$$\frac{1}{v_g}\frac{\partial A}{\partial t} + \frac{\partial A}{\partial z} = \frac{G}{2}A, \tag{4.65}$$

$$\frac{1}{v_g}\frac{\partial \theta}{\partial t} + \frac{\partial \theta}{\partial z} = j\frac{G^2}{4k_o n_g}\theta \quad . \tag{4.66}$$

In the subsequent analysis the phase variation is not of interest and will be ignored. This is because, under the conditions modelled for the active waveguide, there is limited coupling between the forward and backward travelling waves. However, for other devices the phase information is essential as it can affect operating frequency (chirp) in resonant cavity devices such as lasers, SLEDs, Fabry-Perot Laser Amplifiers [1,12].

The final step to producing the familiar rate equations for variations in z and t [13] is to consider spontaneous noise, and photon flux instead of electric field. This has the advantage that it connects clearly with the gain and spontaneous terms calculated in chapter 3. In terms of electric field, the photon flux is given by,

$$P = v_g \cdot \left(\frac{\varepsilon_o n_g^2}{2\,h\upsilon}\right) \int |E|^2 dV \quad , \tag{4.67}$$

where $\bar{h}\,\omega$ is the photon energy.

From the definitions of E(z,t) and A, it is clear that $P \propto A^2$. Equation (4.65) can be rewritten for the forward travelling flux, $P(z,t,\lambda)$,

$$\frac{1}{v_g}\frac{\partial P(z,t,\lambda)}{\partial t} + \frac{\partial P(z,t,\lambda)}{\partial z} = G \cdot P(z,t,\lambda) + \delta \cdot S(z,t,\lambda). \qquad (4.68)$$

The final $\delta S(z,t,\lambda)$ term is included to show the effect of spontaneous emission and is essential for the analysis of the active waveguide. $S(z,t,\lambda)$ is given from a combination of equations (3.32) and (3.34), as described in sections 3.5 and 3.6, suitably modified to give flux rather than emission rate. The spontaneous emission factor, δ gives the fraction of the spontaneous emission that is coupled into the confined propagating flux.

The photon conservation equation for the backward travelling flux, $Q(z,t,\lambda)$ is calculated by taking the counterpart of (4.59) with z replaced by -z, eventually yielding,

$$\frac{1}{v_g}\frac{\partial Q(z,t,\lambda)}{\partial t} - \frac{\partial Q(z,t,\lambda)}{\partial z} = G \cdot Q(z,t,\lambda) + \delta \cdot S(z,t,\lambda). \qquad (4.69)$$

Thus, the behaviour of light propagating in the active waveguide has been reduced to two photon conservation equations, for optical fluxes propagating in the forward and backward directions. These conservation equations show the variation of the flux in time,t longitudinal dimension, z and wavelength, λ and the coupling of spontaneous emission into that flux. The lateral and transverse variations are represented by the combined confinement factor, Γ.

4.4.2 Carrier Conservation Equation

The description of the guide parameters is complete when the carrier density at a point in time and space can be determined. As was shown in chapter 3, the stimulated gain and spontaneous emission in the guide is dependent on the carrier density, as are the losses due to free carrier absorption. Hence, the flux density in the guide can only be calculated if the carrier density is known.

The buried heterostructure or rib-guide structure for the active waveguide provide excellent carrier confinement, in both the lateral and transverse directions. If the guide dimensions are sufficiently small compared with the diffusion length (≈ 3-5 μm) the carrier density may be assumed to independent of position in the transverse and lateral dimension. Thus the active region of the guide may be treated as a "black-box" which has carriers input in the form of a pumping current, and photons output in the form of a photon flux.

The rate of carrier density input to the active region, per unit volume is determined by,

$$N_{in} = \frac{J}{e \cdot d} = \frac{I}{e \cdot d \cdot w \cdot L} \qquad (4.70)$$

where, d,w, and L are the active region depth, width and length respectively; J is the injected current density, which in the case of a buried heterostructure with a narrow stripe = I/wL, in the active region and ≈ 0 outside; e is the electron charge.

Carriers are 'lost' due to recombination. There are several recombination mechanisms which may be considered. Radiative recombination, stimulated and spontaneous emission, has been described in detail in chapter 3. In addition non-radiative recombination occurs, where no photons are produced. In this case, non-radiative recombination is ignored but a term of the form $A_{nr}N$ could easily be included, where A_{nr} is the non-radiative recombination rate.

From chapter 3 it is known (equation (3.40) that the total spontaneous emission rate for a particular carrier density, N is given by,

$$R_{sp(total)} = B_r N \cdot (N + n_o) \; . \qquad (4.71)$$

The total stimulated emission rate is given by the integral of the emission rates over the entire spectrum. From section 3.3.4 it known that the net rate of stimulated emission is

given by the product of photon flux and gross optical gain. Hence the total stimulated emission rate is,

$$R_{st(total)} = \int_0^\infty g(N,\lambda)\left(P(z,t,\lambda) + Q(z,t,\lambda)\right)\, d\lambda \quad . \tag{4.72}$$

The carrier conservation equation can be therefore be written as,

$$\frac{\partial N}{\partial t} = \frac{J}{ed} - B_r N\cdot (N + n_0) - \int_0^\infty g(N,\lambda)\cdot \left(P(z,t,\lambda) + Q(z,t,\lambda)\right) d\lambda). \tag{4.73}$$

At any point, the total spontaneous emission rate must be consistent with the spontaneous emission rates given in the photon conservation equations (4.68) and (4.69),

$$R_{sp(total)} = B_r N\cdot (N + n_0) = \int_0^\infty S(N,\lambda)d\lambda \quad . \tag{4.74}$$

ie, the total spontaneous emission rate is the integral of the rate over the entire spectral range.

4.4.3 Discretisation of the Continuity Equations

It should be noted that the photon conservation equations, (4.68) and (4.69) are continuous in λ, and the carrier conservation equation, (4.73) contains an integral over λ of the stimulated emission rate. Such a set of equations are unwieldy for numerical analysis techniques. In order to make the modelling more tractable, the range of wavelengths considered is restricted to an upper and lower bound, and the spectral behaviour is discretised.

At shorter wavelengths (higher energy), the gross optical gain is highly negative, hence any flux at such a wavelength is heavily attenuated and can be ignored. Whilst at long wavelengths, where the quantum energy is less than the forbidden band energy, there is no loss or gain. Hence, there is no interaction between the flux and carrier density. For the model described in chapter 3, the range where there is significant flux / carrier interaction is between 780 and 840 nm.

In resonant cavity devices, the optical wavelength is restricted to a few longitudinal modes. However, in the case of the active waveguide there are no strong cavity resonances, and as an alternative the optical spectrum is divided into a number of discrete wavelength 'slots'. In each slot, it is assumed that the stimulated gain, spontaneous emission and optical flux are constant across the slot, and can be approximated to the central value. This gives a family of photon conservation equations that can be solved independently, for each slot, whilst the total stimulated emission rate is given by the **summation** of the gain/flux product for each slot.

The photon conservation for the forward and backward fluxes for the i^{th} wavelength slot are,

$$\frac{1}{v}\cdot\frac{\partial P_i}{\partial t} + \frac{\partial P_i}{\partial z} = G_i P_i + \delta S_i \ , \qquad (4.75)$$

$$\frac{1}{v}\cdot\frac{\partial Q_i}{\partial t} - \frac{\partial Q_i}{\partial z} = G_i Q_i + \delta S_i \ , \qquad (4.76)$$

and the carrier continuity equation becomes,

$$\frac{dN}{dt} = \frac{J}{e.d} - B_r N\cdot(N + p_o) - \sum_{i=1}^{i=u} g_i\cdot(P_i + Q_i) \ . \qquad (4.77)$$

Equations (4.75) - (4.77) are the starting point for subsequent analyses in this thesis.

The number of wavelength slots is determined by the accuracy required. For each slot, the gross optical gain, $g_i(N,\lambda)$ and the spontaneous emission factor must be

calculated, $S(N,\lambda)$. In this thesis two sets of discretised stimulated gain and spontaneous emission data were used, both covering the range 780-840 nm. One relatively coarse set, with thirty one 2 nm slots, and a fine set with one hundred and fifty one 0.4 nm wide slots. In general, the coarse set was used for exploratory work, and the fine set for final results. The data sets were generated from the model discussed in chapter 3, by fitting polynomials in N, to the central values in each wavelength slot.

References, Chapter 4

1. AGGRAWAL, G.P. and DUTTA, K., 'Long-wavelength semiconductor lasers',
Van Nostrand Reinhold Company, New York 1986.

2. MAGID, L.M., 'Electromagnetic fields, energy and waves',
Chapter 9, Wiley , New York, 1972.

3. SONG - TSUEN PENG, and OLINER, A.A., 'Guidance and leakage properties of a class of open dielectric waveguide: part I – mathematical formulation',
IEEE Trans. Microwave Theory Tech., 1981, MMT-29, (9), pp843-855.

4. MARCATILI, E.A.J., 'Dielectric rectangular waveguide and directional coupler for integrated optics',
Bell Syst. Tech. J., 1969, 48, pp2071-2102.

5. KONX, R.M. and TOULIOS, P.P., 'Integrated circuits for the millimeter wave through optical frequency range,' in
Proc. Symp. Subillimeter Waves, Polytechnic Press, New York, 1970, pp497-516.

6 BUUS, J., ' The effective index method and its application to semiconductor lasers',
IEEE J. Quantum Electron., 1982, QE-18, (7), pp1083-1089.

7. GOELL, J.E., 'A circular-harmonic computer analysis of rectangular dielectric waveguides',
Bell Syst. Tech. J., 1969, 48, pp2133-2160.

8. MARCUSE, D., 'Theory of dielectic optical waveguides',
Academic Press, New York, 1974.

9. ADAMS, M.J., 'An introduction to optical waveguides',
Wiley, New York, 1981.

10.KAPANY, N.S., AND BURKE, J.J., 'Optical waveguides',
Academic Press, New York, 1972.

11 BOTEZ, D., 'Analytic approximation of the radiation confinement factor for the TE_0 mode of a double-heterojunction laser'
IEEE J. Quantum Electron., 1981, QE-17, pp178.

12 MORTON, P.A., ORMONDROYD, R.F., BOWERS, J.E., and DEMOKAN, M.S., 'Large-Signal harmonic and intermodulation distortions in wide-bandwidth GaInAsP semiconductor lasers'

IEEE J. Quantum Electron, 1989, QE-25, (1), pp1559-1567.

13 STATZ, H., and deMARS, G.A., 'Transients and oscillation pulses in masers', in *Quantum Electronics, ed C.H. Townes, Columbia University Press, New York, 1960.*

5 SOURCE COUPLING AND DETUNING

5.1 Introduction

The problem of coupling light from a source device into a waveguide is critical to any form of integrated optics system, indeed, any commercial optical communications system. This problem has been studied by many authors for different cases. In this chapter, the originally proposed case of a semiconductor laser coupled to a pumped waveguide, across and etched or milled gap will be considered. This type of geometry has considerable similarity to the cleaved-coupled cavity (C^3) laser and the butt-coupling of a laser and a passive guide. However, as the guide is only lightly pumped, a C^3 analysis would be inappropriate, as the system will be unlikely to form coupled laser-waveguide modes. The butt-coupling analyses are therefore adapted to this particular case.

Mueller et al [1] and Hammer and Neil [2] examine the case of "butt-coupling" an AlGaAs laser into a $LiNbO_3$ type passive waveguide, by approximating the modes in the laser and waveguide to Gaussian beams. In the butt-coupling technique, the laser is aligned so that the active region is parallel to the passive waveguide and on the same axis, as shown in figure 5.1. The laser is moved, using micro manipulators until the maximum power is coupled into the guide. The laser is then bonded to the guide using epoxy resin.

Hunsperger, Yariv and Lee [3] have also examined the butt-coupling of an AlGaAs laser and a passive guide but use a sophisticated modal analysis to obtain an analytic expression for the coupling efficiency. The coupling between lasers and the optical fibres has been extensively studied both theoretically and practically, see for instance Cohen [4].

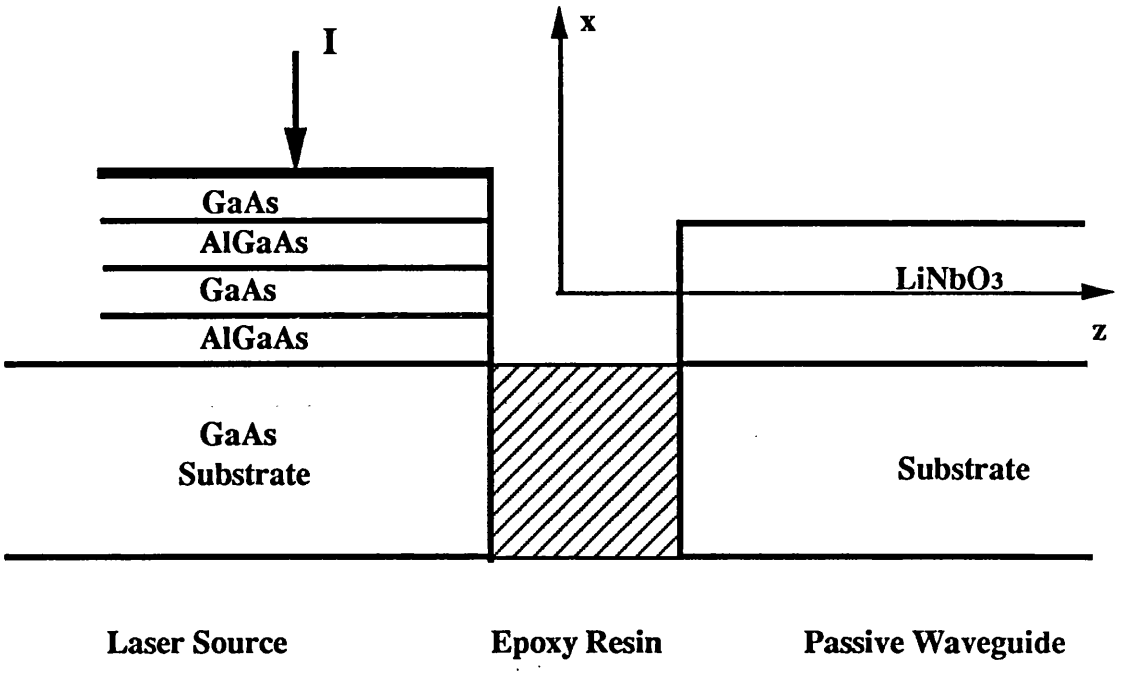

Figure 5.1 : Butt-Coupling of an AlGaAs Double Heterostructure Laser to a $LiNbO_3$ Waveguide

Unfortunately, many authors fail to address the detuning effect that such coupling has on the laser source. Work on optical fibre systems [5] has shown that the power reflected from : the input end of the fibre; discontinuities inside the fibre and the output end of the fibre, can effect the behaviour of the source. Hammer [6] has performed a multiple Fabry-Perot cavity type analysis to derive analytic expressions to predict the behaviour of a laser with several external reflectors. This type of F-P analysis tends to overestimate the effects in a butt-coupling geometry as it does not take into account the beam divergence in the gap between the laser and the guide.

The presence of external cavities and the coupling of light back into the source can also have advantages. The cleaved-coupled cavity (C^3) laser [8] has been developed to give semiconductor lasers with a high degree of optical frequency stability and selectivity. External optical injection can also have the effect of damping out relaxation oscillations in lasers [Otsuka, 7], which can be of advantage in digital communications systems.

In the analysis presented the transverse modes of the laser and the waveguide are described by approximating the buried heterostructure to the box dielectric guide discussed in chapter 4. The far-field pattern of the laser in the gap is determined using a Fourier transform technique. An effective reflectance and transmittance of the gap can then be calculated from the coupling between the laser far field and the waveguide modes. The advantage of this method is that it does not rely on the Gaussian beam approximation used in [1,2,4 and 9], but it still takes into account the divergence of the laser beam and the multiple reflections in the gap. The model can also predict the stimulation of higher order modes in the waveguide.

Once an effective reflectance and transmittance have been determined, the detuning effect on the laser source can also be examined using the standard laser rate equations. Rather than quoting these equations in their standard form, they are derived from the spatial rate equations derived in chapter 4. This is to show the range of validity of the two sets of commonly used rate equations and to establish some key concepts.

5.2 Laser Output Beam Divergence

A detailed knowledge of the output beam of a semiconductor laser is a crucial to the understanding of the coupling between the laser and the guide. A very sophisticated analysis and a review of other techniques is presented by Rozzi and In't Veld [15], general reviews of the work performed in this area are also given in [12] and [13]. The method used by Rozzi and In't Veld [15] includes the effects of gain guiding in the laser, which leads to curved rather than plane wavefronts at the output facet. As a buried heterostructure has been used for both the laser and the waveguide, the primary guiding mechanism is assumed to be index guiding. This allows the use of a much simpler expression detailed by Casey and Panish [12].

There is very little to be gained from repeating, verbatim, the analysis given in pages 71-79 of [12]. Instead a brief outline will be given of the method. The topology considered is shown in figure 5.2.

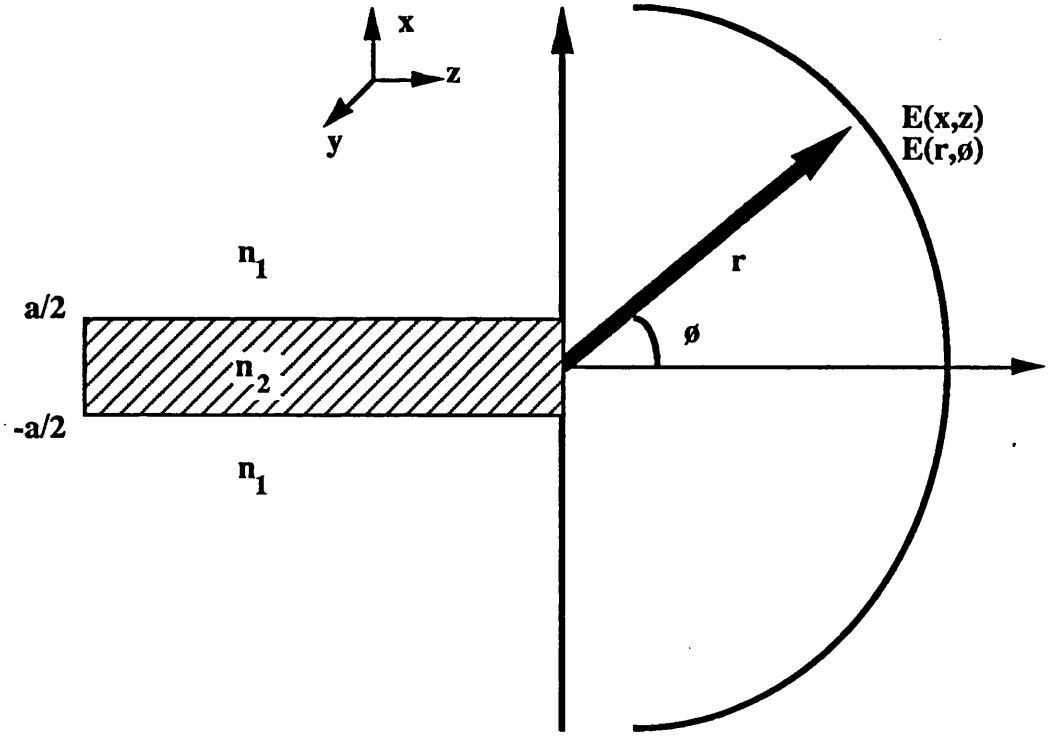

Figure 5.2 : Far Field Pattern For a Double Heterostructure laser

The shaded region in figure 5.2 is the GaAs active region of the laser with refractive index n_2, surrounded by the buried heterolayers of AlGaAs, refractive index n_1. The refractive indices are assumed to be purely real and the layers are infinite in the y-direction.

For a TE-mode in the laser, the far field mode in free space ($z > 0$) will have three zero components, $E_x = E_y = H_z$ and $\partial/\partial y = 0$. The wave equation from chapter 4 can be written as,

$$\frac{\partial^2 E_y}{\partial x^2} + \frac{\partial^2 E_y}{\partial z^2} = \mu_o \varepsilon_o \frac{\partial^2 E_y}{\partial t^2} \qquad (5.1)$$

The separation of variables technique may be applied to give solutions of the form,

$$E_x(x,z,t) = X.Z.T \qquad (5.2)$$

then (5.1) becomes,

$$\left(\frac{X''}{X}\right) + \left(\frac{Z''}{Z}\right) = \mu_o \varepsilon_o \left(\frac{T''}{T}\right) = -\omega^2 \mu_o \varepsilon_o = -k_o^2 \qquad (5.3)$$

Equation 5.3 shows that the x and z components of the free space wavevector are related to the free space propagation constant k_o. This relationship can be shown more clearly by figure 5.3. The parameter u, is dimensionless and gives the difference between the propagation constants in the x and y directions.

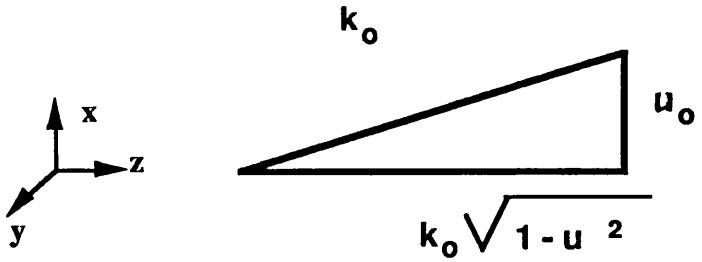

Figure 5.3 : Components of Free Space Propagation Constant k_o, in x and z given in terms of the dimensionless parameter u.

Using this concept (5.3) may be written as,

$$\left(\frac{X''}{X}\right) = -\left(\frac{Z''}{Z}\right) - k_o^2 = -u^2 k_o^2 \qquad (5.4)$$

where $-u^2 k_o^2$ is the separation constant. The solution for X and Z can now be calculated from (5.4), assuming a single value of u in x and z,

$$X = A\cdot \exp(juk_o x) + B\cdot \exp(-juk_o x), \qquad (5.5)$$

$$Z = C\cdot \exp\left(jk_o\sqrt{1-u^2}\cdot z\right) + D\cdot \exp\left(-jk_o\sqrt{1-u^2}\cdot z\right). \qquad (5.6)$$

The particular solution of $\mathcal{E}_y(x,z)$, for a given value of u is then,

$$\mathcal{E}_y(x,z) = e(u)\cdot \exp(-juk_o x)\cdot \exp\left(-jk_o\sqrt{1-u^2}\cdot z\right). \qquad (5.7)$$

Only one term of equations (5.5) and (5.6) is taken as the other is included by u having the opposite sign, e(u) represents the product of B and D. The general solution is obtained by integrating over all values of u :

$$E_y(x,z) = \int_{-\infty}^{\infty} e(u)\cdot \exp(-juk_o x)\cdot \exp\left(-jk_o\sqrt{1-u^2}\cdot z\right)\cdot du \qquad (5.8)$$

Casey and Panish [12] go on to show, by solving (5.8) and matching fields at the z=0 boundary (at the laser facet), that the solution to (5.7) in polar co-ordinates is,

$$E_y(r,\phi) = \left(\frac{k_o}{2\pi r}\right)^{\frac{1}{2}}\cdot \exp\left(\frac{j\pi}{4}\right) \exp(-jk_o r)\cdot G(\phi)\cdot \int_{-\infty}^{\infty} E_y(x,0)\cdot \exp(-jk_o \sin(\phi))\cdot du$$

$$u = \sin\phi, \qquad (5.9)$$

The first three terms in equation (5.9) are simple propagation terms for a cylindrical wavefront. G(ø) is the Huygen's obliquity factor, which is a correcting pre-factor to the final terms, which show that the far field pattern of the laser is essentially the Fourier transform of the near field pattern at $z = 0^+$. G(ø) can be reasonable approximated to cos(ø) [12]. A brief examination of equation (5.9) shows, that for a plane wave incident at $z = 0^-$ (ie $E_y(x,0)$ has a constant phase), the far field pattern, $E_y(r,\phi)$ will be symmetrical. This symmetry can be used to half the range of calculation when solving (5.9) to calculate the coupling coefficients.

Using the effective index method, detailed in chapter 4 it is possible to estimate the fundamental and higher order modes in both the laser and the waveguide. For an index-guided buried heterostructure laser operating in the fundamental mode, equation (5.9) can be solved in both the x and y directions. Figure 5.4 shows the far field pattern of the fundamental box waveguide mode.

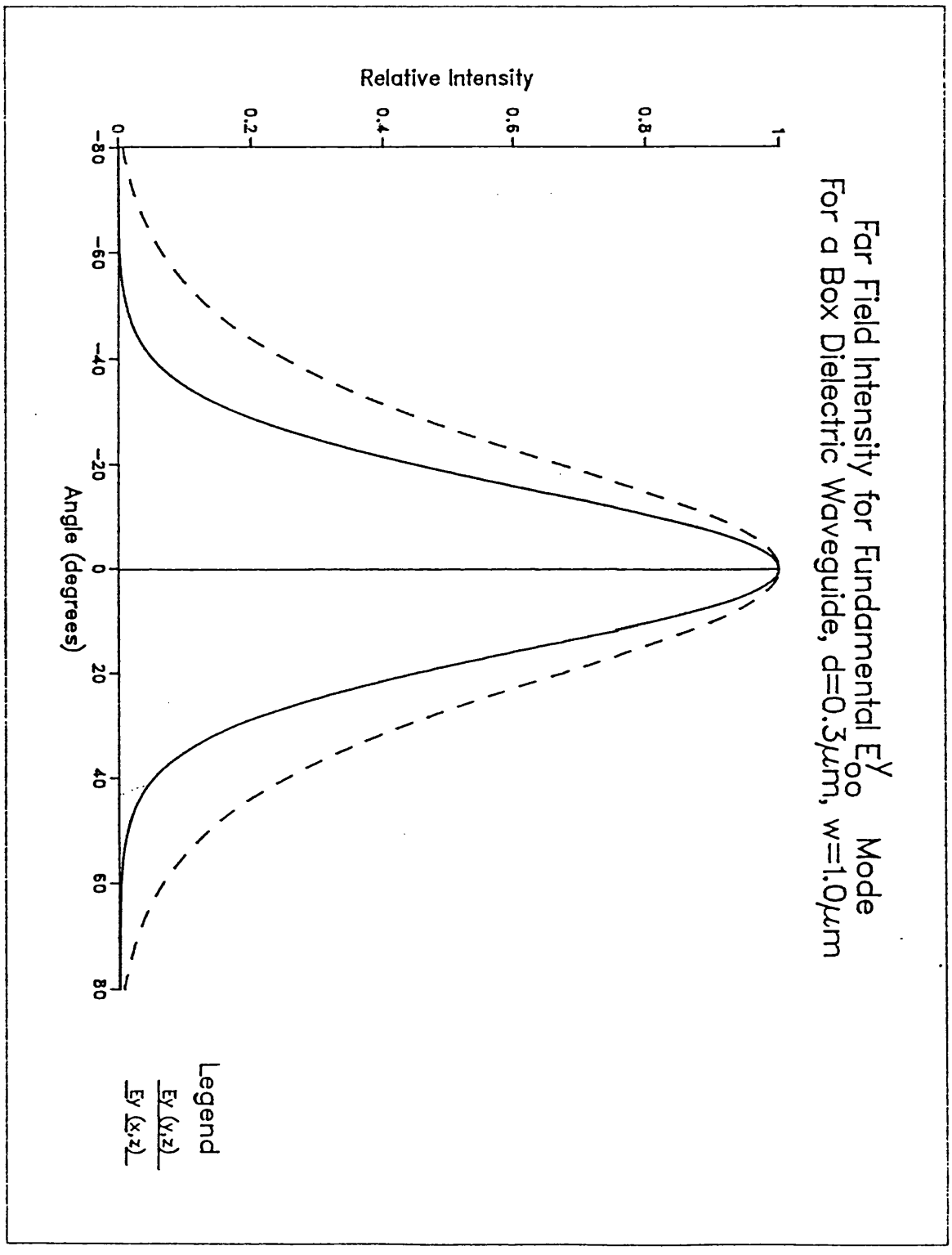

Figure 5.4 : Far field distribution of the fundamental mode (E^y_{00}) of a box dielectric waveguide. Using the effective dielectric constant approximation.

5.3 Coupling Coefficients and Effective Mirror Formalism

5.3.1 Coupling coefficients

The diverging laser beam in the gap is assumed to undergo multiple reflections at the etched facets as shown in figure 5.5.

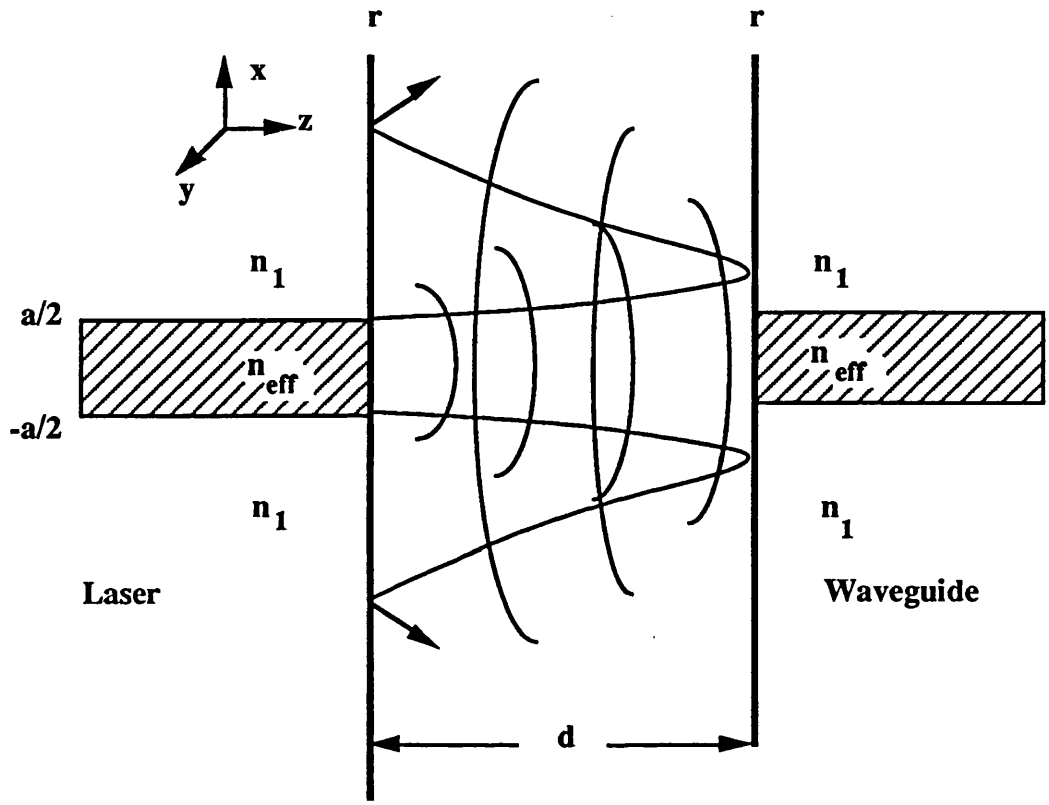

Figure 5.5 : Beam Pattern in an Etched Gap Between Laser and Guide.

In general the coupling between two fields E_1, E_2 is given by the overlap integral [14],

$$k_{1,2} = \frac{\int_{-\infty}^{+\infty} E_1 E_2^* \, dx}{\left(\int_{-\infty}^{+\infty} E_1 E_1^* \, dx \cdot \int_{-\infty}^{+\infty} E_2 E_2^* \, dx \right)^{\frac{1}{2}}} \qquad (5.10)$$

where * indicates the complex conjugate.

For a symmetrical system, the integrals need only be considered over the range $0 \rightarrow \infty$. The self-coupling between the laser far field and near field, as well as the cross coupling between the laser far field and the guide modes can now be calculated using the far field pattern equation (5.9) and the effective index approximation of the laser and guide modes.

For simplicity, it may be imagined that at each reflection at either facet, a fixed proportion of the field is transmitted whilst the remainder is perfectly reflected, governed by the reflectively, r of the facet. The coupling between the transmitted field and a mode in the laser or waveguide is given by (5.10). Summing over an infinite number of reflections will give the total field coupled into the guide and back into the laser. If the notation $k_{f,m}[z]$ is used to denote the coupling between the laser far field at a distance z from the facet and a particular mode in the laser or guide, the total field coupled into a mode in the waveguide is then given by,

$$X_m = \left(1 - r^2\right) \cdot \sum_{n=1}^{\infty} r^{2(n-1)} \, k_{f,m}\left[(2n-1) \cdot d\right], \qquad (5.11)$$

where d is the width of the gap, r is the reflectivity of the GaAs / Air facet. The total field coupled into a mode in the laser is,

$$S_m = \left(1 - r^2\right) \cdot \sum_{n=1}^{\infty} r^{(2n-1)} \, k_{f,m}\left[2n \cdot d\right] . \qquad (5.12)$$

ie., the sum of all the coefficients for each refection.

5.3.2 Effective mirror formalism

In common with other authors [1,9] the gap can now be replaced with an effective mirror as shown in figure 5.6.

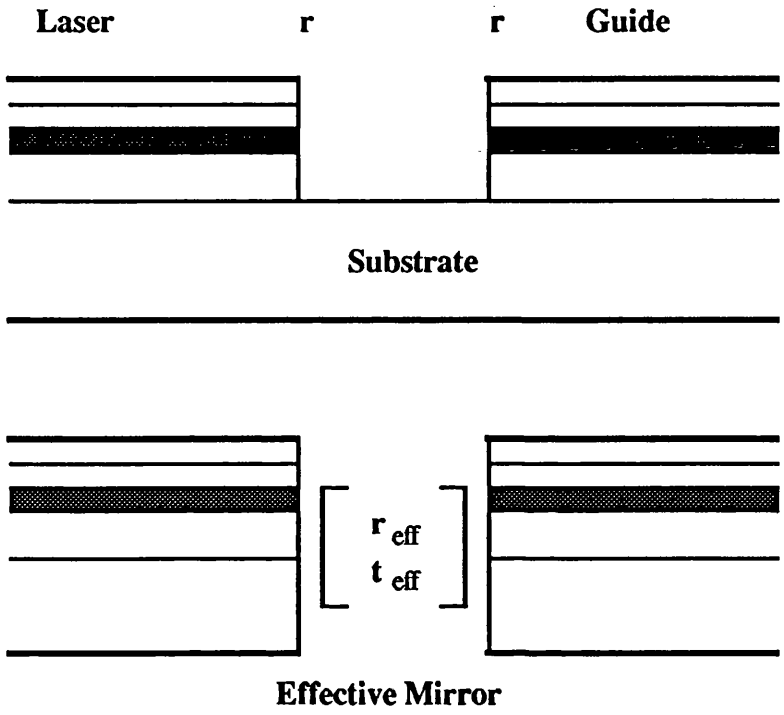

Figure 5.6 : Effective Mirror Formalism.

In the effective mirror formalism, the behaviour of the gap is reduced to a matrix of reflection and transmission coefficients. The gap is reciprocal so that the parameters apply to both directions, from the laser to the guide or from the guide to the laser. For each far field mode of the laser (or guide) there will be an infinite number of coupling parameters X_m, S_m for both the cross and self coupling cases. However, only the coupling between guided modes need be considered. The energy coupled into non-guided modes is assumed to be 'lost' as is energy that escapes from the gap. Throughout the analysis, it is assumed that the laser is operating with only the fundamental lateral mode present.

The effective reflectivity for the laser far field coupling back into the fundamental laser mode is therefore,

$$r_{eff,0} = r - S_o \qquad (5.13)$$

whilst for the higher order modes, the effective reflectivity for the field coupled back into the m^{th} propagating mode is,

$$r_{eff,m} = -S_m \ , \qquad m = 1, 2, ...M \qquad (5.14)$$

where M is the number of the highest order mode which will propagate. For all waveguide modes the effective transmittivity, for the laser fundamental far field is simply the cross-coupling parameter given in equation (5.11),

$$t_{eff,m} = -X_m \ , \qquad m = 1, 2, ...M. \qquad (5.15)$$

From the above analysis and the derivation of the far field pattern in section 5.2, it is clear that these coupling coefficients are complex quantities, dependent on the width of the gap, d, the reflectivity of the facets, r and the free space wavelength, λ. In the next section, results are presented for the variation of the gap coupling coefficients with gap width, waveguide dimensions and operating wavelength.

5.4 Reflection and Transmission Coefficients

5.4.1 Introduction

The results in this section were calculated in the following manner, The modes of the buried heterostucture laser and waveguide were found by approximating the guide to the dielectric box and applying the effective index method to the solution of the propagation constants (β, β_{eff}), detailed in chapter 4. The expression given by Casey and Panish [12], equation (5.9), is used to give the far field variation of $E_y(r,\phi)$ in both the x-z and y-z planes. Using the overlap integral (5.10) and the summations in (5.11) and (5.12), the effective reflectivity and transmittivity are calculated (5.13) - (5.15). Unless otherwise stated, the dimensions of the laser and waveguide are identical and the parameters used are shown in table 5.1.

Lasing Wavelength, λ_k	= 824 nm
Active Layer Refractive Index, n_1	= 3.590
Cladding Layer Refractive Index, n_2	= 3.350
Facet Reflectivity, r	= 0.56
Facet Reflectance, R	= 0.31
Active Layer Thickness, d	= 0.30 μm
Active Layer Width, w	= 5.00 μm

Table 5.1 : Gap Coupling Simulation Parameters.

In practice it is found that an infinite number of terms is not required in (5.11) and (5.12) and only 3 or 4 reflections need to be considered to give accurate values of r_{eff} and t_{eff}.

The results presented show the power reflection and transmission coefficients (or reflectance and transmittance) given by,

$$R_{eff} = r_{eff} \cdot r_{eff}^{*} , \tag{5.16}$$

$$T_{eff} = t_{eff} \cdot t_{eff}^{*} , \tag{5.17}$$

where * indicates the complex conjugate. For comparison the coefficients for a lossless Fabry-Perot etalon were also calculated.

5.4.2 Fabry-Perot Etalon

If the gap is modelled as a Fabry-Perot etalon and the laser beam is assumed to perpendicular to the facets and non-divergent, then Yariv [14] gives the effective power coupling coefficients for the fundamental mode as,

$$R_{eff} = \frac{4R \cdot \sin^2(\alpha)}{(1 - R)^2 + 4R \cdot \sin^2(\alpha)} , \tag{5.18}$$

$$T_{eff} = \frac{(1 - R)^2}{(1 - R)^2 + 4R \cdot \sin^2(\alpha)} , \tag{5.19}$$

where R is the facet reflectance, $r \cdot r^*$ and $\alpha = 2\pi d/\lambda$. From (5.18) and (5.19) the transmittance will be unity and the reflectance zero, when $\alpha = i\pi$, ie. $d = i \cdot \lambda /2$, where i = and integer. Conversely, when $\alpha = (2i\pi - 1)/2$, ie. $d = (2i \cdot \lambda - 1)/4$ then the reflectance has a maximum value of,

$$R_{eff} = \frac{4 \cdot R}{(1 + R)^2} \quad , \tag{5.20}$$

and the transmittance has a minimum value of,

$$T_{eff} = \frac{(1 - R)^2}{(1 - R)^2 + 4 \cdot R} \quad . \tag{5.21}$$

For GaAs, $R \approx 0.3$, giving a maximum value of effective reflectance of 0.7, whilst the minimum value of transmittance is 0.3. From (5.18) and (5.19) it can be seen that for all α,

$$T_{eff} = 1 - R_{eff} \quad , \tag{5.22}$$

ie., no power is lost in the etalon.

Figure 5.7 shows the variations of the power reflectance and transmittance for a non-divergent beam in a Fabry-Perot etalon, and confirms the derived maximum and minimum values. The transmittance maxima and reflectance minima occur at $d/\lambda = i/2$, whilst the reflectance maxima and transmittance minima occur at $d/\lambda = (2i - 1)/4$. Figure 5.7 clearly shows the periodic nature of an ideal Fabry-Perot etalon and the fact that no power is lost in such an etalon.

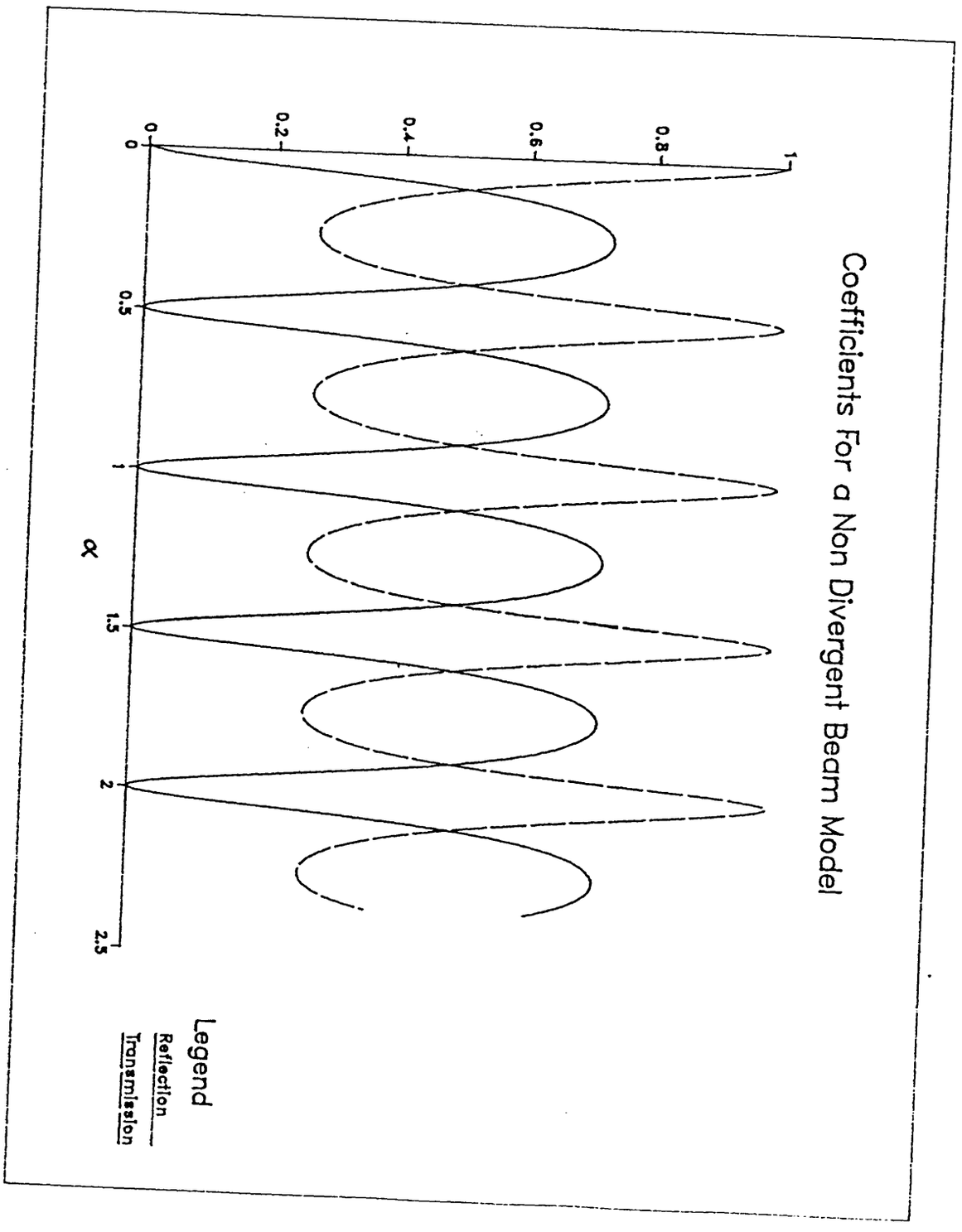

Figure 5.7 : Reflection and transmission coefficients for a non-divergent beam model (Fabry-Perot etalon).

5.4.3 Fundamental mode coupling coefficients

Figures 5.8 and 5.9 show the effective power coupling coefficients, for the coupling between the fundamental far-field and the fundamental laser or guide mode, calculated using the method described at the start of this section.. The effect of beam divergence in the gap is to damp the fluctuations of the quantities as the gap width increases. In addition the transmittance tails off with an exponential envelope, due to the mismatch between the fields. A similar characteristic has been observed for the coupling between a laser and a passive waveguide [3]. For large values of gap width the transmittance in figure 5.9 tends to smooth out to 0.10 - 0.15, which is consistent with practically observed values [2].

5.4.3 Higher order mode coupling coefficients

The coupling into higher-order modes is shown in figures 5.10 and 5.11. It is immediately obvious that there is no coupling between the (even) laser far-field and any odd guide mode. This is because the numerator integral in equation (5.8) is of an odd function over a symmetrical range. Any such integral will always yield a zero result. Figures 5.10 and 5.11 also show that the maxima and minima of the coefficients are shifted away from the values predicted by the F-P etalon analysis. In addition the transmittance maxima (minima) do not necessarily coincide with the reflectance minima (maxima) and the characteristics no longer have a smooth $\sin^2(\alpha)$ shape as the field overlap is highly dependent on the gap width.

Although power is coupled into these higher order modes, it is debatable whether they will propagate. In the laser, the principal lasing mode is determined by the threshold conditions described later in this chapter. However, the gap may promote higher order laser modes given the correct conditions. Such modes are undesirable as they lead to unpredictable behaviour and a 'kinked' light output / current characteristic [11, 12 and 13].

Higher order modes may also be promoted in the waveguide. In the derivation of the rate equations it was assumed that the guide structure gives rise to a flat gain

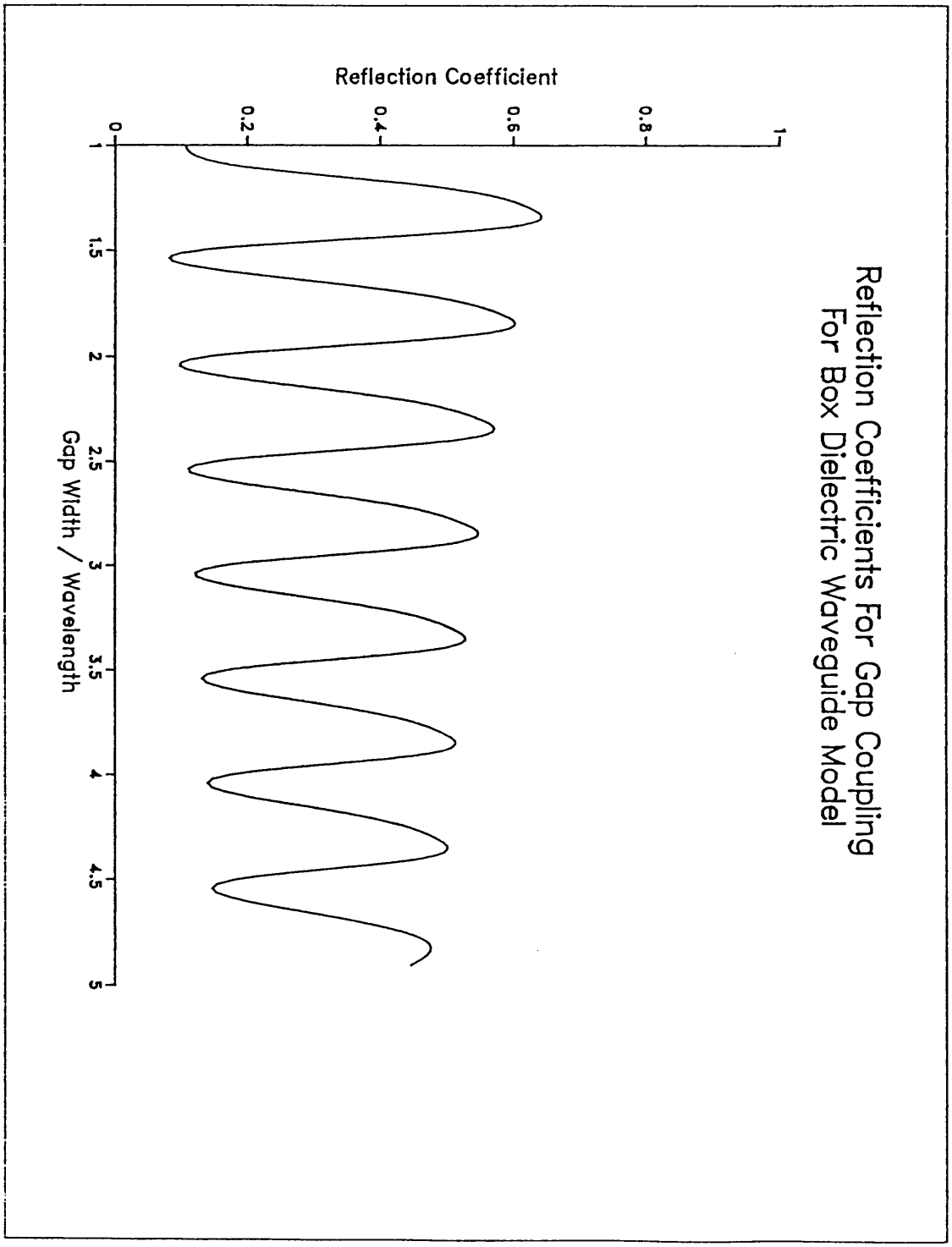

Figure 5.8 : Reflectance (reflection coefficient) for the box dielectric waveguide model.

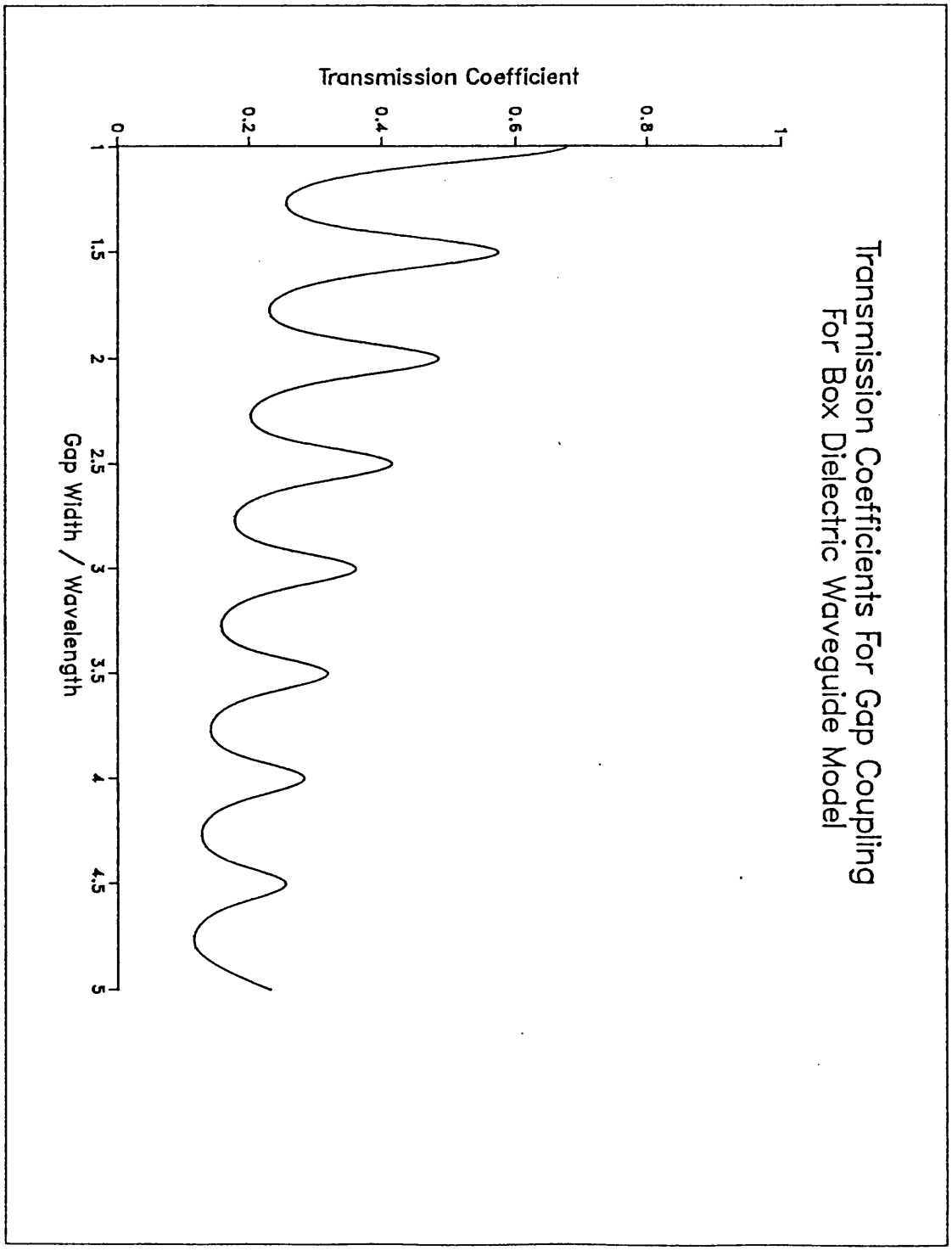

Figure 5.9 : Transmittance (transmission coefficient) for the box dielectric waveguide model.

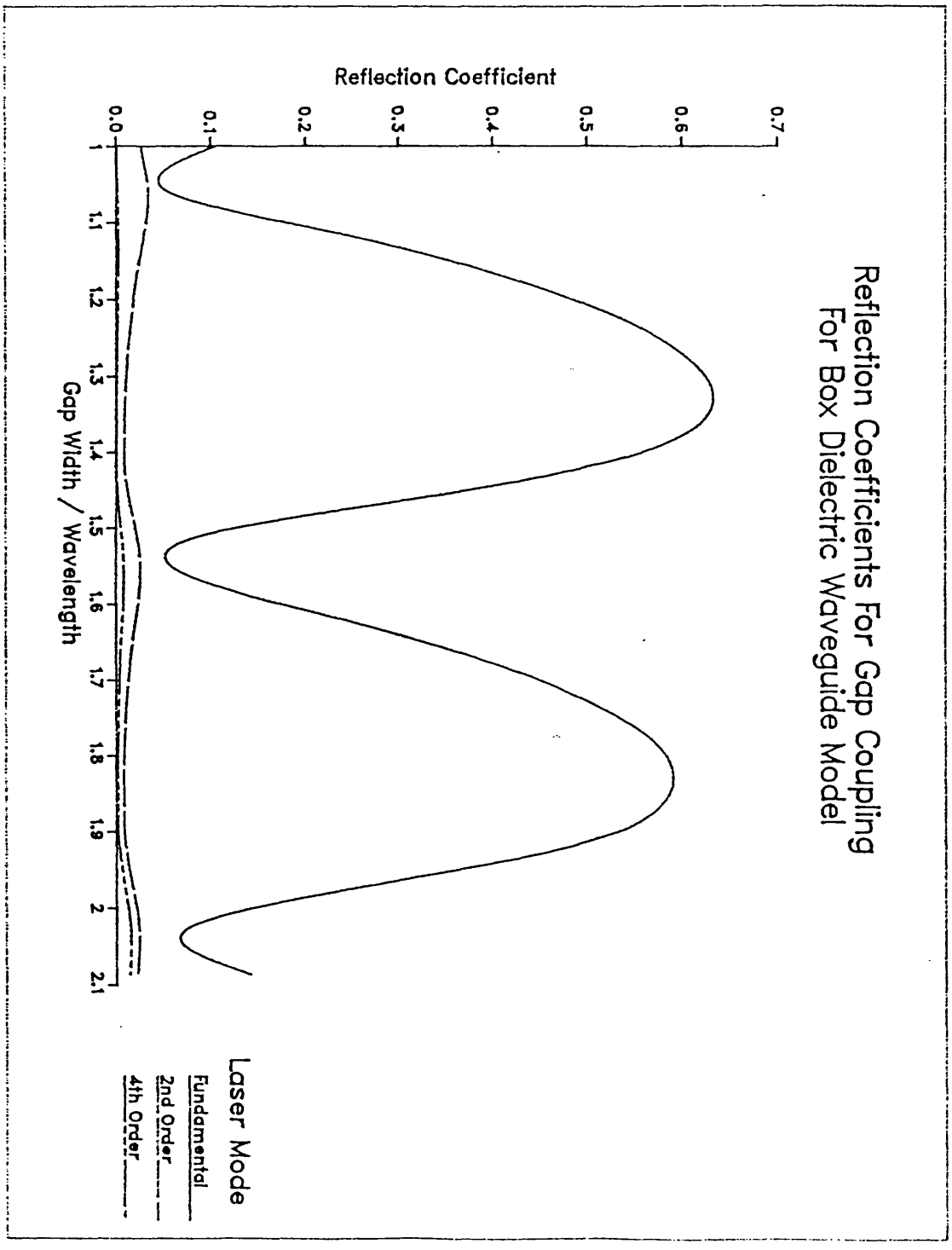

Figure 5.10 : Reflectance (reflection coefficient) from laser fundamental mode to fundamental and higher order modes.

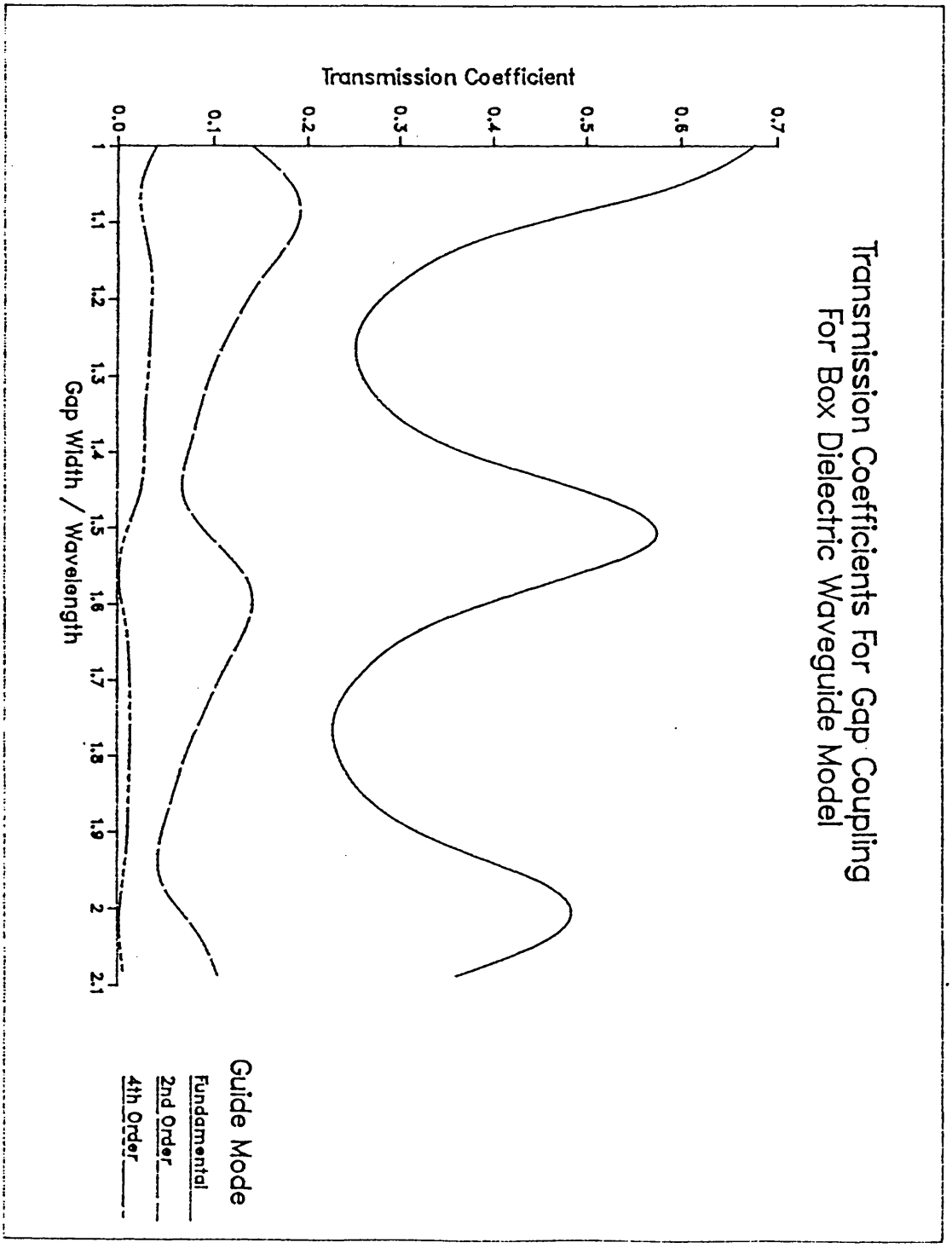

Figure 5.11 : Transmittance (transmission coefficient) from laser or waveguide fundamental mode to fundamental and higher order modes.

profile as shown in figure 5.12(a). In general, the fundamental mode experiences the highest net modal gain as it has the highest confinement factor. However, if the power in the fundamental mode is high, spatial hole burning can occur, where the high rate of stimulated recombination locally reduces the carrier density. Hence the carrier density and optical gain can have a distribution as shown in figure 5.12(b). This shape of gain distribution may favour higher modes. The coupling of power into higher order modes is undesirable as it leads to increased losses and signal dispersion [13]. Unfortunately, the 2nd order transmittance in figure 5.11 can be as high as 0.2, almost 30% of the total power coupled into the guide.

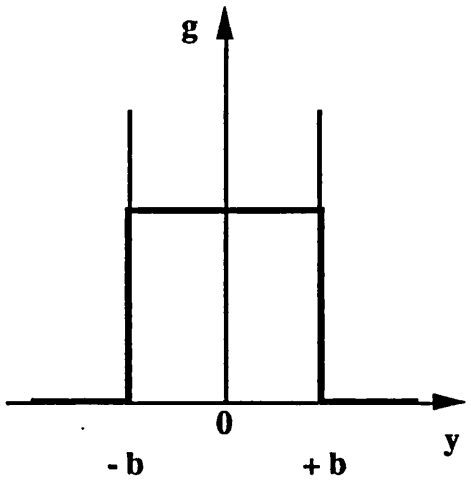

Figure 5.12 (a) : Optical Gain Distribution for a BH-guide, Normal Distribution.

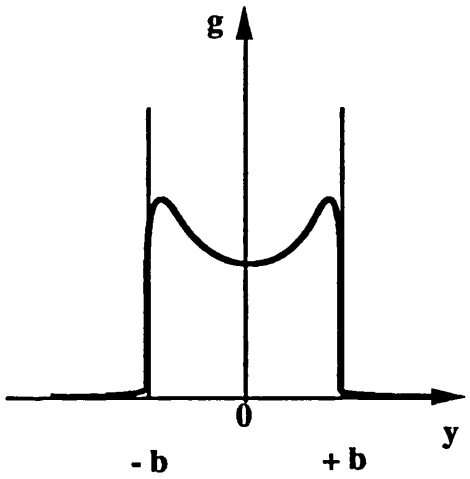

Figure 5.12 (b) : Optical Gain Distribution for a BH-guide, With Spatial Hole Burning

5.4.3 Variation of coupling coefficients with wavelength

The effective reflectance and transmittance also vary with wavelength. Figure 5.13 shows the case for a gap width of 3 μm which should yield a peak transmission at 833 nm, for a Fabry-Perot etalon. However, the peak has been shifted down to approximately 790 nm. The variation of R_{eff} and T_{eff} across the range of interest is quite slow, with only a few percent change between 820 and 830 nm. A summary of these results and their implications for the behaviour of an ideal laser source is given at the end of this chapter.

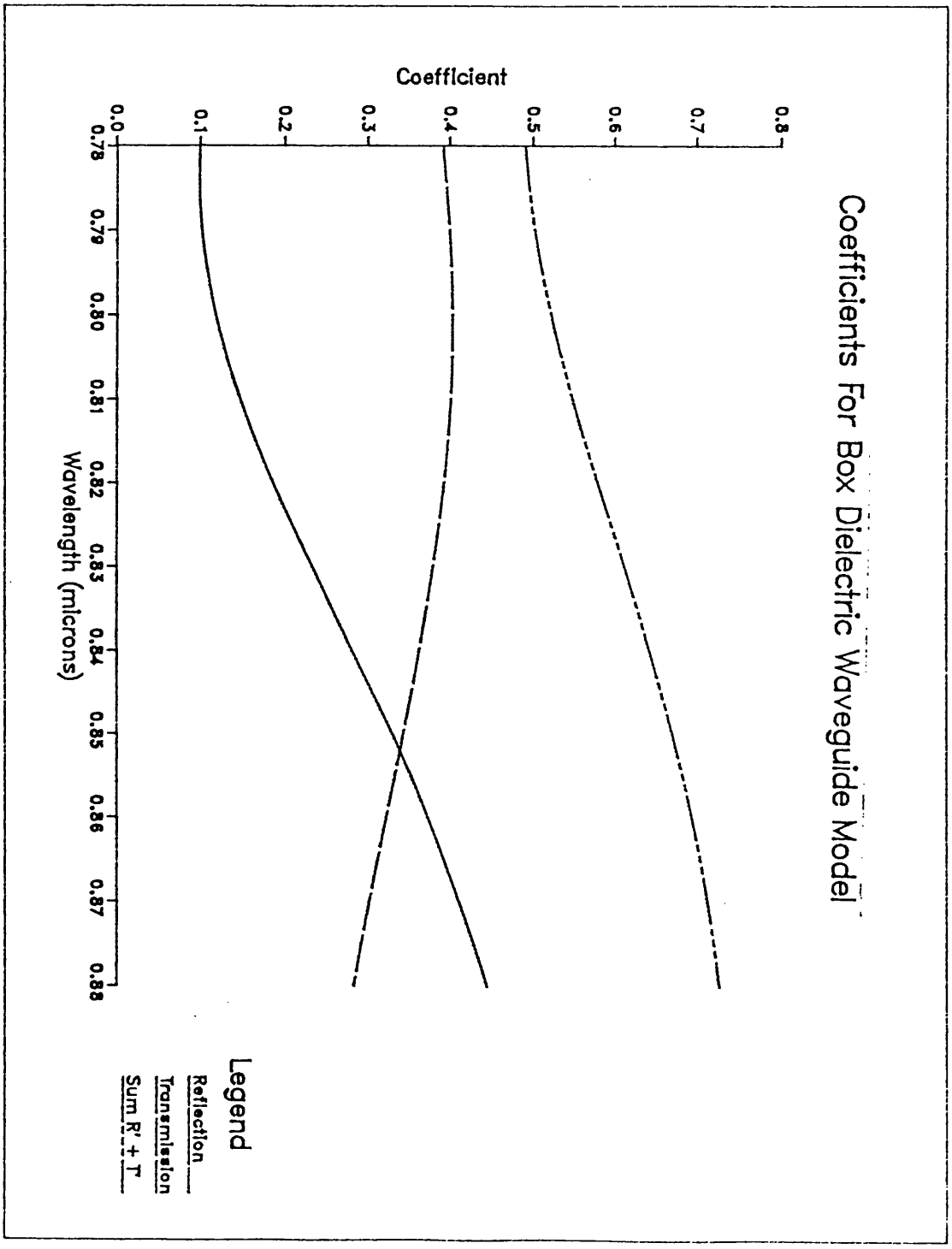

Figure 5.13 : Variation of reflectance and transmittance with wavelength.

5.5 Volume Averaged Rate Equations

Many authors use the spatially independent or volume averaged rate equations whilst neglecting to consider their range of validity. It is essential to this thesis to understand the spatially averaged rate equations and why they can not be used to describe the behaviour of an active waveguide, but are perfectly adequate for a laser diode operating above threshold. The analysis of the volume averaged rate equations begins with the conservation equations for forward and backward flux, and carrier density, determined in chapter 4,

$$\frac{1}{v}\frac{\partial P_i}{\partial t} + \frac{\partial P_i}{\partial z} = G_i \cdot P_i + \delta \cdot S_i \ , \tag{5.23}$$

$$\frac{1}{v}\frac{\partial Q_i}{\partial t} - \frac{\partial Q_i}{\partial z} = G_i \cdot Q_i + \delta \cdot S_i \ , \tag{5.24}$$

$$\frac{dN}{dt} = \frac{J}{e.d} - B_r N \cdot (N + p_o) - \sum_{i=1}^{i=u} g_i \cdot (P_i + Q_i) \ , \tag{5.25}$$

where i is the wavelength slot index. The following analysis is based on that presented by Lau and Yariv [16], which in turn relies heavily on that presented by Moreno [10]. To spatially average the conservation equations for the forward and backward propagating fluxes, equations (5.23–5.25) are integrated over z, for each wavelength slot. For a Fabry-Perot laser with cleaved facets the end facets are assumed to have an identical reflectance, R. This gives rise to the boundary conditions,

$$Q_i(L) = R \cdot P_i(L) \ , \tag{5.26}$$

and

$$P_i(0) = R \cdot Q_i(0) \ . \tag{5.27}$$

If the principle of symmetry is applied, then

$$P(L) = Q(0), \qquad (5.28\ a)$$

and more importantly

$$P(z) = Q(L-z)\ . \qquad (5.28\ b)$$

Finally, the amplitudes of P and Q are assumed to vary slowly in time, hence the temporal fluctuations of the spatially averaged and spatially varying fluxes will be approximately equal. Using these conditions and integrating from 0 – L in z, where L is the device length, the summation of equations (5.23) and (5.24) yields

$$\frac{1}{v}\frac{dX_i^*}{dt} + \frac{2\cdot(1\ -\ R)\cdot X_i(L)}{L\cdot(1\ +\ R)} = (G_i\cdot X_i)^* + 2\cdot\delta\cdot S_i^*\ , \qquad (5.29)$$

where, * denotes the spatial average, $\frac{1}{L}\int_0^L dz$ and $X(L) = (1+R)\,P(L) = P(L) + Q(L)$. The second term on the LHS of equation (5.29) represents the spatial average of the losses at either end of the cavity. The integration of equation (5.25) gives,

$$\frac{dN^*}{dt} = \frac{J}{e.d} - B_r N^*\cdot\left(N^* + p_o\right) - \sum_{i=1}^{i=u}\left(g_i\cdot X_i\right)^*\ . \qquad (5.30)$$

In order to convert (5.29) and (5.30) into the familiar rate equations used by most authors, the $(g_iX_i)^*$ terms must be separated into terms of the form $g_i^*\cdot X_i^*$.

From chapter 4 it is known that a polynomial function can be fitted to the gain curves, for each wavelength slot,

$$g_i = g_{o,i} + g_{1,i}N + g_{2,i}N^2 + g_{3,i}N^3 + \text{etc.} \qquad (5.31)$$

Hence, when the spatially averaged quantities are considered, the product of the spatially averaged gross optical gain, and flux density is,

$$g_i^* X_i^* = \left(g_{o,i} + g_{1,i}N^* + g_{2,i}\left(N^*\right)^2 + g_{3,i}\left(N^*\right)^3 + \text{etc.}\right)X_i^* \quad , (5.32)$$

and the spatial average of the product of the above quantities is

$$\left(g_i\ X_i\right)^* = g_{o,i}\left(N^0 X_i\right)^* + g_{1,i}\left(N^1 X_i\right)^* +$$

$$g_{2,i}\left(N^2 X_i\right)^* + g_{3,i}\left(N^3 X_i\right)^* + \text{etc}. \qquad (5.33)$$

Hence,

$$\left(g_i\ X_i\right)^* = f_i\ g_i^*\ X_i^* \quad , \qquad (5.34)$$

where,

$$f_i = \frac{\left(N \cdot X_i\right)^*}{\left(N \cdot X_i^*\right)} \quad . \qquad (5.35)$$

A similar argument can be applied to determine the spatial average of net effective gain, G_i^*. If a second term is defined,

$$f_o = \frac{X_i(L)}{X_i^* (1 + R)} \tag{5.36}$$

then equations (5.29) and (5.30) can be written as,

$$\frac{1}{v}\frac{dX_i^*}{dt} = f_i G_i^* X_i^* + 2\cdot\delta\cdot S_i^* - \frac{2\cdot f_o(1 - R) X_i^*}{L}, \tag{5.37}$$

$$\frac{dN^*}{dt} = \frac{J}{e.d} - B_r N^*\cdot\left(N^* + p_o\right) - \sum_{i=1}^{i=u} f_i\, g_i^*\, X_i^* . \tag{5.38}$$

Equations (5.37) and (5.38) will give the desired objective of the standard rate equations if $f_i = 1$ and $f_o = \ln[1/R] / 2\cdot(1 - R)$. In qualitative terms it is possible to say that the first condition will be met, **for a lasing mode** in a wavelength slot i, if the spatial average of the product of the flux in the mode and the carrier density is equal to the product of the respective spatial averages, ie, $\left(N\cdot X_i\right)^* = \left(N\cdot X_i^*\right)$. This will be true if the carrier density is uniformly distributed and if the facet reflectivity is high, implying that the flux does not drop significantly at the facets due to mirror losses. The second condition is met if the flux loss rate from a cavity mode can be described by $1 / v\cdot\tau_p$, where τ_p is the conventional photon lifetime.

A quantitative analysis of the validity of the two criteria was performed by Moreno [10] for a single lasing mode, where the optical gain and spontaneous emission terms were assumed to vary linearly with N. The results from [10] can still be applied to the multi-dimensional case despite these restrictions, as the definitions of f_o and f_i are identical. In [10] f_1 and f_o are calculated from a full analysis of the spatially varying rate

equations and compared with the desired values given above (NB, f_1 is used rather than f_i as only one lasing mode is considered).

Two key figures from [10] are reproduced as figures 5.14 and 5.15. In both figures the concept of a total unsaturated gain, G_i^* L is used, that is the net effective gain that would be present in the absence of stimulated recombination, ie the solution of equation (5.38) with the $\sum_{i=1}^{i=u} f_i\, g_i^*\, X_i^*$ term removed. In crude terms the lasing threshold occurs when,

$$G^* L - 2 \cdot f_0 \cdot (1 - R) = 0 . \qquad (5.39)$$

The variation of f_0 and this crude threshold gain is shown in table 5.2.

R	f_0	G^* L (Threshold)
0.2	1.00	1.60
0.1	1.28	2.32
0.01	2.32	4.59
0.001	3.45	6.91
0	∞	∞

Table 5.2 : Variation of f_0 Parameter and Unsaturated Threshold Gain, G^* L.

In figure 5.14 the laser is pumped to give an unsaturated gain of G > 10, ie well above threshold for all the values of R shown. Clearly, the desired values of f_0 and f_1 are obtained for reflectivities above 0.2, as the dotted (desired) and solid (calculated) lines coincide. In figure 5.15 the variation of f_0 with unsaturated gain and spontaneous emission factor, δ is examined. With reference to table 5.2 it can be seen that the desired value of f_0 (dotted) is only obtained when the laser is above threshold and the facet reflectance > 0.2.

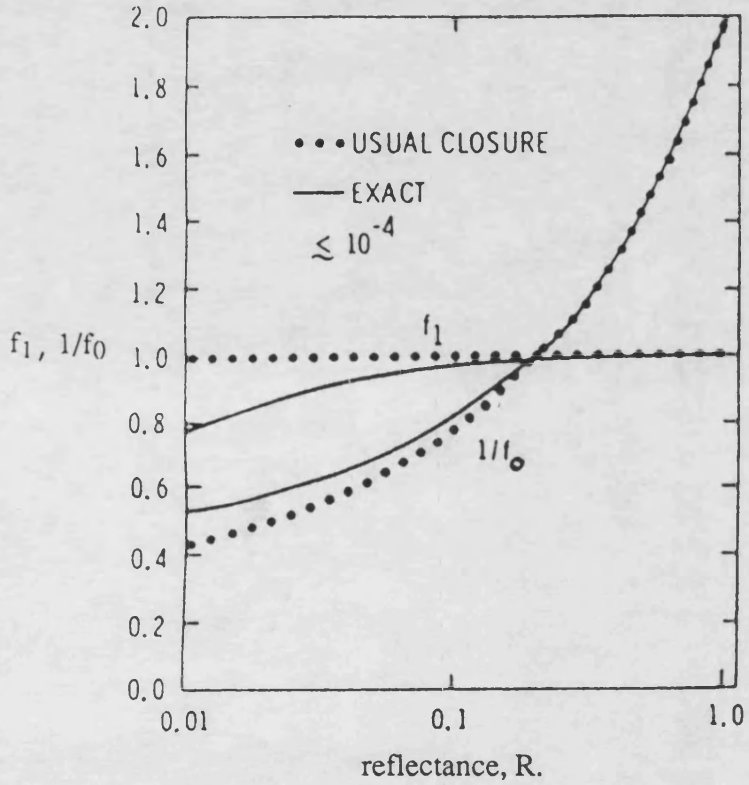

Figure 5.14 : Dependence of f_1 and $1/f_0$ parameters with R, well above threshold (GL > 10).

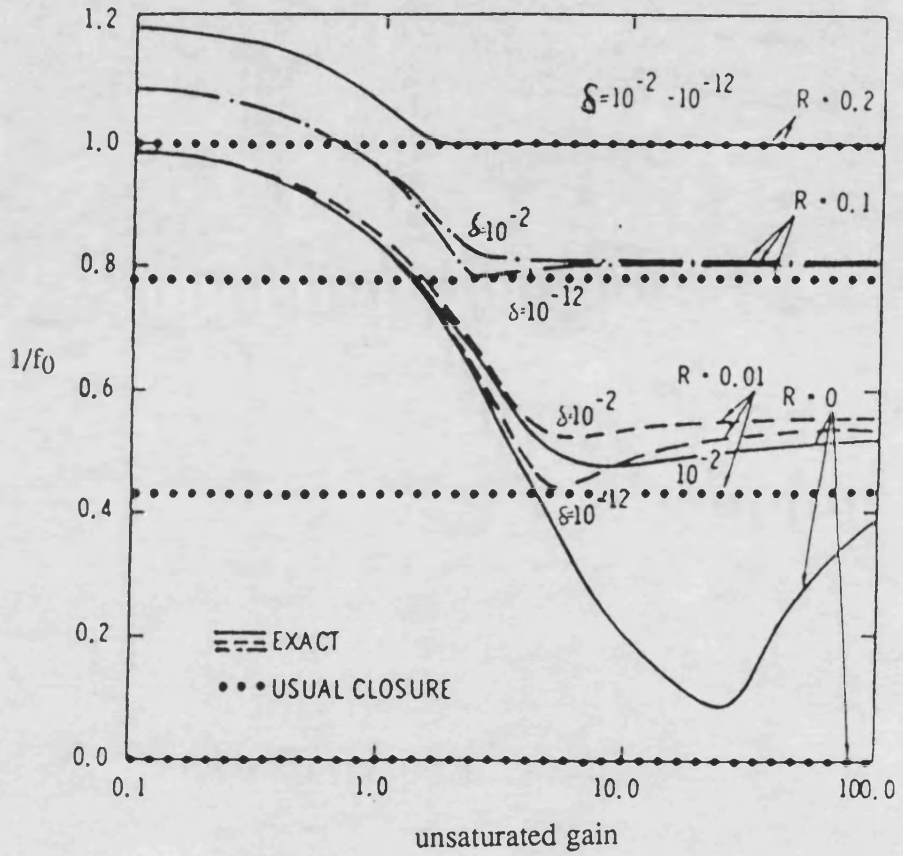

Figure 5.15 : Dependence of $1/f_0$ on unsaturated gain and reflectance, R.

To summarise then, the behaviour of the laser cavity can be described by two spatially averaged quantities, N and X, determined by the rate equations,

$$\frac{1}{v}\frac{dX_i}{dt} = G X_i + 2\cdot\delta\cdot S_i - \frac{X_i}{v\cdot\tau_p} \quad , \tag{5.40}$$

$$\frac{dN}{dt} = \frac{J}{e\cdot d} - B_r\cdot N\cdot(N+p_o) - \sum_i g_i X_i \tag{5.41}$$

if the following criteria are met. The i subscript now refers to the wavelength (slot) of an above threshold lasing mode, the facet reflectances should be greater than 0.2 and the spontaneous emission factor, δ, should be greater than 10^{-5} - 10^{-6}. The flux loss from the cavity is described by the photon lifetime,

$$\frac{1}{\tau_p} = \frac{v}{L}\ln\left[\frac{1}{R}\right] \quad . \tag{5.42}$$

The photon lifetime concept allows us to clarify the earlier statement that the fluxes should vary slowly. The photon lifetime describes the average time that a photon, emitted in the cavity and coupled into a lasing mode, will spend in the cavity. It is unreasonable to examine changes on a time scale smaller than this lifetime. Hence these rate equations will be valid for variations up to approximately 30 GHz for a 250 μm cavity with R = 0.3.

5.6 Steady State Laser De-tuning

5.6.1 Threshold conditions.

Using equations (5.40) and (5.41) it is possible to determine both the threshold current and lasing wavelength, using the spectrally dependent gross optical gain and spontaneous emission terms shown in chapter 4. For lasing to occur the effective gain, G_i must be high enough to overcome the losses in the cavity and the power coupled out of the cavity (In addition, the wavelength must coincide with a cavity resonance, ie. $\lambda_i = 2L/m\pi$, where m is a (large) positive integer).

By inspection, at threshold,

$$\Gamma \cdot g_{k,th} - f_{cc} \cdot \left(2N_{th} + p_o\right) - \frac{1}{2L} \ln\left[\frac{1}{R_1 \cdot R_2}\right] = 0 , \qquad (5.43)$$

where the subscript k denotes the lasing wavelength slot, $g_{k,th}$ is the gain at the lasing wavelength and N_{th} the threshold carrier density. Below threshold the amount of stimulated recombination is limited and can be neglected. Therefore, in the steady state (d/dt = 0), equation (5.41) can be written as,

$$\frac{J_{th}}{e \cdot d} - B_r \cdot N_{th} \cdot \left(N_{th} + p_o\right) = 0 . \qquad (5.44)$$

For a particular L, R_1, and R_2 the threshold carrier density and wavelength are found by solving (5.43), k can then be determined by solving (5.43) for each wavelength slot (i) and taking the slot where the condition is true for the lowest value of N_{th}. The threshold current density, J_{th} and current , $I_{th} = J_{th} \cdot wL$ is given by (5.44).

Above threshold, a single mode (k) is assumed to dominate both rate equations, hence in the steady state,

$$0 = \left(G_k - \frac{1}{v \cdot \tau_p} \right) X_k \ , \tag{5.45}$$

and

$$0 = \frac{J}{e \cdot d} - B_r \cdot N \cdot \left(N + p_o \right) - g_k \cdot X_k \ . \tag{5.46}$$

As the photon lifetime is independent of the pumping current, equation (5.45) can only be true if $G_k = 1 / (v \cdot \tau_p) = G_{k,th}$. The implication of this condition is, as the above threshold net effective gain is pinned to a single value, $G_{k,th}$, then the carrier density in the laser must also be pinned to the threshold value, N_{th}. Hence (5.46) can be rearranged to give,

$$X_k = \frac{1}{g_{k,th} \cdot ed} (J - J_{th}) \ , \tag{5.47}$$

where $J_{th} = B_r \cdot N_{th} \cdot (N_{th} + p_o)$, from equation (5.44). The variation of the single facet output power of a 250 μm symmetrical laser with 30% facets and all other dimensions given in table 5.1 is shown in figure 5.16. The solid characteristic shows the approximate solution calculated using equation (5.47), whilst the dashed characteristic was calculated using the full numerical solution of the travelling flux equations presented in chapter 6. It is clear that there is a small but acceptable discrepancy between the models, which is mainly due to the assumption that only one above threshold mode is present in (5.47).

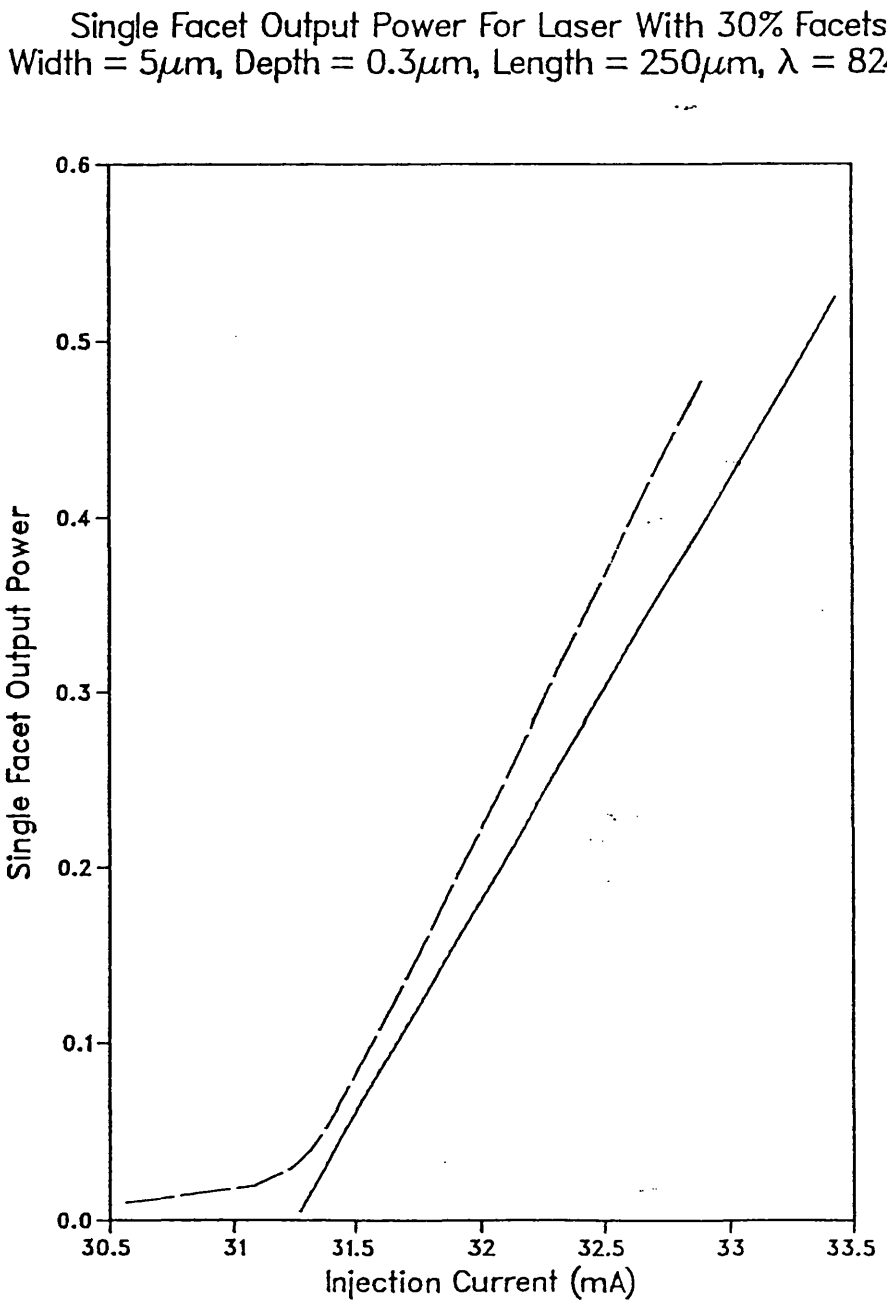

Figure 5.16 : Single facet output power for a laser with 30% facets.

5.6.2 Threshold current (density)

Using the effective mirror formalism described in section 5.3, it is possible to determine the detuning effects of the gap by replacing R_2 in equation (5.43) with the effective reflectance, R_{eff}. Figures 5.17 and 5.18 show the variation of the threshold current and current density for laser lengths of 250 and 400 μm.

As the effective reflection coefficient increases, the photon lifetime will also increase, as the the flux coupled out of the device at the effective mirror is reduced. Hence the threshold current comes down. The threshold current density is lower for all R_{eff} at 400 μm, as the photon lifetime is inversely proportional to the laser length, L. From figure 5.17 it is seen that the threshold current is higher for all R_{eff} for the 400 μm device. This increase in I_{th} is merely a function of the increase in active region plan area. The current density shown in figure 5.18 gives, therefore, a better indication of the underlying behaviour of the laser.

5.6.3 Lasing wavelength

Figure 5.19 shows the consequent shift to higher lasing wavelengths as the threshold current density, J_{th} and hence the carrier density, N_{th} decrease. From chapter 3 it is known that the peak in the gross optical gain curves shifts towards higher wavelength as the carrier density decreases. Figure 5.19 highlights both the advantages and the disadvantages of dividing the spectral variations of g and S into a number of wavelength slots. The output wavelength is seen to hop to the next wavelength slot as R_{eff} increases. It is known that the lasing modes will only occur at a cavity resonance and that the spacing between these resonances is given by [13],

$$\delta\lambda = \frac{\lambda^2}{2n_g \cdot L}, \qquad (5.48)$$

where n_g is the group index ≈ 4.3. At 820 nm, $\delta\lambda$ = 0.31 nm for L = 250 μm, whilst for L = 400 μm $\delta\lambda$ falls to 0.23 nm. When 151 wavelength slots are used, the

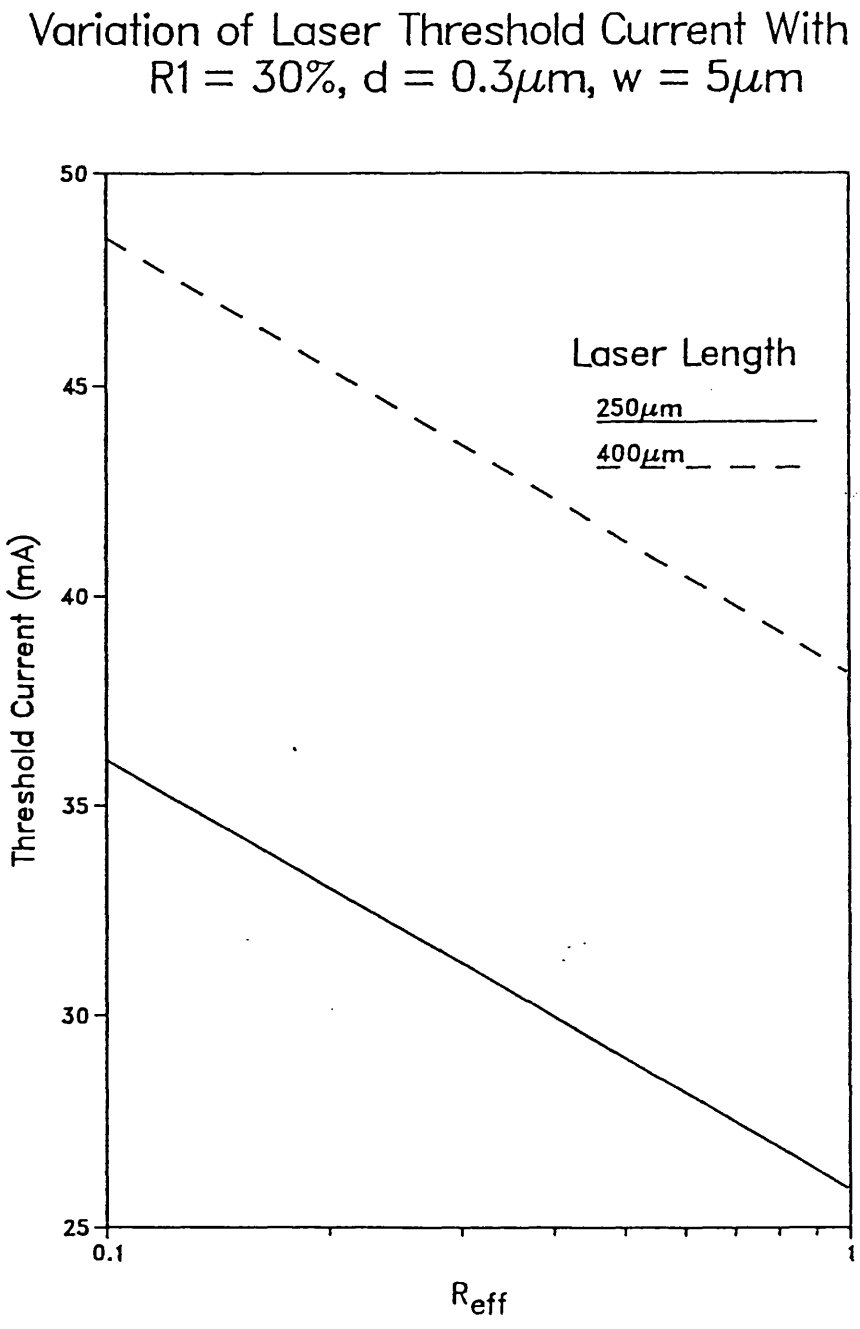

Figure 5.17 : Variation of laser threshold current with effective facet reflectance (R_{eff}).

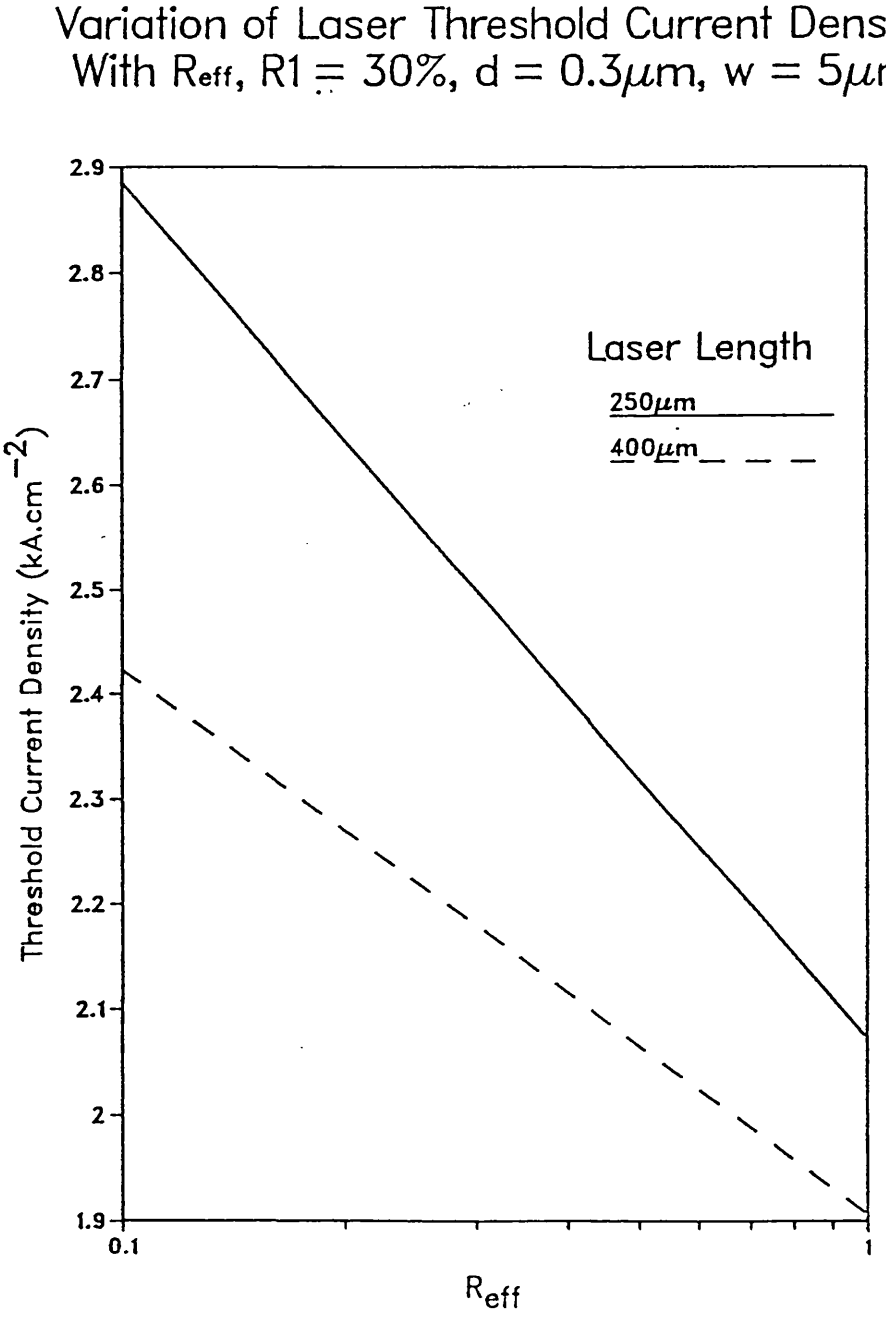

Figure 5.18 : Variation of laser threshold current density with effective facet reflectance (R_{eff}).

wavelength spacing between the slots is 0.4 nm. Thus, it can been seen that the width of the slots used in the model are of the correct order of magnitude, but it is only feasible to match the slot widths to one laser length to accurately predict the lasing modes and that the the slot widths will be dependent on wavelength and group index.

5.6.4 Power coupled into the coupling gap

The variation of power coupled into the gap, P_{out} as a ratio of the total output power of the laser, P_{tot} and the power coupled out of the back facet of the laser P_{back} is shown in figure 5.20. When the $R_{eff} = R_1$ equal power is coupled out of both facets. The ratio of P_{out} to P_{tot} can be written as,

$$\frac{P_{out}}{P_{tot}} = \frac{1}{\left(1 + \frac{(1 - R_2)}{(1 - R_{eff})}\left(\frac{R_{eff}}{R_{eff}}\right)^{1/2}\right)} \quad , \tag{5.49}$$

and

$$P_{back} = P_{tot} - P_{out} \quad . \tag{5.50}$$

As would be expected, the power coupled out of the laser toward the waveguide increases as R_{eff} decreases.

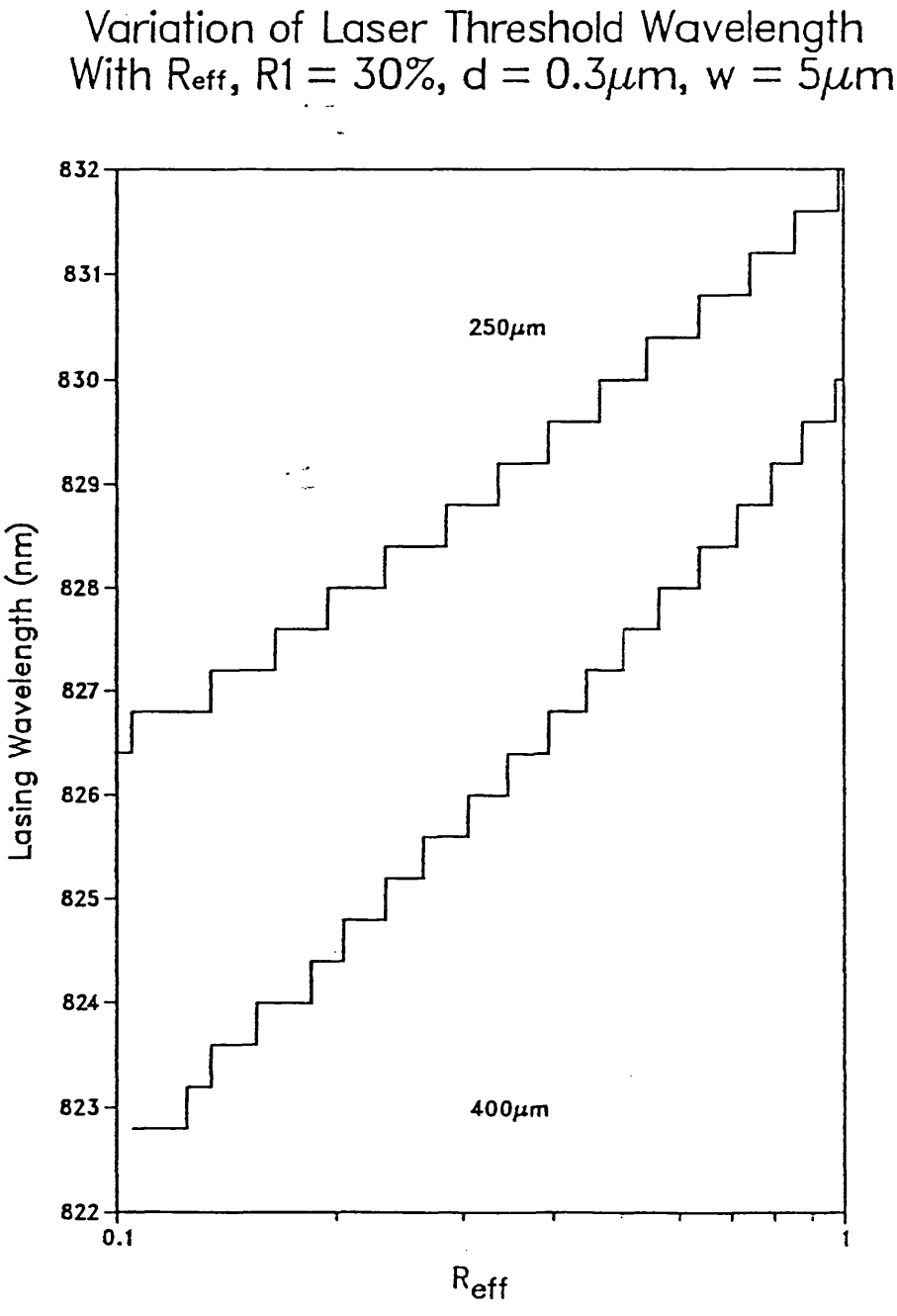

Figure 5.19 : Variation of laser threshold wavelength with effective facet reflectance (R_{eff}).

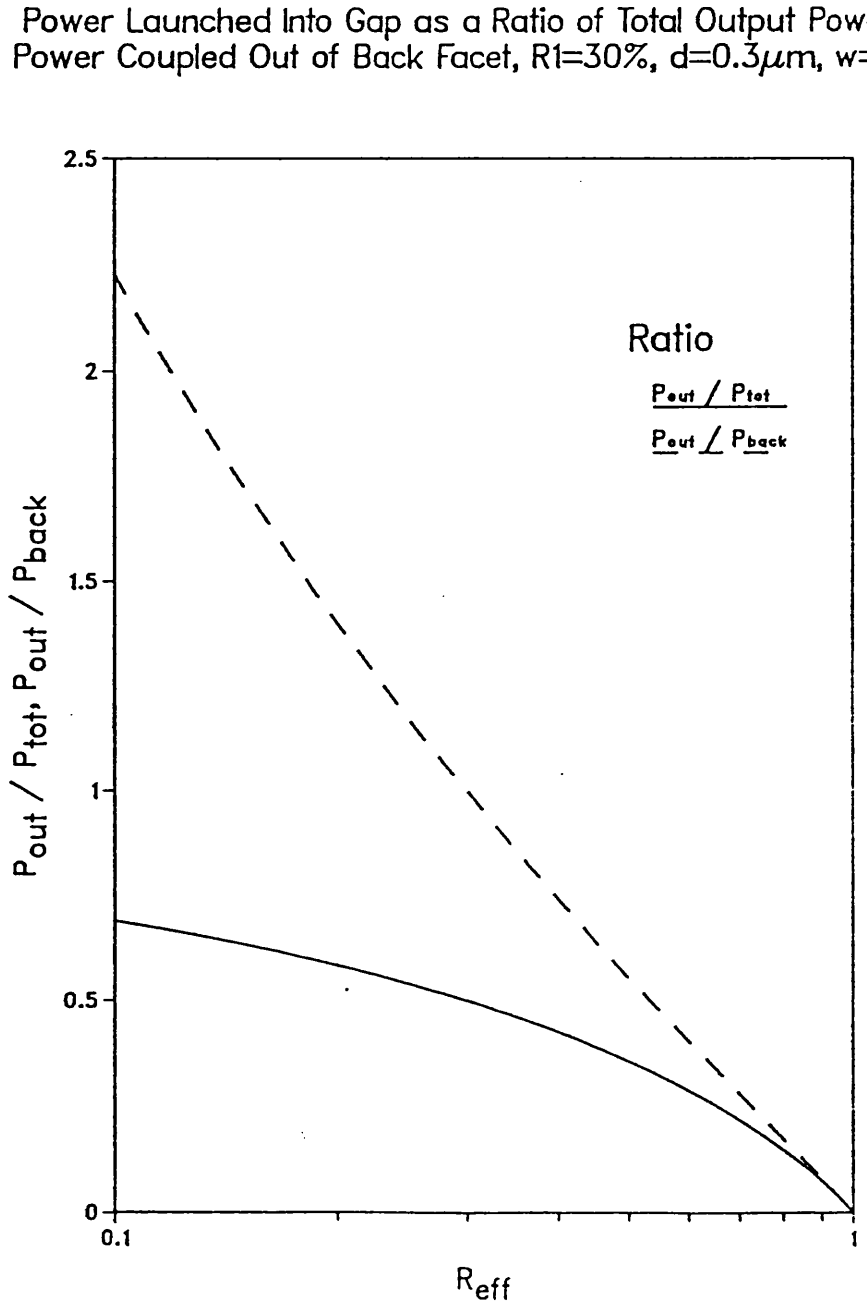

Figure 5.20 : Power coupled into the etched gap as a ratio of total output power, or power coupled out of the back facet.

5.7 Summary and Conclusions

The design of an efficient gap coupling geometry would have to be a compromise between several considerations, not least of which is controlling the gap dimensions. The results in section 5.4 demand that the gap width should be (approximately) an integral number of half wavelengths, for maximum coupling into the guide. This width should be controlled to a tolerance of better than approximately 0.05 λ. Such sub-micron fabrication techniques are totally beyond current fabrication technology.

Further, the results in section 5.6 show that it is impossible to maximise the transmission coefficient in this simple geometrical fashion. These results were calculated assuming that R_{eff} is independent of wavelength. Figure 5.13 shows that this is not the case and the possible laser modes will 'see' a different R_{eff} which will affect the threshold conditions, (5.43) - (5.47). As was explained in the previous section, the longitudinal modes of the laser are quite closely spaced and adjacent modes have nearly identical values of g_i. The lasing modes will, therefore, be pulled to either higher or lower wavelengths, depending on the spectral distribution of R_{eff}.

This effect of pulling towards lasing wavelengths with a higher R_{eff} will be most significant for the lowest values of R_{eff}, as the rate of change of photon lifetime with R_{eff} is given by,

$$\frac{d\tau_p}{dR_{eff}} = \frac{1}{L \cdot R_{eff}} \quad . \qquad (5.51)$$

As the T_{eff} maxima almost coincide with the R_{eff} minima, if the gap is constructed to give the maximum transmission of power into the guide, the laser detuning effect will be at its most significant. Clearly, the laser detuning will reduce the power coupled into the guide. A crude estimation of this detuning was achieved by approximating the spectral variation of R_{eff} to a straight line over the region of interest, 810 – 840 nm.

R_{eff} was allowed to vary between 0.1 and 0.5. The results of this estimation are summarised in table 5.3, which clearly shows the pulling of the laser wavelength depending on the slope of R_{eff}.

Reflectance @ Wavelength		Lasing Wavelength	Threshold Current	Effective Reflectance	Power Into Gap
810 nm	840 nm	λ_{th} (nm)	I_{th} (mA)	@ λ_{th}	(% P_{tot})
0.3	0.3	825.6	31.25	0.3	50.0
0.1	0.5	828	30.8	0.341	46.8
0.5	0.1	824	31.5	0.312	49.1

Table 5.3 : Variation of Threshold Parameters with Spectrally Dependent R_{eff}.

If stable and controllable laser action is to be achieved, an alternative to a simple etched gap laser must be used as the integrated guide source, such as Distributed Feedback (DFB) and Distributed Bragg Reflector (DBR) lasers, which have more reliable mechanisms for controlling the lasing wavelength. Another advantage of using either a DFB or DBR laser is that the active layer of the waveguide can be made to be an extension of that of the laser.

References, Chapter 5

1. MUELLER, C.T., SULLIVAN, C.T., CHANG, W.S.C., HALL, D.G., ZINO, J.D., and RICE, R.R., 'An Analysis of the Coupling of an Injection Laser Diode to a Planar $LiNbO_3$ Waveguide',
IEEE J. Quantum Electron., 1980, QE-16,(3), pp363-372.

2. HAMMER, J.M., and NIEL, C.C., 'Observations and Theory of High Power Butt Coupling to $LiNbO_3$ -Type Waveguides',
IEEE Trans Microwave Tech., 1982, MTT-30, (10), pp1739-1746.

3. HUNSPERGER, R.G., YARIV, A. and LEE, A., 'Parallel End - Butt Coupling for Optical Integrated Circuits',
Appl. Opt., 1977, 16, (4), 1977, pp1026-1032.

4. COHEN, L.G., 'Power Coupling form GaAs Injection Lasers into Optical Fibers',
Bell Syst. Tech. J., 1972, 51, 3, pp573-594.

5. KANADA, T. and NAWATA, K., 'Injection Laser Characteristics due to Reflected Optical Power',
IEEE J. Quantum Electron, 1979, QE-15, (7), pp559-565.

6. HAMMER, J.M., 'Closed Form Theory of Multi-Cavity Reflectors and the Output Power of External Cavity Diode Lasers',
IEEE J. Quantum Electron, 1984, QE-20, (11), pp1253-1259.

7. OTSUKA, K., 'Analysis of the Effects of External Injection and Diffusion of Excited States on Relaxation Oscillations in Lasers',
IEEE J. Quantum Electron, 1977, QE-13, (7), pp520-525.

8. STREIFER, W., YEVICK, D., PAULI, T.L. and BURNHAM, R.D., 'An Analysis of Cleaved Coupled- Cavity Lasers',
IEEE J. Quantum Electron, 1984, QE-20, (7), pp754-764.

9. KOCH, T.L. and COLDREN, L.A., 'Optimum Coupling Junction and Cavity Lengths for Coupled Cavity Semiconductor Lasers',
J. Appl. Phys., 1985, 57, (3), pp740-754.

10. MORENO, J.B., 'Volume-Averaged Rate Equations for Planar and Disk-Cavity Lasers',

J. Appl. Phys., 1977, 48, (10), pp4152-4162.

11. BUUS, J., 'Principles of Semiconductor Laser Modelling',

IEE Proc. Part J, 1985, 132,(1), pp42-51.

12. CASEY, H.C. Jr and PANISH, M.B., 'Heterostructure Lasers, Part A : Fundamental Principles',

Academic Press, New York, 1978.

13. THOMPSON, G.H.B, 'Physics of Semiconductor Devices',

Wiley, Chichester, 1980.

14. YARIV, A., 'Introduction to Optical Electronics' 3rd Edition,

Holt, Rinehart and Winston, 1985.

15. ROZZI, T.E. and in't VELD, G.H., 'Variational Treatment of the Diffraction at the Facet of d.h. Lasers and of Dielectric Millimetre Wave Antennas'

IEEE Trans Microwave Tech., 1980, MTT-28, (2), pp61-73.

16. LAU, K.Y and YARIV, A., 'High Frequency Current Modulation of Semiconductor Injection Lasers', in

'Semiconductors and Semimetals, Volume 22 - Lightwave Communications Technology, Part B: Semiconductor Injection Lasers, I' ed, Tsang, W.T.,

Academic Press, New York, 1985.

6 STEADY STATE CHARACTERISTICS

6.1 Introduction

When modelling the performance of an AIOW it is possible to draw on the theory developed for other semiconductor devices : notably laser amplifiers and SLED's (super luminescent diodes). In chapter 5 it was shown that a spatially averaged model can not be applied to devices which have low end facet reflectances and low gains. These are precisely the operating conditions that prevail in an AIOW which is pumped to transparency. Therefore, it is necessary to use a model which can take account of the longitudinal variations is flux and carrier density.

Several longitudinal models have been devised for a variety of devices, such as lasers [1 – 4], SLED's [5] and laser amplifiers [6]. With lasers it is possible to ignore the variation of the gain and spontaneous terms with wavelength because above threshold the output is confined to a few modes with similar optical wavelength (see chapter 5). The models presented by Hasou and Ohmi [1] and Marcuse and Nash [3] are one dimensional solutions, considering only longitudinal variations. Shore [2] and Agrawal [4] extend the analysis to two dimensions by examining lateral variations as well.

The models presented by Perkins and Ormondroyd [5] and Marcuse [6] are of particular interest. Both models allow the injection of an optical input signal into the active region and can take account of longitudinal and spectral variations. In addition Perkins [5] allows inhomogeneous pumping, ie. different pumping currents can be applied along the device. Marcuse's [6] model has been developed primarily for quaternary devices and employs empirical Lorentzian functions to describe the variation of stimulated gain and spontaneous emission.

Other models have been developed for laser amplifiers, where optical injection is applied to a pumped device with overall gain [7 – 10]. However these models, in the main, assume that the quantities, including the optical injection can be spatial averaged

along the amplifier. Whilst this assumption has some validity for the cases examined in these references it cannot be universally applied. Indeed, Mukai [10] admits that for low gains, low reflectance and long devices, the assumption becomes invalid.

The model presented by Perkins et al [5] has been adapted because it allows an accurate analysis of the proposed system. The effects of optical injection, longitudinal variation, spectral dependence and spontaneous noise are easily included and controlled.

Some words of caution must be expressed at this point about the results given in this chapter, and indeed of any numerical analysis. Although great care has been taken when determining parameter values, as Marcuse and Nash [3] point out, there is still much heated debate in the literature regarding such values. The aim of this thesis is not to provide precise values for (say) the current required to achieve transparency, but to show *trends* and give some *design rules*. Where appropriate real units have been used for the input and output quantities (mA for current, mW for power, dBm for noise power, etc), all such values are subject to the accuracy of the parameters and the assumptions made in the model. Throughout the thesis, relative values are preferred to absolute measurements in order to give a better feel for the underlying trends.

6.2 Theoretical Considerations

6.2.1 Time Independent Rate Equations

As was detailed in chapter 5, the spatially averaged rate equations have a limited range of validity and cannot be successfully applied to the situation of an AIOW pumped to transparency. Therefore, the longitudinal rate equations presented in chapter 4 must be used.

To recap, for a waveguide where the gross optical gain and spontaneous emission terms have been discretised into a number of wavelength 'slots', then the variation of the the forward and backward travelling flux for the i^{th} slot is given by the photon conservation equations,

$$\frac{1}{v}\cdot\frac{\partial P_i}{\partial t} + \frac{\partial P_i}{\partial z} = G_i P_i + \delta S_i \ , \qquad (6.1)$$

$$\frac{1}{v}\cdot\frac{\partial Q_i}{\partial t} - \frac{\partial Q_i}{\partial z} = G_i Q_i + \delta S_i \ . \qquad (6.2)$$

Where, P_i and Q_i are the longitudinally varying forward and backward travelling fluxes in the longitudinal dimension z, and time t.

$G_i = \Gamma \cdot g_i - f_{cc}\cdot (2N + p_o)$, is the net effective gain for the i^{th} wavelength slot and taking into account the optical confinement in the transverse and lateral dimensions.

The gross optical gain g_i and the emission term S_i, for the i^{th} wavelength slot are polynomial functions of the carrier density.

The carrier density, N along the guide is determined by the carrier continuity equation,

$$\frac{dN}{dt} = \frac{J}{e.d} - B_r N\cdot (N + p_o) - \sum_{i=1}^{i=u} g_i\cdot (P_i + Q_i) \ , \qquad (6.3)$$

Where, l and u are the subscripts of the lower and upper wavelength slots; J is the injected carrier density; $B_r N\cdot (N + p_o)$ is the total spontaneous emission rate and $\sum_{i=l}^{i=u} g_i\cdot (P_i + Q_i)$ the total stimulated emission rate.

For the modelling of steady state characteristics, all the time effects may be ignored and the derivatives with respect to time become equal to zero. Equations (6.1) to (6.3) now reduce to,

$$\frac{\partial P_i}{\partial z} = G_i P_i + \delta S_i \ , \qquad (6.4)$$

$$-\frac{\partial Q_i}{\partial z} = G_i Q_i + \delta S_i \ , \qquad (6.5)$$

$$0 = \frac{J}{e.d} - B_r N\cdot (N + p_o) - \sum_{i=l}^{i=u} g_i\cdot (P_i + Q_i) \ , \qquad (6.6)$$

The family of equations (6.4 - 6.6) still present a non-trivial modelling problem, as N and hence g, G and S vary with z. In addition the carrier density is highly coupled to the variation in flux. The model complexity is considerably reduced if the guide is discretized, along its length into a number of regions where the carrier density can be assumed constant [4-6]

6.2.2 Continuity Equations in Regions of Constant Carrier Density

The topology used is shown in figure 6.1. The guide is divided into regions of length l_m, where m is the region index. Each region has an injected current density of J_m which may be set independently, but in all the cases examined here the injected current density is assumed to be the same for each region of the guide. Thus it would be relatively simple to amend this model to take account of current distribution effects for instance.

Figure 6.1, Guide Divided Into Regions of Constant Carrier Density

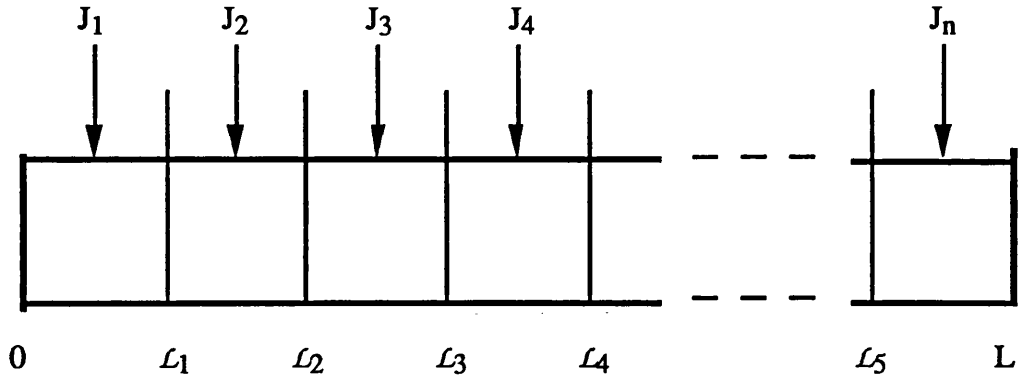

In chapter 4 the effect of diffusion on the carrier density distribution was discussed. This has the effect of smoothing out any spatial variations in N which may occur at the sub-micron level, due to the peaks and troughs in the optical field [4]. For dimensions greater than the diffusion length, ($\approx 1 - 3$ μm) the effects can largely be ignored if the flux density does not vary significantly over a region, or the if the total stimulated emission rate is negligible compared to the other factors in the carrier continuity equation. If a region is perfectly transparent then the flux will not vary across it, however it is only possible to achieve transparency for a single wavelength slot, as the gross optical gain is different for each slot.

Therefore, in order to be able to assume that the carrier density does not vary within a region, one or more of the following has to be satisfied :

- The length of the region is 'short'.
- Stimulated emission in the guide is negligible compared to the other parameters in the carrier continuity equation.
- The variation in stimulated emission across the region is negligible.

The choice of an appropriate region length is largely a matter of trial and error, depending on the conditions in the guide. For very low input powers (<0.1 mW) when the guide is pumped to transparency a region length of 100 μm can be used with

very little error. For high input powers or high gains the region length has to be decreased to a minimum of approximately 10 μm.

In a region of constant carrier density the material parameters, g_i, G_i and S_i will also be constant. Equations (6.4) and (6.5) can now be solved analytically by integrating over the region. For the first region of the guide, a solution to equation (6.4) for the forward travelling flux at any point in the region is,

$$P_i(z) = P_i(0)\exp[G_i z] + \frac{\delta S_i}{G_i}.(\exp[G_i z] - 1) \qquad (6.7)$$

$$0 \le z \le l_1$$

A similar solution can be found for the backward travelling flux. The carrier density in the region is given by (6.6) modified to take account of the averaging over the region,

$$0 = \frac{J}{e.d} - B_r N_1.(N_1 + p_o) - \sum_{i=1}^{i=u} g_{1,i}.(\bar{P}_{1,i} + \bar{Q}_{1,i}) \qquad (6.8)$$

There is only one real solution to (6.8). $\bar{P}$ and $\bar{Q}$ indicate that the quantities are spatially averaged over the region, eg.

$$\bar{P}_{1,i} = \frac{1}{l_i}\int_0^{l_i} P_i.\,dz \quad . \qquad (6.9)$$

Using equation (6.7), the average forward flux in the region becomes,

$$\bar{P}_{1,i} = \frac{1}{G_{1,i}} \cdot \left(\frac{P_i(l_1) - P_i(0)}{l_1} - \delta S_{1,i} \right) \qquad (6.10)$$

From 6.10, it is clear that it is only necessary to calculate the flux at the region boundaries, rather than continuously through the guide. The ability to calculate the flux

at region boundaries from simple analytic expressions of the from shown in equation (6.7) reduces the computation required for a solution compared with finite difference and finite element techniques [5,6].

For the m^{th} region of the guide a consistent solution must be found for the forward and backward fluxes and the carrier density. It is relatively easy to show that for the m^{th} region of the guide the flux at the $m+1^{th}$ boundary is given by,

$$P_{m+1,i} = P_{m,i} \exp\left[G_{m,i}\, l_m\right] + \frac{\delta S_{m,i}}{G_{m,i}} \cdot \left(\exp\left[G_{m,i}\, l_m\right] - 1\right) . \qquad (6.11)$$

A similar solution can be found for Q. The spatially averaged flux in the m^{th} region is given by,

$$\bar{P}_{m,i} = \frac{1}{G_{m,i}} \cdot \left(\frac{P_{m+1,i} - P_{m,i}}{l_m} - \delta S_{m,i} \right) . \qquad (6.12)$$

Note, for instantaneous fluxes P and Q the m subscript refers to the *boundary* number, whilst for region length and spatially averaged flux the subscript refers to the *region* number.

6.3 Modelling Considerations.

6.3.1 Boundary Conditions.

For a pumped guide there are two inputs which may be controlled, the pumping current I and the optical flux, P_{in} injected at the input port or front facet (z=0). The current density injected into the active region, J is assumed to be,

$$J = \frac{I}{w.L} \quad . \tag{6.13}$$

It is assumed that the current is provided by a constant current source.

The effect of the injected optical flux is incorporated into the input port boundary conditions. The flux in the guide is assumed to be reflected at the input and output ports with reflectances of R1 and z=0 and R2 at z=L. Hence,

$$P_{1,i} = R_1 \cdot Q_{1,i} + P_{in,i}, \tag{6.14}$$

$$Q_{n+1,i} = R_2 \cdot P_{n+1,i}, \tag{6.15}$$

where, $P_{in,i}$ is the optical flux injected into the i^{th} wavelength slot at z=0, taking into account the coupling efficiency discussed in chapter 5. The relationship between the flux and the optical output power, in Watts at a particular wavelength is given by,

$$W_i = \frac{h.c}{\lambda_i} \cdot A \cdot P_i, \tag{6.16}$$

where, λ_i is the free space wavelength and A the cross sectional area $\approx w \cdot d$

There are two other boundary conditions that must be applied. Firstly the instantaneous fluxes P and Q must be continuous across the region boundaries. Finally,

the sum of the spontaneous emission terms must be consistent with the overall spontaneous emission rate determined in chapter 3, ie.

$$\sum_{i=1}^{i=u} S_{m,i} = B_r N_m \cdot (N_m + p_o) \quad . \qquad (6.17)$$

6.3.2 Transparency Condition and Bulk Parameters

In the introduction it was stated that the guide will be biased to transparency and the operating characteristics measured around that point. It is important to define what is meant by transparency for the guide. As the gain is allowed to vary longitudinally, a microscopic definition of transparency, such as $G_{m,i} = 0$ is not very useful. For the case when the input flux is confined to a single wavelength slot λ_k, transparency is defined to occur when the single pass gain is equal to 1.

For each region of the guide there is a coherent gain which determines the variation of signal flux across the region. Equation (6.11) can be split into two parts,

$$P_{m+1,i} = P_{m,i} \exp [G_{m,i} . l_m] \qquad \text{– coherent amplification,}$$

$$+ \frac{\delta S_{m,i}}{G_{m,i}} . (\exp [G_{m,i} . l_m] - 1) \qquad \text{– incoherent noise.}$$

The coherent gain for the m^{th} region and the i^{th} slot can be written as,

$$M_{m,i} = \exp \left[G_{m,i} \, l_m \right] , \qquad (6.18)$$

this gain applies equally to the forward and backward travelling fluxes. The overall coherent single pass gain (ie for a signal travelling from one end of the guide to the other) is the product of the individual coherent gains of each region,

$$\bar{M}_{m,i} = \prod_{m=1}^{n} M_{m,i} \,. \tag{6.19}$$

As the flux and carrier density are allowed to vary along the guide, $M_{m,i}$ will not necessarily be equal to one for each region.

When modelling multi-mode or broadband inputs such as LED's, SLED's and multi-mode lasers the definition of transparency may be slightly modified. However, due to the change in gain with wavelength, it is not possible to achieve transparency across the spectrum of a broadband input.

In addition to the coherent single pass gain it is useful to define a forward pass gain, which gives the relationship between the injected input optical signal, $P_{in,i}$ and the output optical signal, $P_{out,i}$. Taking into account multiple reflections at the guide facets, the forward pass gain is,

$$F_i = \frac{P_{in,i}}{P_{out,i}} = (1 - R_2).\left(\frac{\bar{M}_i}{1 - R_1 R_2 \bar{M}_i^2}\right) \,. \tag{6.20}$$

Using $\bar{M}_i$ and F_i it is possible to define consistently the transparency condition for single mode input at different wavelengths, and to separate the output signal from the amplified spontaneous emission noise.

As the round trip gain $R_1R_2\bar{M}_i^2 \rightarrow 1$, recognised as the familiar laser threshold condition, the coupling between the forward and backward fluxes becomes high, and (6.20) is no longer valid. In addition many of the assumptions made in section 6.2 are also invalidated. In such cases, a fabry-perot analysis has to be used. However, Simon

[9] suggests that for round trip gains < 0.25 these F-P effects will be small and for values < 0.0025, they can be ignored. If R_1 and R_2 are assumed to be 10^{-4} then single pass gains of upto 30 dB can be tolerated without having to resort to an F-P analysis. Similarly, if the gain is 0 dB, reflectances as high as 0.5 can be tolerated.

6.3.3 Static Model Algorithm

Due to the high degree of coupling between the carrier density and the photon fluxes, it is not possible to find an exact solution for these quantities using a one step technique. The equations describe a 'stiff' system, which may be solved using an iterative technique such as Euler's step halving method, or a customised stepping method. For ease of use and clarity, a customised method was adopted.When iterating the coherent single pass gain discussed in the previous section is made the independent variable, and the injected current the dependent variable.

The initial conditions in the guide are calculated by assuming transparency at the desired input wavelength, buthigh loss for all other slots. For each region, the forward flux is set to $P_{in,k}$ where k is the input wavelength slot, for the k^{th} slot, and zero in all other slots. The backward flux is set to $R_2 \cdot P_i$. An estimate value for N can be calculated using equation (6.18) by assuming that the coherent gain is equal to 1 for the k^{th} slot in each region. Hence an initial value of the drive current (density) can be determined from equation (6.8).

The model then iterates, employing two passes for each iteration. In the forward pass, a consistent solution is found for the forward flux P_i in each slot and the carrier density, with fixed values for $\bar{Q}_i$. For the backward pass the situation is reversed and Q_i is solved with $\bar{P}_i$ fixed. The consistent solution is determined using an efficient quadratic interpolation routine (Müller) for each region [5]. At the end of each iteration the boundary conditions given in equations (6.14) and (6.15) are applied and the injected current (6.13) is trimmed depending on the deviation of the coherent gain from the desired value. Iterations continue until the calculated value of $\bar{M}_k$ is within a certain tolerance of the desired value, usually less than 10^{-4}.

6.4 Results and Discussion

Unless otherwise stated the following values are used throughout this section.

Optical confinement factor, Γ	= 0.75
Spontaneous emission factor, δ	= 10^{-4}
Guide width, w	= 5.0 μm
Active layer thickness, d	= 0.3 μm
Guide Length, L	= 1 mm
Free carrier absorption coefficient, f_{cc}	= 10^{-21} m^2
Bimolecular recombination coefficient, B_r	= 10^{-16} m^3s^1
Active layer doping density, p_o	= 4.0×10^{23} m^{-3}
Facet reflectances, R_1, R_2	= 10^{-4}

Table 6.1, Parameter values used in the steady state model

6.4.1 Transparency Conditions

A primary consideration in the feasibility of an active waveguide is the current density required to pump the guide to transparency, particularly in relation to the threshold current of a laser of typical geometry. The current required for transparency sets the electrical power requirements of the AIO chip and more importantly, it's thermal dissipation. Figures 6.2 and 6.3 show how the current density required to pump a 1mm guide to transparency depends upon the optical input power level and the wavelength of the source. The left hand scale of each graph is in kA/cm^2 whilst the right hand scale is normalized to the threshold current density of a 250 μm laser with 30% facets fabricated from the same material as the guide (see chapter 5). Figure 6.2 shows the variation of transparency current as a function of optical input bias power for three input wavelengths, whilst figure 6.3 shows the variations as a function of wavelength at four optical input bias powers.

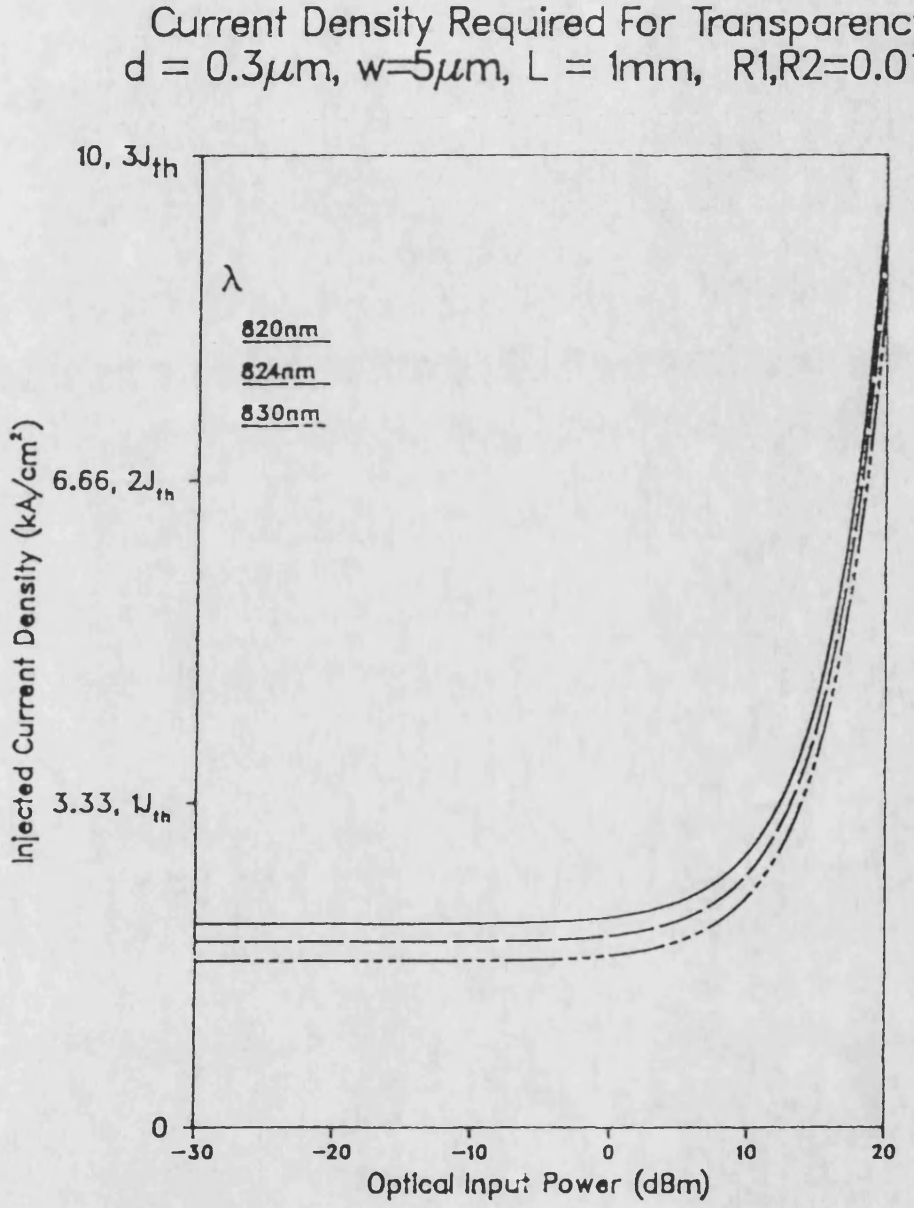

Figure 6.2 : Effect of optical input power and wavelength on current density required for transparency.

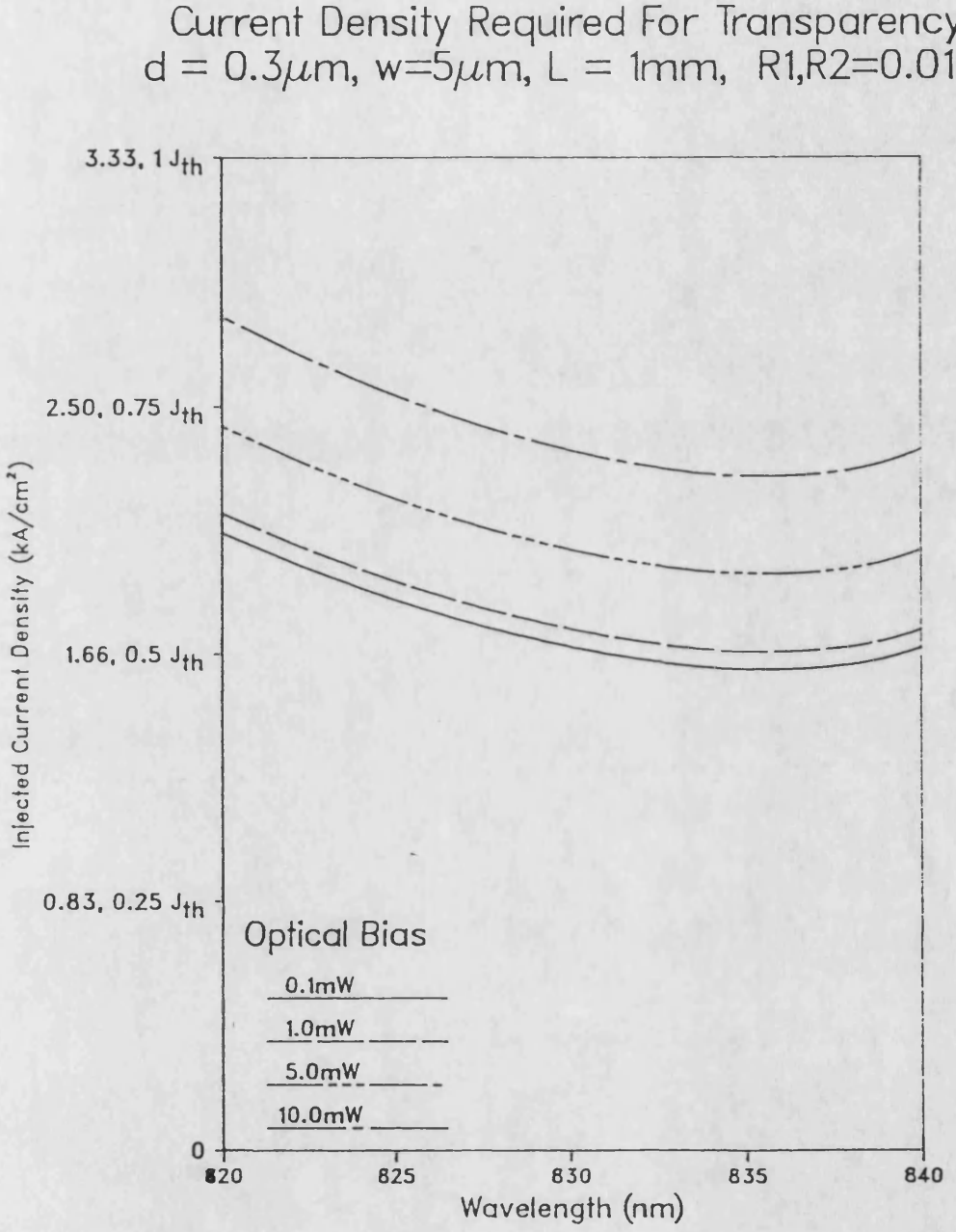

Figure 6.3 : Effect of wavelength and optical input power on current density required for transparency.

It is clear from fig 6.2 that for a 5 μm wide guide the transparency current is virtually independent of optical input power upto 0.5 mW,, and then rises with the input power. This is due to the increased stimulated recombination depleting the carrier density in the active layer of the guide (and hence the optical gain). This can only be compensated by an increase in the rate of carrier injection.

Fig 6.3 shows how the transparency current density varies due to the wavelength dependence of the gross optical gain, g_i. Because the carrier density in the guide is approximately constant at transparency, the minimum transparency density occurs at a wavelength of 836nm, irrespective of the optical input power level. However, in practice it is likely that the guide would be biased to transparency at the wavelength of the integrated laser source. In chapter 5 it was seen that a 250 μm laser with 30% reflectance facets and the same active layer composition as table 6.1, has an output wavelength in the region of 820 - 825 nm, depending on the output power. Consequently the transparency current of the guide to match the lasing wavelength will be marginally higher than the minimum, unless the laser is specifically tuned to the guide.

The main conclusion which may be drawn is that for optical inputs below 10 - 15 mW, the current density required to pump the 1mm guide to transparency is in the region 0.5 - 0.8 J_{th}. For many applications this is a practical value and would not give rise to excessive heating effects.

6.4.2 Output Noise Spectrum and Carrier Density Distribution

One advantage of a model with wavelength dependent gain and spontaneous emission data, is that it is possible to calculate the broadband output noise spectrum of the guide. The output noise is due to amplified spontaneous emission (ASE) in the guide. Fig 6.4 shows the output spectrum normalized to wavelength slot width, for four optical input powers. The guide is biased to give transparency to a 1 mW input signal, and the figure shows the effect on output spectrum of perturbing the input power from the bias point while maintaining a constant current.

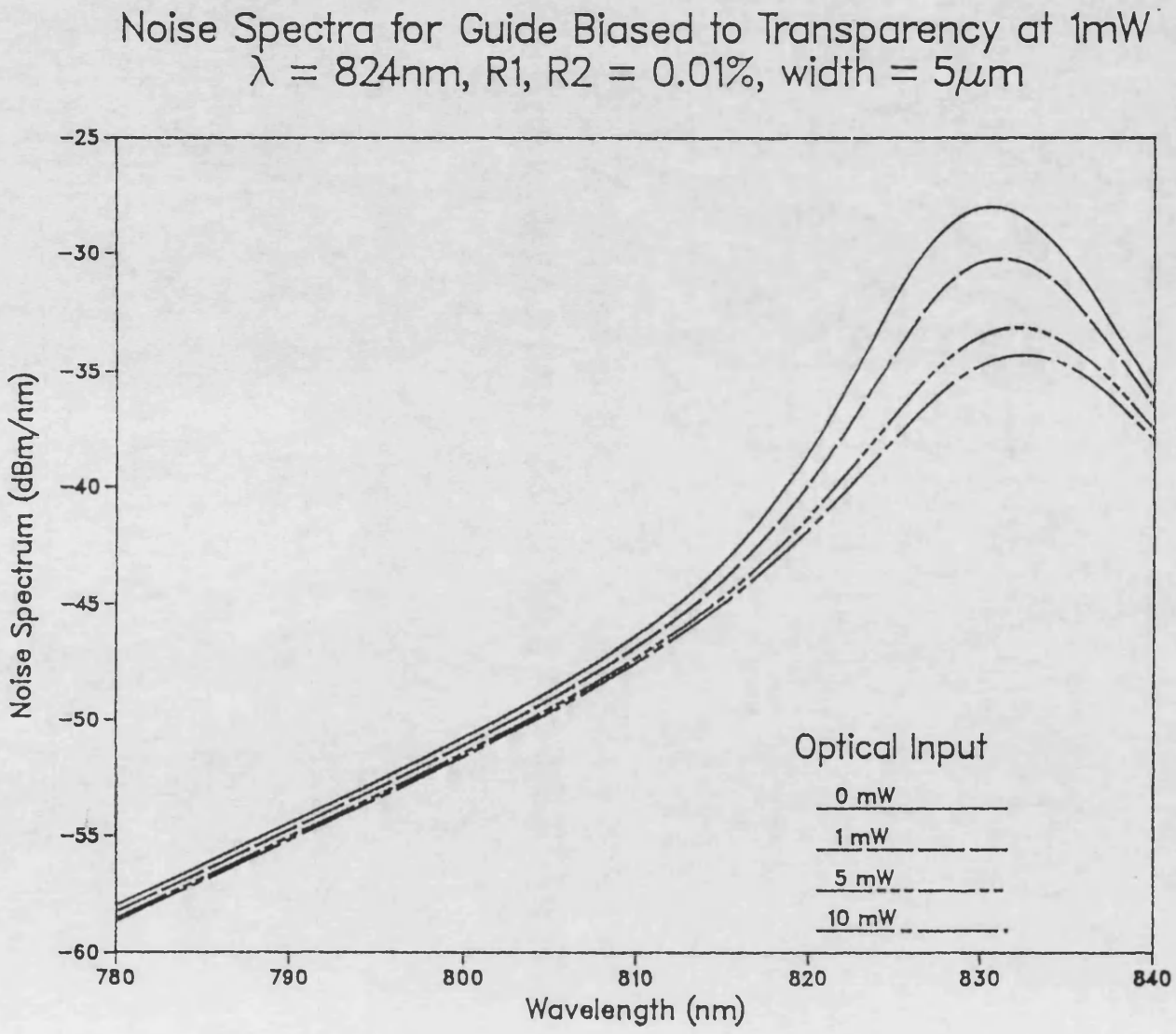

Figure 6.4 : Output noise spectra for a guide transparent to a 1mW optical bias power.

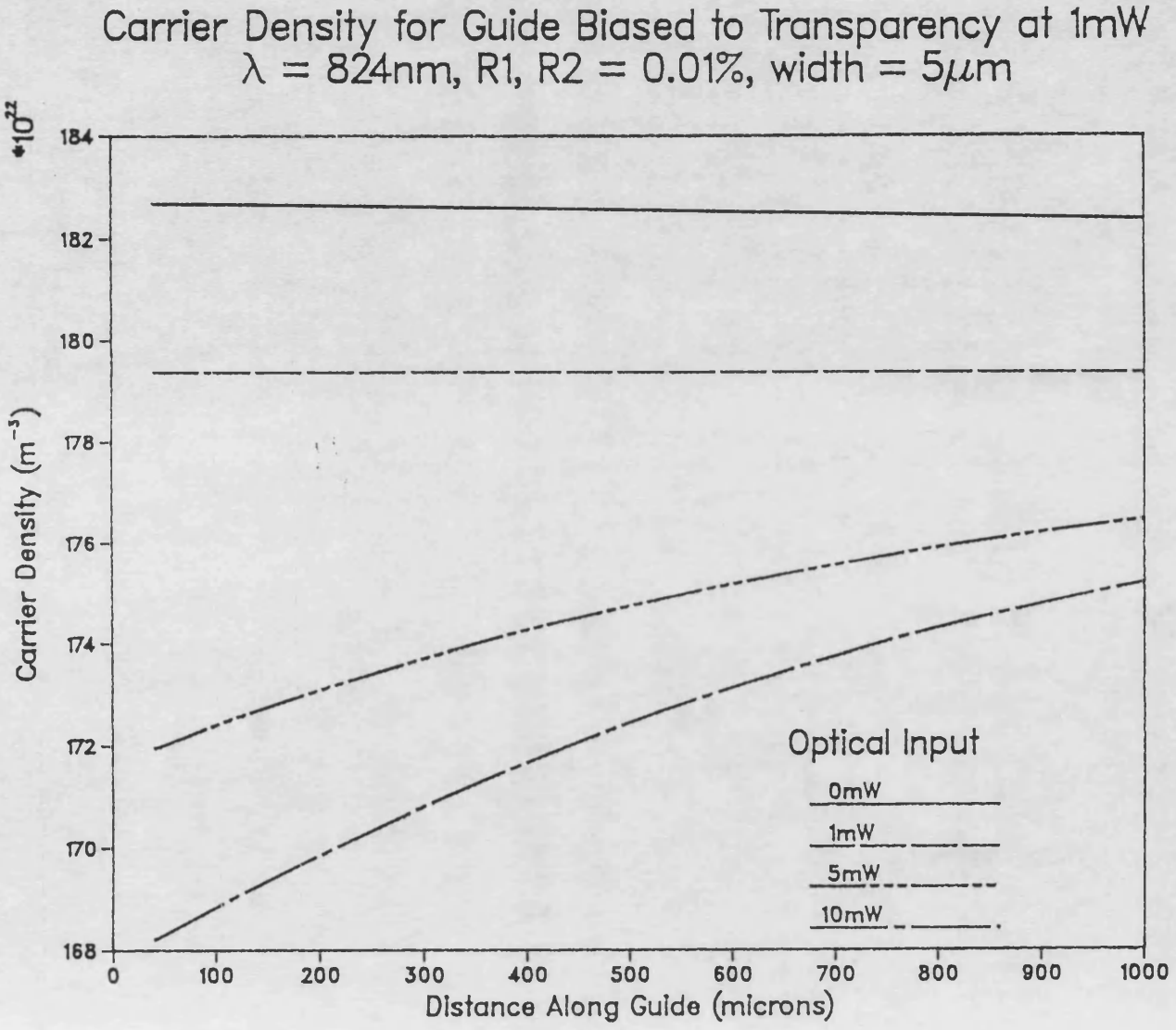

Figure 6.5 : Longitudinal carrier density distribution for a guide transparent to a 1mW optical bias power.

The differences in the curves are due to the changes in carrier density along the guide, due to the change in the stimulated recombination term of equation (6.8). This not only modifies the total amount of spontaneous emission along the guide but, more importantly, modifies the amplification of this spontaneous emission down the guide. This is clearly shown for the curve when no optical input is applied. Under this condition the guide, nominally biased to transparency when the input is 1 mW, actually has gain and this amplifies the spontaneous emission. Whereas for the case of a 10 mW signal the guide has an overall loss which reduces the noise output and causes the spectral peak to shift to longer wavelength.

The underlying process of these changes is shown in fig 6.5, which shows the longitudinal variation of carrier density for the optical input conditions used in fig 6.4. For no optical input power, the guide has gain and the ASE along the guide causes a small decrease in carrier density towards the guide output. For 1 mW input power the guide is transparent, hence the flux and carrier density are virtually constant along the guide. As the input power is increased above 1 mW the increased stimulated recombination at the guide input locally depresses the carrier density and associated quantities. As the optical signal power is attenuated down the guide the carrier density recovers towards the output port.

6.4.3 Transmission Characteristics of an Active Guide

Four key parameters are identified in the characterization of the system performance of the AIOW. These are,

- The input / output linearity.
- The coherent forward pass gain.
- The total output noise power.
- The output signal to noise ratio.

In this section, these parameters are examined for the AIOW under the following conditions. The waveguide injection current is trimmed to give transparency at one of three optical input power; 1, 5 and 10 mW for three different wavelengths; 820, 830

and 840nm. The input optical power is then varied but the guide bias current is maintained at the initial transparency value. This is likely to be the case for a practical AIO system, where the guide is pumped from a fixed external current source, at a value appropriate to some mean optical input power. The optical input power may then be changed, either by direct modulation of the laser source or by using some other integrated modulator or switching element, inserted between the laser and the guide. Table 6.2 shows the transparency current densities, both 'real' and normalized to the threshold current density of a 250 μm, 30% facet laser.

Wavelength, λ (nm)		820nm		830nm		840nm	
Current Density,J (KA/cm^2)		J_t	J_t/J_{th}	J_t	J_t/J_{th}	J_t	J_t/J_{th}
Optical	1 mW	2.15	0.65	1.76	0.53	1.75	0.53
Input	5 mW	2.45	0.73	2.03	0.61	2.03	0.61
Power	10 mW	2.82	0.84	2.36	0.71	2.37	0.71

Table 6.2. Variation of transparency current density with wavelength and optical input power

6.4.3.1 Input / Output Characteristic

The input / output characteristics of the active guide are shown in figures 6.6 (a), (b) and (c) for guides pumped to transparency for 1, 5 and 10 mW respectively. The labels accompanying these figures show the drive current in mA corresponding to the current density required to pump the guide to transparency. All three graphs show the highly non-linear input / output behaviour of the guide due to gain saturation.

The non-linearity is most pronounced around the shortest (lasing) wavelengths, whilst the characteristics at 830 and 840nm are of interest because the transparency current is virtually identical in both cases. The reason for the different characteristic is due to the reduction in the value of the stimulated gain coefficient, g_i at longer wavelengths. This alters the interaction term between the flux and carrier densities in equation (6.18), which consequently pushes the gain compression point to higher optical input powers for the longer wavelength inputs.

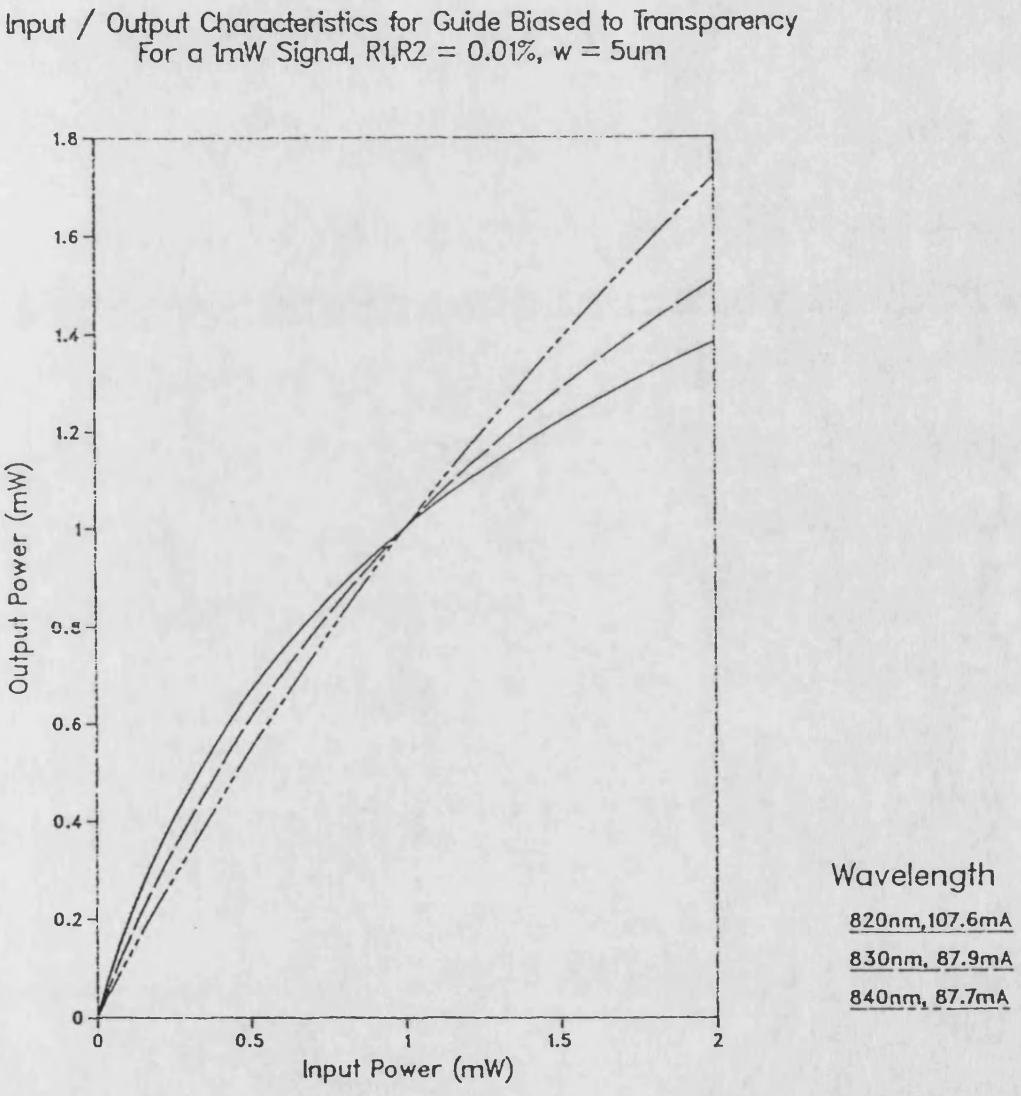

Figure 6.6a Effect of optical input power on optical input / output characteristic, as a function of wavelength of optical input signal.

(a) At 1 mW optical input power,

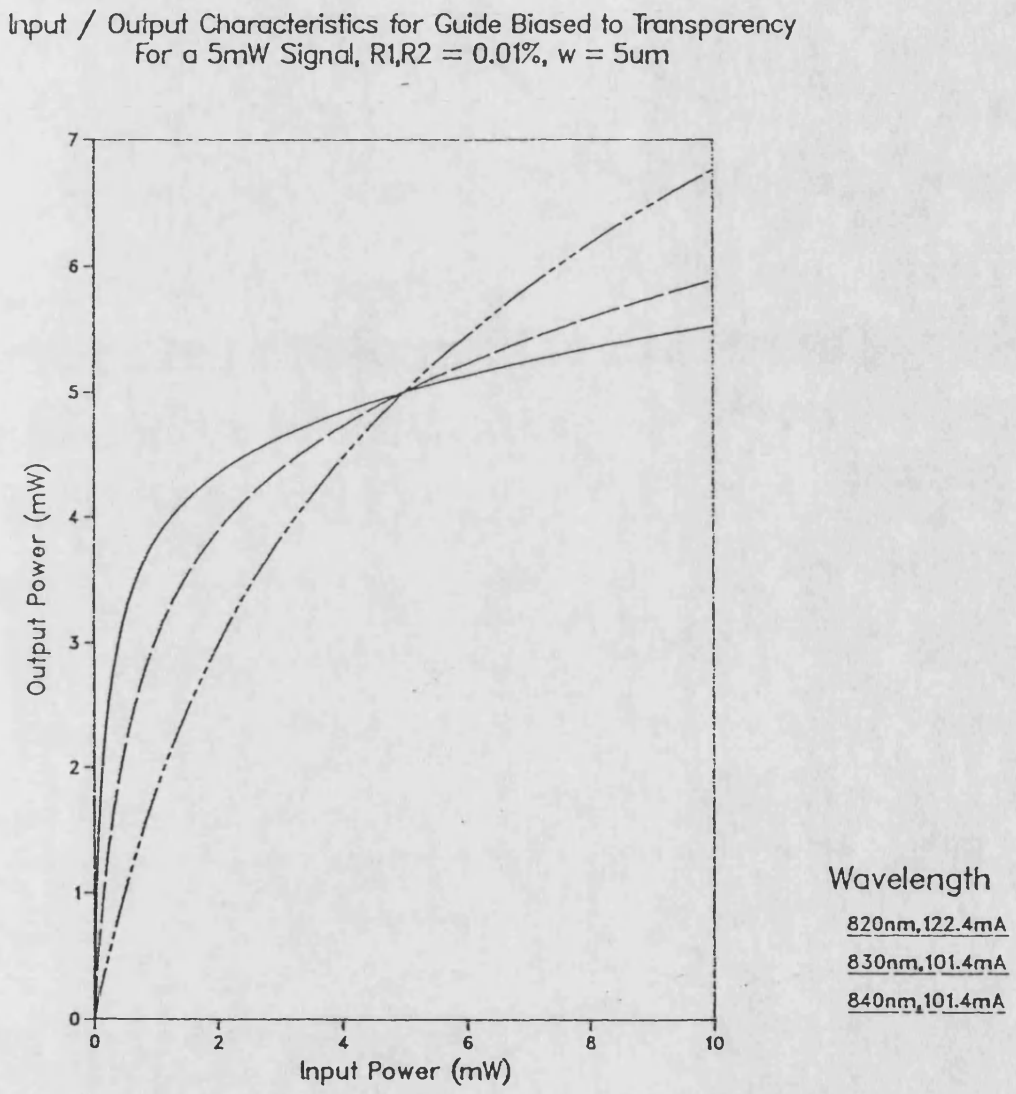

Figure 6.6 Effect of optical input power on optical input / output characteristic,

as a function of wavelength of optical input signal.

(b) At 5 mW optical input power,

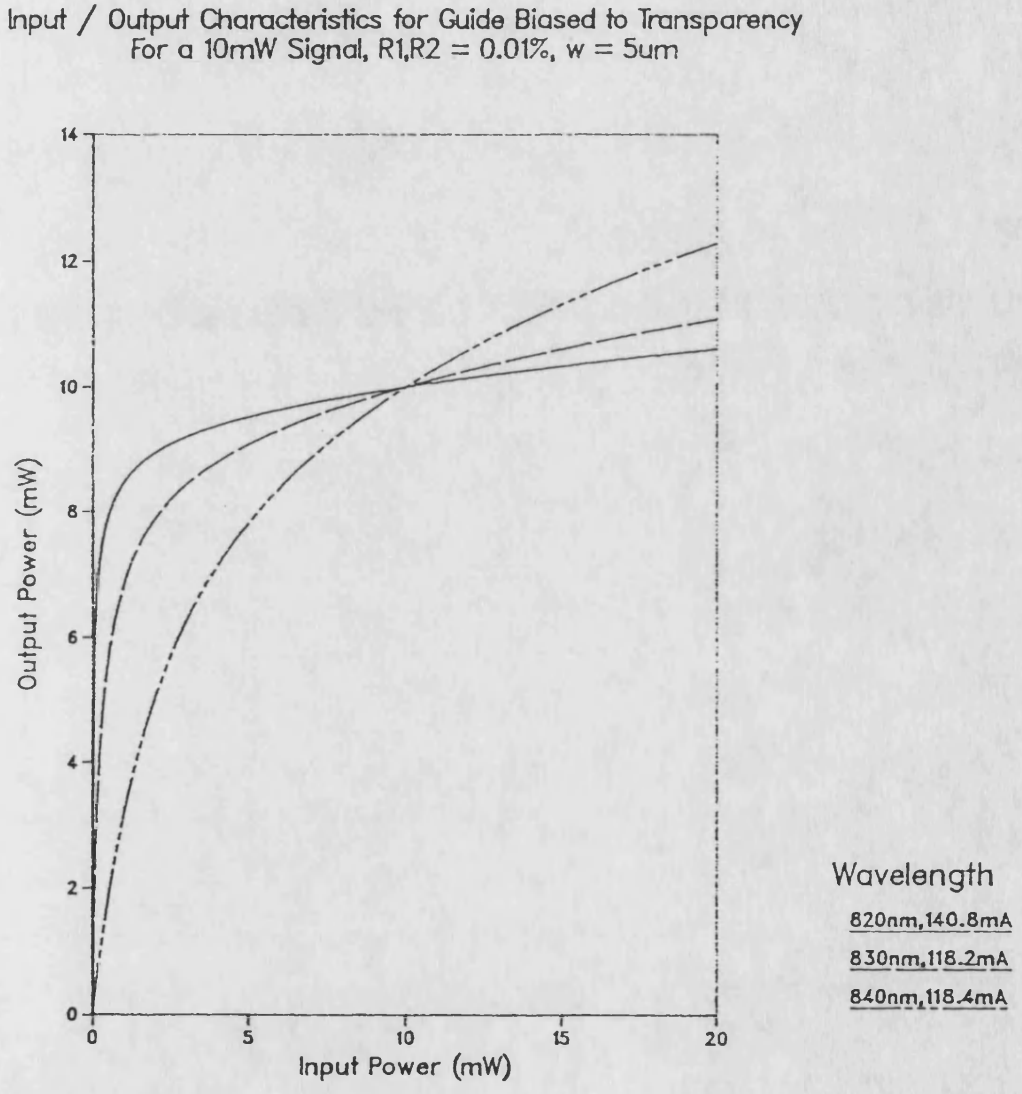

Figure 6.6: Effect of optical input power on optical input / output characteristic, as a function of wavelength of optical input signal.

(c) At 10 mW optical input power.

6.4.3.2 Forward Pass Gain Characteristic

Figures 6.7(a), (b) and (c) show the forward pass gain for the guide biased for transparency to optical input powers of 1, 5 and 10 mW respectively. The underlying mechanism to the input / output non-linearity is shown quite clearly in these graphs. As the input power increases, the gain can be seen to saturate due to the increased stimulated recombination in the guide. The degree of saturation increases with optical input power and bias point. When the input optical power is below the transparency bias point the guide is seen to have net gain as the carrier density will be greater than the transparency density N_t.

6.4.3.3 Total Output Noise Characteristic

The total broadband output noise from the guide is defined as,

$$N_{bb} = \int_{\lambda_l}^{\lambda_u} N_s(\lambda)\, d\lambda , \qquad (6.21)$$

where $N_s(\lambda)$ is the noise spectral density function at the the guide output. For the descrete wavelength model this simply becomes :

$$N_{bb} = \sum_{i=l}^{u} N_{s,i} \qquad (6.22)$$

where $N_{s,i}$ is the noise power in the i^{th} wavelength slot at the guide output.

Figures 6.8 (a), (b) and (c) show this broadband noise output for each of the optical bias powers. It should be noted that the broadband noise also reduces as the input power rises due to the effects of gain saturation and reduced spontaneous emission along the guide. The broadband noise at the transparency point is seen to increase as the input bias power rises, and there is significantly higher noise around the

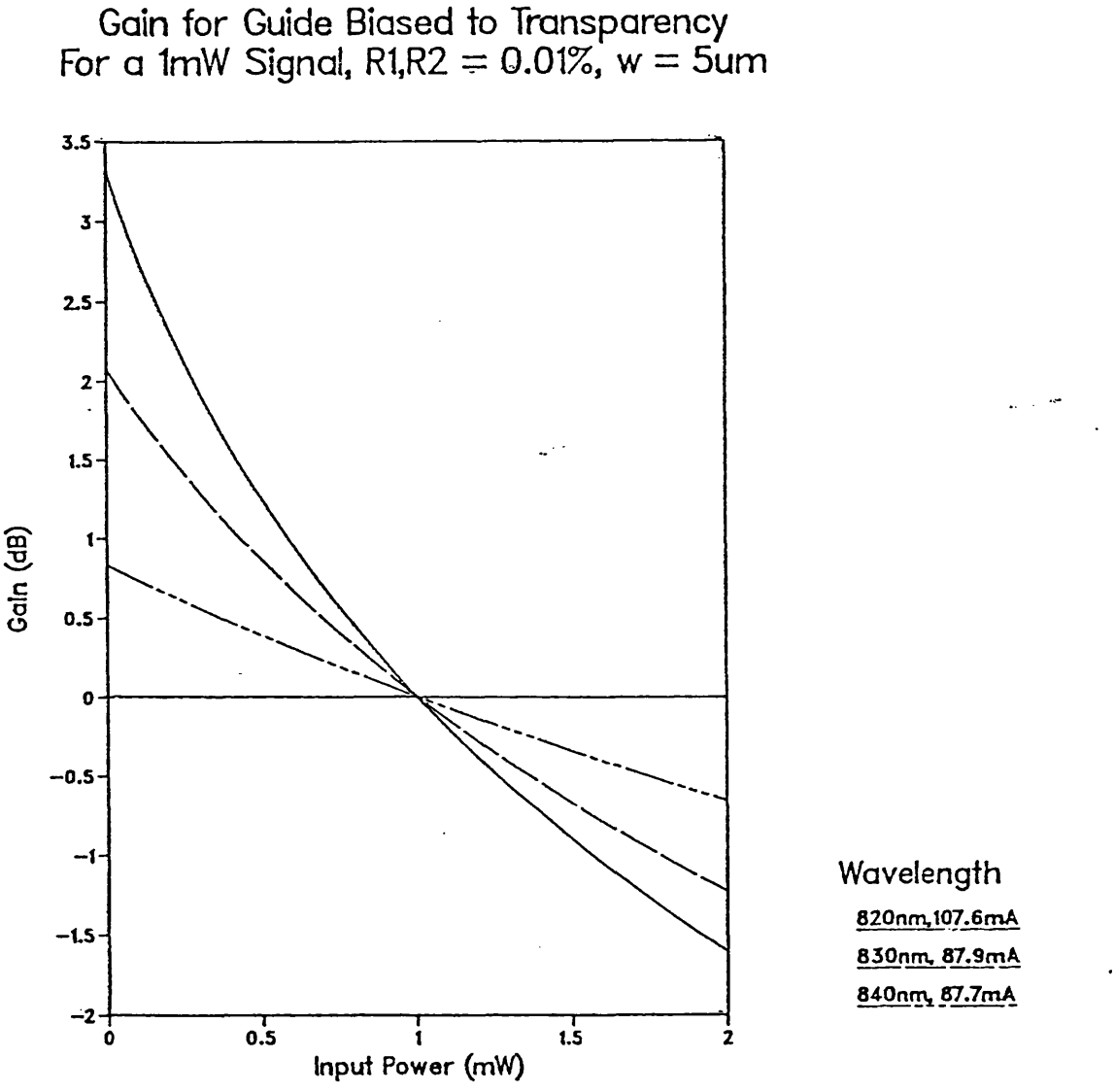

Figure 6.7a Effect of optical input power on coherent forward pass gain, F, as a function of wavelength of optical input signal.

(a) At 1 mW optical input power,

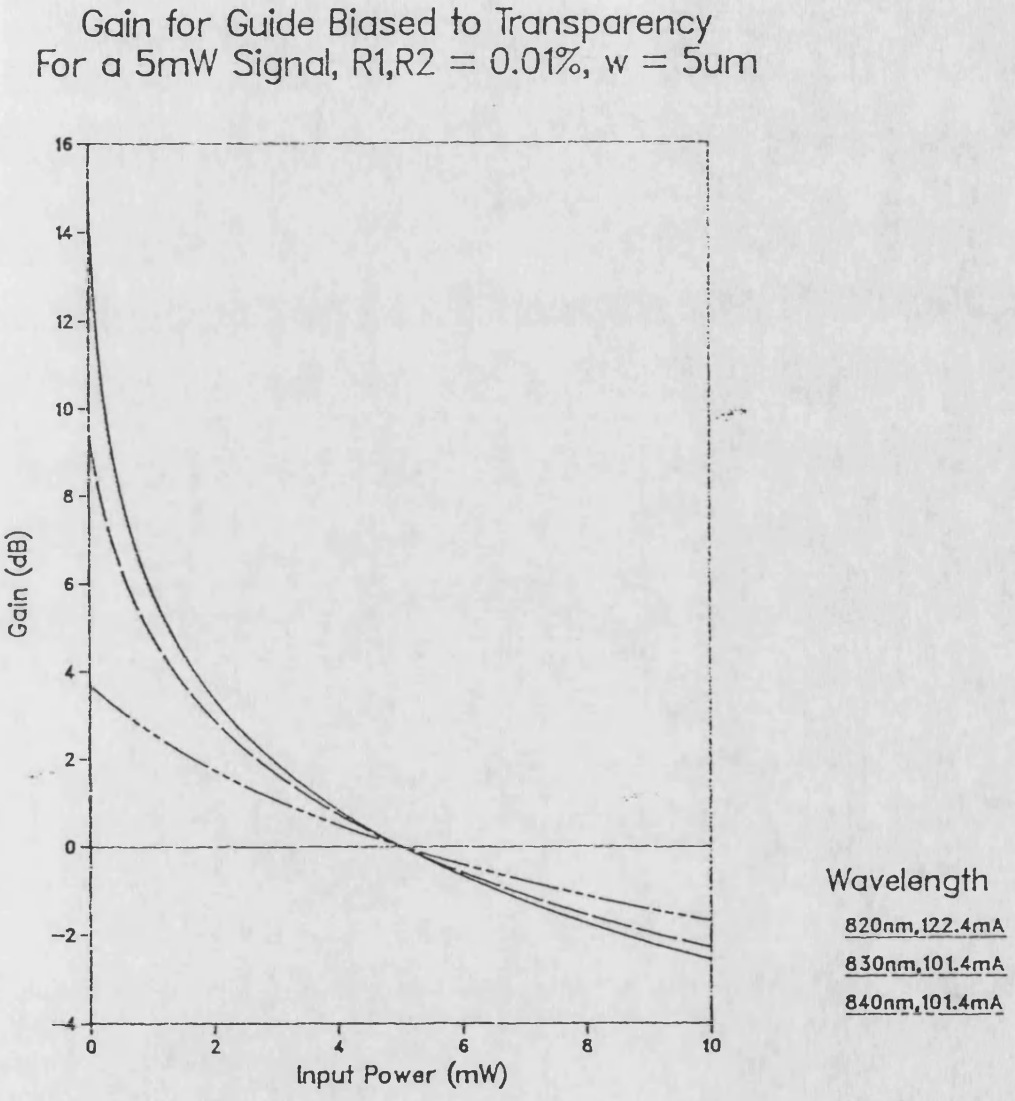

Figure 6.7b Effect of optical input power on coherent forward pass gain, F, as a function of wavelength of optical input signal.

(b) At 5 mW optical input power,

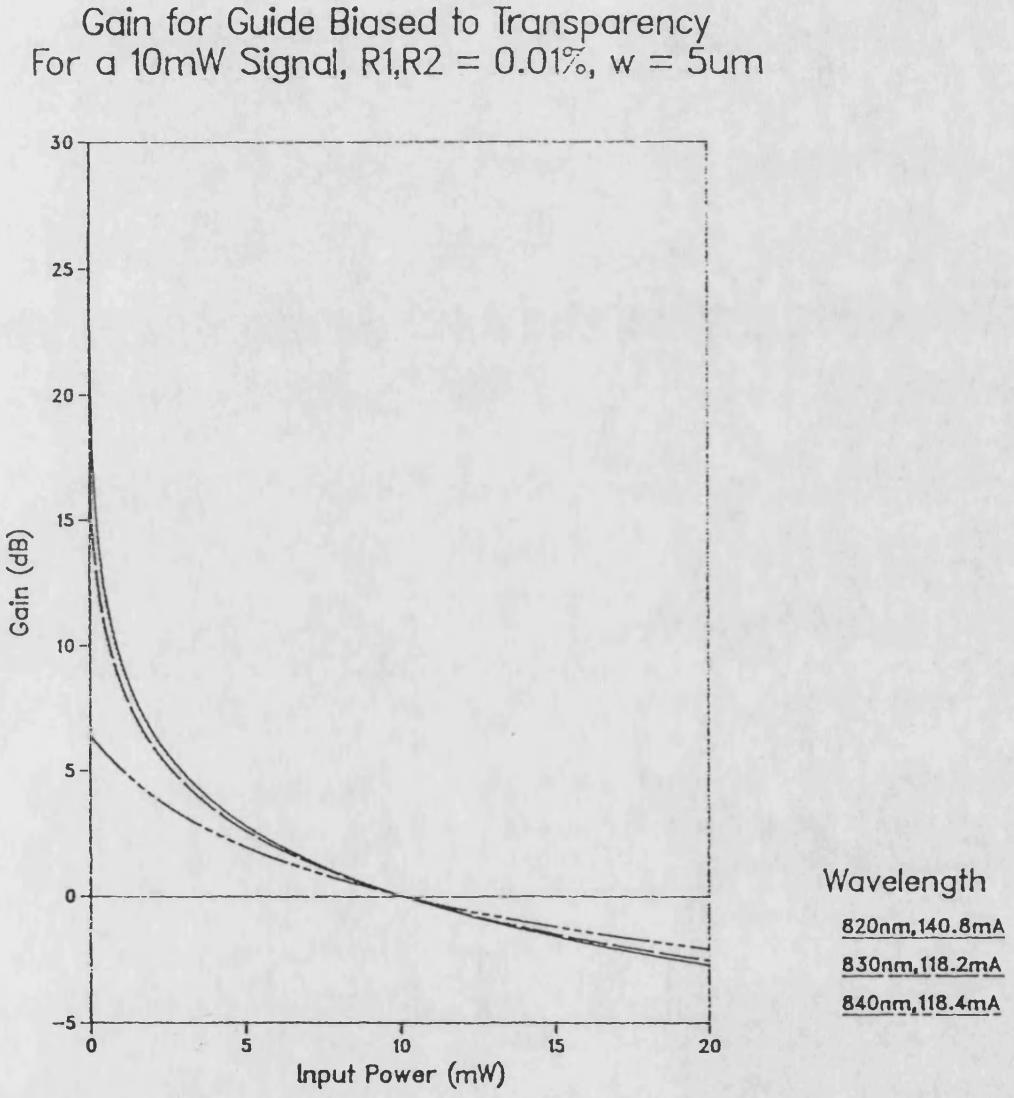

Figure 6.7*c* Effect of optical input power on coherent forward pass gain, F, as a function of wavelength of optical input signal.

(c) At 10 mW optical input power.

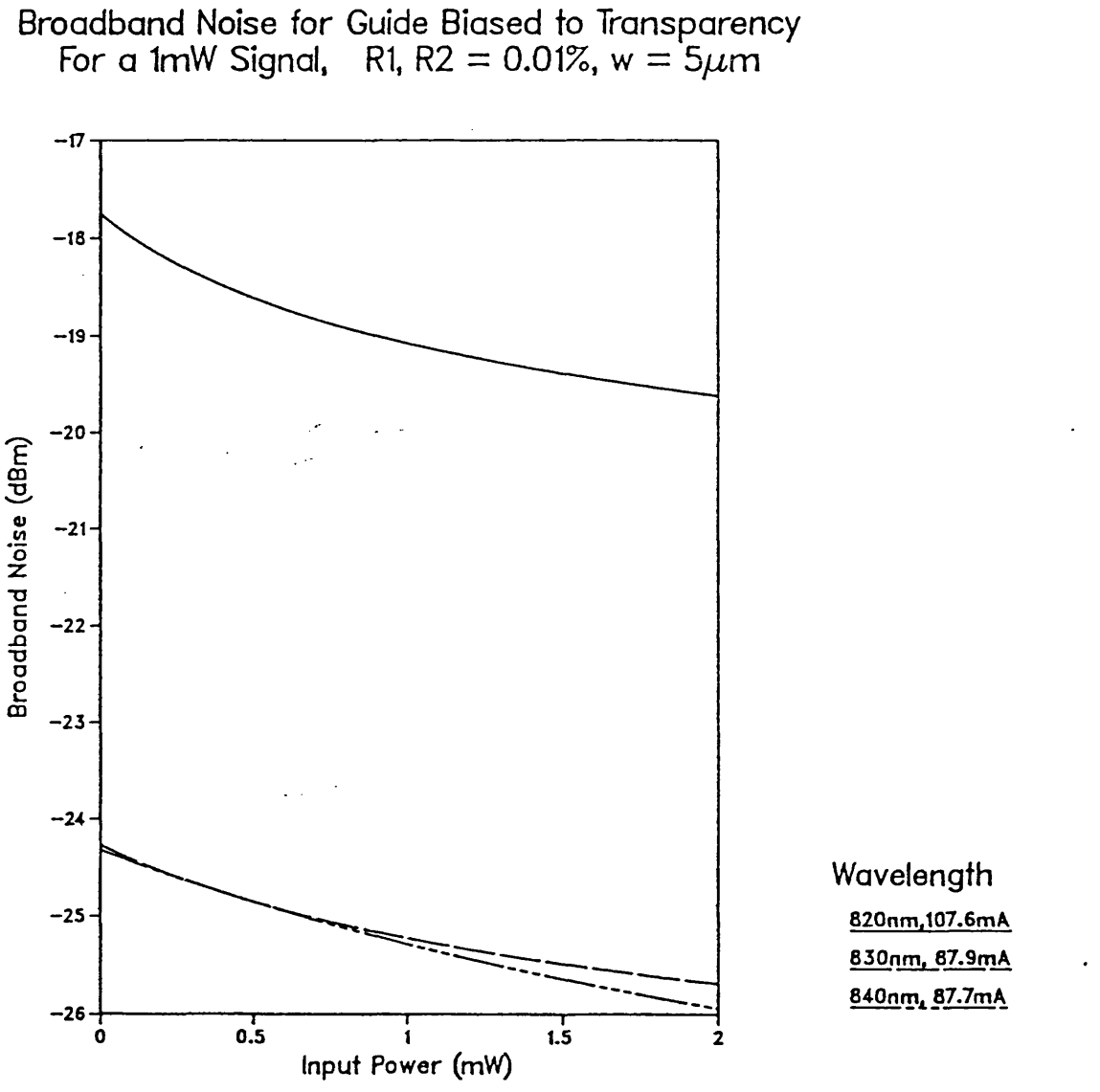

Figure 6.8a Effect of optical input power on broadband noise output N_{bb}, as a function of wavelength of optical input signal.

(a) At 1 mW optical input power,

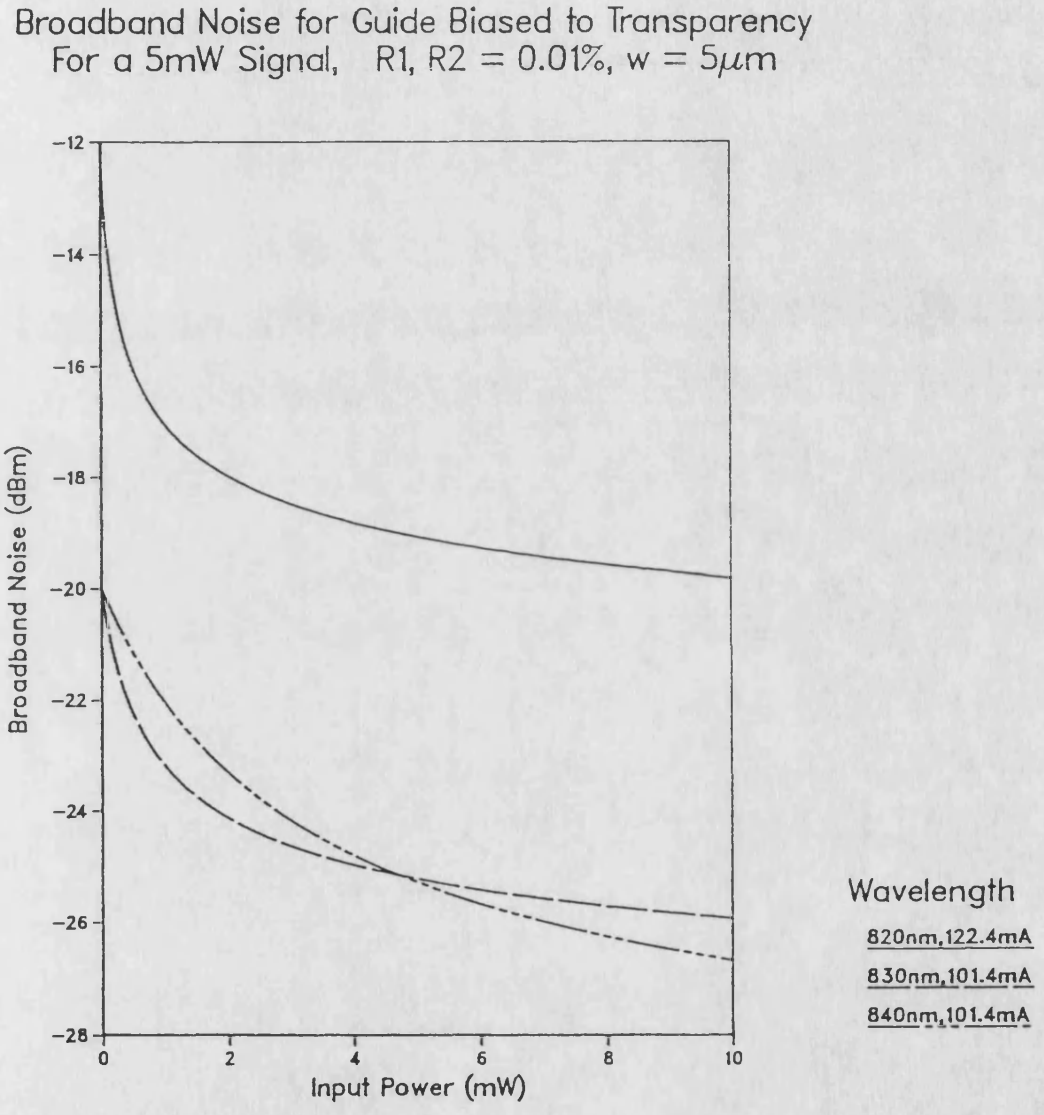

Figure 6.8b Effect of optical input power on broadband noise output N_{bb}, as a function of wavelength of optical input signal.

(b) At 5 mW optical input power,

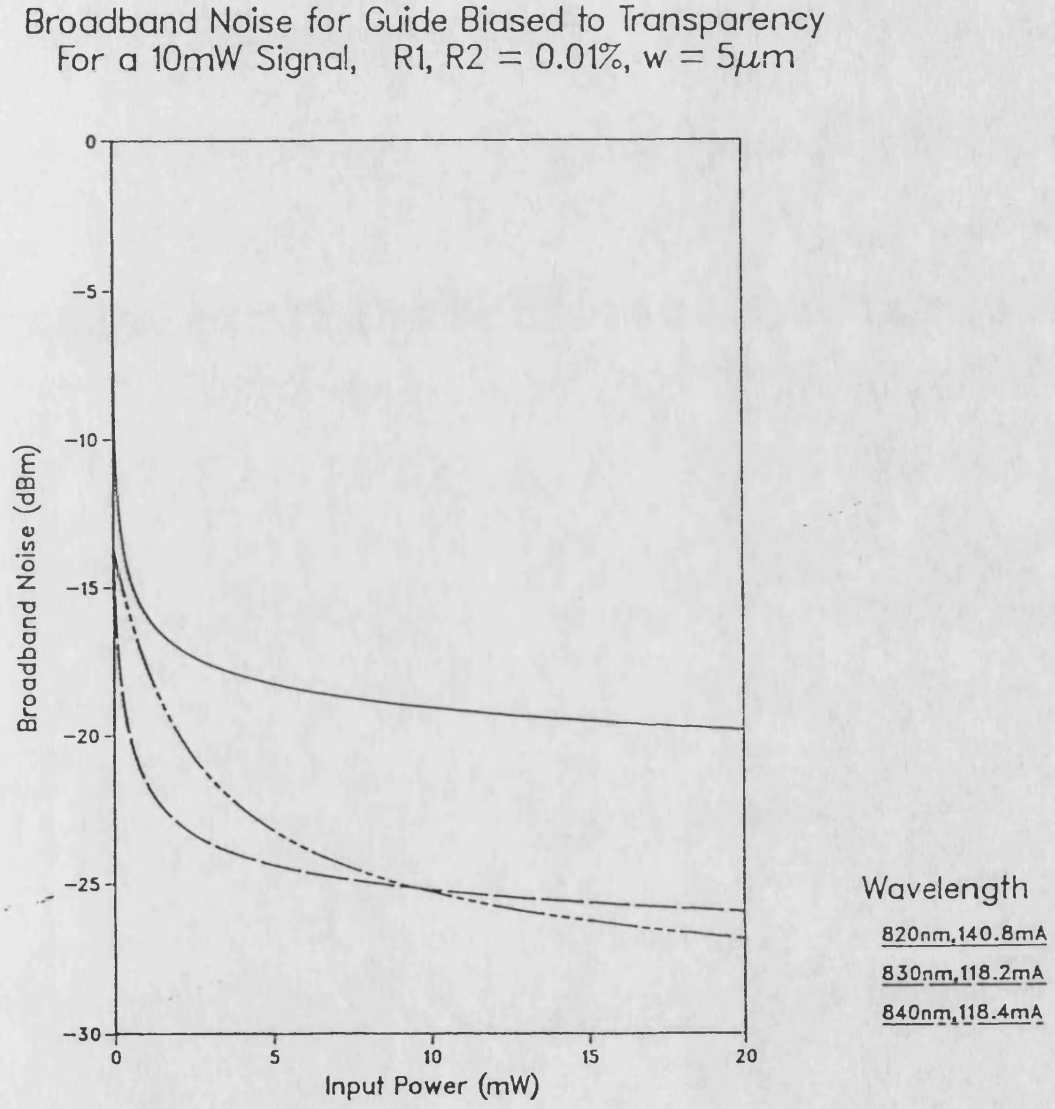

Figure 6.8c Effect of optical input power on broadband noise output N_{bb}, as a function of wavelength of optical input signal.

(c) At 10 mW optical input power.

lasing wavelength. In the main this is due to the higher carrier densities required to achieve transparency.

6.4.3.4 Signal to Noise Characteristic

Figures 6.9 (a),(b) and (c) show the resulting output signal to noise ratio where the SNR is defined as :

$$SNR_k = F_k \cdot \frac{P_{in,k}}{N_{bb}}, \qquad (6.23)$$

where $P_{in,k}$ is the optical input power at some wavelength slot k, F_k is the forward pass gain at the k^{th} wavelength slot for the appropriate level of optical bias and N_{bb} is the broadband noise defined in equation (6.22).

The most striking feature of these graphs is that the SNR saturates with increasing input power to a value determined by both the optical bias power to which the guide has been electrically biased to transparency and the wavelength. At the lasing wavelength ≈ 820nm, the SNR saturates to a value of approx 23 dB for a 1 mW bias. As the bias is increased so the saturation value increases, to approximately 28 dB for 5 mW and 32 dB for 10 mW.

For input powers well below the transparency point the broadband noise is seen to be high whilst the product, $F_k \cdot P_{in,k}$ is relatively low, hence the SNR is very small. As the input power increases, the signal strength increases whilst the noise power decreases, hence the SNR rises. Above the transparency point a plateau is reached where the SNR continues to slowly rise with input power. Although the gain continues to fall, the increase in input signal is sufficient to increase the SNR. The output SNR is better at higher input powers as the gain and broadband noise are the same as at the lower biases.[1]

---

[1] For a particular input wavelength the transparency current density N_t is constant.

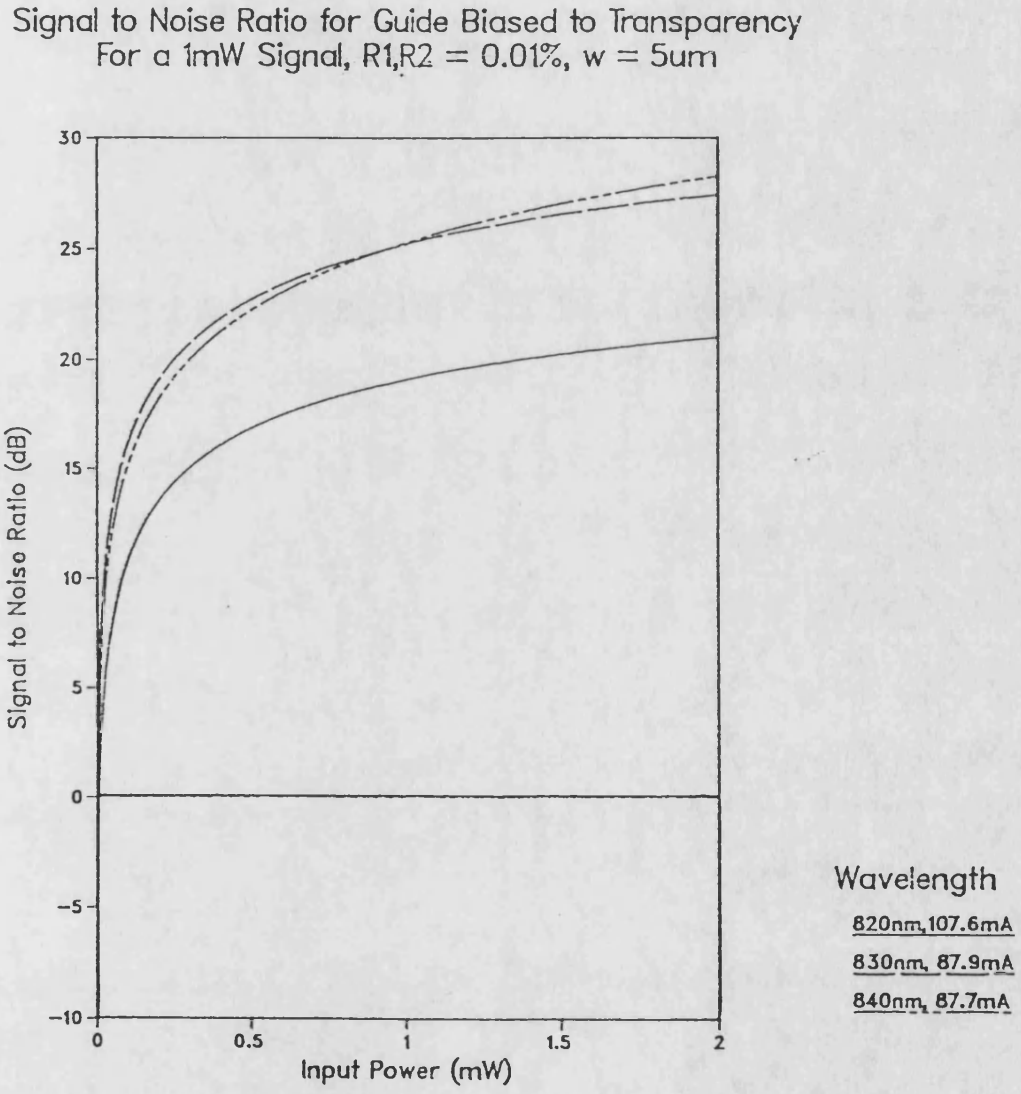

Figure 6.9a Effect of optical input power on output signal to noise ratio, SNR, as a function of wavelength of optical input signal.

(a) At 1 mW optical input power,

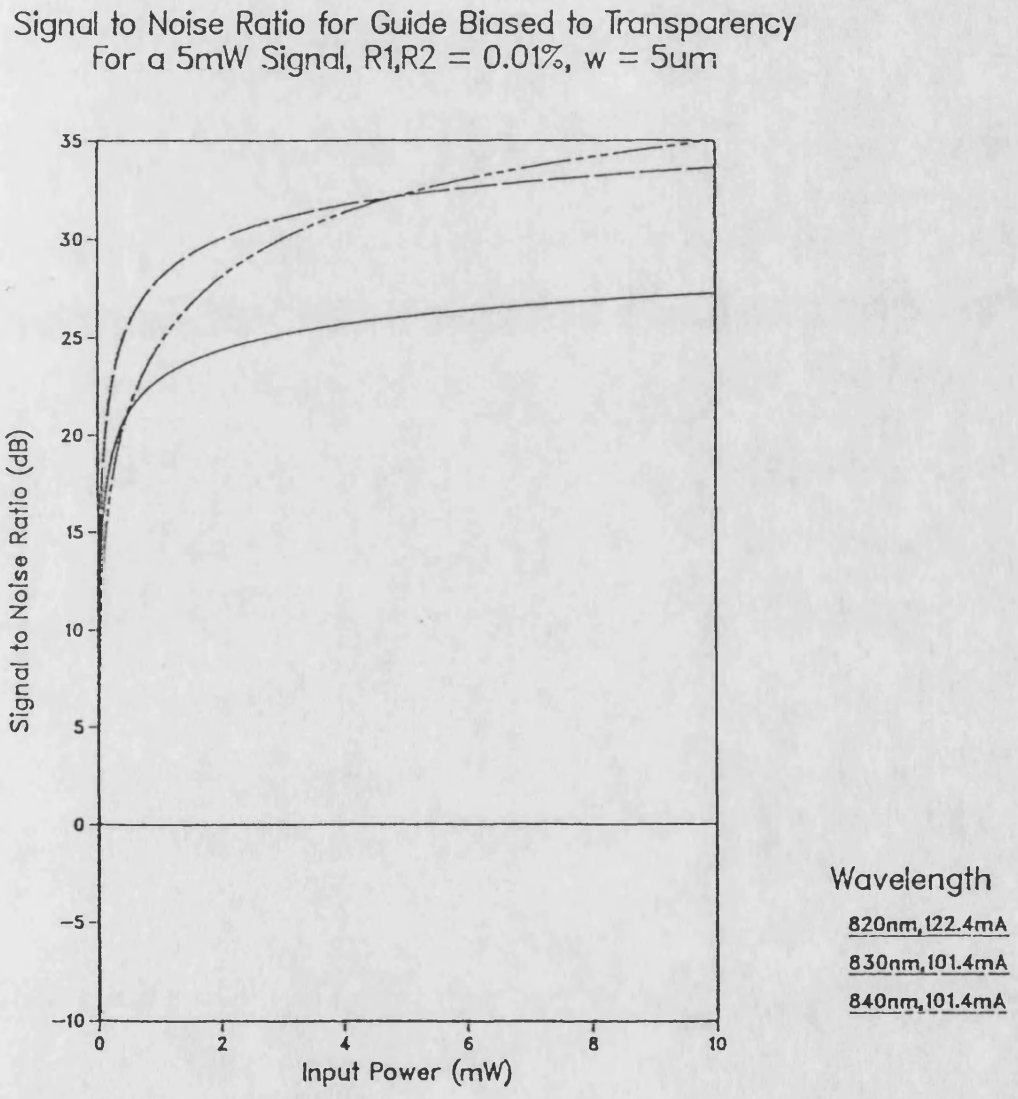

Figure 6.9b Effect of optical input power on output signal to noise ratio, SNR, as a function of wavelength of optical input signal.

(b) At 5 mW optical input power,

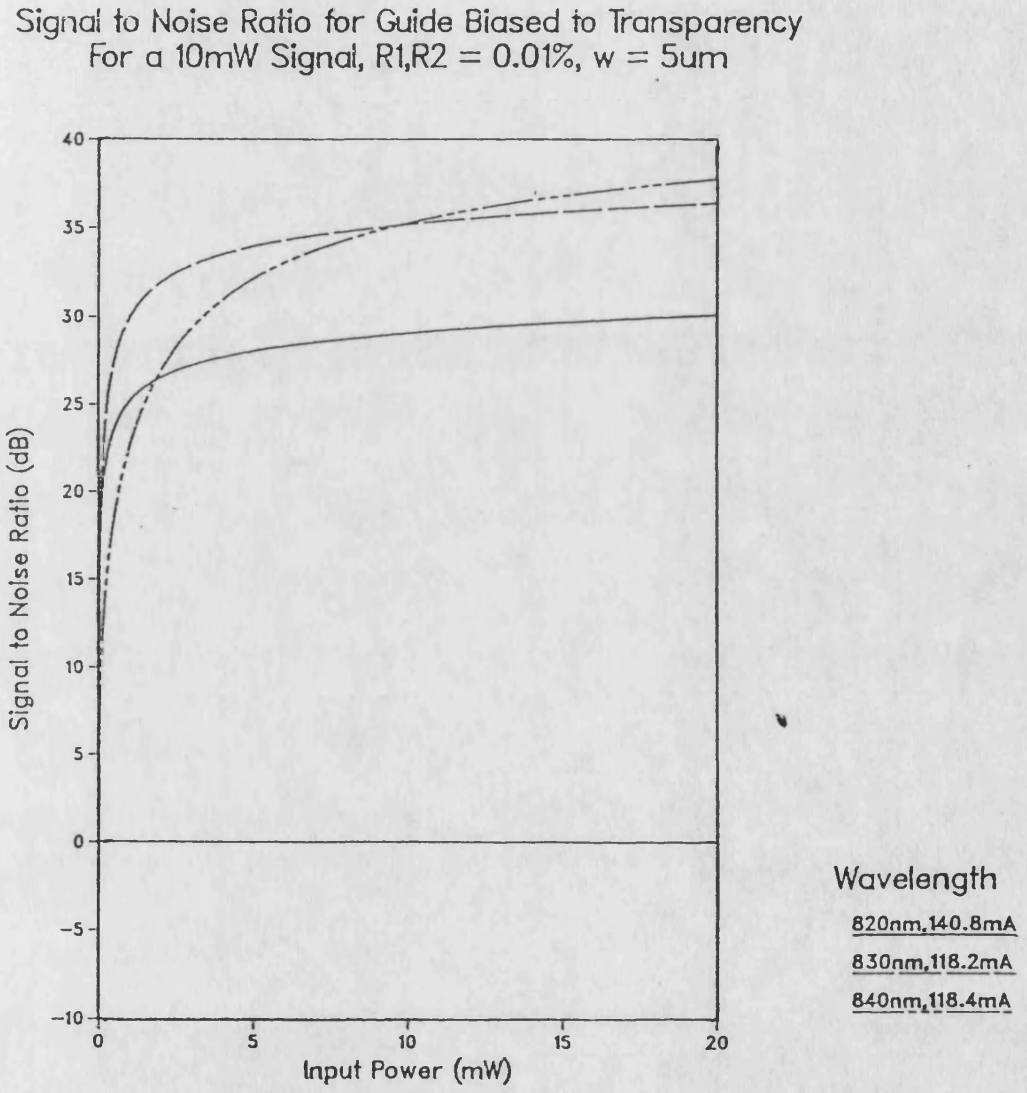

Figure 6.9c Effect of optical input power on output signal to noise ratio, SNR, as a function of wavelength of optical input signal.

(c) At 10 mW optical input power.

To summarize subsection 6.4.3, this set of results shows the effect of varying the input optical power about a value at which the guide is transparent. As the input power rises, the stimulated recombination term in the carrier continuity equation also rises, causing a consequent decrease in carrier density, stimulated gain and spontaneous emission terms. Thus the transmission characteristics of the guide are highly non-linear, showing saturation for high input powers.

6.4.4 Effect of Width of the Active Guide

It is of interest to examine the effect of width of the active guide on the four parameters identified in the previous section (6.4.3), as this determines the carrier and flux densities and hence the strength of interaction. In this case it is assumed that the input source is perfectly coupled to the guide for each width, as might be the case for a fully integrated laser / waveguide system. Table 6.3 show the variation of optical confinement factor Γ, and the spontaneous emission coupling factor, δ appropriate for the given waveguide parameters [see for instance Boeck et al, 11]. Also given in table 6.3 are : the corresponding transparency current density, J_t for a 1 mW optical bias level at 824nm wavelength; the threshold current density J_{th} of a 250 μm laser with the same parameters and 30% facet reflectance; and the ratio of J_t / J_{th}.

		Γ	δ	J_t kA/cm^2	J_{th} kA/cm^2	J_t/J_{th}
Guide	1	0.50	1.33×10^{-5}	2.70	3.74	0.72
Width	5	0.75	1.00×10^{-4}	2.01	2.72	0.74
μm	10	0.80	2.30×10^{-4}	1.93	2.59	0.75

Table 6.3. Variation of waveguide parameters with active layer width.

Figures 6.10 and 6.11 show that the input / output characteristics and forward pass gain, are considerably more non-linear for the 1 μm wide guide than the 5 or 10 μm guides. However, fig 6.12 shows that the broadband noise is virtually 20 dB

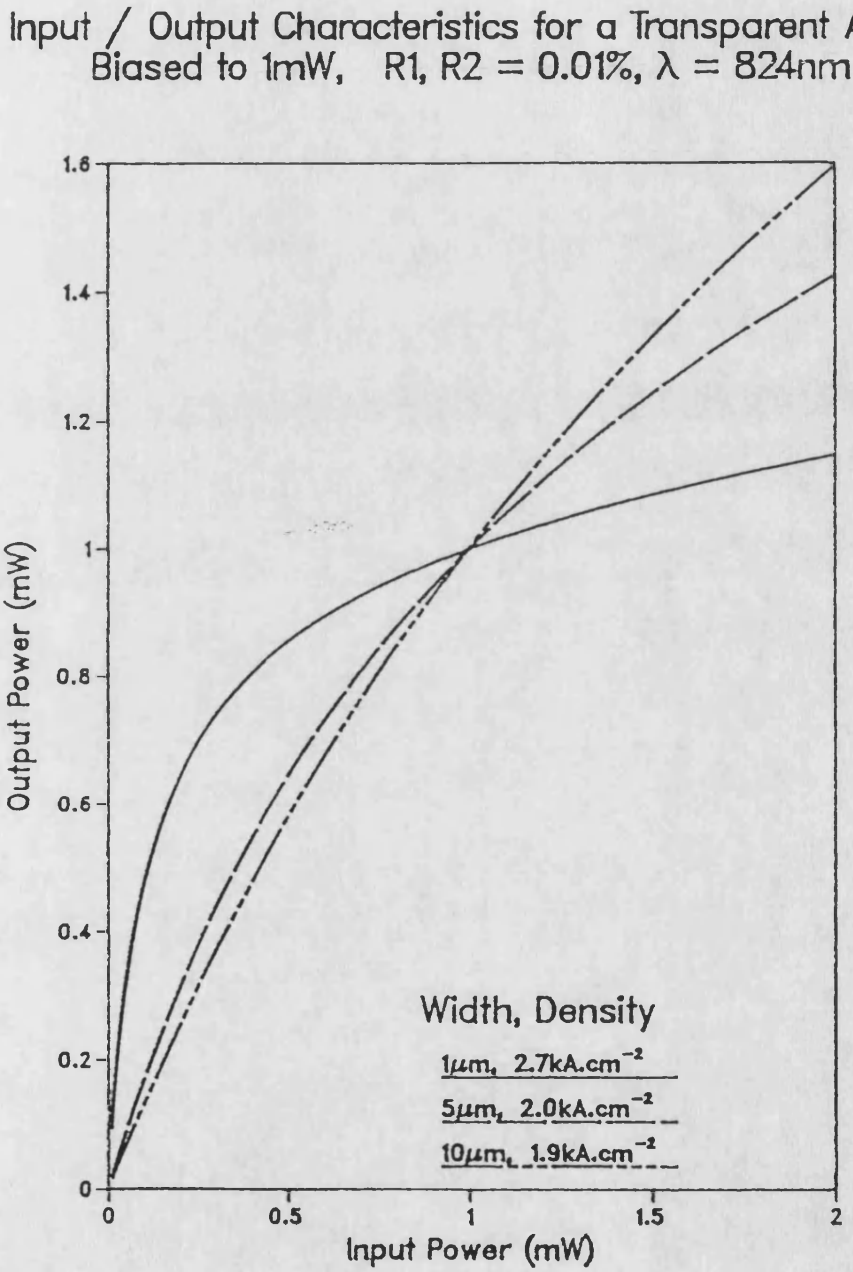

Figure 6.10 : Effect of optical input power on optical input / output characteristic, as a function of waveguide width.

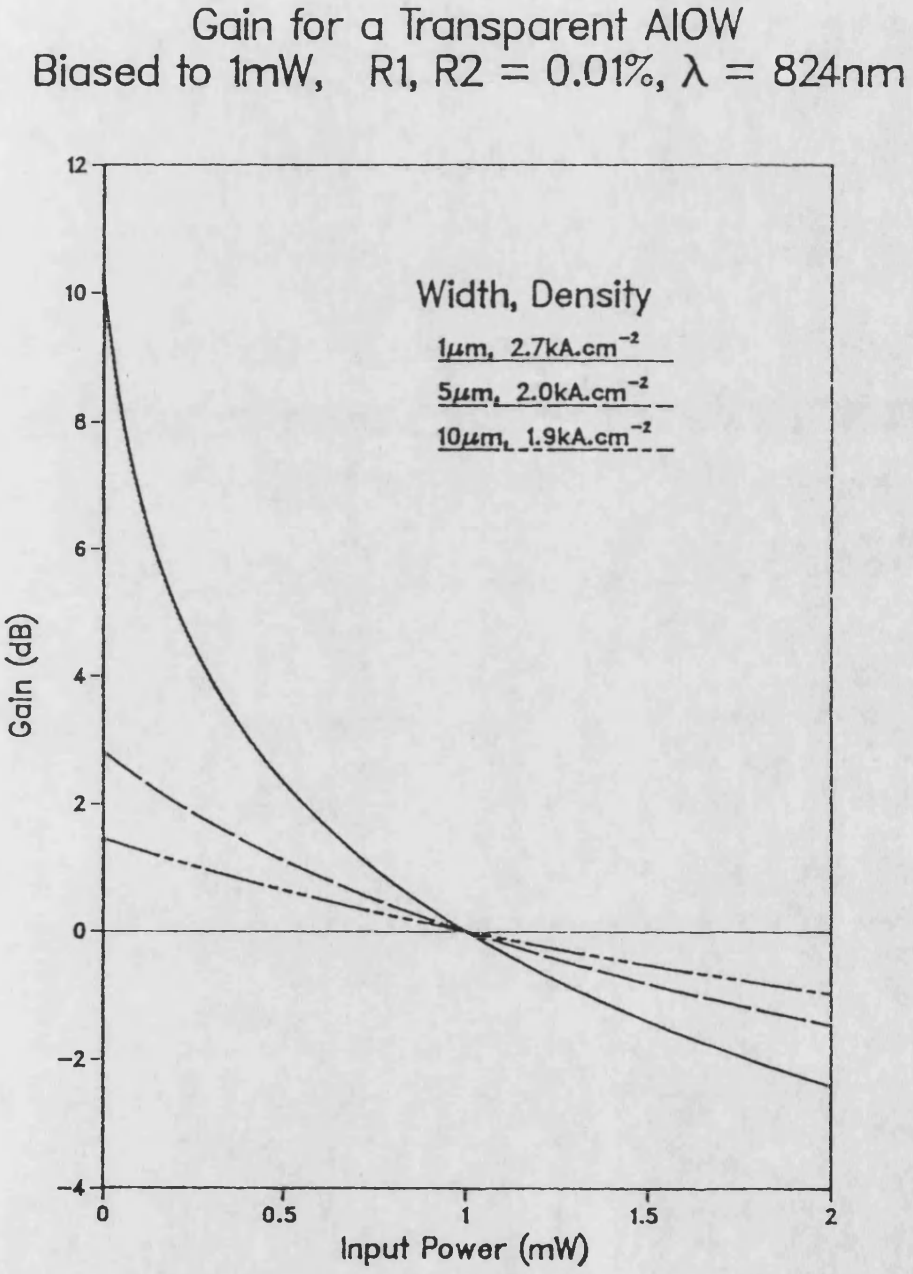

Figure 6.11 : Effect of optical input power on coherent forward pass gain, F, as a function of waveguide width.

lower for the 1 μm guide than the 5 μm wide guide. This gives a substantial rise in the output SNR (fig 6.13) which saturates to a value in excess of 39 dB for optical input powers >2 mW, compared with a value of only 23 dB for the 5 μm guide. It should also be noted that the output SNR can be further improved if the guide is biased to transparency at higher optical input powers. Clearly the output SNR can be made to be satisfactory for many systems applications, particularly digital modulation and switching schemes, where the gain non-linearities are less likely to cause problems.

One of the main effects of changing the guide width is that the flux density coupled into the guide is inversely proportional to the cross sectional area for a constant input power, see equation (6.16). As the width is reduced the flux coupled into the guide increases, causing a greater interaction with the carrier density through increased stimulated recombination. This effect is shown quite clearly in figures 6.10 and 6.11.

However, the behaviour of the broadband noise and SNR cannot be explained by the reduction in cross section. If constant values were assumed for Γ and δ, then the transparency current density and the noise **flux** would be identical for each width. The broadband output noise **power** would therefore be directly proportional to the cross sectional area, giving rise to a 7 dB increase from 1 to 5 μm, and a 3 dB increase from 5 to 10 μm. The observed increases are 15 dB and 6.5 dB, despite the fact that the transparency current density is seen to fall which would normally suggest a decrease in the ASE. The higher than expected values for broadband noise can only be caused by the increase in δ, the factor which determines the amount of spontaneous emission which is available for amplification in the guide. The choice of δ is therefore critical and will have a significant effect on the broadband noise output from the guide.

Clearly there are a number of advantages and disadvantages associated with varying the guide width. As the width is increased the optical flux density is decreased (for a constant input power), gain saturation is reduced and the input / output characteristic becomes more linear. However, the increase in the spontaneous emission coupling factor δ has a significant effect on worsening the broadband optical noise and output SNR.

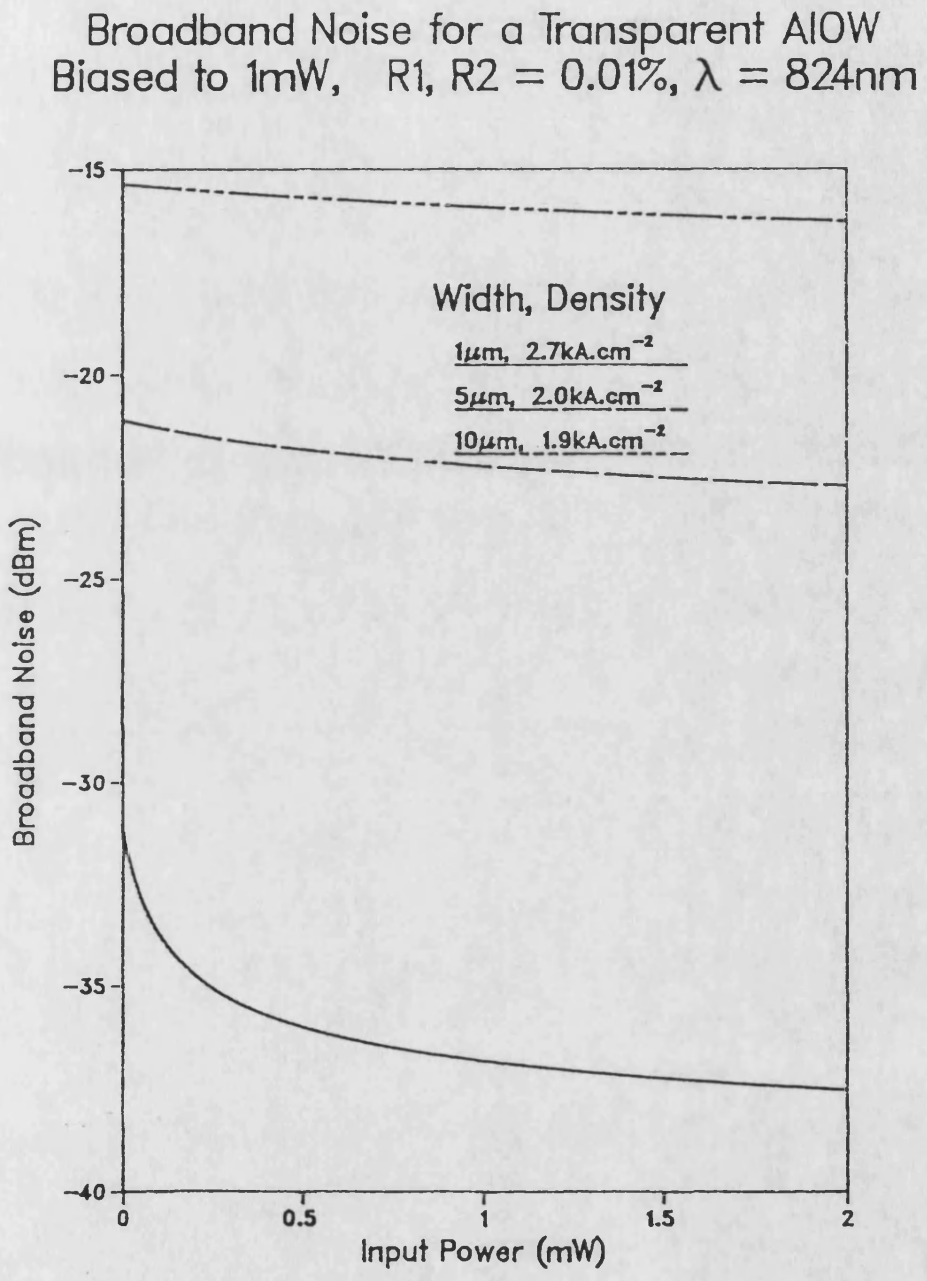

Figure 6.12 : Effect of optical input power on broadband noise output N_{bb}, as a function of waveguide width.

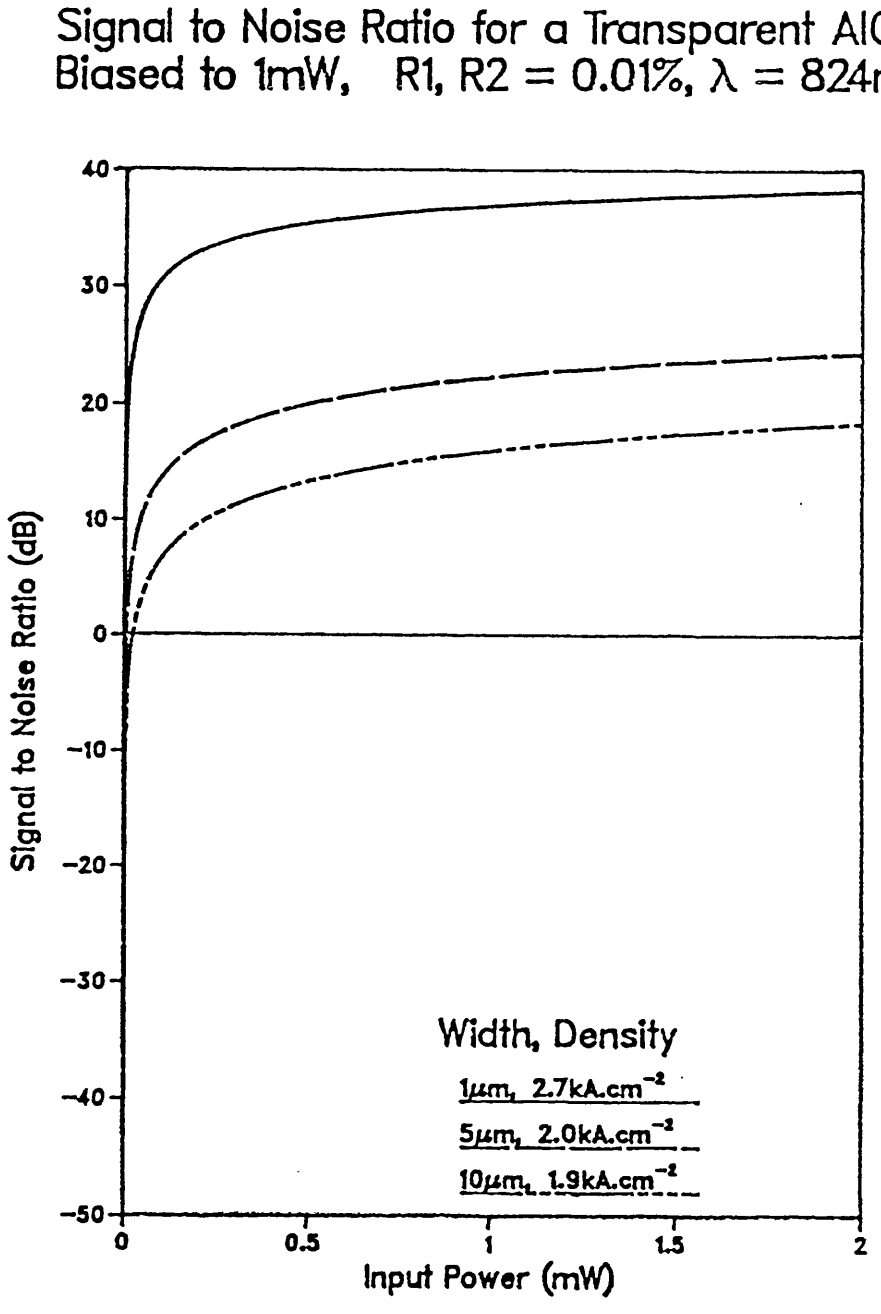

Figure 6.13 : Effect of optical input power on output signal to noise ratio, SNR, as a function of waveguide width.

6.4.5 Comparison of a Transparent Guide with a TWLA.

Figures 6.14 - 6.17 show the variation of the four parameters when the guide is electrically biased to give net loss or gain to a 0.1mW optical input bias. The characteristics are typical of those for TWLAs [6-10]. The input / output characteristics showb that at very low input powers in the region -50 to -30dBm, the output from the guide is totally dominated by the ASE in the guide, whilst at higher input powers, gain saturation becomes dominant. This is shown clearly in the gain and broadband noise characteristics in figures 6.15 and 6.16. At low input powers the gain and ASE are independent of input power but as stimulated recombination becomes more significant, both quantities decay.

The shape of the SNR curves in fig 6.17 are at first sight somewhat puzzling. For low input powers, the ratio F_k / N_{bb} will be virtually constant, hence the SNR is directly proportional to the input power, see equation (6.23). However, in the saturating region, the gain and broadband noise roll off at different rates, giving rise to the saturation in the SNR.

From figures 6.14 - 6.17 it would seem that there are significant advantages to be had from operating the guide as a TWLA. Although the noise power at the output is higher for all input powers, the signal overcomes this noise at much lower input powers, giving linear characteristics. In particular, fig 6.17 shows that for every value of input power the SNR will be improved by increasing the gain, until the guide reaches the laser threshold condition discussed in section 6.3.2.

However the linear region of the input / output characteristics becomes shorter as the gain increases. At transparency, the linear region is approximately 22dBm, whilst for the 20dB gain the region has been reduced to 10dBm. Clearly, the product of gain and dynamic range is increased by approximately 20dB between the two cases, but is this the issue for a waveguide? For an optical waveguide hi-fidelity transmission of optical signals over a range of optical input powers is required. Hence, a wide dynamic range is essential, as well as a good SNR performance.

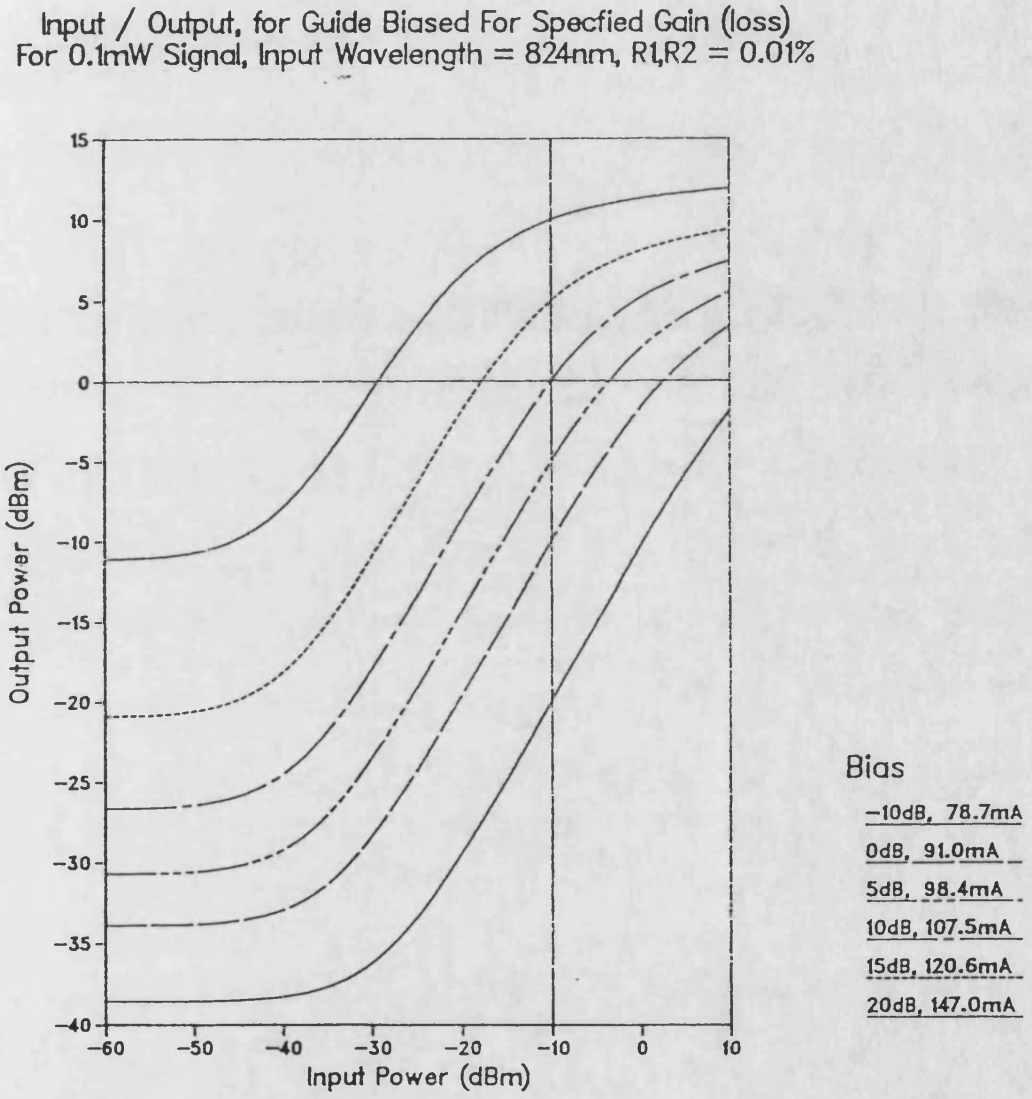

Figure 6.14 : Effect of optical input power on input / output characteristic of a 5 μm wide guide, as a function of coherent forward pass gain, F, specified for an 0.1 mW optical input power at 824 nm wavelength.

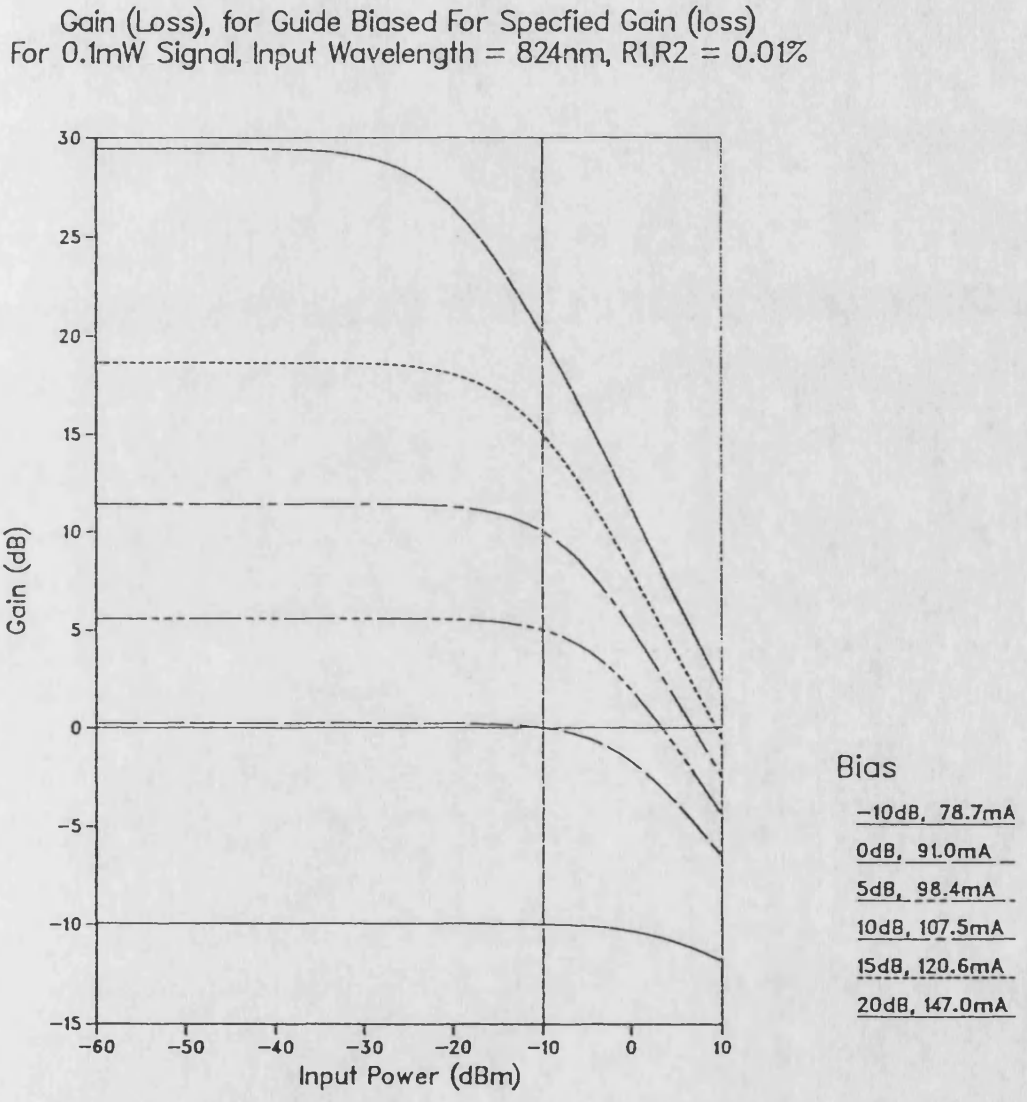

Figure 6.15 : Effect of optical input power on coherent forward pass gain, F, of a 5 μm wide guide, as a function of coherent forward pass gain, F, specified for an 0.1 mW optical input power at 824 nm wavelength.

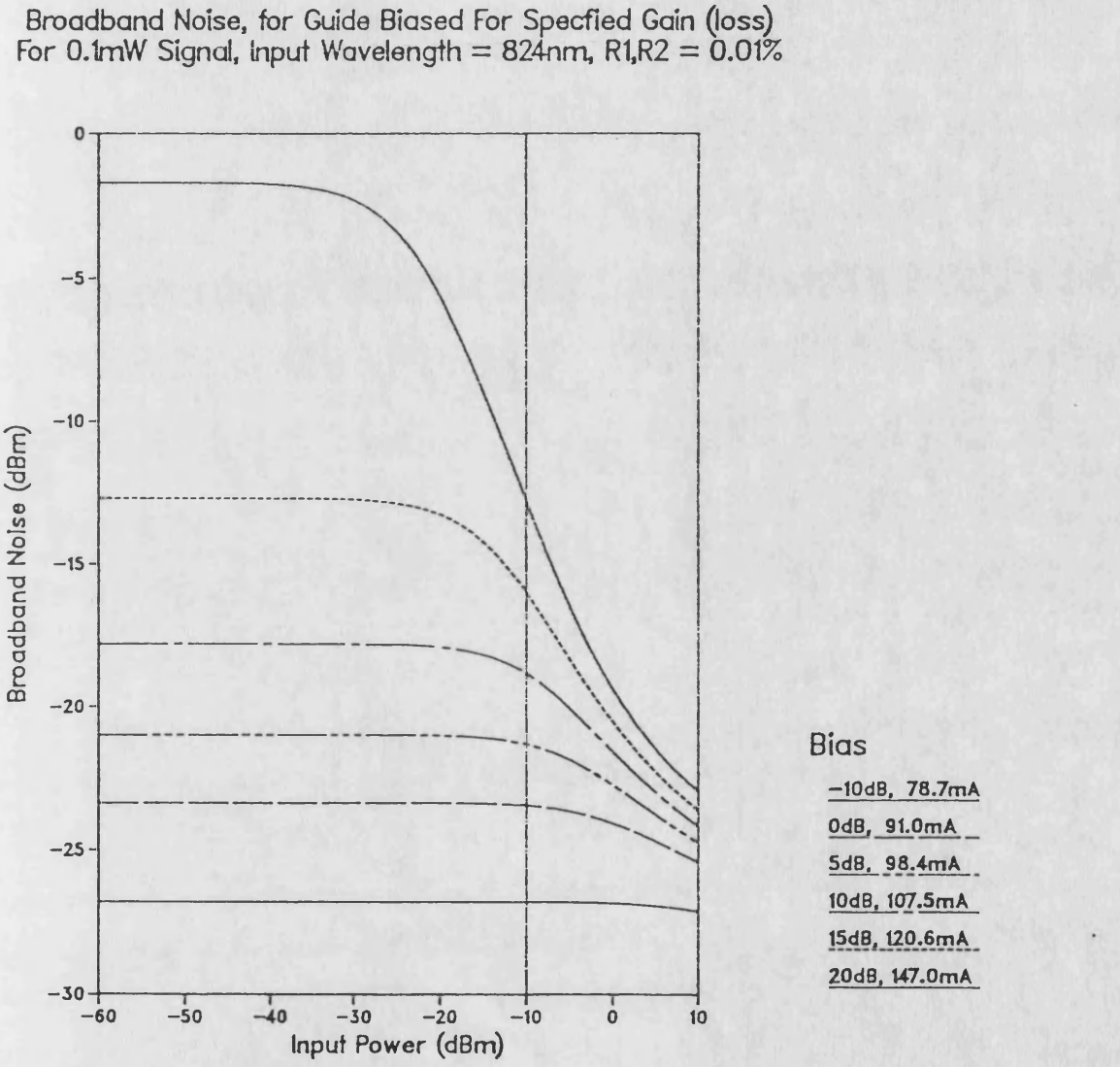

Figure 6.16 : Effect of optical input power on broadband noise output N_{bb}, of a 5 μm wide guide, as a function of coherent forward pass gain, F, specified for an 0.1 mW optical input power at 824 nm wavelength.

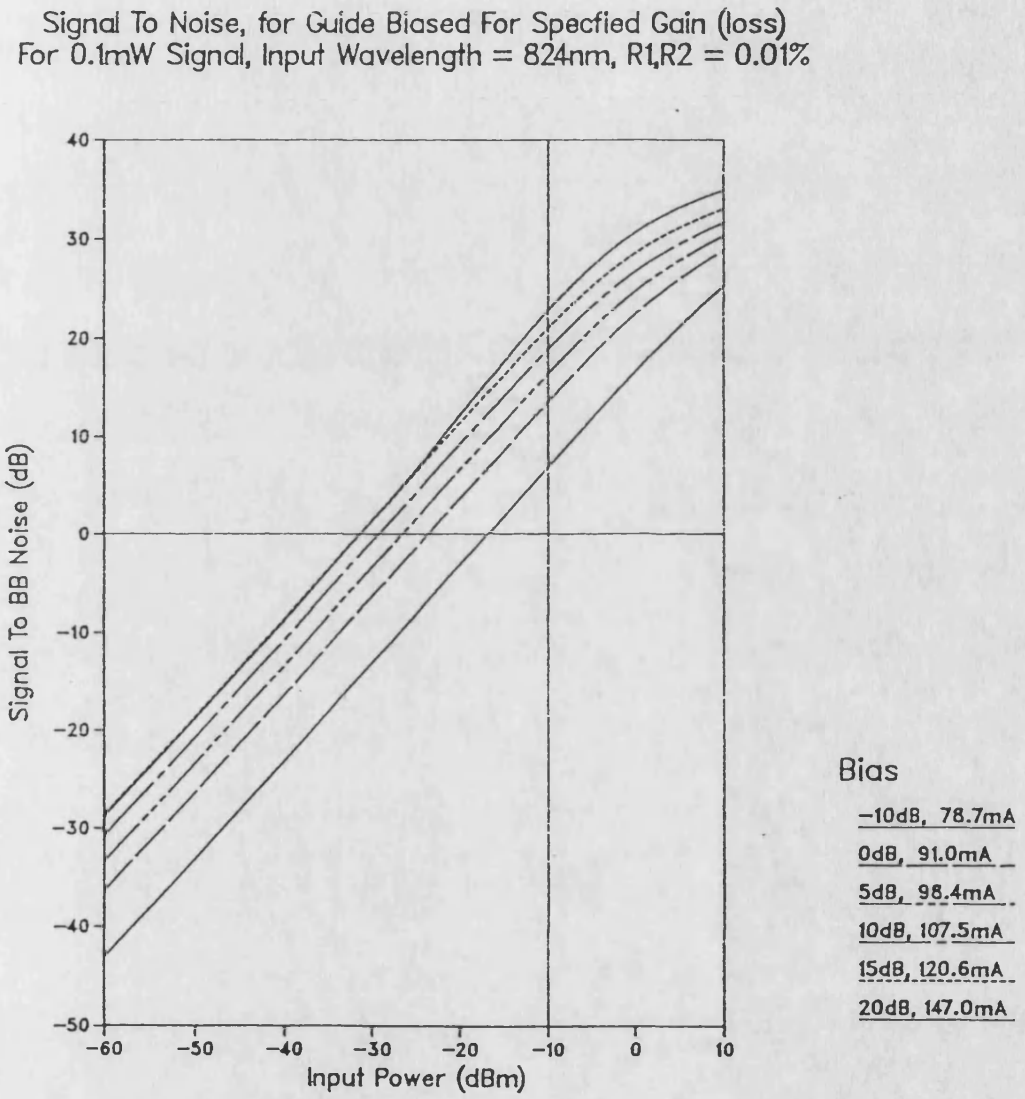

Figure 6.17 : Effect of optical input power on output signal to noise ratio, SNR, of a 5 μm wide guide, as a function of coherent forward pass gain, F, specified for an 0.1 mW optical input power at 824 nm wavelength.

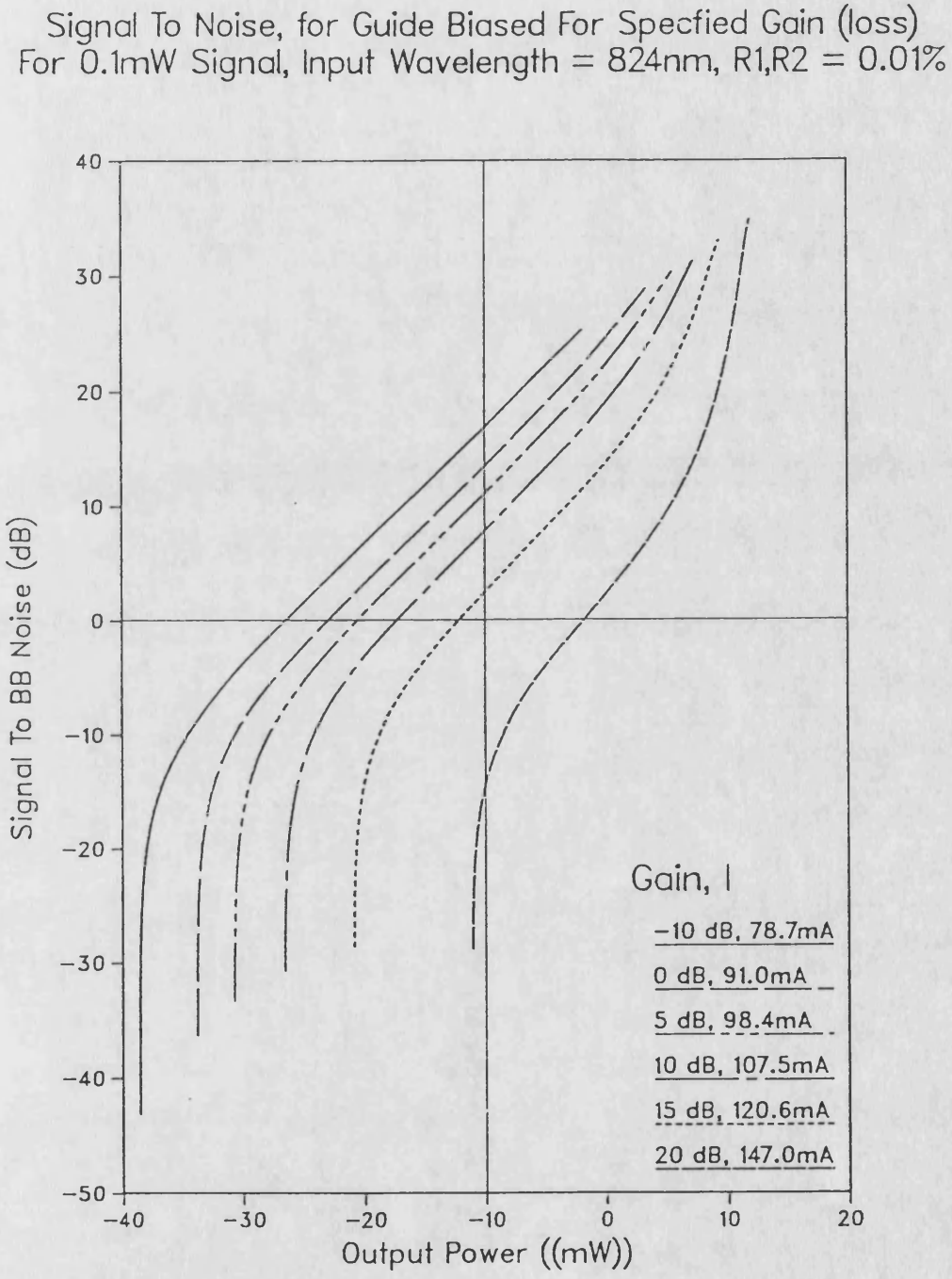

Figure 6.18 : Output signal to noise ratio, SNR, against optical output power for a 5 μm wide guide, as a function of coherent forward pass gain, F, specified for an 0.1 mW optical input power at 824 nm wavelength.

It has been shown in section 6.4.3 and 6.4.4 that the SNR is improved when the input power is increased, simply because the output signal is increased. Figure 6.17 does not clearly show the effect that biasing the guide to have gain has on the SNR. If fig 6.17 is redrawn against total output power, then a different type of characteristic is seen. Figure 6.18 clearly shows the effect of noise washing out the output in the lower third of the graph. As the input power rises, the SNR improves rapidly but the output power remains small. In the central region the SNR varies linearly with output power. However, the best SNR and dynamic range is achieved for the lowest gain. The top portion of the curves show the effect of gain saturation. In the saturation region, there is little change in output power but the SNR continues to rise due to the continued depletion of the carrier density in the active layer.

From this section it is seen that operating the guide at transparency can have some advantages over operation as a TWLA. At transparency a better dynamic range can be achieved with significantly lower output broadband noise. If the guide is pumped to give gain, the higher carrier densities required could lead to power dissipation and heating problems. Perhaps the most obvious reason for avoiding high forward pass gains is that the round trip may become equal to one, causing the guide to lase. This becomes more likely as the length of the guide increases.

6.4.6 Quasi - Static Harmonic Distortion Response

Because the guide has a non-linear static optical input / output characteristic, when a low frequency sinusoidally modulated optical signal is input to the guide :

$$W_{in} = \hat{W}_{in} \cdot \left(1 + m \cos(\omega_m t)\right) \qquad (6.24)$$

distortion of the optical intensity occurs and the detected signal suffers harmonic distortion. There is an upper bound modulation frequency set by the dynamics of the interaction between the carriers and the optical flux, below which the harmonic distortion is independent of modulation frequency. As will be shown in chapters 7 and

8, this upper bound lies in the region of 50 MHz, depending on the parameter values and operating conditions.

6.4.6.1 Estimating Modulation Response

Two method for estimating modulation response were chosen, for the reasons outlined below. In the first method the input / output curve is fitted with a polynomial of the form,

$$W_{out} = A_0 + A_1 \cdot W_{in} + A_2 \cdot W_{in}^2 + A_3 \cdot W_{in}^3 + \ldots + A_n \cdot W_{in}^n \quad (6.25)$$

using a standard least squares curve fitting algorithm. Substituting equation (6.24) into (6.25) yields a harmonic expansion for the output power,

$$W_{out} = B_0 + B_1 \cdot \cos(\omega_m t) + B_2 \cdot \cos(2\omega_m t) + B_3 \cdot \cos(3\omega_m t) + \ldots + B_n \cdot \cos(n\omega_m t) \quad (6.26)$$

Once the coefficients A_0 to A_n have been found it is relatively straight forward to obtain the distortion coefficients B_0 to B_n for a given input power W_{in} and modulation depth, m. When the curves are relatively linear this method is both efficient and accurate. However, as the non-linearity increases the number of polynomial terms required to accurately describe the curve rises dramatically, making this method of estimating the modulation response both inaccurate and unwieldy.

The second method involved generating a pseudo time series by finding the output power corresponding to input powers calculated by incrementing the $\omega_m t$ term in equation (6.24) in equally sized steps over the range 0 - 2π. This requires running the full static model for each discrete value of $\omega_m t$ and hence is quite 'costly' in terms of computing resources (each point can take upto 3 minutes CPU time). A Fast Fourier Transform (FFT) is then applied to the output pseudo time series. The output from the

FFT when suitably normalized are the B coefficients of equation (6.26). The main drawback of the FFT method is that quantization noise is introduced, due to the discritization process. This becomes more significant when the input / output curve is linear. In this case the output becomes a pure sinusoid with a dc bias and the higher harmonics become lost in the quantization noise.

Therefore, for fairly linear input / output curves, at low input powers say, the polynomial fit is preferred for it's speed and freedom from quantization noise. For increasingly non-linear curves the FFT method is preferred for it's accuracy when the polynomial fit method breaks down.

In either case, once the B coefficients in equation (6.26) have been obtained, the harmonic distortion coefficients defined as,

$$D_k = \frac{|B_k|}{|B_1|}, \qquad k = 2,3,4 \ldots,n \tag{6.27}$$

and the total harmonic distortion, THD,

$$THD = \sum_{k=2}^{n} D_k, \tag{6.28}$$

can be calculated. The modulation response, modulation distortion and total harmonic distortion estimated by these two methods are discussed in the next three sections.

6.4.6.2 Modulation Characteristics at 824nm

In an AIO system, the wavelength of interest will be the lasing wavelength of the integrated source. The results from chapter 5 suggest that this will be in the region 820 to 825nm. The quasi-static modulation estimates are therefore made at this wavelength. Figures 6.19 - 6.21 detail both the modulation response (a) and modulation distortion (b) calculated from equations (6.26) and (6.27) respectively, for

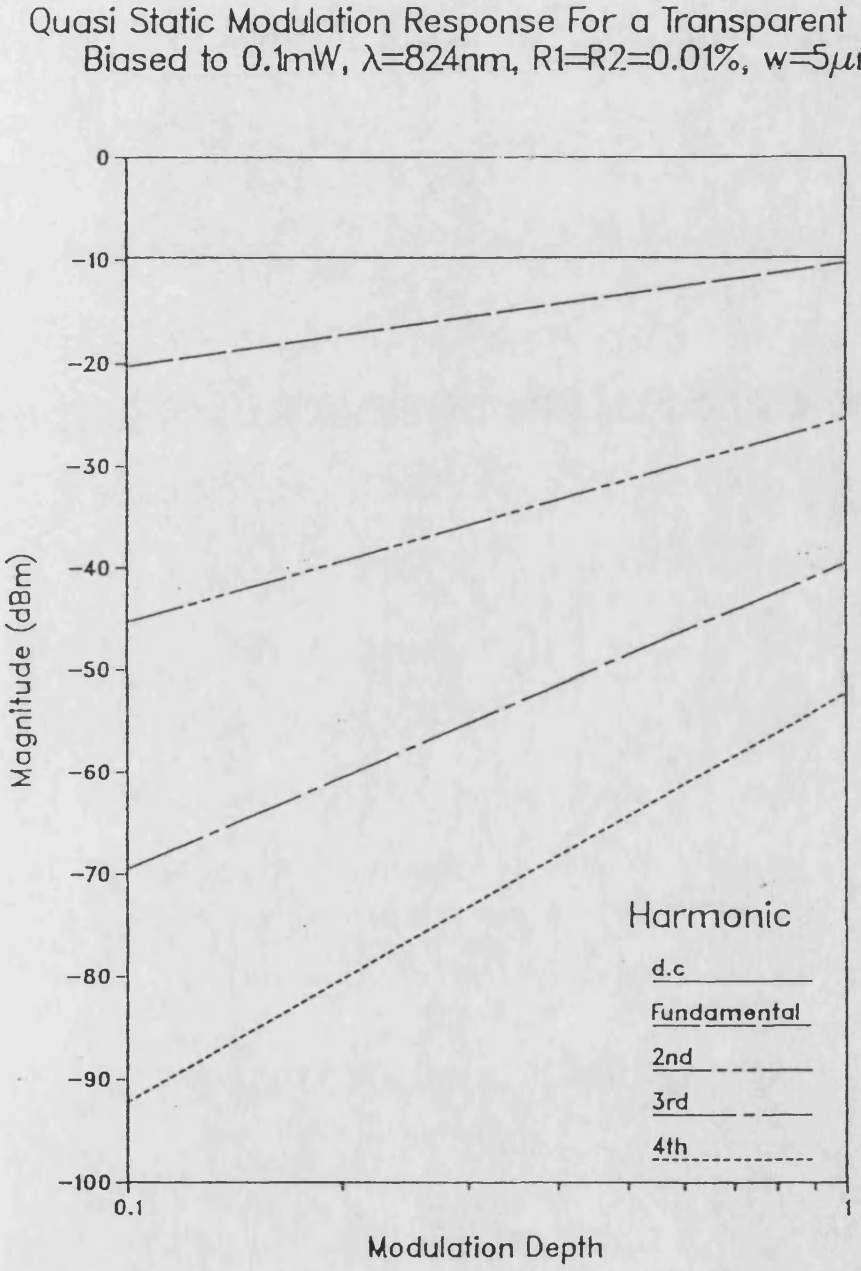

Figure 6.19 a Quasi-static modulation response for a guide biased to transparency, for an optical input power of 0.1 mW at 824 nm wavelength. (a) Modulation response,

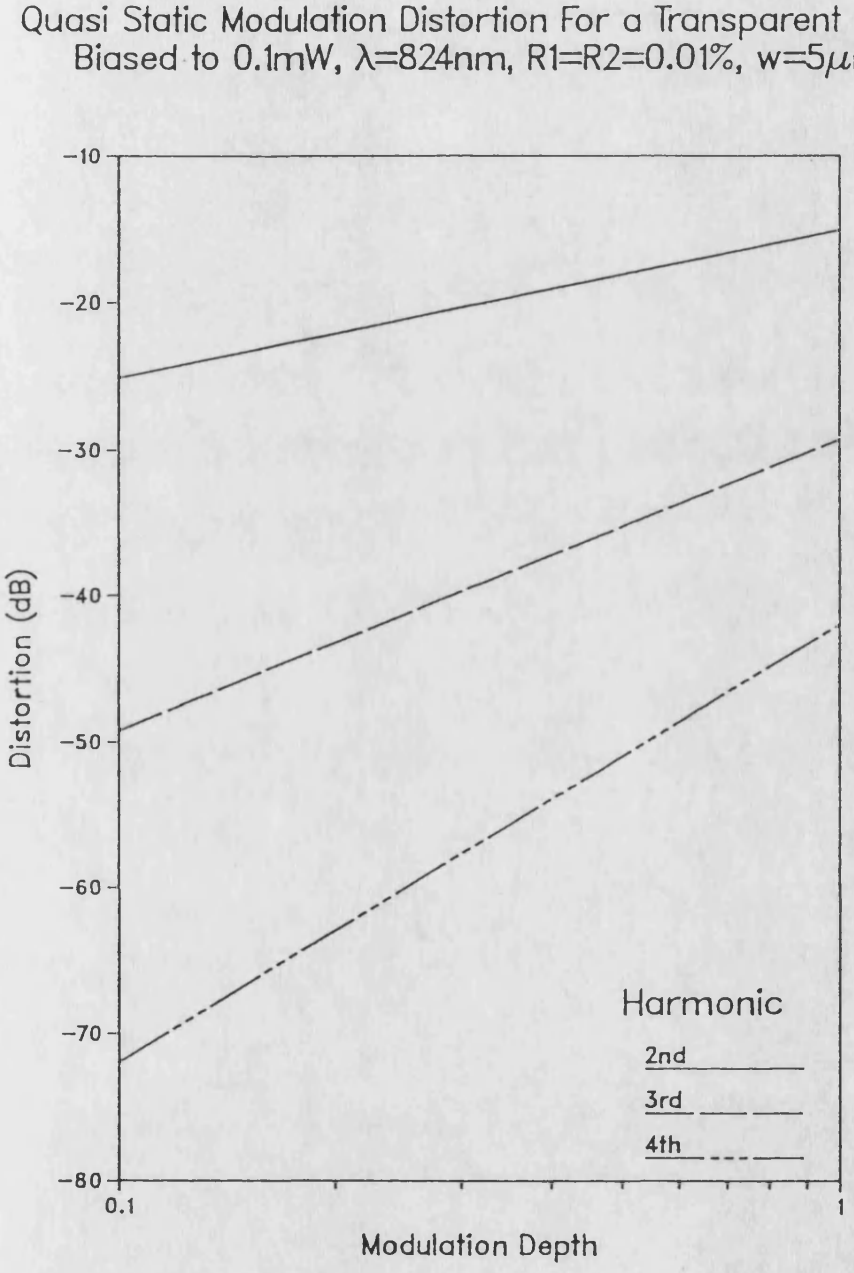

Figure 6.19 b Quasi-static modulation response for a guide biased to transparency, for an optical input power of 0.1 mW at 824 nm wavelength. (b) Harmonic distortion.

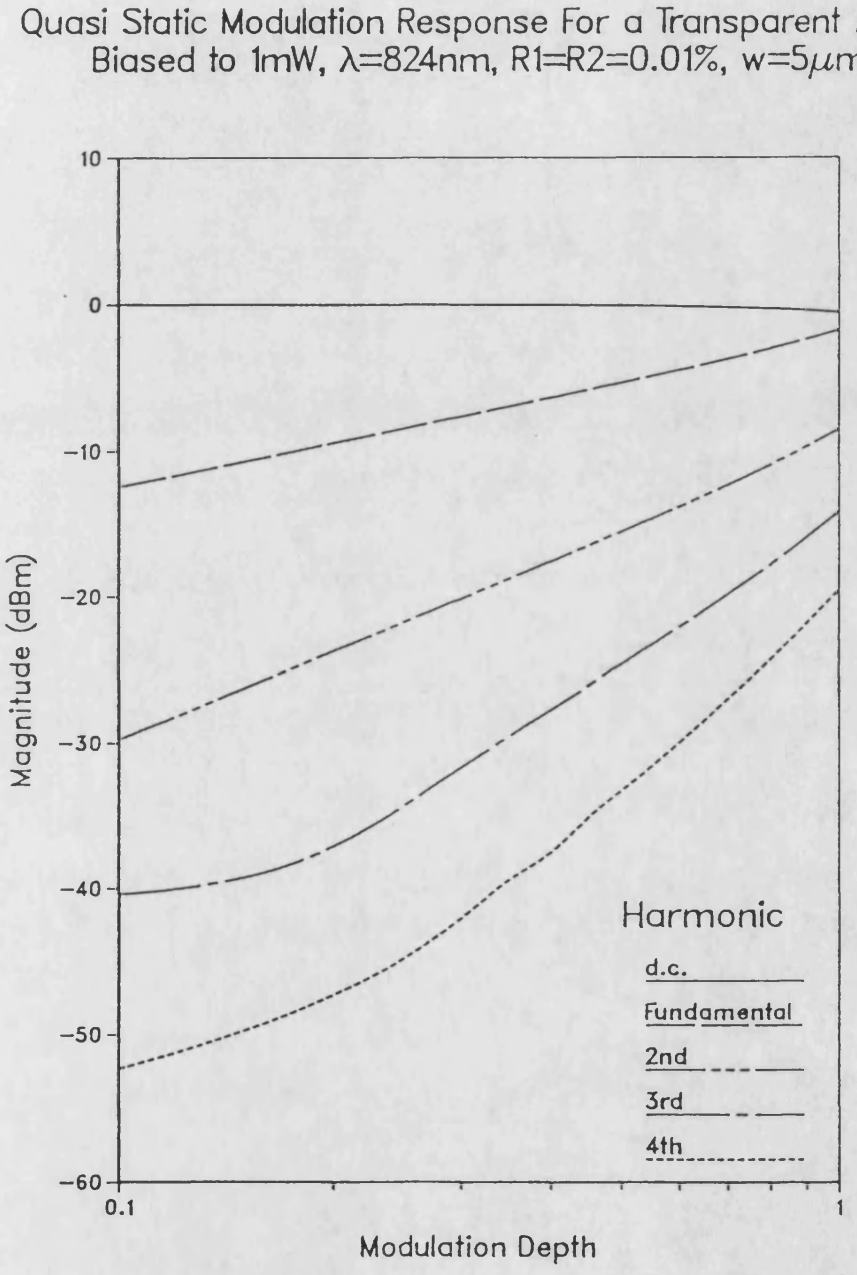

Figure 6.20*a* Quasi-static modulation response for a guide biased to transparency, for an optical input power of 1 mW at 824 nm wavelength. (a) Modulation response,

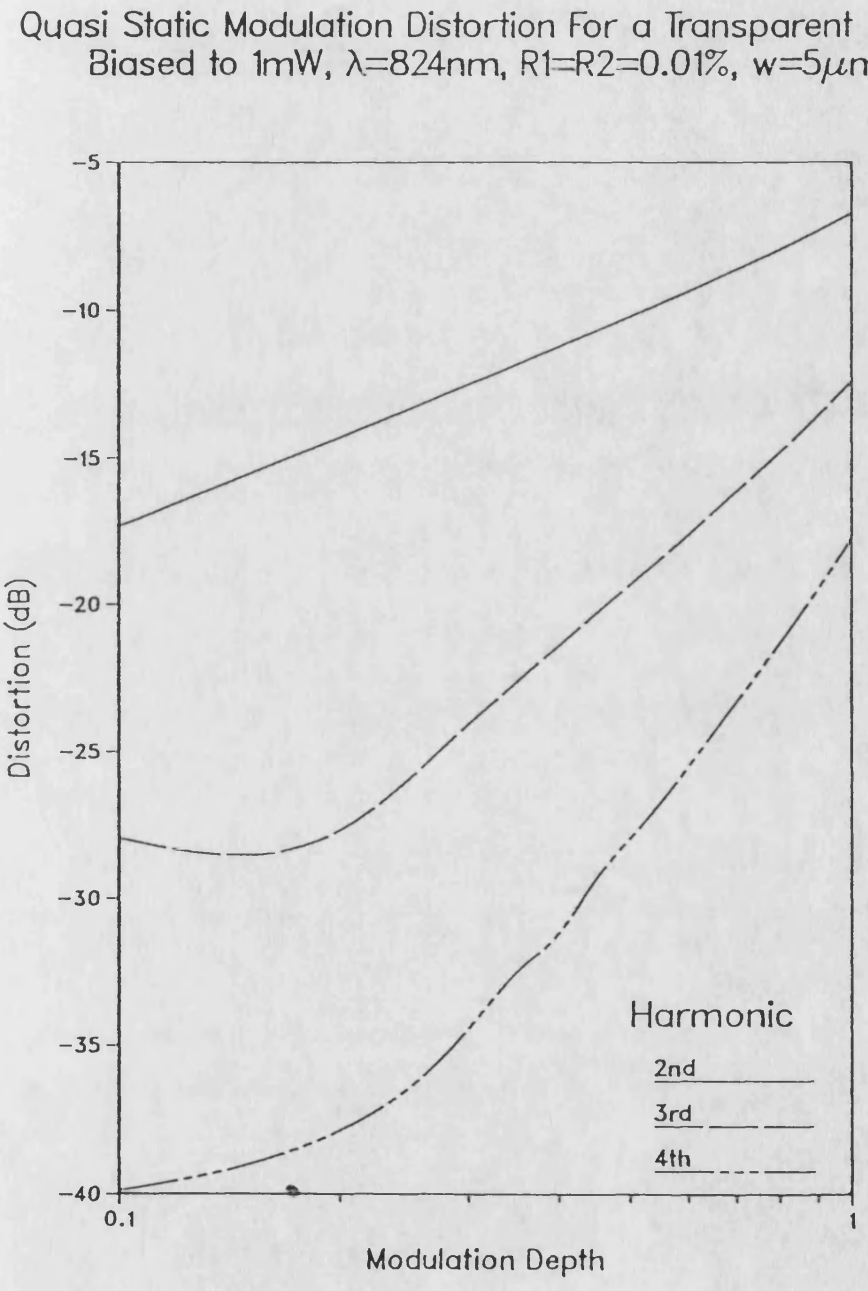

Figure 6.20 (a) Quasi-static modulation response for a guide biased to transparency, for an optical input power of 1 mW at 824 nm wavelength. (b) Harmonic distortion.

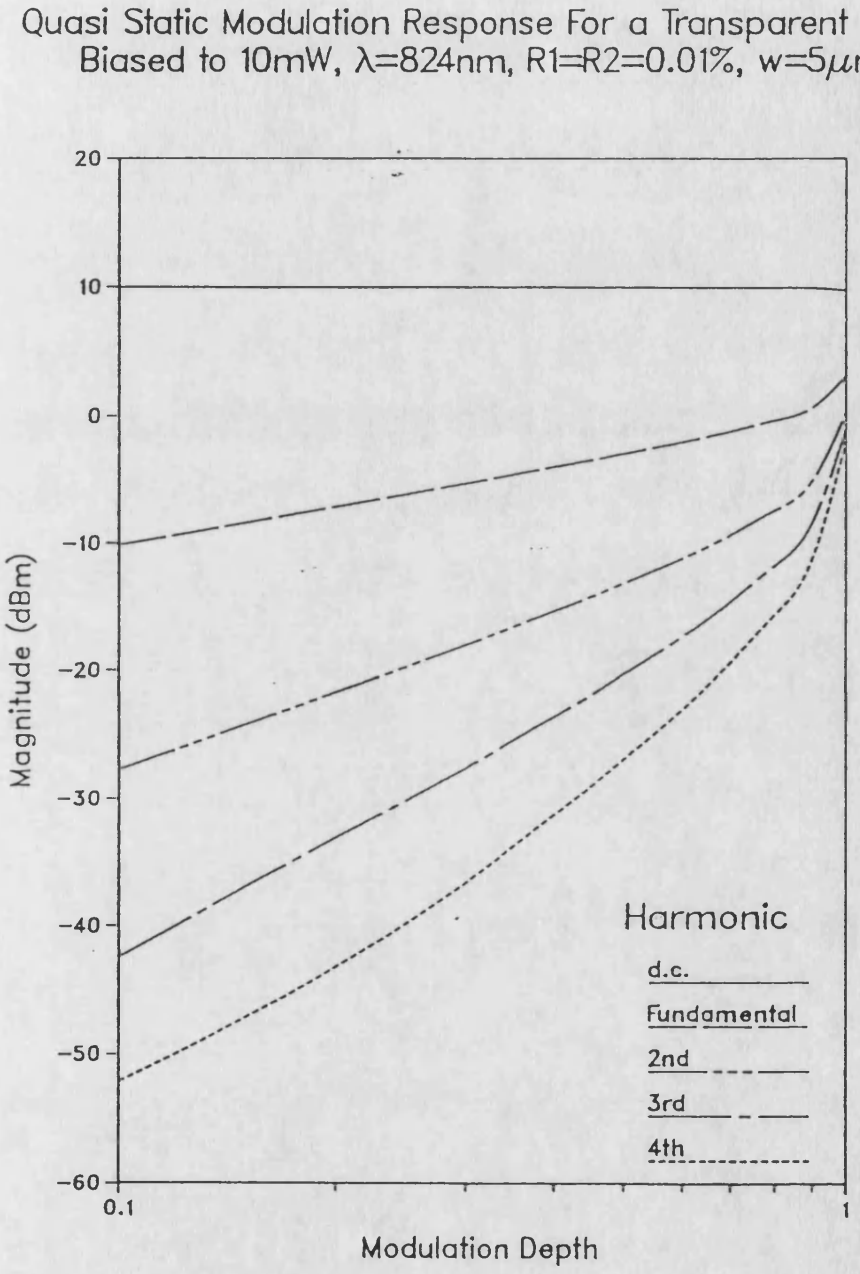

Figure 6.21 a Quasi-static modulation response for a guide biased to transparency, for an optical input power of 10 mW at 824 nm wavelength. (a) Modulation response,

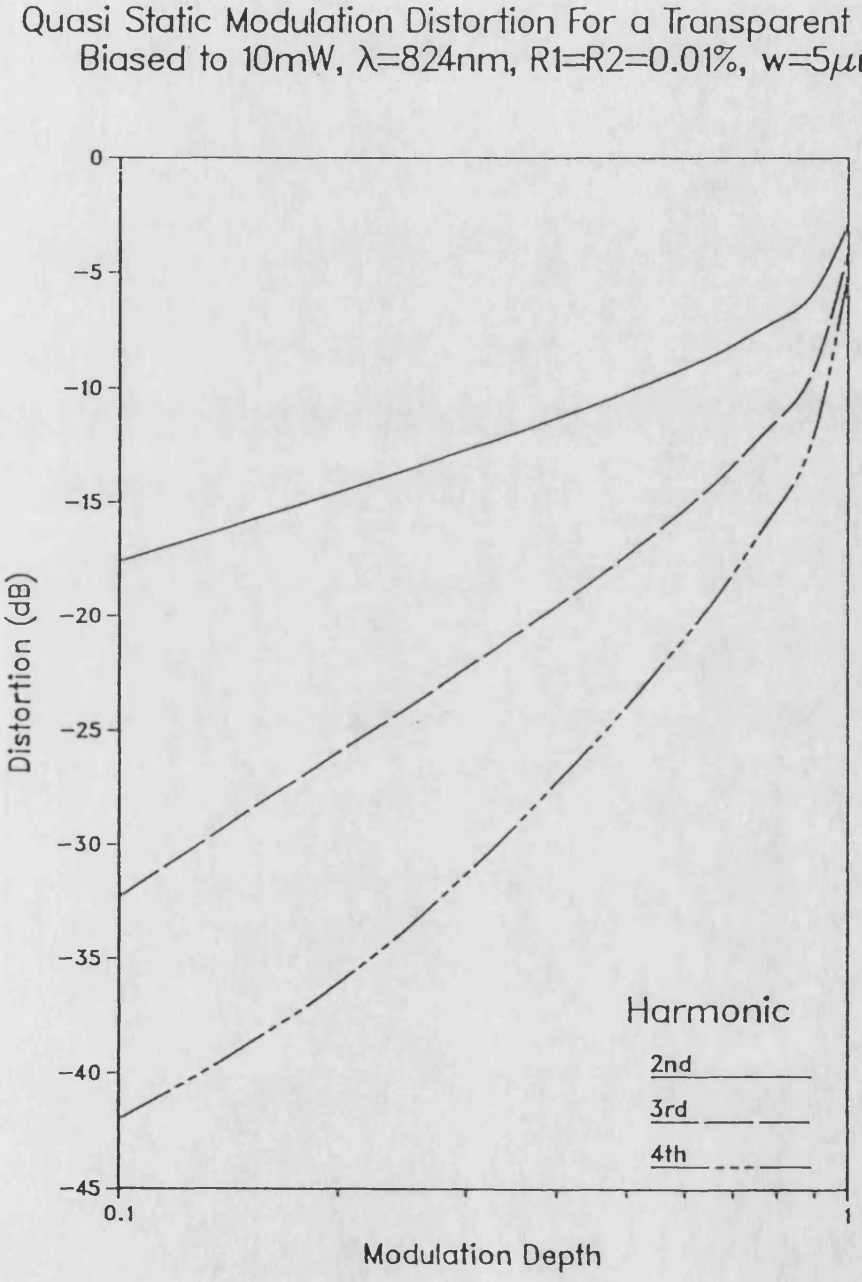

Figure 6.21 b Quasi-static modulation response for a guide biased to transparency, for an optical input power of 10 mW at 824 nm wavelength. (b) Harmonic distortion.

optical input bias powers of 0.1, 1 and 10mW . These powers represent a low, moderate and high input flux for this guide geometry.

For a low input flux, the stimulated recombination is negligible and hence the guide characteristics will be relatively linear. This is clearly shown in figures 6.19(a) and 6.19(b). The DC component in the modulation response corresponds to the optical bias level whilst the fundamental corresponds to the input modulation. As the figures are plotted on a log / log, the linear characteristics indicate some power law relationship between the modulation index (m) and the relative and actual magnitude of the higher harmonics. In this case the harmonic power is seen to be proportional to m^n where n is the harmonic index, as shown in figs 6.19 - 6.21. Whilst the harmonic distortion is proportional to m^{n-1}. The nature of this dependency will be examined in chapter 8.

When the guide is pumped to transparency for a low input flux, the magnitude of the fundamental component is equal to the input modulation, $m \cdot \hat{W}_{in}$. However, for input powers of 1 and 10mW (figs 6.20(a) and 6.20(b)), this is no longer the case, as the gain saturation reduces the fundamental output power from the expect value. For the moderate case this compression is approximately -3dB, rising to ≈ -10dB for the high input power case.

For the 1mW case the harmonic powers follow roughly the same relationship to the modulation index as for the 0.1mW case. This would indicate that the gain compression is similar across the modulation range. For the 10mW case, the relationship no longer holds and the higher harmonics become increasing significant. In addition, the dc component of the output signal is seen to drop below the bias level.

6.4.6.3 Total Harmonic Distortion at 824nm

Figure 6.22 shows the THD for the three case considered in the previous sub-section, and an additional case when the input bias power is 5mW . It must be remembered that each characteristic in this figure has a different drive current and bias level, and that the base variable is modulation index and not modulation power (ie the

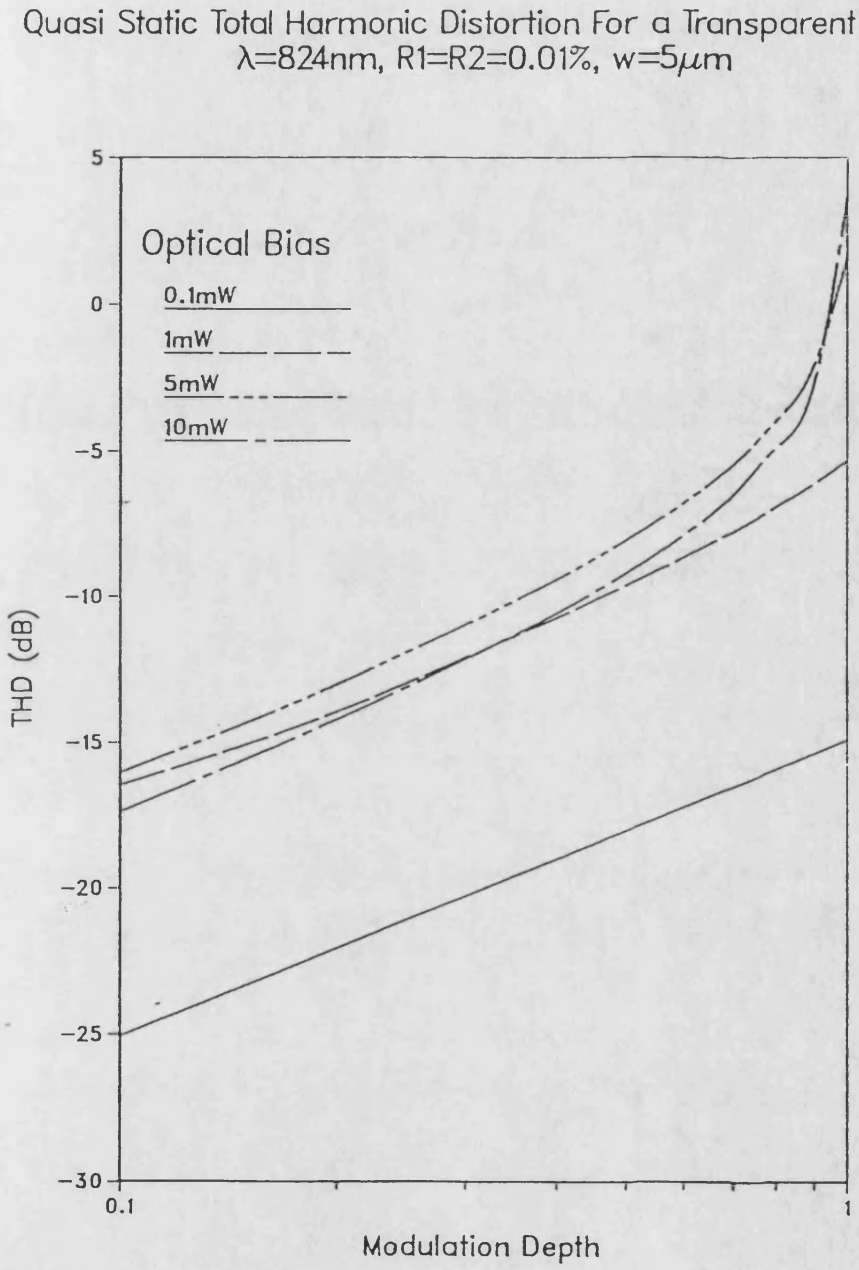

Figure 6.22 : Effect of modulation depth and optical input bias power on total harmonic distortion at 824 nm wavelength.

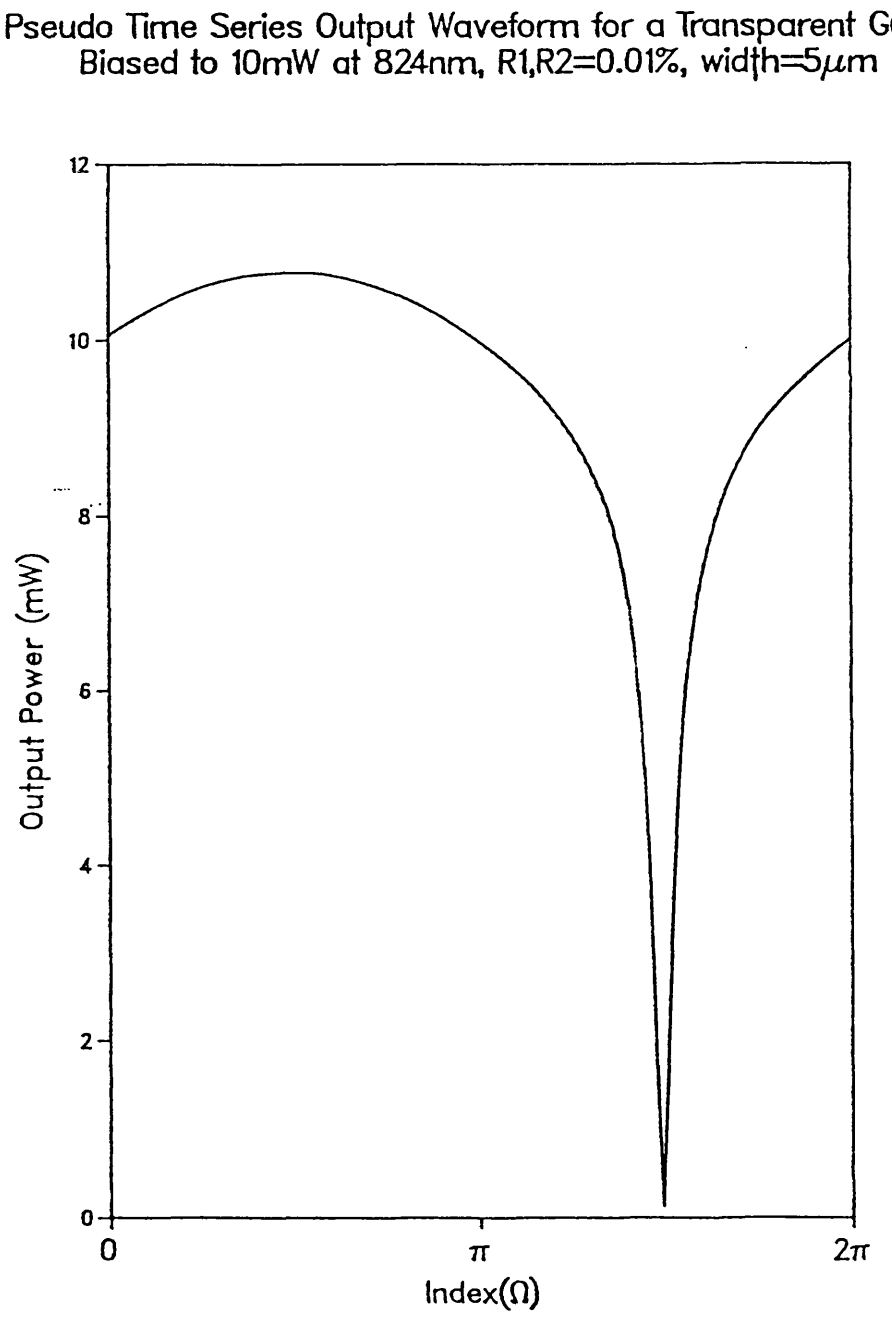

Figure 6.23 : Pseudo - time series output waveform, for a guide transparent to an optical bias power of 10 mW at 824 nm wavelength (100% modulation).

peak to peak swing is 0.2 mW for a 0.1 mW bias and 20 mW for a 10 mW bias, when the modulation index is 1.0).

As would be expected the lowest THD is achieved in the most linear input / output case, when the bias power is 0.1 mW. Referring back to fig 6.19(b) shows that this THD is dominated by the 2nd harmonic distortion. At successively higher biases the situation is not so straight forward. For a modulation index of 0.1 - 0.4, the THD for 10 mW bias is lower than that for both 1 mW and 5 mW. It is only when the modulation index approaches 1 that the THD increases with increasing bias.

If the input / output curves in section 6.4.3.1 are examined for high biases, it is clear that the characteristics no longer resemble smooth curves but rather two almost linear regions joined at a 'knee'. When the modulation index is small the input is restricted to one linear region and the THD is reduced, despite the gain compression effect. If the input modulation is pushed beyond the knee, the output waveform will be perturbed from the expected sinusoidal form. The most extreme case for a 10 mW optical input bias and a modulation index of 1 is shown in figure 6.23. Here the output is seen to be spiked, such spikes lead to many significant higher harmonics, hence the rapid increase in THD. Indeed in this extreme case more power is present in the harmonics than the fundamental (THD > 0).

6.4.6.4 Variation of THD with Wavelength

An estimation of the quasi-static modulation response for different input wavelengths was also obtained. It is not necessary to reproduce the complete set of modulation response and distortion graphs as they will be very similar to those presented in section 6.4.6.2. The results can be summarized by the compression due to gain saturation as shown in table 6.4 and the total harmonic distortion, figures 6.24 - 6.26.

It is seen from table 6.4 that the gain compression increases with optical bias power and decreasing wavelength. This is because the interaction between the optical flux and carrier density is lowest for the longer wavelengths. As the interaction

decreases then so does the THD, as shown in figures 6.24 and 6.25, where the general trend is for the THD to decrease in line with the gain compression term.

Bias Power	0.1 mW		1 mW		10 mW	
Modulation Index	0.1	1.0	0.1	1.0	0.1	1.0
λ = 820nm	1	0.5	3	1.5	11	7
λ = 824nm	1	0.5	2.5	1	10	7
λ = 830nm	≈0	≈0	2	1	8.5	5
λ = 840nm	≈0	≈0	1	0.5	5	3

Table 6.4 Compression of fundamental output component (dB).

In figure 6.26 the effect of extreme gain compression is again apparent, the trend is reversed and the THD increases with wavelength for modulation indices less than 0.8. For high modulation the THD is seen to rise steeply to above 0 dB for wavelengths in the range 820 - 830nm, whilst the response at 840nm continues to rise smoothly. (Note, in fig 6.26 the characteristics for 820 and 824nm coincide).

6.4.7 Model Verification

The model can be verified in two ways, by comparison with other models and by investigating the assumptions of the guide and its behaviour. As was stated in the introduction, the model presented here is based on that developed by Perkins et al [5], where the model is verified in detail. In the context of an AIOW it is possible to compare the results of the model presented here and those for TWLAs. In order to do this it is necessary to modify the gain and spontaneous emission terms to fit in with the comparison model. To compare the model with that of Adams in [8] the following modifications are necessary :

- The gain and spontaneous emission wavelength dependence is removed.
- The gross optical gain is approximated to, $g(N) = a(N - N_0)$.
- The total spontaneous emission term, $B_r N(N+p_0)$ is replaced by N/τ_{sp}.
- The waveguide parameters are altered to those in [8], (table 6.5).

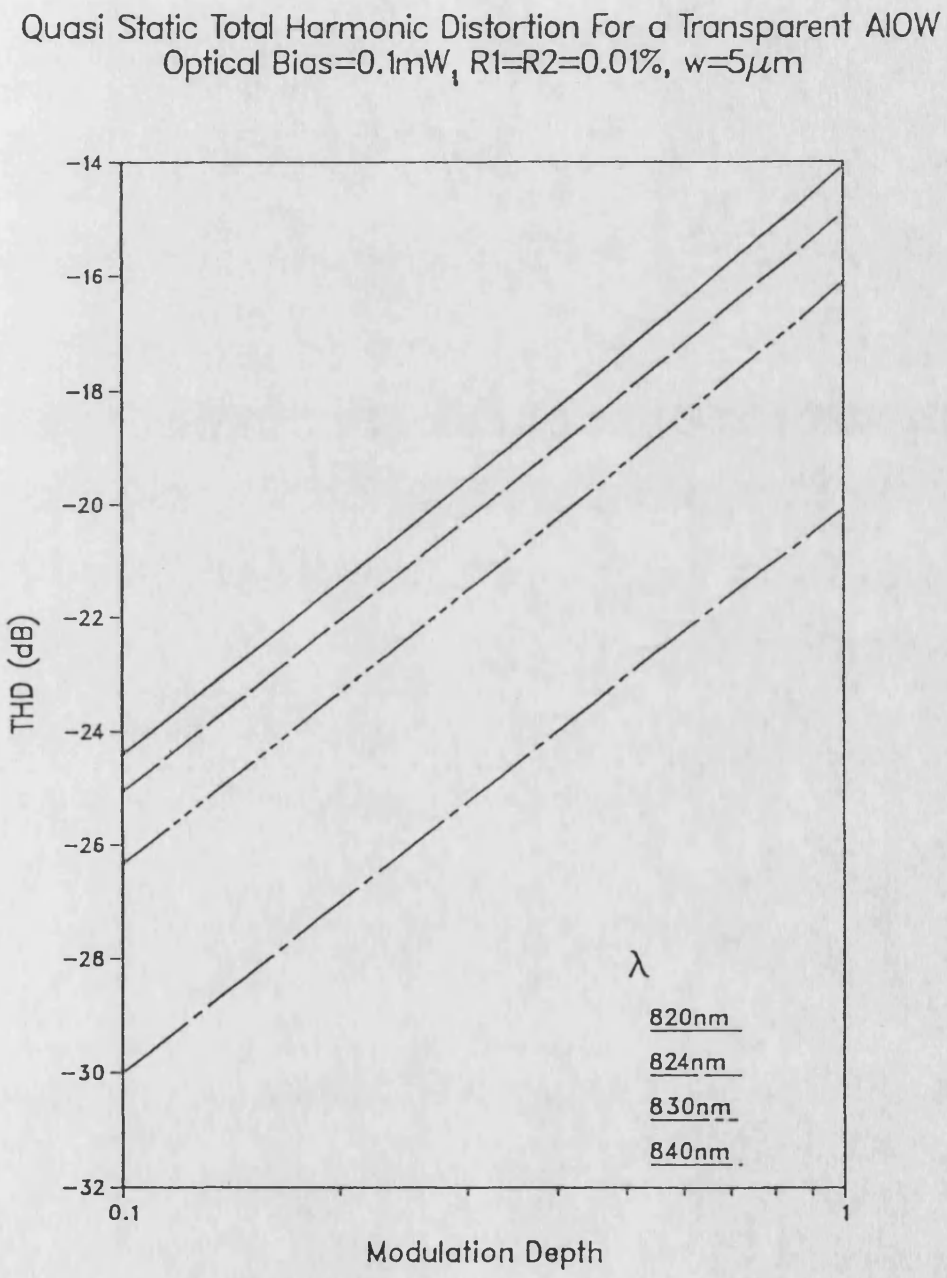

Figure 6.24 : Effect of modulation depth on total harmonic distortion as a function of wavelength, for a guide transparent to an optical bias power of 0.1 mW at 824 nm wavelength.

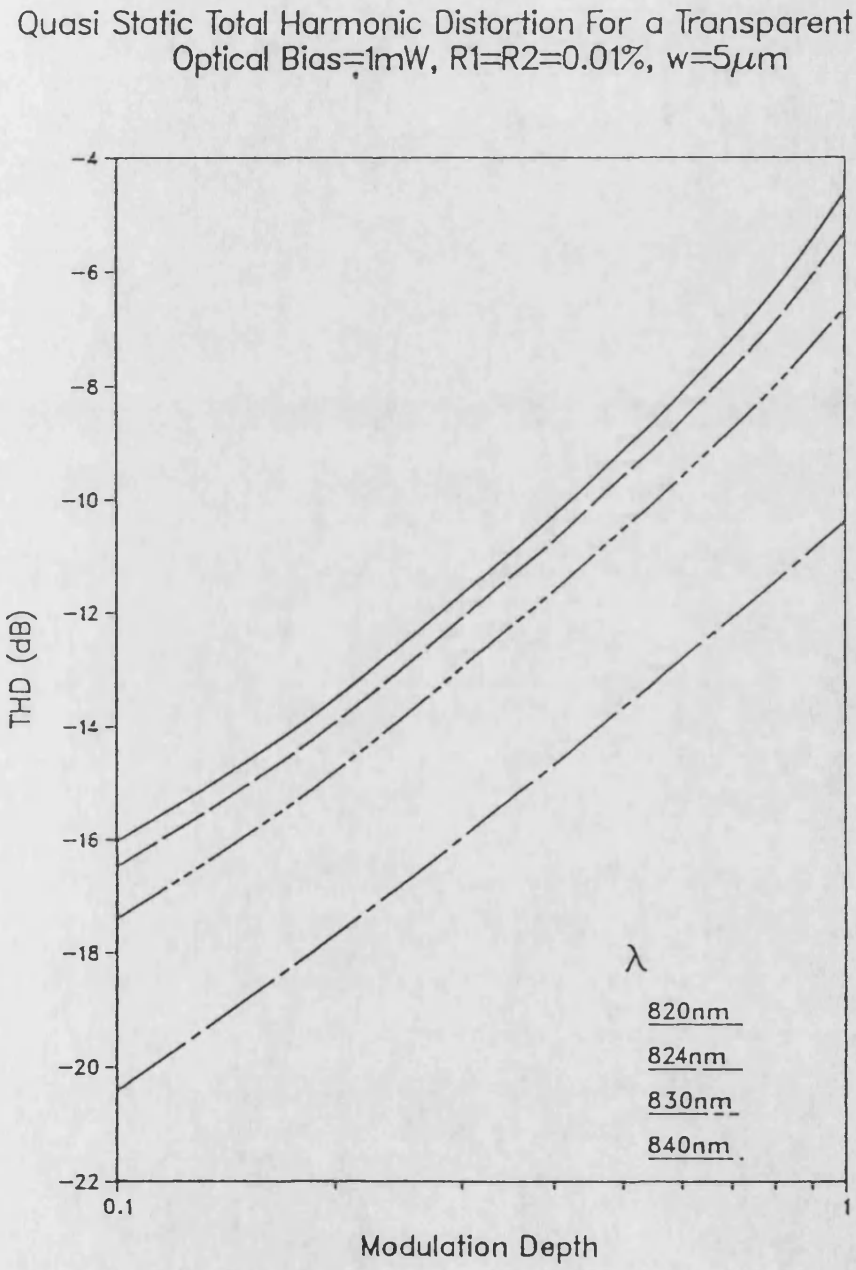

Figure 6.25 : Effect of modulation depth on total harmonic distortion as a function of wavelength, for a guide transparent to an optical bias power of 1 mW at 824 nm wavelength.

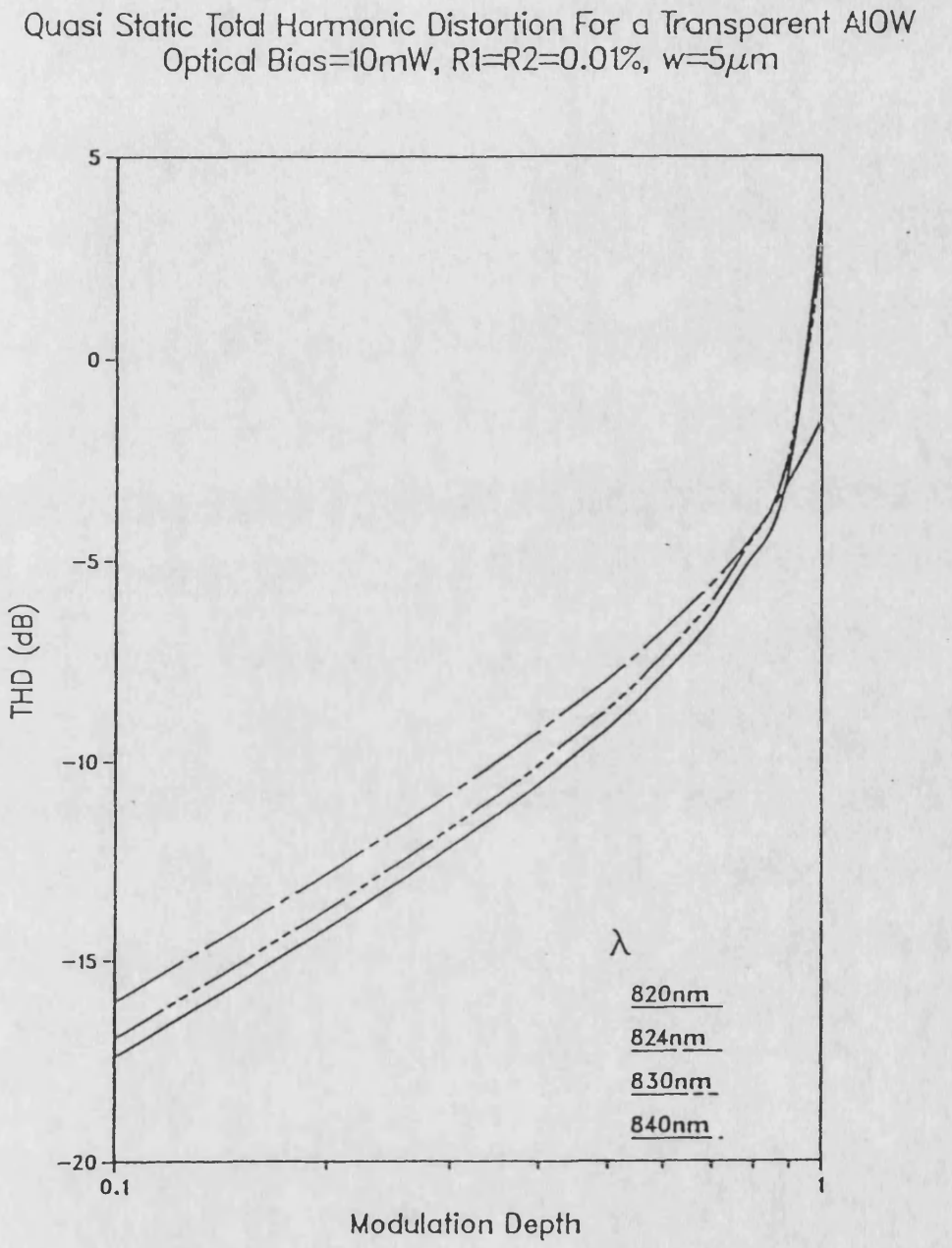

Figure 6.26 : Effect of modulation depth on total harmonic distortion as a function of wavelength, for a guide transparent to an optical bias power of 10 mW at 824 nm wavelength.

τ_{sp}	4 ns
Γ	0.5
a	5×10^{-16} cm^{-2}
N_o	10^{18} cm^{-3}
L	200 μm
d	0.2 μm
w	1.5 μm
λ	1.47 μm

Table 6.5, Material Parameters (after Adams [8]).

However, the basic algorithm and the numerical solution techniques remain unchanged. When these adjustments are made the results of the model, shown in figure 6.27, agree very closely with those presented in figure 1 of [8], thus confirming the operation of the modelling technique. Figure 6.27 shows the results when the carrier density is assumed to be constant over the entire length of the TWLA. As the length of the region of assumed constant carrier density is reduced, the characteristics are seen to move away from those generated from Adams' model, especially for high forward pass gain and input power.

The change of characteristic with region length is shown most graphically for the case of the input / output curves in figure 6.28. In this case the non-linearity in the guide is maximised by biasing a 1 μm wide guide to transparency for a 10 mW optical input power, at a wavelength of 824 nm. It is clear that in this highly non-linear case, a region length of 10 μm is adequate and for the majority of situations a higher region length will yield sufficiently accurate results.

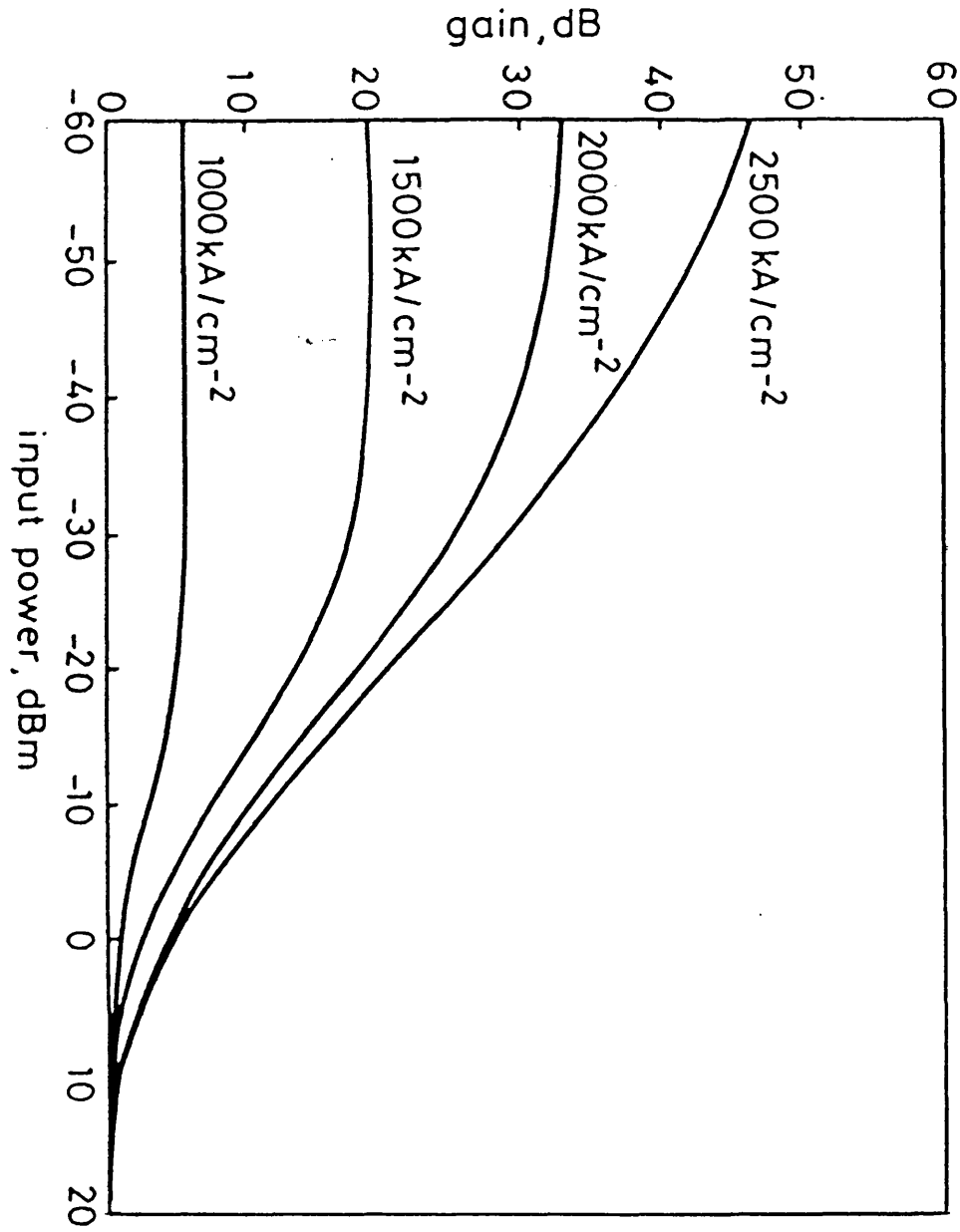

Figure 6.27 : Variation of gain of a TWLA / guide, as a function of optical input power and injection current density, when the model is modified to behave as a spatially averaged flux model, for comparison with results reported in references 8 and 9.

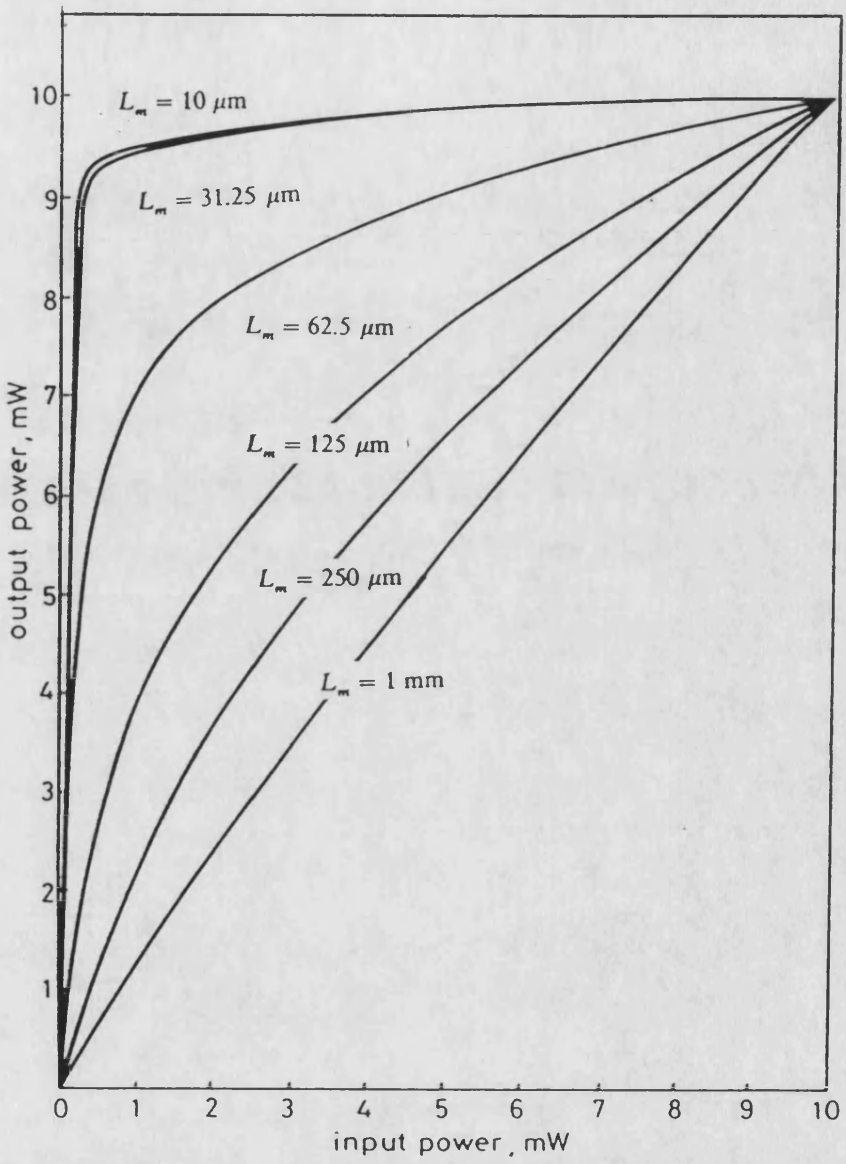

Figure 6.28 : Effect of segment length on non-linearity of input / output characteristics of a 1 μm wide waveguide, biased to transparency at an optical input power of 10 mW at 824 nm wavelength.

6.5 Conclusions

A model has been developed to predict the steady state and longitudinal behaviour of a pumped GaAs/AlGaAs waveguide with an arbitrary length and low end facet reflectances. The behaviour and stability of the model has been verified both for the case of a pumped waveguide and in comparison to a TWLA. It has been shown that the current required to pump the guide to transparency varies with both optical input power and wavelength. For simple applications the current required for a 1mm guide is not excessive in relation to the threshold current of a typical laser made from the same material.

The necessity of including the spontaneous emission term in the flux continuity equations is demonstrated by the examination of the noise output from the guide and the comparison of an AIOW pumped to transparency with a TWLA. In the former, the output noise spectrum is seen to be quite broadband resulting from the amplification of the spontaneous emission (ASE) in the guide. The output noise power is greatest when there is no optical input. This highlights the main disadvantages of the pumped guide, not only is it noisy but it also draws power from the electrical pumping source when there is no optical input. When compared to a TWLA, it is seen that the output noise is quite significant and has the effect of drowning the static output signal.

The output SNR has been found to be dependent upon the optical power at which the guide is transparent as well as the actual optical input power and wavelength, due to the effect of gain saturation. Furthermore the output SNR is particularly dependent upon the guide width. For a 1 μm guide biased to a 1 mW optical input, the output SNR saturates to ≈40 dB which for many systems applications should be adequate. The SNR can be further improved by increasing the transparency optical bias power to 5 mW or more.

The penalty of using a narrow guide width is a significantly worse non-linear optical input / output characteristic which gives rise the distortion of any input signal. The non-linearity is found to be dependent on the transparency bias power, the actual

optical input power and the source wavelength. In the extreme case the characteristic can be approximated to two linear regions joined at a knee. For a modulated input this gives rise to lower distortion, but a compressed output signal.

The harmonic distortion for low frequency sinusoidal modulation can be very large, especially for large modulation depths and high optical biases. In the extreme case, the total output harmonic power can exceed that of the fundamental. In many cases this may be the most significant factor in the design of an active waveguide. However, for a digital system the gain compression features may be more important than the modulation distortion. To the author's knowledge the method of quasi-static estimation of modulation response has not been presented elsewhere. The range of validity of such a method must be established but does allow an estimation of dynamic performance of the guide using a steady state model.

References, Chapter 6.

1. HASUO, S., and OHMI, T. 'Spatial distribution of the light intensity in the injection laser',

Japan J. of Appl Phys., 1974, 13, (9), pp1429-1434.

2. SHORE, K.A., 'Model for laser structures incorporating longitudinal and transverse variations',

IEE Proc. Part J, 1985, 132,(1), pp52-57.

3. MARCUSE, D., and NASH, F.R., 'Computer model of an injection laser with asymmetrical gain distribution',

IEEE J. Quantum Electron, 1982, QE-18,(1),pp30-43.

4. AGRAWAL, G.P., 'Fast Fourier transform based beam-propagation model for stripe geometry semiconductor lasers : inclusion of axial effects',

J. Appl. Phys., 1984, 56, (11), pp3100-3109.

5. PERKINS, M.C.J., ORMONDROYD, R.F., and ROZZI, T.E., 'Analysis of absorptive bistability characteristics of multi-segment lasers',

IEE Proc. Part J, 1986, 133,(4), pp283-292.

6. MARCUSE, D., 'Computer model of an injection laser amplifier',

IEEE J. Quantum Electron, 1983, QE-19,(1),pp63-73.

7 OTSUKA, K. and IWAMURA, S., 'Analysis of a multistable semiconductor light amplifier',

IEEE J. Quantum Electron, 1983, QE-19, (7),pp1184-1186.

8. ADAMS, M.J., COLLINS, J.V. and HENNINGS, I.D., 'Analysis of semiconductor laser optical amplifiers',

IEE Proc. Part J, 1985, 132, (1), pp58-63.

9. SIMON, J.C., 'Semiconductor laser amplifier for single mode optical fibre communications',

J. Opt. Commun, 1983, 4, (1), pp51-62.

10. MUKAI, T. and YAMAMOTO, Y., 'Gain, frequency bandwidth, and saturation output power of AlGaAs DH laser amplifiers',
*IEEE J. Quantum Electron, 1981, **QE-17**, (6), pp1028-1034.*

7 SMALL SIGNAL DYNAMIC MODEL

7.1 Introduction

The small signal analysis (SSA) technique has been used by several authors to estimate the frequency response of Lasers [1,2,3] and SLEDs [4,5] and TWLAs [6]. In the majority of cases, the analysis is directed towards determining the optical output in response to the modulation of the device drive current [1-5]. For the AIOW the drive current is held constant and the input optical signal is modulated, either directly in the laser source or using a specific modulating element. An analysis is therefore required of how the waveguide modifies the input optical signal.

In the previous chapter a quasi-static analysis was presented as an estimation of the low frequency guide performance. However, the method used gives no indication of when this estimate becomes invalid. This small signal analysis will show when the frequency is low enough for the quasi-static analysis to hold, and give an indication of the (optical input modulation) frequency response of the guide.

In addition, the SSA gives a good feel for the underlying dynamic behaviour of the carrier and flux densities. As will be seen in the next chapter, the full large signal dynamic model does not make the underlying guide behaviour apparent and the small signal expressions are essential for a complete understanding.

In common with other analyses of the rate equations, most authors assume that the spatially averaged quantities can be used. As was discussed in chapters 5 and 6 these can only be used for low frequencies (compared with the photon lifetime or cavity transit time) and low gains, and are not appropriate to the case of an AIOW. In order to model the AIOW a small signal analysis of the travelling flux equations is developed, in a similar manner to those presented by Boeck, et al [4] for SLEDs and Lau and Yariv[5] for SLEDs and lasers. The resulting equations are markedly different from [4] and [5] as they consider the performance of the guide when the optical rather than the electrical input is modulated.

In the SSA technique, the temporal behaviour of the device is examined by considering small time varying perturbations in optical input power about a fixed bias value. In the absence of a time varying input the waveguide characteristics are determined by the bias level, and the solution can be obtained using a modified version of the steady state model presented in chapter 6. The effect of introducing a time varying perturbation in the optical input power is to introduce deviations in the guide quantities of a correspondingly small size. If the deviations in guide quantities are sufficiently small when compared with the bias quantities, the guide parameters are assumed to vary linearly about the steady state bias point. The variation of the small signal quantities can then be (mathematically) separated from the bias quantities, and relatively simple solutions to the time varying behaviour can be obtained.

7.2 Manipulation of the Travelling Wave Rate Equations

7.2.1 Wavelength Independent Rate Equations

Although a SSA may be performed for each wavelength slot in the spectral dimension, such a set of expressions would be quite difficult to manipulate and would not further the understanding of the underlying principles. Thus, the rate equations are reduced to consider one wavelength only. Essentially, this may be imagined as approximating the optical gain and spontaneous emission spectra by a single wavelength slot, centred at the source wavelength, λ_k. Using this method it is possible to select the source wavelength and the gain polynomial associated with that wavelength from the gain spectra. The spontaneous emission, on the other hand is described by the total spontaneous emission rate, given in chapter 4 as,

$$R_{sp} = B_r N\cdot (N + p_o) = \int_0^{+\infty} S(\lambda).d\lambda \ . \qquad (7.1)$$

The forward and backward travelling fluxes in the guide are now described by the two equations,

$$\frac{1}{v}\frac{\partial P}{\partial t} + \frac{\partial P}{\partial z} = G.P + \delta B_r N\cdot (N + p_o) \qquad (7.2)$$

$$\frac{1}{v}\frac{\partial Q}{\partial t} - \frac{\partial Q}{\partial z} = G.Q + \delta B_r N\cdot (N + p_o) \qquad (7.3)$$

and the carrier density at any point in z (ignoring carrier diffusion) is,

$$\frac{dN}{dt} = \frac{J}{e.d} - B_r N\cdot (N + p_o) - g\cdot (P + Q) \qquad (7.4)$$

Note that the simulated recombination term in (7.4) is no longer a summation but a single expression, as all the flux in the guide is centred at the same wavelength and is assumed to 'see' the same gross and net effective optical gain. G and g are evaluated according to the polynomial $g_k(N)$, ie the gain polynomial with N at the input wavelength λ_k.

7.2.2 Small Signal Quantities

In the small signal analysis, the flux and carrier densities in the guide are assumed to be perturbed by a small amount about a dc value,

$$\begin{aligned} P &= \hat{P} + \Delta P \quad (a) \\ Q &= \hat{Q} + \Delta Q \quad (b) \\ N &= \hat{N} + \Delta N \quad (c), \end{aligned} \tag{7.5}$$

where the Δ quantities are much smaller than the dc values (^). The optical flux injected into the guide at the z=0 facet, is assumed to be time varying and have the form,

$$P_{in} = \hat{P}_{in}\,(1 + m\cdot e^{j\omega_m t}) \tag{7.6}$$

ie, a sinusoidal variation about a dc value of $\hat{P}_{in}$, with an angular frequency of ω_m and a modulation index, $m \ll 1$. The next assumption is that the Δ quantities in (7.5) are also sinusoidal varying, so that (7.5) becomes,

$$\begin{aligned} P &= \hat{P} + p\cdot e^{j\omega_m t} \quad (a) \\ Q &= \hat{Q} + q\cdot e^{j\omega_m t} \quad (b) \\ N &= \hat{N} + n\cdot e^{j\omega_m t} \quad (c). \end{aligned} \tag{7.7}$$

Note, this assumption restricts the analysis to a single frequency and hence cannot be used to predict the magnitude of the higher harmonics observed in the quasi-static analysis in chapter 6.

The quantities in (7.7) are substituted into equations (7.2 - 7.4), which after some manipulation yield a set of equations to described the steady state behaviour,

$$\frac{\partial \hat{P}}{\partial z} = G.\hat{P} + \delta B_r \hat{N}\cdot\left(\hat{N} + p_o\right) \qquad (7.8)$$

$$-\frac{\partial \hat{Q}}{\partial z} = G.\hat{Q} + \delta B_r \hat{N}\cdot\left(\hat{N} + p_o\right) \qquad (7.9)$$

$$0 = \frac{J}{e.d} - B_r \hat{N}\cdot\left(\hat{N} + p_o\right) - g\cdot\left(\hat{P} + \hat{Q}\right) \qquad (7.10)$$

and a complementary set for the small signal quantities,

$$\frac{dp}{dz} = \left(G - \frac{j\omega_m}{v}\right) p + \left(\delta\cdot B_r\left(2\hat{N} + p_o\right) + \frac{d\,G}{dN}\hat{P}\right) n \qquad (7.11)$$

$$-\frac{dq}{dz} = \left(G - \frac{j\omega_m}{v}\right) q + \left(\delta\cdot B_r\left(2\hat{N} + p_o\right) + \frac{d\,G}{dN}\hat{Q}\right) n \qquad (7.12)$$

$$n = \frac{-g\cdot(p + q)}{\left(B_r\left(2\hat{N} + p_o\right) + \frac{dg}{dN}\left(\hat{P} + \hat{Q}\right) + j\omega_m\right)}. \qquad (7.13)$$

Equations (7.8 - 7.10) are recognisable as the steady state equations from chapter 6, with the spontaneous emission terms replaced with total spontaneous term in equation (7.1). For equations (7.11 - 7.13) as the quantities p,q and n are assumed to be small all Δ^2 terms (eg pq, p^2, etc) are ignored. The variation of gain with carrier density is approximated by using a Taylor's expansion,

$$g\left[\hat{N}+n\cdot e^{j\omega_m t}\right] = g\left[\hat{N}\right] + n\cdot e^{j\omega_m t}\cdot \frac{dg\left[\hat{N}\right]}{dN} + n^2\cdot e^{j2\omega_m t}\cdot \frac{d^2g\left[\hat{N}\right]}{dN^2} + \text{etc} \quad (7.14).$$

Thus, g, G, dg/dN and dG/dN are all evaluated at the dc bias point, $N=\hat{N}$. The appearance of the gain slope terms, dg/dN and dG/dN, highlights the flexibility of using a polynomial approximation for the gain variation with carrier density. In this case it is relatively straight forward to evaluate the gain slopes for any value of N and know that they will be continuous over all N. Using other interpolation based methods they may have discontinuities.

Equations (7.11-7.13) show that the small signal quantities are dependent on the dc bias, the modulation frequency ω_m and the other small signal quantities, whilst the gain and gain slopes are independent of the small signal quantities and frequency. The linkage between small signal flux and carrier density is shown explicitly in equation (7.13).

7.2.3 Estimation of Frequency Response.

Using several gross approximations it is possible to predict the small signal frequency response. The approximations made are as follows :

- The end facet reflectivities, R_1 and R_2 are assumed to be zero, hence there are no cavity effects.
- Both the small signal and steady state backward travelling fluxes are neglected ($\hat{Q}$, q = 0).
- The guide is assumed to be perfectly transparent in the steady state, hence $\hat{P}$ will be constant along the guide and the effective gain $G \approx 0$.
- Finally, the entire guide is assumed to have a constant carrier density, hence the gain and gain differential terms will be invarient with z.

Using the static model in chapter 6, it is possible to calculate the steady state values at transparency, table 7.1. It should be noted that, given the approximations of the

preceding paragraph, the transparency **carrier** density is independent of optical input power, at a particular input wavelength.

Carrier Density, $\hat{N}$	=	1.80×10^{24} m^{-3}
Gross Optical Gain, g [$\hat{N}$]	=	5.32×10^{3} m^{-1}
Net Effective Gain, G [$\hat{N}$]	=	0 m^{-1}
Gross Optical Gain Differential, dg/dN	=	2.85×10^{-20} m^{2}
Net Effective Gain Differential, dG/dN	=	1.94×10^{-20} m^{2}
Transparency Current Density, J_t	=	1.90 kA/cm^{2}
Forward Flux, $\hat{P}$	=	$2.77 \times 10^{26} \times \hat{W}_{in}$ m^{-2}s^{-1}

where $\hat{W}_{in}$ is the input optical bias power in mW.

All other quantities are the same as table 6.1.

Table 7.1, Steady State Quantities for Input Wavelength, λ=824 nm

The small signal carrier density is determined by equation (7.13). When the approximations detailed in the first paragraph are taken into account, this may be rewritten as,

$$n = \frac{-g.p}{\omega_n \left(1 + \frac{j\omega}{\omega_n}\right)}, \qquad (7.15)$$

where,

$$\omega_n = B_r (2\hat{N} + p_o) + \frac{dg}{dN} \hat{P}. \qquad (7.16)$$

Clearly, at low input powers (< 1 mW) the natural frequency ω_n is fixed as (7.16) is dominated by the steady state value of carrier density. For higher input optical bias powers ω_n rises as the right hand term in (7.16) becomes more significant. Using the values in table 7.1, $\omega_n \approx 4 \times 10^8$ rad s^{-1} (63 MHz) for $\hat{P}_{in} < 1$ mW. Below the natural frequency $n \approx g.p/\omega_n$, whilst the term relating n to p rolls off at 10dB per decade above that frequency.

The small signal forward travelling flux, p can be estimated by rewriting equation (7.11) as,

$$\frac{dp}{dz} = \left[G - \frac{\gamma}{\left(1 + \frac{j\omega}{\omega_n}\right)} \right] \cdot p \,, \qquad (7.17)$$

where,

$$\gamma = \frac{g \cdot \left(\delta \cdot B_r (2\hat{N} + p_o) + \frac{d\,G}{dN} \hat{P} \right)}{\omega_n} \qquad (7.18)$$

The limits of effective gain compression term, γ are determined by the steady state flux, $\hat{P}$ and the gain g. At the extremities,

$$\hat{P} \Rightarrow 0, \qquad \gamma \Rightarrow g.\delta \quad (a)$$
$$\hat{P} \Rightarrow \infty, \qquad \gamma \Rightarrow g.\Gamma \quad (b). \qquad (7.19)$$

Thus, γ is seen to lie in a region determined by the gross optical gain, and the waveguide parameters for optical confinement and spontaneous emission coupling factor. In the former case the guide flux is dominated by the Amplified Spontaneous Emission, ASE(see section 6.4.5), whilst in the latter the dominant component of flux

in the guide is the coherently amplified injected input flux. From tables 7.1 and 6.1 this region is $0.53 < \gamma < 4 \times 10^3$ (m^{-1}).

The frequency response of the forward pass gain of the guide $F(\omega)$, ie the ratio of output power to input power, is found by integrating (7.18) in z over the length of the guide. When the expression is divided into magnitude and phase parts, the following is obtained,

$$F(\omega) = \frac{p_z(\omega)}{p_0(\omega)} = \frac{w_{out}(\omega)}{w_{in}(\omega)} \tag{7.20}$$

$$= \exp\left\{ GL - \frac{\gamma L}{\left(1 + \left(\frac{\omega}{\omega_n}\right)^2\right)} \right\} \cdot \exp\left\{ \frac{j\,\gamma L \cdot \omega\ \omega_n}{\left(\omega_n^2 + \omega^2\right)} \right\} .$$

Magnitude Phase

where, w_{in} and w_{out} are the small signal input and output power respectively. The output magnitude is therefore determined by the magnitude of the forward pass gain and the input magnitude, $|w_{in}|$. The frequency dependent magnitude of the forward pass gain is,

$$|F(\omega)| = \exp\left\{ GL - \frac{\gamma L}{\left(1 + \left(\frac{\omega}{\omega_n}\right)^2\right)} \right\}, \tag{7.21}$$

in the limits,

$$\omega \Rightarrow 0 \qquad |F(\omega)| \Rightarrow |F(0)| = \exp\{(G - \gamma)L\}, \quad (a)$$

and (7.22)

$$\omega \Rightarrow \infty \qquad |F(\omega)| \Rightarrow |F(\infty)| = \exp\{GL\} \quad (b).$$

From equation (7.22) it is clear that the forward pass gain at low frequencies is compressed by $\exp\{\gamma L\}$, ie $p_\infty/p_0 = \exp\{\gamma L\}$. This is the gain compression term

discussed in chapter 6 for static and quasi-static signals. Using the parameters in table 7.1 and given the range of γ calculated above, $1 < \exp\{\gamma L\} < 55$, (0 to 17 dB). At high frequencies $|F(\omega)|$ the guide is transparent to the small signal input as well as the dc input optical power.

There must be two break frequencies in $|F(\omega)|$ as the gain rises between the two frequency independent portions determined by (7.22) with a slope of 20 dB/decade. From equation (7.21) the 3dB break frequencies are,

$$|F(\omega_l)| = 2 \cdot \exp\{(G - \gamma)L\}, \quad \text{(a)}$$

and (7.23)

$$|F(\omega_u)| = \frac{\exp\{GL\}}{2} \quad \text{(b)},$$

where ω_l and ω_u are the lower and upper break frequencies respectively. Clearly, these definitions are only valid if $\exp\{\gamma L\} > 2$. After some manipulation equations (7.21) and (7.23) yield,

$$\omega_l = \omega_n \cdot \sqrt{\frac{\ln(2)}{\gamma L - \ln(2)}} \quad \text{(a)},$$

and (7.24)

$$\omega_u = \omega_n \cdot \sqrt{\frac{\gamma L - \ln(2)}{\ln(2)}} \quad \text{(b)}.$$

For values of $\exp\{\gamma L\} < 2$, the frequency response can still be estimated as the natural frequency, ω_n lies in the centre of the step in gain on a log/log scale.

Therefore, using the SSA technique the frequency response of the small signal carrier density and output signal can be estimated. Table 7.2 shows the values of break frequencies ω_n, ω_l and ω_u, and gain compression term $\exp\{\gamma L\}$, using the values in tables 6.1 and 7.1.

$\hat{W}_{in}$ (mW)	exp (γL)	Natural Frequency		Lower Break		Upper Break	
Steady State Input Power	(dB)	ω_n (rad s^{-1})	f_n (MHz)	ω_l (rad s^{-1})	f_l (MHz)	ω_u (rad s^{-1})	f_u (MHz)
0.1	0.3	4.1×10^8	63	*	*	*	*
1.0	2.6	4.8×10^8	79	*	*	*	*
5.0	7.8	8.0×10^8	127	6.3×10^8	100	10×10^8	160
10.0	10.4	12×10^8	190	7.7×10^8	122	19×10^8	300

Table 7.2, Estimated Break Frequencies and Gain Compression Term for Guide Biased to Transparency.

7.3 Modelling Considerations

7.3.1 Steady State Solution

In order to calculate the small signal quantities governed by equations (7.11-7.13) it is necessary to solve the steady state quantities at the bias point, equations (7.8-7.10). As the wavelength dimension in the steady state quantities has been removed, it would be possible to solve (7.8-7.10) using a more efficient and accurate model to that discussed in chapter 6. However, for simplicity and clarity an adapted form of the stepping routine is used.

To recap, the steady state flux in the guide is determined by dividing the guide into regions of constant carrier density. This form of discretisation introduces errors in both the steady state and small signal solution but these errors are minimised if sufficiently small regions are used. The steady state model solves the fluxes $\hat{P}$ and $\hat{Q}$ at the region boundaries. For the m^{th} region of the guide ($z_m \le z \le z_{m+1}$), the flux at any point in the region is given by,

$$\hat{P}_m(z) = \hat{P}_m \exp\left[G_m\left(z - z_m\right)\right] \tag{7.25}$$

$$+ \frac{\delta B_r \hat{N}\cdot\left(\hat{N} + p_o\right)}{G_m}\cdot\left(\exp\left[G_m\left(z - z_m\right)\right] - 1\right)$$

and

$$\hat{Q}_m(z) = \hat{Q}_m \exp\left[G_m\left(z_{m+1} - z\right)\right] \tag{7.26}$$

$$+ \frac{\delta B_r \hat{N}\cdot\left(\hat{N} + p_o\right)}{G_m}\cdot\left(\exp\left[G_m\left(z_{m+1} - z\right)\right]\right) - 1),$$

where z_m and z_{m+1} are the longitudinal displacements of the m and m+1 boundaries from the front facet (z=0). Thus for the small signal model, the required steady state values in z can be determined if the fluxes at the region boundaries are known. The gain and gain differential terms are dependent on the carrier density, $\hat{N}$ and for convenience it is assumed that these terms are constant over each region. An alternative method suggested by Boeck et al [5] is to fit polynomials to the point values (in z) of $\hat{P}$, $\hat{Q}$ and $\hat{N}$, however the experience gained from the steady state model suggests that the use of polynomial fits can be problematic.

7.3.2 Small Signal Solution

The solution of a set of differential equations such as (7.11-7.13) is an involved process which lends itself to numerical rather than analytic techniques. These particular equations are complicated by the appearance of the counter propagating flux terms, ie dp/dz is dependent on q. Therefore, an analysis of the form used in chapter 6 cannot be used, as there is no analytic solution for p and q, even in a region of constant carrier density. The approximate solution used in section 7.2.3 is convenient to estimate the break frequencies, but is not sufficient to be used as a full solution.

Fortunately, several library routines exist to solve such sets of non-linear differential equations [7]. The small signal solution as expressed in equations (7.11-7.13), form a boundary value problem in z, where the fixed boundary values are distributed over the two boundaries at z=0 and z=L. The routine chosen uses finite element techniques to solve general, n-dimensional boundary value problems, giving a solution at the fixed boundaries and at intermediate mesh points distributed along the guide.

The equations governing the small signal variation of p and q are complex, hence p and q will be complex. It is convenient to define the input flux as being purely real and that the phase of p and q is with reference to the input. This phase is a measure of the shift **in time** between the quantity and the input reference. This phase is

dependent on both the propagation delay in the guide and the time lag between variations in the fluxes and carrier density.

Unfortunately, it is not possible to have a general purpose solution routine to solve complex boundary value problems [7], so the problem must be divided into real and imaginary parts. Equations 7.11 and 7.12 therefore yield a four dimensional problem described by,

$$\begin{aligned}
\frac{dp'}{dz} &= (Ap' - Bp'') + (Cq' - Dq''), \\
\frac{dp''}{dz} &= (Ap'' + Bp') + (Cq'' + Dq'), \\
-\frac{dq'}{dz} &= (Eq' - Fq'') + (Gp' - Hp''), \\
-\frac{dq''}{dz} &= (Eq'' + Fq') + (Gp'' + Hp'),
\end{aligned} \tag{7.27}$$

where the dash and double dash indicate the real and imaginary parts respectively. The coefficients A-H are,

$$\begin{aligned}
A &= G + C, \\
B &= \omega\left(\frac{1}{v} + D\right), \\
C &= \left(B_r\left(2\hat{N} + p_o\right) + \frac{dg}{dN}\left(\hat{P} + \hat{Q}\right)\right) D, \\
D &= \left(\delta B_r\left(2\hat{N}+p_o\right) + \frac{dG}{dN}\hat{P}\right) \frac{g}{\left\{\left(B_r\left(2\hat{N}+p_o\right) + \frac{dg}{dN}\left(\hat{P}+\hat{Q}\right)\right)^2 + \omega^2\right\}}.
\end{aligned} \tag{7.28}$$

The definitions of E,F,G,H are identical to those for A,B,C,D (respectively) except that the term $dG/dN \cdot \hat{P}$ is replaced with $dG/dN \cdot \hat{Q}$ in the definition for H. Using the set of equations (7.27 - 7.28) it is now possible to use the library routine providing the boundary values at z=0 and z=L can be determined.

7.3.3 Boundary Value Estimation and Solution Technique

In this formulation, there are four variables and the boundary values are all unknown. Therefore, an iterative method must be applied to give a solution. The appropriate boundary values are p' and p" at the z=0, and q' and q" at z=L, as these will lead to true solution from the known value of input flux, $m \cdot \hat{P}_{in}$. There are four boundary conditions which allow the calculation of the boundary values,

$$p'(0) = R_1 \cdot q'(0) + p'_{in}, \quad \text{(a)}$$

$$p''(0) = R_1 \cdot q''(0) + p''_{in}, \quad \text{(b)} \qquad (7.29)$$

$$p'(L) = R_2 \cdot p'(L), \quad \text{(c)}$$

$$p''(L) = R_2 \cdot p''(L). \quad \text{(d)}$$

In (7.29) only the values of p'_{in} and p''_{in} are known when the iteration process begins. As the phase is with respect to the input flux it is convenient to assume that it is purely real, with $p'_{in} = m \cdot \hat{P}_{in}$ and $p''_{in} = 0$. Some authors [4,5] avoid the complication presented by the unknown boundary values by assuming that R_1 and $R_2 = 0$. Hence the boundary values are known exactly and the small signal quantities can be solved in one step.

To start the iteration process an estimate of the boundary values is required. This is achieved by assuming that both components of q(0) are negligible, there is no

gain compression in the guide, and that the carrier density variations can be ignored. These assumptions are most correct for high frequencies. Therefore, $p(0) = p_{in}$, ie purely real, and $q(L) = R_2 . F . p_{in} e^{j\phi}$, where F is the steady state forward pass gain and $\phi = \omega L/v$ is the phase shift due to the propagation delay.

For subsequent iterations, the boundary values are re-calculated using an adapted form of the boundary conditions (7.29),

$$p^+(0) = p_{in} + \zeta_1 \cdot R_1 \cdot q(0) + (1 - \zeta_1) \cdot p(0), \qquad \text{(a)}$$

$$q^+(L) = \zeta_2 \cdot R_2 \cdot p(L) + (1 - \zeta_2) \cdot q(L). \qquad \text{(b)} \qquad (7.30)$$

The terms ζ_1 and ζ_2 are damping factors included to prevent instabilities in the iteration technique, the values of which are determined by R_1 and R_2, and the proximity to a solution. As a stable solution is approached both damping factors become equal to unity. The + superscript in (7.30) indicates that the boundary values are calculated using the corresponding values from the previous iteration. Once a stable solution is reached (absolute error $< 10^{-4}$) the iteration is stopped.

On a general note, this method is applicable to a variety of situations where an estimate of the steady state quantities along the device can be obtained, along with a method of calculating the appropriate boundary conditions.

7.4 Results and Discussion

Unless otherwise stated, the results in this section were calculated using the values given in tables 6.1 and 7.1. Figures 7.1 and 7.2 show the variation of small signal output power with modulation frequency. In figure 7.1 the guide bias current is altered for each dc bias power, $\hat{W}_{in}$ to achieve the transparency condition defined in chapter 6. In figure 7.2 the bias current is maintained at the constant value required for transparency to a 1 mW dc optical bias power (98 mA). In both cases the steady state quantities, $\hat{P}$, $\hat{Q}$ and $\hat{N}$ are re-calculated for each value of optical bias power.

The gain compression term, exp {γL} can be determined from figures 7.1 and 7.2 from the ratio p_∞/p_0. The results obtained are summarised in table 7.3 :

Optical Bias	Biased to Transparency (7.1)		Constant Bias (98 mA) (7.2)	
(mW)	p_∞/p_0 (dB)	γ (m^{-1})	p_∞/p_0 (dB)	γ (m^{-1})
0.1	0.31	71.4	0.43	100
1.0	2.45	564	2.45	564
5.0	7.50	1730	3.43	760
10.0	10.1	2320	3.00	690
20.0	*	*	2.20	510

Table 7.3 Gain Compression Terms (for an active guide biased to transparency or with a constant bias power).

A quick cross check between table 7.3, the results of the quasi-static analysis summarised in table 6.4, and the theoretically derived values in section 7.2.3 shown in table 7.2, shows a good correlation for the particular case examined in that section. However, the approximations made in section 7.2.3 only hold for low input powers and when the guide is transparent. So that analysis cannot, for instance, be used to predict the results shown in figure 7.2, but it can be used to describe the underlying trends.

From figure 7.1 it can been seen that the frequency response of the guide is divided into three regions. At low frequencies, the small signal gain is compressed and the output falls below that expected if the guide were perfectly transparent. Over the

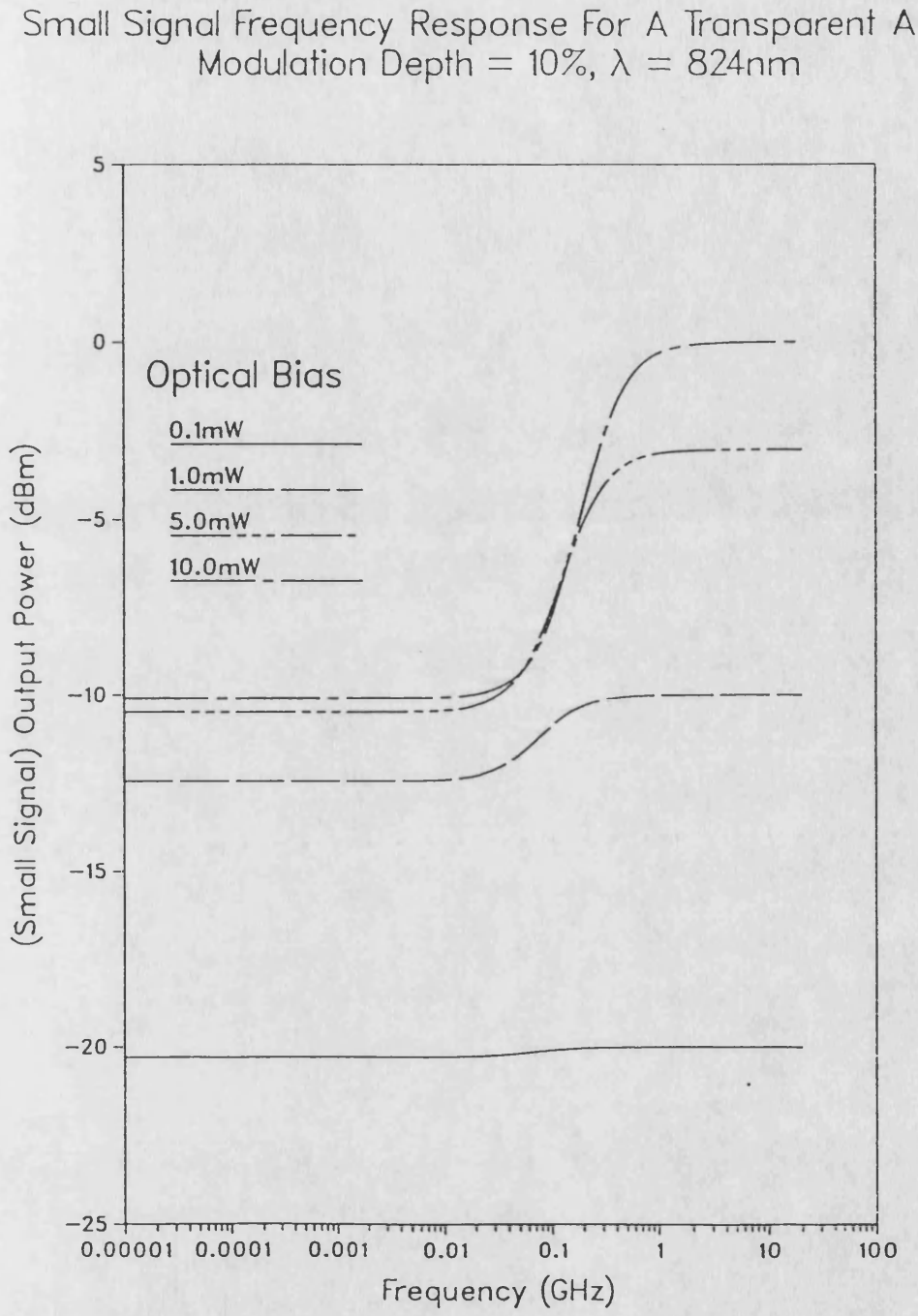

Figure 7.1 : Small signal, output power, frequency response, as a function of optical bias power, for a transparent guide.

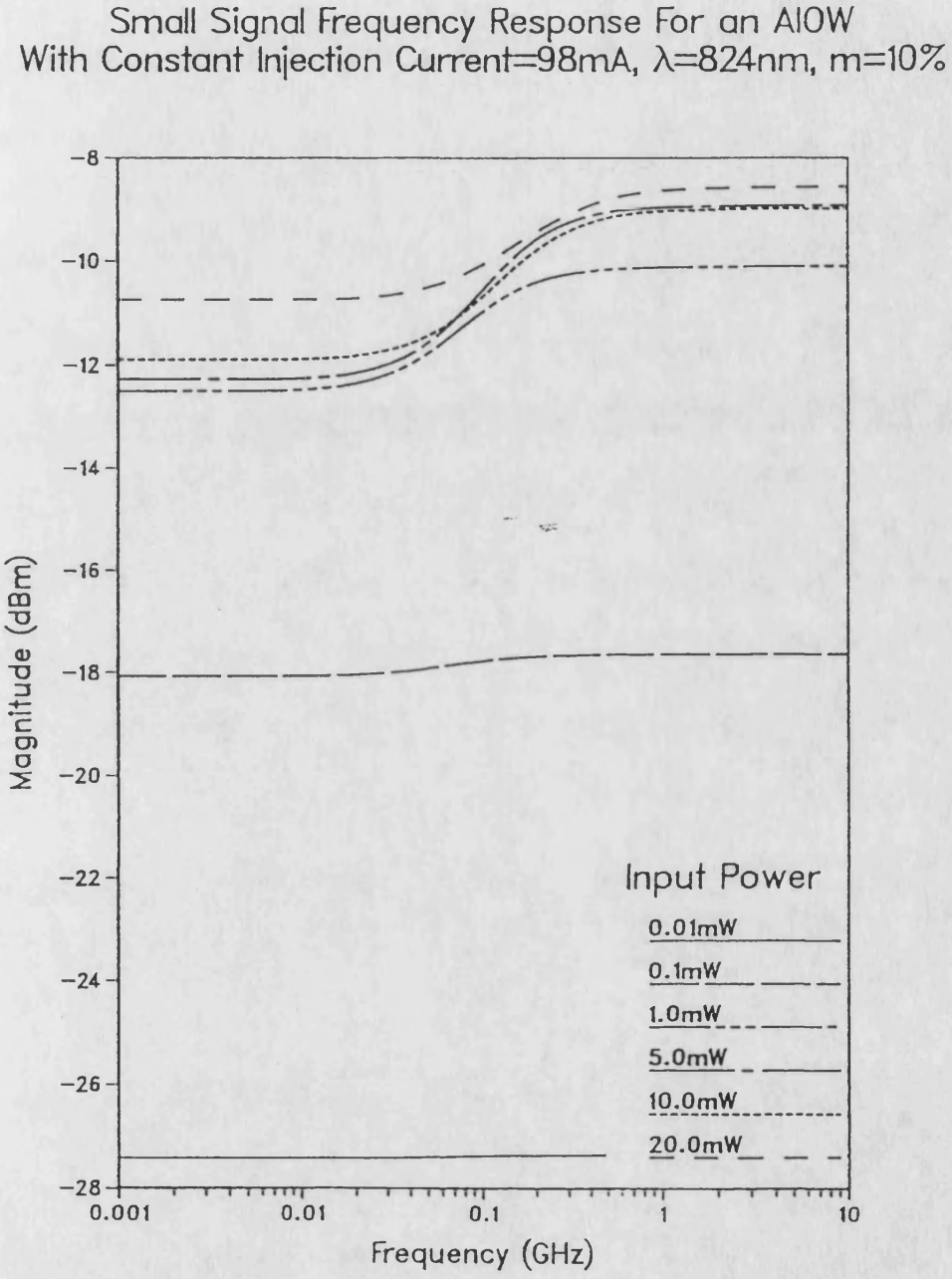

Figure 7.2 : Small signal, output power, frequency response, as a function of optical bias power, for a guide with a constant current bias of 98 mA.

intermediate range the power rises at 20 dB/decade, until at high frequencies the guide appears transparent to both the dc and small signal components of the input signal. As was predicted in section 7.2.3, the gain compression increases with optical bias power. It is clear that there are two regions where the output power is virtually independent of frequency : at low frequencies the carrier density follows the flux variations exactly, whilst at high frequencies there is no interaction between the flux and carrier density.

In figure 7.2 the situation is less straight forward as the steady state carrier density and hence the gain terms all alter with optical bias power. Signals with a bias less than 1 mW will see a guide with net gain of approximately 2 to 3 dB, whilst signals with a greater bias will see a net loss of between -7 and -15 dB. The constantly pumped guide exhibits the same underlying behaviour as the case where the current is trimmed. However, the rise in gain with frequency is reduced as the dc current density falls. This graph demonstrates the need to adjust the current correctly if transparency is to be achieved. From table 7.3, it is seen that above 1 mW the gain compression term is not only lower than that calculated for transparency, but above 5 mW the value comes down with increasing power.

Figures 7.3 and 7.4 highlight the major disadvantage of using a small signal analysis. As all the variations in flux and carrier density are assumed to be small, the small signal output is linear with modulation index, at all frequencies (figure 7.3) and for all input powers (figure 7.4). Thus the type of harmonic distortion modelled in chapter 6 cannot be predicted with this model.

The use of the single wavelength model allows the variation of some of the material parameters which is not practicable for the full model. In figures 7.5-7.7 the effect of varying B_r, p_o, and δ respectively is shown. In the case of varying B_r the gain polynomials are scaled by the ratio of B_r shown in the key and the value in table 6.1. Figures 7.5-7.7 serve to emphasis the assertion that the results shown in this thesis, although internally consistent, are highly dependent on the choice of material parameters.

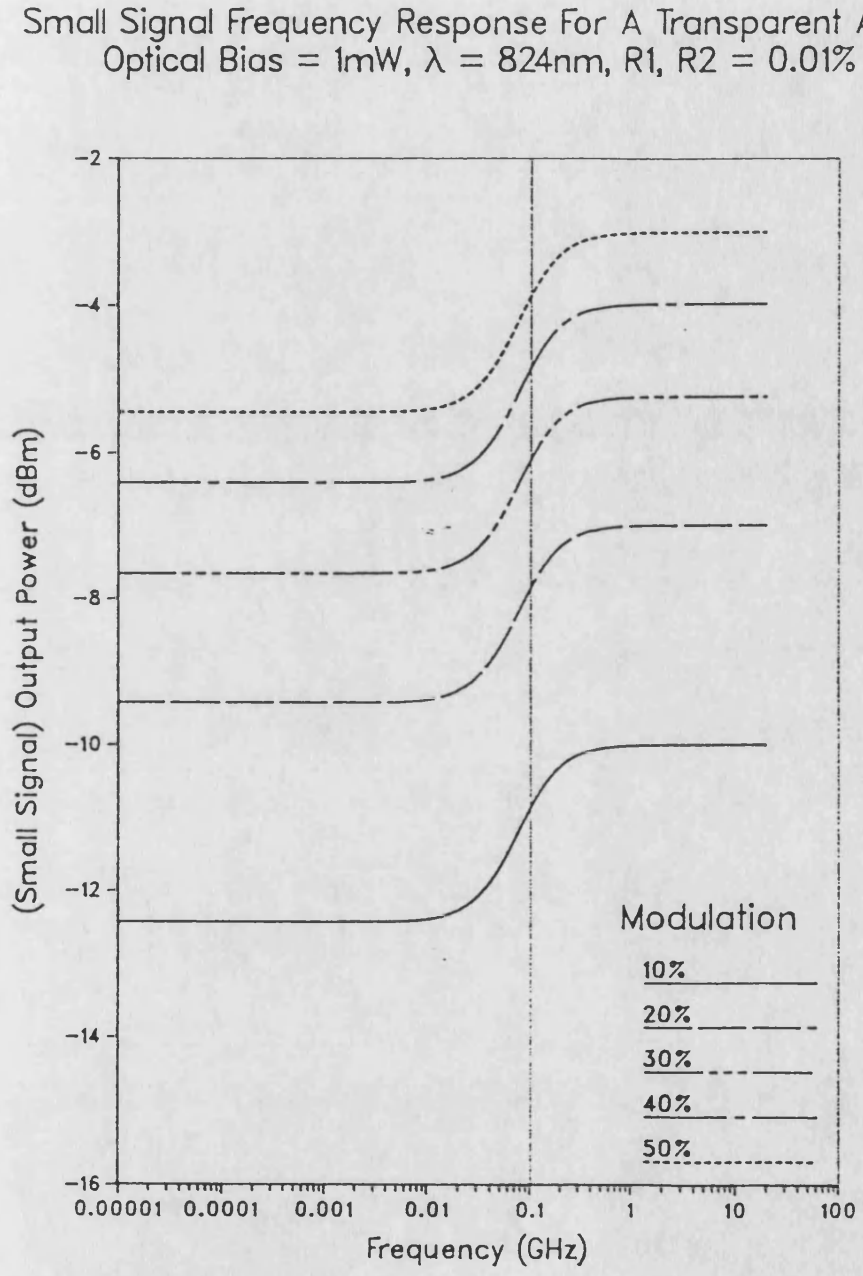

Figure 7.3 : Small signal, output power, frequency response, as a function of modulation depth, for a guide biased to transparency at an input optical bias power of 1 mW.

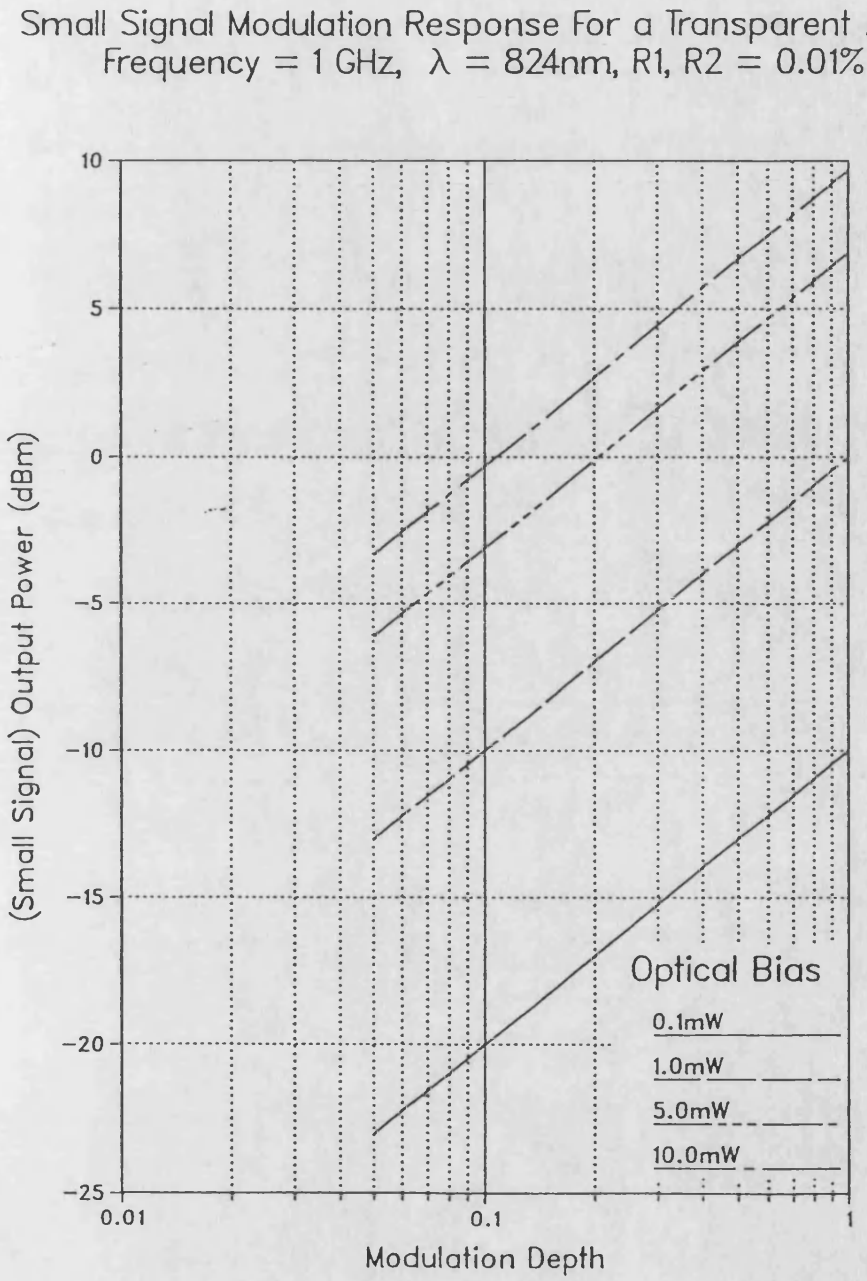

Figure 7.4 : Small signal, modulation response, as a function of input optical bias power, for a transparent guide.

A brief explanation is required for this set of results. In each case the injected current is altered to give transparency. Thus the forward pass gain, F will be the same for each value of parameter chosen. This is clearly the case as the high frequency small signal output power is the same for all cases, -3 dBm. In figure 7.5 it is seen that an increase in B_r pulls the break frequencies upwards according to equation (7.16), whilst the gain compression decreases (equation (7.18)). In figures 7.6 and 7.7 the small change in the gain compression term is determined by changes in the gross optical gain and the increased power coupled into the signal along the guide respectively.

The final figure in this section, 7.8 shows a comparison of the frequency response calculated from the small signal analysis and the large signal dynamic model detailed in the next chapter. Clearly there is a good agreement between the models, better than 1/2 dB for most of the range, with the large signal model being the more accurate. As might be expected the discrepancy grows at higher optical bias powers and as the guide is perturbed from transparency. This agreement between the two models and the gain compression terms in tables 6.4 and 7.3 are sufficient to verify the behaviour of the small signal model.

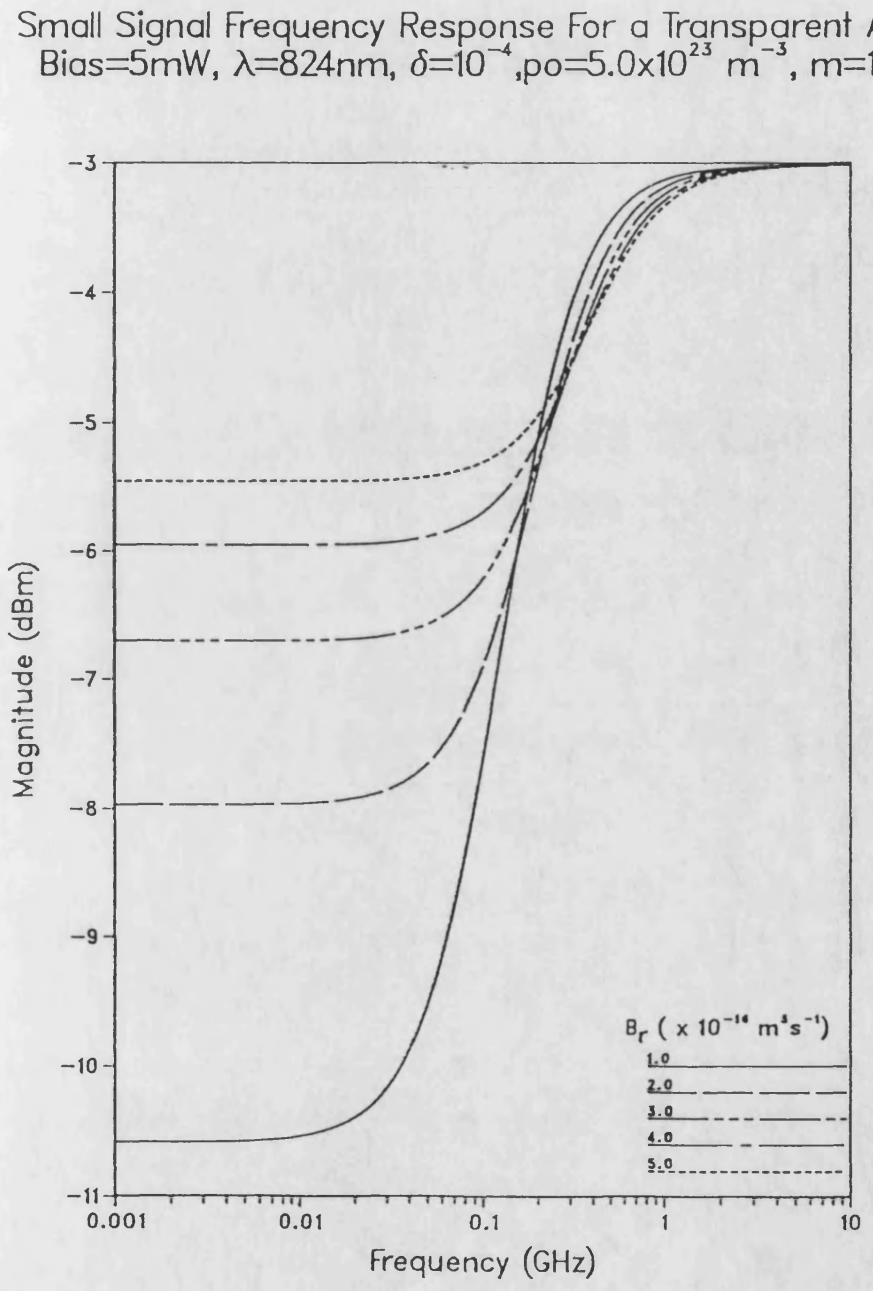

Figure 7.5 : Effect of bimolecular recombination rate, B_r, on small signal, output power, frequency response, for a guide biased to transparency to an input optical power of 1 mW.

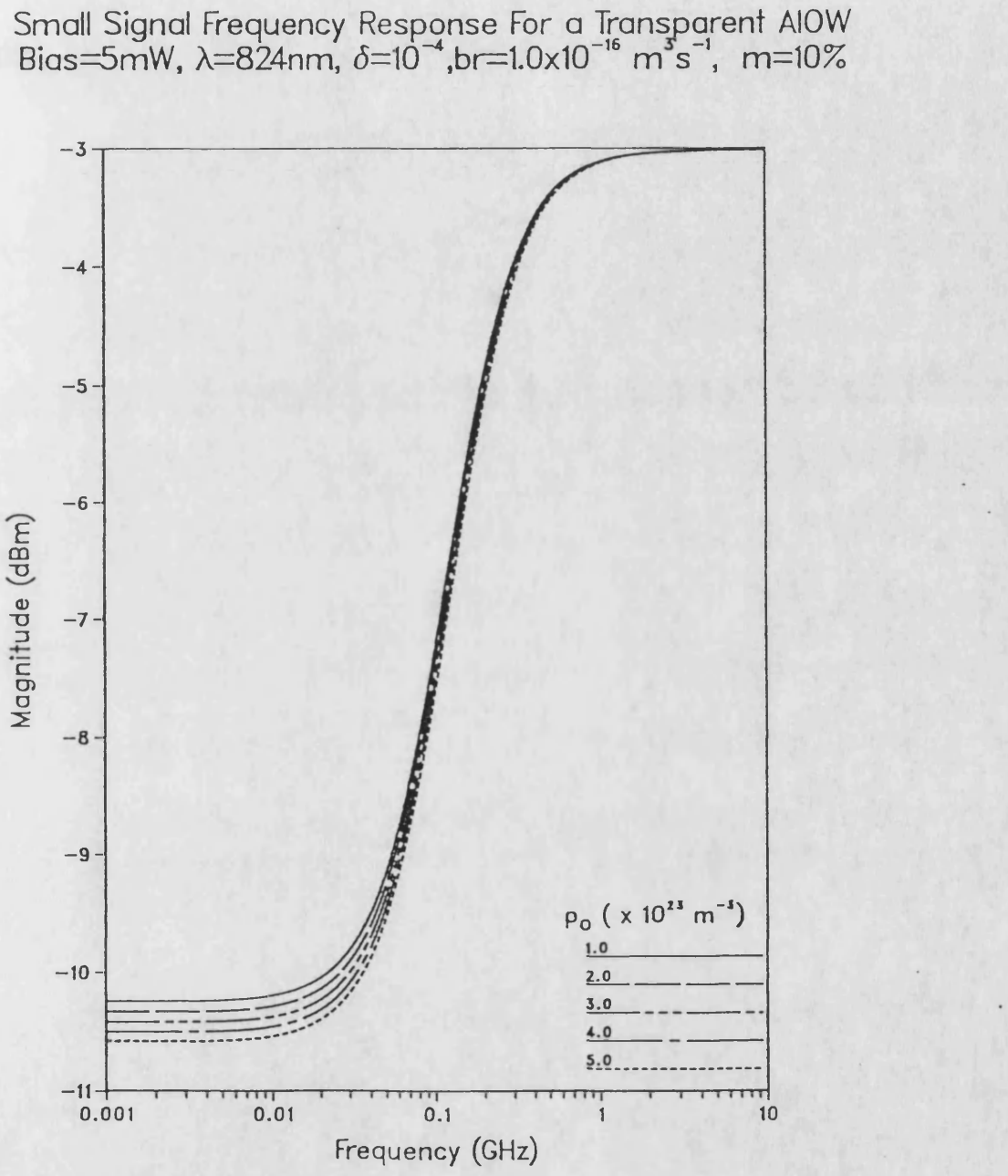

Figure 7.6 : Effect of active layer doping density, p_o, on small signal, output power, frequency response, for a guide biased to transparency to an input optical power of 1 mW.

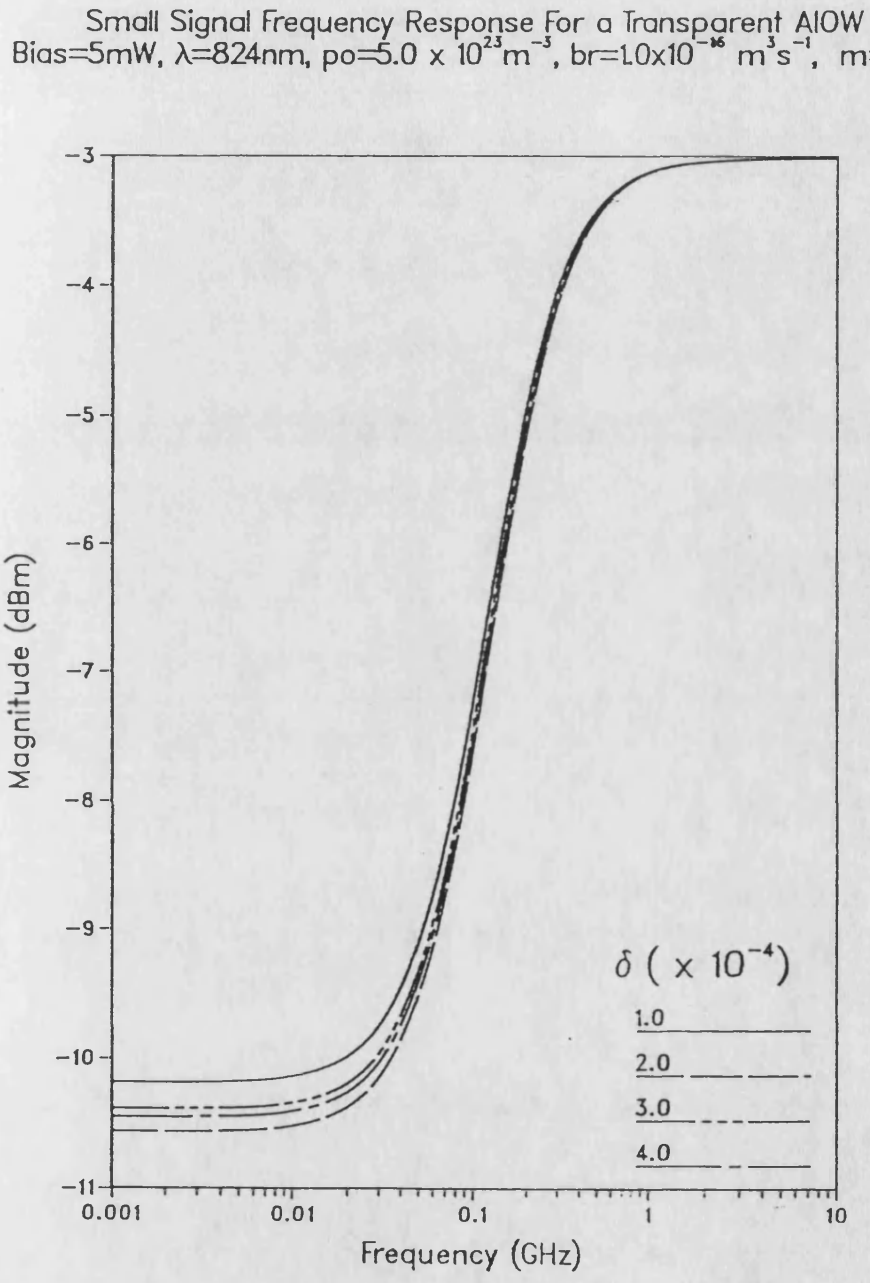

Figure 7.7 : Effect of spontaneous emission factor, δ, on small signal, output power, frequency response, for a guide biased to transparency to an input optical power of 1 mW.

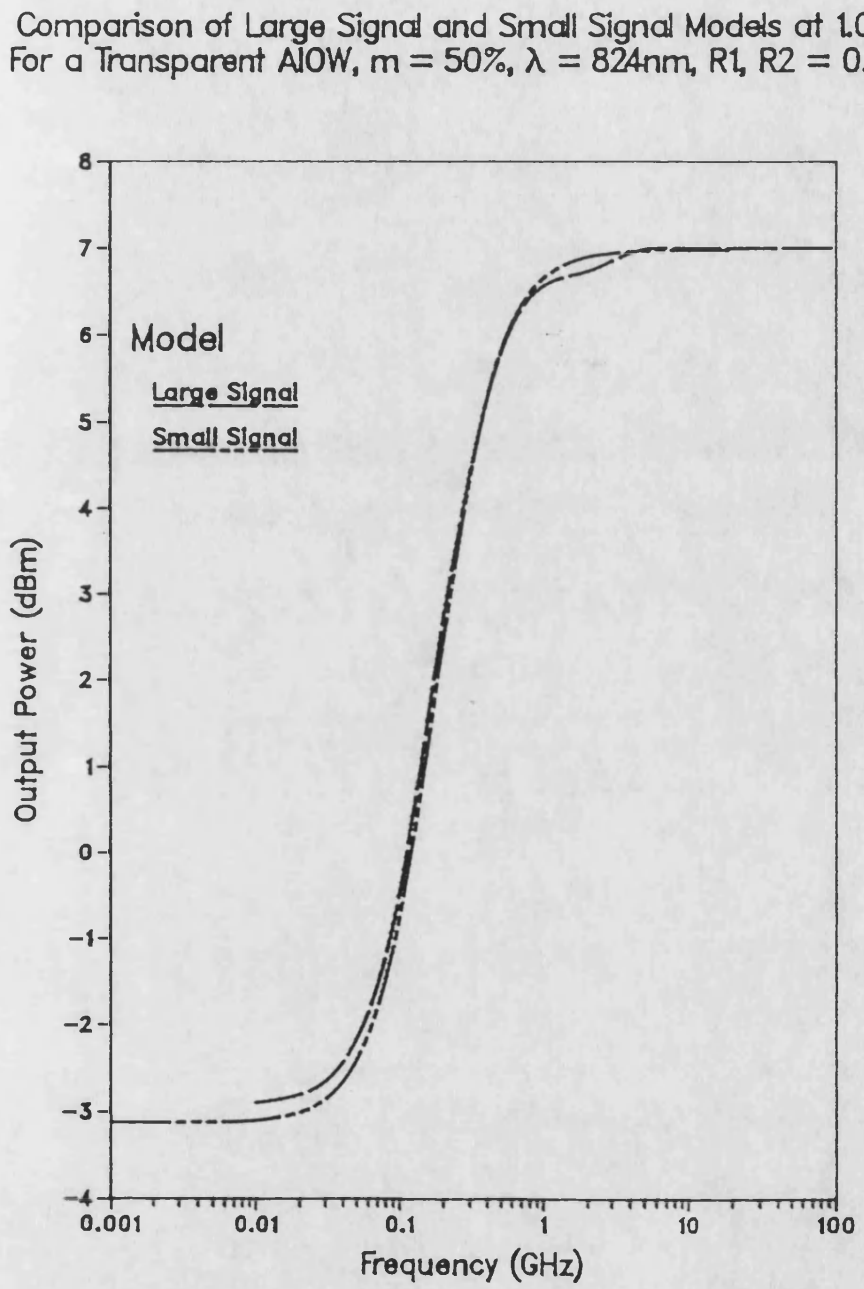

Figure 7.8 : Comparison of large and small signal (fundamental) output power, frequency response, for a guide biased to transparency to an input optical power of 1 mW.

7.5 Conclusions

In this chapter the familiar small signal analysis technique has been applied to the case of the pumped buried heterostructure waveguide. The small signal model has been verified against the static model in chapter 6, an approximate theoretical analysis and the large signal dynamic model in chapter 8. The method presented is applicable to a wide variety of boundary conditions, providing that a suitable steady state solution can be found and the travelling flux method can be applied.

The term that links n to p and q (equations (7.13) and (7.15)) is seen to roll off at 10 dB/decade with ω_n. Thus the interaction between the small signal flux and carrier density is reduced until the small signal input 'sees' the same gain as the optical input bias power. It is this decoupling which limits the high frequency current modulation of laser diodes [1,2,5]. However, due to the different operating point of laser diodes and SLED's, it is possible to modulate them at frequencies in excess of the guide break region [2,5]. Thus it is possible to achieve high frequency, high power linear operation from the guide.

The gain compression term introduced in chapter 6 has been quantified using the approximate analysis in section 7.2.3, as has the region of validity of the quasi-static modulation analysis. It is clear from this chapter, that for frequencies below approximately 10 MHz the quasi-static analysis is sufficient as the carrier density variations follow the flux exactly.

The location of the break frequencies in the small signal output power frequency response is dependent on the waveguiding, material and steady state bias conditions in the guide : as is the gain compression term. It must therefore be emphasised again therefore that it is only possible to accurately predict the guide response if the parameters are known exactly. However, the trends presented in this chapter will hold and the parameters used are typical values taken from the literature.

In this chapter, it has been shown that it is possible to achieve high power, linear operation at high frequencies, ie the small signal gain is the same as the steady

state forward pass gain. Alternatively, if linear operation is required over a wide range of frequencies then the optical bias power must be kept below the saturation power for the guide (≈0.1mW). In this case there will still be a slight compression (<0.3dB) determined by the coupling of the spontaneous emission coupling factor.

There are several drawbacks to attempting to operate the guide at high powers with a predictable gain, as demonstrated by figure 7.2. If the bias power varies, then the steady state gain will also change. Hence some mechanism must be developed to maintain the bias current at the correct value to give transparency. One method may be to use a very low power tuning signal at a particular frequency. Such a signal would not affect the guide parameters but could be separately detected and used to control the guide bias current.

References, chapter 7.

1 AGRAWAL, G.P. and DUTTA, N.K., 'Long wavelength semiconductor lasers',
Van Nostrand Reinholt, 1986.

2. LAU, K.Y., BAR-CHAIM, N., URY, I. and YARIV, A., 'Direct amplitude modulation of semiconductor lasers at f>10 GHz'
*Appl. Phys. Letts, 1983, **43**, (1), pp11-13.*

3. YARIV, A., 'Optical electronics - 3rd edition',
Holt, Reinhart and Wilson, 1985.

4. BOECK, J., AMANN, M.C., and STEGMÜLLER, B., 'On the theory of the superluminescent diode - 2. Small signal modulation behaviour',
*A.E.Ü., 1980, **34**, (11), pp465-468.*

5. LAU, K.Y., and YARIV, A., 'High frequency current modulation of semiconductor injection lasers',
in 'Semiconductors and semimetals, Volume 22 - Lightwave communications technology, Part B: Semiconductor injection lasers, I' - ed Tsang, W.T., Academic Press, 1985.

6. OTSUKA, K., 'Proposals and analyses on laser amplifier based integrated optical circuits',
*IEEE J. Quantum Electron, 1981, **QE-17**, (1), pp23-28.*

7. 'NAG : Fortran library and manual, Mark 11',
Numerical Algorithms Group Limited, Oxford, England, 1984.

8 LARGE SIGNAL DYNAMIC MODEL

8.1 Introduction

In chapter 6 it was shown that the non-linear interaction between the flux and carrier density in the guide leads to harmonic distortion of a modulated signal propagating down the guide. A quasi-static analysis was developed to predict this distortion at 'low' frequencies. The small signal analysis presented in chapter 7 has been used to show the range of validity of this quasi-static analysis and to predict the frequency response of the guide. The analysis in chapter 7 could be extended to take account of multi (modulation) frequency inputs and multi (optical) wavelength behaviour but this would not yield a greater understanding of the guide behaviour.

The fundamental draw-back of the SSA that cannot be overlooked, is that the guide parameters are assumed to vary by a small amount about the bias point. Therefore such an analysis cannot be used to examine the change in modulation distortion with modulation index, or any bias point drift due to changes in the mean carrier density. The examination of such behaviour demands a large signal dynamic analysis.

Many large signal models have been developed for laser diodes [1,2], SLEDs [4], travelling wave [7], and Fabry-Perot [5,6,8] laser amplifiers. In common with most static models, the majority of these assume that the spatially averaged rate equations discussed in chapter 5 can be used. However such an assumption limits the type of inputs that can be considered, to time scales greater than the photon lifetime or the guide propagation time. For this reason and those outlined in chapter 6 a spatially averaged model will not be used here and a solution to the travelling fluxes and carrier density along the guide will be developed.

In this chapter an analytic solution to the travelling flux rate equations will be developed in a similar manner to that presented by Perkins and Ormondroyd [4]. Although alternative methods do exist (see, for example, the excellent review paper by Buus [2] and the references therein and Lowery [7] where a transmission line rather

than the conventional rate equation approach is used) the adopted method follows logically from the analysis in chapter 6, and the steady state solutions generated from that model are used as the starting point for the dynamic analysis.

The major advantages of this large signal model is that it allows the modelling of the temporal and spectral properties of the guide whilst avoiding the pit-falls of the spatial averaging procedure. In addition, the spectrally dependent spontaneous emission terms are still included, which many authors choose to ignore.

8.2 Large Signal Dynamic Rate Equations

8.2.1 Continuity Equations in Regions of 'Constant' Carrier Density

The solution of the rate equations, described in chapter 4, for large variations in flux and carrier density has considerable similarities with the steady state solution presented in chapter 6. Essentially one can allow the guide parameters to vary over a small step in time, in response to a time varying input flux. Providing the time step is sufficiently small, the change in carrier density will be negligible [2,4]. Therefore it is possible to solve the photon conservation equations assuming constant, rather than time varying, gain and spontaneous emission parameters.

The arguments relating to the damping out of spatial effects less than the diffusion length discussed in section 6.2.2, still hold in the time domain. Hence the diffusion can be neglected for variations greater than a few microns, and sub-micron variations are removed. Using this information it is possible to write the conservation equations for the i^{th} wavelength slot and the m^{th} region along the guide,

$$\frac{1}{v}\frac{\partial P_i}{\partial t} + \frac{\partial P_i}{\partial z} = G_{m,i}\cdot P_i + \delta \cdot S_{m,i} \ . \qquad (8.1)$$

$$\frac{1}{v}\frac{\partial Q_i}{\partial t} - \frac{\partial Q_i}{\partial z} = G_{m,i}\cdot Q_i + \delta \cdot S_{m,i} \ . \qquad (8.2)$$

$$\frac{dN_m}{dt} = \frac{J_m}{e.d} - B_r N_m\cdot (N_m + p_o) - \sum_{i=l}^{i=u} g_{m,i}\cdot (P_i + Q_i) \ , \qquad (8.3)$$

The definition of the terms in equations (8.1-8.3) is the same as for the previous chapters, hence the results of the large signal model can be compared with those from the quasi-static and small signal analyses. Using equations (8.1-8.3) it is possible to develop analytic solutions to the temporal flux in a similar manner to that presented in [4].

8.2.2 Photon Continuity Equations

8.2.2.1 Intuitive Approach

It is possible to 'solve' equations (8.1) and (8.2) using a simple intuitive argument to extend the steady state solution. From chapter 6 it is known that integrating P_i over the region of constant carrier density,

$$P_{m+1,i} = P_{m,i} \cdot \exp\{G_{m,i}\, l_m\} + \frac{\delta S_{m,i}}{G_{m,i}} \left(\exp\{G_{m,i}\, l_m\} - 1\right), \qquad (8.4)$$

If the flux is travelling at a constant propagation velocity, v down the guide and the amplitudes $P_{m,i}$ and $P_{m+1,i}$, and all other terms do not vary in time, then the steady state solution can be seen as a special case of the temporal model. The flux $P_{m,i}$ will take a time of,

$$\Delta t_m = \frac{l_m}{v} \qquad (8.5)$$

to traverse the region. Thus the time domain version of equation (8.4) may be written as,

$$P_{m+1,i}[t+\Delta t] = P_{m,i}[t] \exp\{G_{m,i}\, l_m\} \qquad (8.6)$$

$$+ \frac{\delta S_{m,i}}{G_{m,i}} \cdot \left(\exp\{G_{m,i}\, l_m\} - 1\right),$$

ie, after the time step Δt, the flux at the $m+1^{th}$ boundary is dependent on the flux at the m^{th} boundary before the time step and the gain and spontaneous terms.

8.2.2.2 Mathematical Approach

Given the assumption that the carrier density is constant in each region over a small step in time Δt, equations (8.1) and (8.2) are quasi-linear equations which can be described by the general equation,

$$A\cdot\frac{\partial u}{\partial x} + B\cdot\frac{\partial u}{\partial y} + C\cdot u = D\ , \tag{8.7}$$

where A,B,C and D are constants and u = u[x,y]. Equation (8.7) yields solutions of the form [13],

$$\begin{aligned} u[x,y] &= f_1\left[\frac{x}{A} - \frac{y}{B}\right]\cdot\exp\left\{\frac{-C\cdot y}{B}\right\} + \frac{D}{C}\ , \quad \text{(a)} \\ &= f_2\left[\frac{x}{A} - \frac{y}{B}\right]\cdot\exp\left\{\frac{-C\cdot x}{A}\right\} + \frac{D}{C}\ , \quad \text{(b)} \end{aligned} \tag{8.8}$$

where f_1 and f_2 are complementary arbitrary functions determined by the initial conditions. Taking one solution to equation (8.1), say for the first region of the guide during the time interval $0 \le t \le \Delta t$,

$$P[t,z] = f\,[vt - z]\cdot\exp\{Gz\} - \frac{\delta S}{G}\ , \tag{8.9}$$

$$\Delta t = \frac{l_1}{v} \quad 0 \le t \le \Delta t, \quad 0 \le z \le l_1,$$

(where, for convenience, the m and i subscripts have been omitted). A similar solution exists for the backward travelling wave, Q[t,z].

If the time varying input is applied at t=0 and the guide is assumed to be in the steady state for all $t < 0$, then the distribution of flux at $t=0^-$ can be determined by the steady state model, eg

$$P[0,z] = P[0,0]\cdot \exp\{Gz\} - \frac{\delta S}{G}(\exp\{Gz\} - 1) \; . \qquad (8.10)$$

Given that the solution must be continuous at the t=0 boundary, equations (8.9) and (8.10) can be equated with t set to zero in (8.9), ie

$$f[-z]\cdot \exp\{Gz\} - \frac{\delta S}{G} = P[0,z]. \qquad (8.11)$$

Therefore,

$$f[-z] = \left(P[0,z] - \frac{\delta S}{G}\right)\exp\{Gz\} \qquad (8.12)$$

and

$$f[vt-z] = \left(P[0,z-vt] - \frac{\delta S}{G}\right)\exp\{G(z-vt)\} \; . \qquad (8.13)$$

Substituting (8.13) into equation (8.9) yields the general solution of the forward travelling flux,

$$P[t,z] = P[0,z-vt]\cdot \exp\{G\cdot vt\} + \frac{\delta S}{G}\cdot \left(\exp\{G\cdot vt\} - 1\right) , \qquad (8.14)$$

$$\text{for } 0 \le vt \le l_1.$$

In a similar manner to the steady state analysis detailed in chapter 6, it is sufficient to calculate the fluxes at the region boundaries. However this immediately presents a problem in a dispersive medium such as GaAs, as the propagation velocity is dependent on the group refractive index. In order to calculate the guide properties over small steps in time and have fixed region boundaries, all dispersive effects are ignored. For the case of a transparent AIOW with low end facet reflectivities, this restriction is acceptable as the variation in refractive index is negligible.

Therefore, all regions of the guide must be of equal length, $l = v \cdot \Delta t$ and it is clear that (8.14) and its counterpart for backward travelling flux can be extended to give the variation for the m^{th} region and i^{th} slot

$$P'_{m+1,i} = P_{m,i} \exp\left\{G_{m,i}\, l\right\} + \frac{\delta S_{m,i}}{G_{m,i}} \cdot \left(\exp\left\{G_{m,i}\, l\right\} - 1\right), \quad (8.15)$$

and

$$Q'_{m,i} = Q_{m+1,i} \exp\left\{G_{m,i}\, l\right\} + \frac{\delta S_{m,i}}{G_{m,i}} \cdot \left(\exp\left\{G_{m,i}\, l\right\} - 1\right), \quad (8.16)$$

where the dash indicates that the quantities after the time step. Thus it has been shown that the intuitive expression developed in the previous sub-section is correct but that the length of each region must be the equal.

In [4] Perkins and Ormondroyd go on to develop several sophisticated expressions for the behaviour of both stimulated and spontaneous emission in the device (a SLED) on a much coarser time scale, as the carrier density is assumed to vary little over many 'round-trips' of the SLED cavity. Although such a technique could be applied to this case it does limit the type and range of optical inputs that can be considered. Therefore, equations (8.15) and (8.16) will be considered sufficient and a method will be developed to calculate the change in carrier density over a time step Δt.

8.2.3 Carrier Continuity Equation

Now that it has been established that the guide characteristics will be calculated at small steps in time, Δt it is essential to rewrite the carrier continuity equation (8.3) to take this into account. In the analysis of the photon conservation equations it was assumed that N_m is constant over the time step, thus is must be re-calculated between steps.

If the change in N_m is ΔN_m then it is possible to approximate (8.3) to,

$$\frac{\Delta N_m}{\Delta t} = \frac{J_m}{e.d} - B_r N_m \cdot (N_m + p_o) - \sum_{i=1}^{i=u} g_{m,i} \cdot \left(\tilde{P}_{m,i} + \tilde{Q}_{m,i} \right) , \quad (8.17)$$

where $\tilde{P}$ and $\tilde{Q}$ are now the temporally and spatially averaged fluxes over the time step Δt and the region length l,

$$\tilde{P}_{1,i} = \frac{1}{l} \frac{1}{\Delta t} \int_0^{\Delta t} \int_0^{l} P_{m,i}[z,t] .\, dz\, dt , \quad (8.18)$$

a similar expression exists for $\tilde{Q}_{m,i}$. For simplicity and to ensure continuity at the t=0 boundary it will be assumed that the process can be linearised so that,

$$\hat{P}_{m,i} = \frac{\bar{P}'_{m,i} + \bar{P}_{m,i}}{2} . \quad (8.19)$$

Thus the temporally and spatially averaged flux is assumed to be the linear average of the spatially averaged fluxes, $\bar{P}$, at the start and end of the time step. From chapter 6 it is known that the spatially averaged flux is given by,

$$\bar{P}_{m,i} = \frac{1}{G_{m,i}} \cdot \left(\frac{P_{m+1,i} - P_{m,i}}{l} - \delta S_{m,i} \right) \quad (8.20)$$

and more importantly,

$$\bar{P}'_{m,i} = \frac{1}{G_{m,i}} \cdot \left(\frac{P'_{m+1,i} - P'_{m,i}}{l} - \delta S_{m,i} \right) \quad . \qquad (8.20)$$

Equations (8.20) and (8.21) indicate that the average fluxes at the start and end of the time step are calculated with the same values of G and S.It is clear from equations (8.19 - 8.21) that the steady state model is just a special case of the temporal model where $P'_{m,i}$ is equal to $P_{m,i}$ for all t.

Using equation (8.17) it is possible to define the (constant) carrier density for the next time step,

$$N''_m = N_m + \Delta N_m \qquad (8.22)$$

$$= N_m + \Delta t \cdot \left(\frac{J_m}{e.d} - B_r N_m \left(N_m + p_o \right) - \sum_{i=1}^{i=u} g_{m,i} \cdot \left(\tilde{P}_{m,i} + \tilde{Q}_{m,i} \right) \right)$$

where the double dash indicates that the carrier density is constant for the duration of the next time step. It should be noted that other methods exist for calculating equations of the form (8.3), such as Runge-Kutta and Predictor-Corrector routines. However, these routines have computing overheads and for very small time steps and (relatively) slowly moving fluxes equations (8.22) is sufficient.

In this section, it has been shown that it is sufficient to calculate the temporal fluxes at the region boundaries only, in a similar manner to the steady state solution. These fluxes and the carrier density are calculated after small steps in time, $\Delta t = l/v$. In the next section the boundary conditions will be established and the model algorithm described.

8.3 Modelling Considerations

8.3.1 Boundary Conditions

In a similar manner to the steady state model the two ends of the guide are assumed to be simple 'facets' with reflectances, R_1 and R_2. Hence,

$$P_i[t,0] = R_1 \cdot Q_i[t,0] + P_{in,i}[t] , \tag{8.23}$$

$$Q_i[t,L] = R_2 \cdot P_i[t,L] . \tag{8.24}$$

where $P_{in,t}[t]$ is the time dependent input optical flux.

In addition the guide parameters have to be established at the t=0 boundary. This can be achieved in two ways. Firstly, the guide and source can be assumed to be in a particular steady state, calculated using the steady state model in chapter 6. Alternatively, the results of a previous run of the temporal model can be used. This allows very long times to be modelled, despite any computational limits.

Although the current density, J_m in equation (8.22) is shown to be constant, this need not necessarily be so and a time varying current may be modelled. Thus guide turn-on effects could be examined, although they have not been in this thesis.

In contrast to the steady state model the instantaneous fluxes are not continuous over the region boundaries. Instead the value of $P'_{m,i}$ is used as the driving value of flux for the next time step in the $m+1^{th}$ region. In the general case, $P'_{m,i} \neq P_{m,i}$. In practice this means that the model is taking 'snap-shots' of the fluxes at discrete steps in time. However if a wavefront of a travelling flux is followed from boundary to boundary along the guide in space and time, then the growth or decay of the wavefront will be continuous, as shown in figure 8.1.

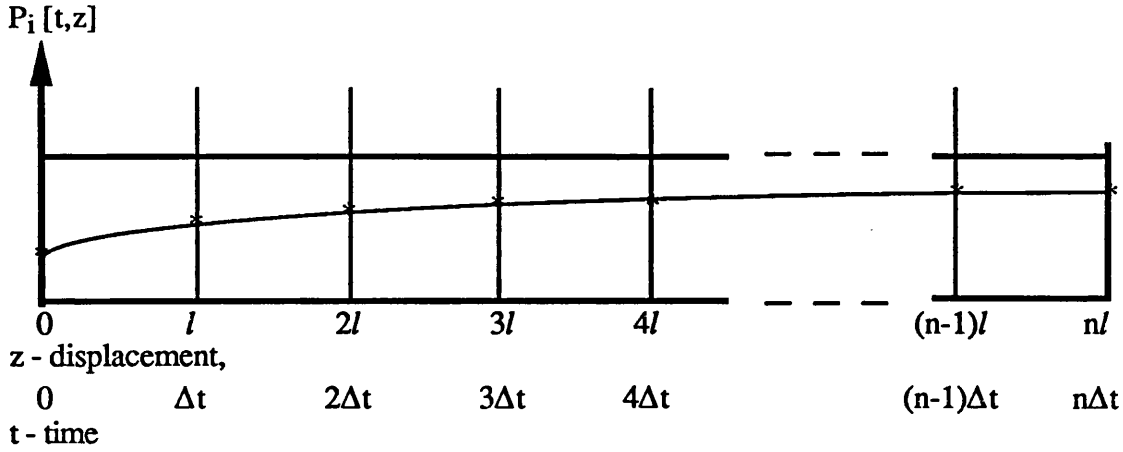

Figure 8.1 Time and Space Variation of a Flux Wavefront Propagating Down a Pumped Waveguide.

8.3.2 Large Signal Algorithm

The majority of the algorithm has been described in the discussion of the boundary conditions and the manipulation of the continuity equations, so only a brief summary is required here. Using the steady state model or a previous run of the temporal model, the initial conditions (t=0) are established. The forward and backward travelling flux are simultaneously allowed to 'walk' in their respective directions of propagation. After each step in time and for each region of the guide, the carrier density and associated terms are calculated, and the boundary conditions are applied. This is the major difference between the large and small signal techniques, in the SSA these quantities are linearised about the bias point and may only vary by a small amount. No such restriction is made in the large signal model, hence effects such as bias point drift can be modelled.

Depending on the nature of the input the model continues to step in time until a satisfactory solution is obtained. In a similar manner to the static model, the guide characteristics are calculated on a region by region basis. However, unlike the static case, P and Q are solved simultaneously without the need for multiple iterations. Because of the inclusion of the longitudinal variation of flux and carrier density this model is applicable to a wide variety of situation where spatial averaging techniques cannot be used.

8.3.3 Timing Considerations and Model Limitations

From the steady state analysis it has been found that regions of constant carrier density of approximately 10 - 50 μm are sufficient for the situations modelled. Taking the group velocity of light in the guide to be,

$$v = \frac{c}{n_g} \tag{8.25}$$

where, n_g is the group refractive index and c is the velocity of light in a vacuum. For a particular value of group velocity, there is constant ratio between the time step and the region length,

$$\frac{\Delta t}{l} = \frac{ng}{3.0\times10^8} \approx 15\ \text{fs}/\mu\text{m}, \tag{8.26}$$

for $n_g \approx 4.3$ - 4.5 [2,4,6,7]. Thus the time step lies in the range 0.15 - 0.75 ps for the range for region lengths given above. Clearly the model cannot be used to consider sub-pico second effects using region lengths of this order and the assumption that the gain is instantaneous breaks down on these time scales. However, as the modulation frequencies of AlGaAs lasers and SLEDs are limited to approximately 10 GHz, and relaxation oscillations to several pico seconds [1,2,3,4] the model is more than sufficient for the cases considered.

It is quite difficult to decrease the time step to below these values as the computational time required is proportional to the number of regions squared (and a lower time step requires more regions). For the machine used [1] the following empirical formula was derived for the maximum number of regions permissible when considering an overall time of 100 ns,

$$N_{max} = \sqrt{0.8\cdot L}, \tag{8.27}$$

---

[1]SWURCC : ICL 3580

where L is the guide length in micrometers. Using (8.27) 100 seconds CPU time is used for each model nano second.

There are two other limitations which must be addressed. In this analysis it is assumed that the optical gain is instantaneous and is not effected by the magnitude of the flux density, ie totally homogeneous broadening on the time scales considered. This assumptions is in keeping with other authors [1, 3, 7] but its validity is questioned [2,12]. In GaAs devices the intraband scattering times are sufficiently small (≈0.1 ps or less) to assume homogeneous broadening for most practical values of flux density . However for InP devices this is not the case and spectral hole burning effects have to be taken into account.

The other effect that has to be addressed is the change in refractive index with carrier density. It is generally accepted that the refractive index in pumped GaAs is complex . The imaginary part is dependent on the gross optical gain and increases with carrier density, whilst there is a corresponding decrease in the real part [2]. In the steady state this is not a problem as the refractive index does not have a great effect on the solution. However, in the dynamic case the solution is dependent on the group refractive index which is in turn dependent on the real refractive index. There are many undesirable features associated with a change in refractive index, such as: spectral dispersion, smearing of signals, and wave mixing effects [11, 12]. It is not possible to take account of these effects using this type of model as the region length is fixed. However it is possible to incorporate it into other models, such as the spatially averaged model presented by Adams [6] and the transmission line model presented by Lowery [7].

8.4 Results

Unless otherwise stated the parameter values used are the same as for table 6.1.

8.4.1 Basic Output Spectra

In the majority of cases examined in this chapter the optical input power is a simple sinusoidally modulated signal about a dc bias level, restricted to a single wavelength slot,

$$W_{in,k} = \hat{W}_{in}\left(1 + m\cdot\cos(\omega_m t)\right), \qquad (8.28)$$

$$W_{in,j} = 0, \quad j \neq k \qquad (8.29)$$

where $\hat{W}_{in}$ will be referred to as the optical bias power, m is the modulation index and ω_m is the modulation frequency.

The total output from the guide is sampled at an integral number of time steps in order to reduce the storage requirements but a sufficient number of output points and total output cycles are sampled to ensure the required accuracy. In general the model is allowed to run for at least twenty full periods of the modulated input, after a 20 ns delay, during which no output samples are taken. This delay is included to ensure that any initial transient or dc drift has settled out before sampling takes place.

The sampled output can be examined directly, as shown by Otsuka [6], but such a time series holds little information as it merely shows that the output is distorted without quantifying the distortion. It is far more profitable to transform this series into the frequency domain using the Fast Fourier Transform technique describe in section 6.4.6.

In the FFT technique the output is transformed into a descretized frequency spectrum. The bandwidth of each component of the spectrum is determined by the time 'window' width, ie the total time over which samples are taken,

$$BW = \frac{1}{T_w} . \tag{8.30}$$

From (8.30) it is clear that the frequency resolution can only be improved if the time window width is increased. Thus several output cycles must be considered if the behaviour of the output frequency components between the harmonics is to be examined. In addition, there must be exactly an integral number of full output cycles in the window, otherwise so called 'windowing' effects occur. The total number of sampling points taken in the window determines the maximum frequency that can be resolved,

$$f_{max} = \frac{N_{pts} \cdot BW}{2} \tag{8.31}$$

where the factor of 2 is included to prevent aliasing.

In figures 8.2 to 8.5 the basic response of the guide to a 1 GHz modulated input can be seen. As is expected from the form of the input, the two dominant components are situated at the fundamental modulation frequency and dc. The magnitude of the dc component is determined by the optical bias power and the gain in the guide. At transparency,

$$W_{out}\Big|_{dc} \approx \hat{W}_{in}\Big|_{dc} \tag{8.33}$$

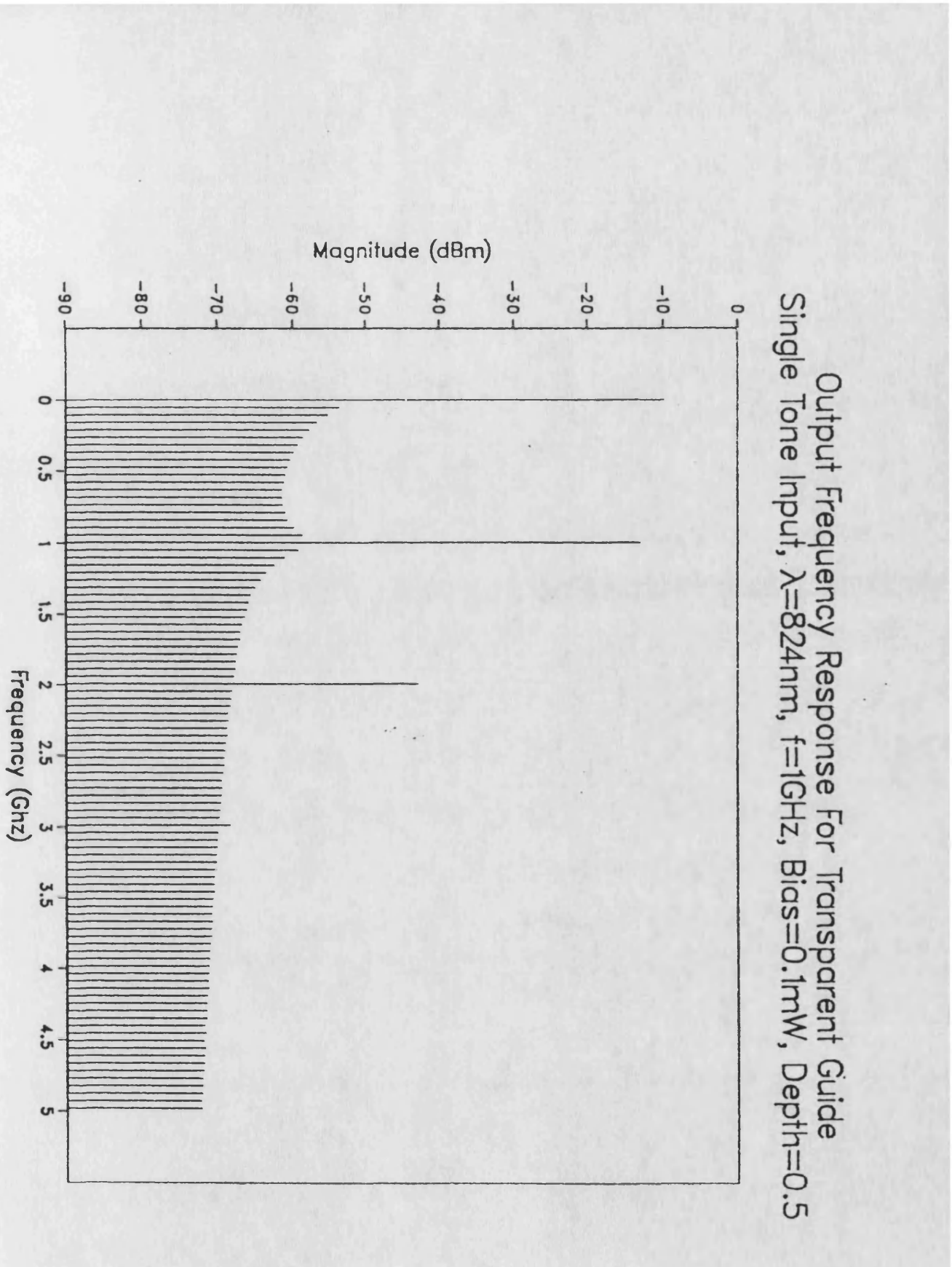

Figure 8.2 : Discrete frequency, optical output power spectrum, for a guide biased to transparency, for a single tone optical input signal, 1 GHz frequency, 0.1 mW bias power, 824 nm wavelength.

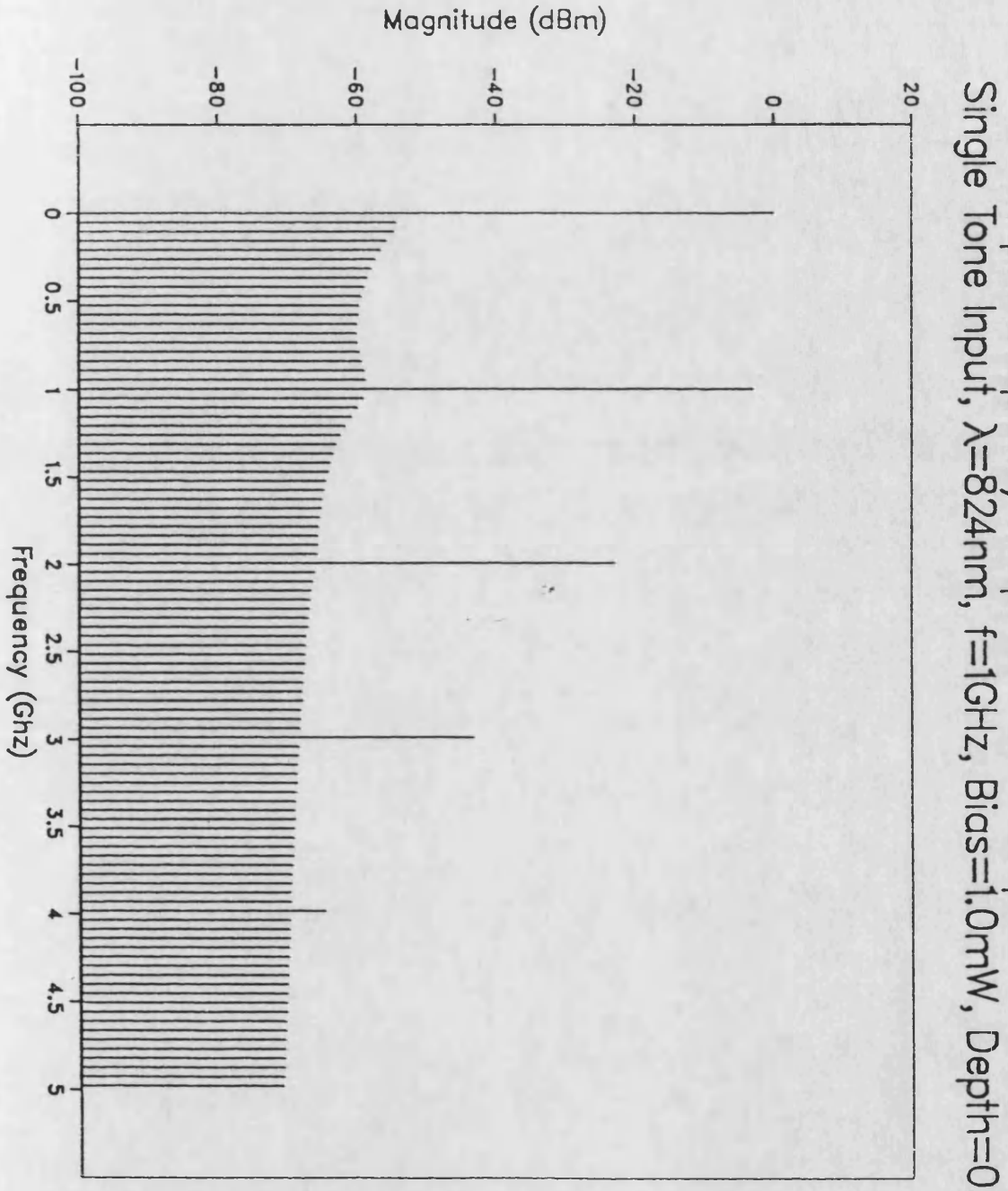

Figure 8.3 : Discrete frequency, optical output power spectrum, for a guide biased to transparency, for a single tone optical input signal, 1 GHz frequency, 1 mW bias power, 824 nm wavelength.

and the fundamental power is given by,

$$W_{out}\Big|_{fun} \approx \frac{m}{\Delta F}\hat{W}_{in}\Big|_{fun} , \qquad (8.34)$$

where ΔF is the forward pass gain compression term, $\exp(\gamma L)$, discussed in chapters 6 and 7.

Figure 8.3 shows a typical output spectrum. As well as the dc and fundamental terms, there are also higher harmonics which fall off regularly with increasing frequency and a noise 'floor' which also falls off with frequency. This noise is due to ASE in the guide and the interaction between the optical input and the carrier density. It is **not** numerical noise due to rounding or the FFT analysis. When the model was developed the effects of numerical noise were examined and were **at least** 100 dB down on the signal for a 0.1 mW input. The 'shoulders' in the noise response around the fundamental are due to interaction between the fundamental and the low frequency variations in the carrier density.

As the optical bias power is raised to 5 or 10 mW the output spectrum becomes cluttered. At these powers there is considerable interaction between the flux and carrier density. As the natural frequency of the carrier density variations is below the modulation frequency they must lag the flux variations. This gives rise to a time varying gain lagging the flux, which will generate many high power harmonics as the output is distorted away from a pure sinusoid.

From these output spectra it is clear that the SNR figures presented in chapter 6 are perhaps over pessimistic. If some form of frequency filtering is applied, then an output SNR in the region 40 - 50 dB can easily be achieved. In this case the total noise power is spread over 512 frequency components, so on average, each component will be 27 dB lower than the total. Hence if two components on either side of the fundamental are considered (say), then a 20 dB improvement over the SNRs calculated in chapter 6 can be achieved.

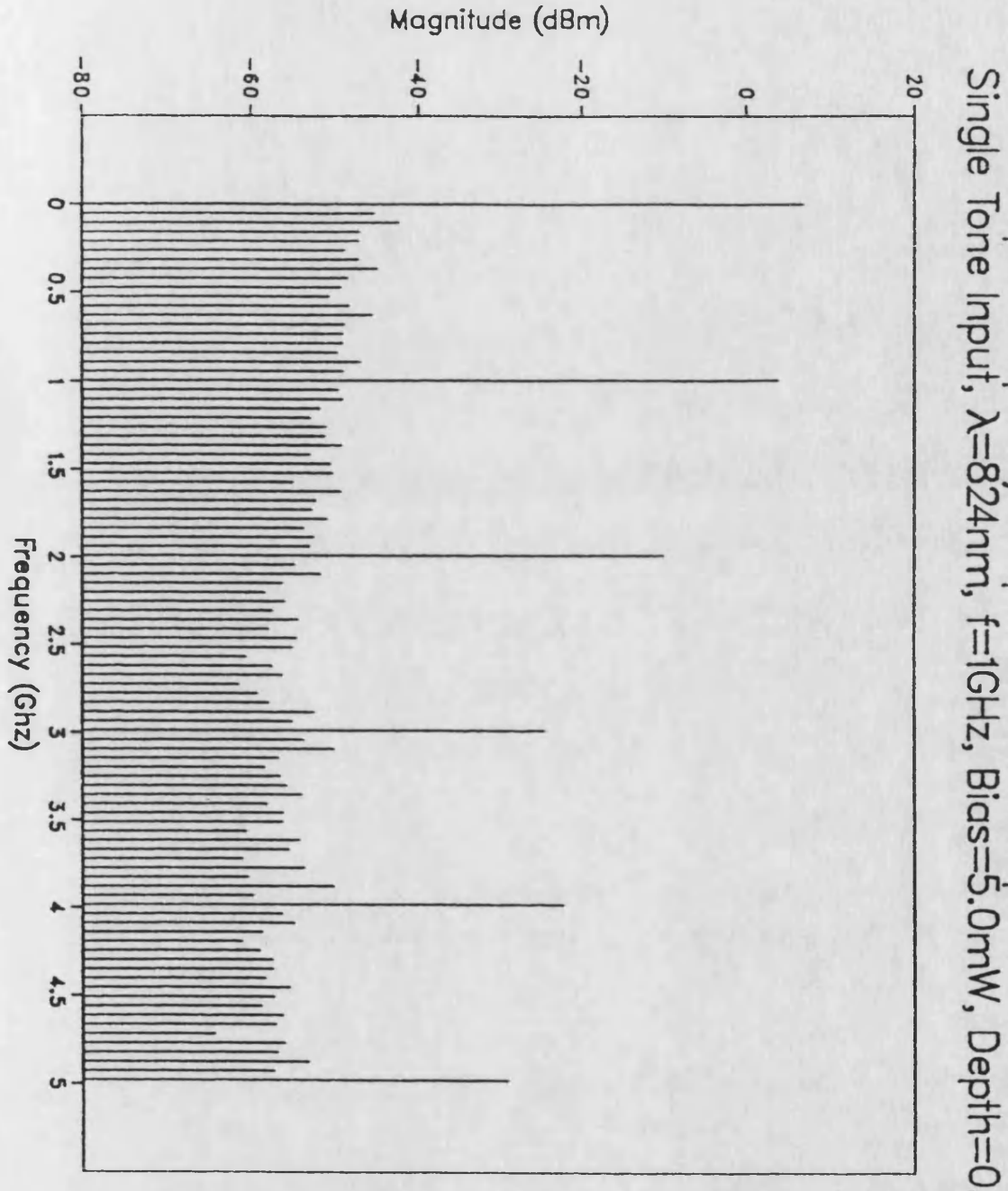

Figure 8.4 : Discrete frequency, optical output power spectrum, for a guide biased to transparency, for a single tone optical input signal, 1 GHz frequency, 5 mW bias power, 824 nm wavelength.

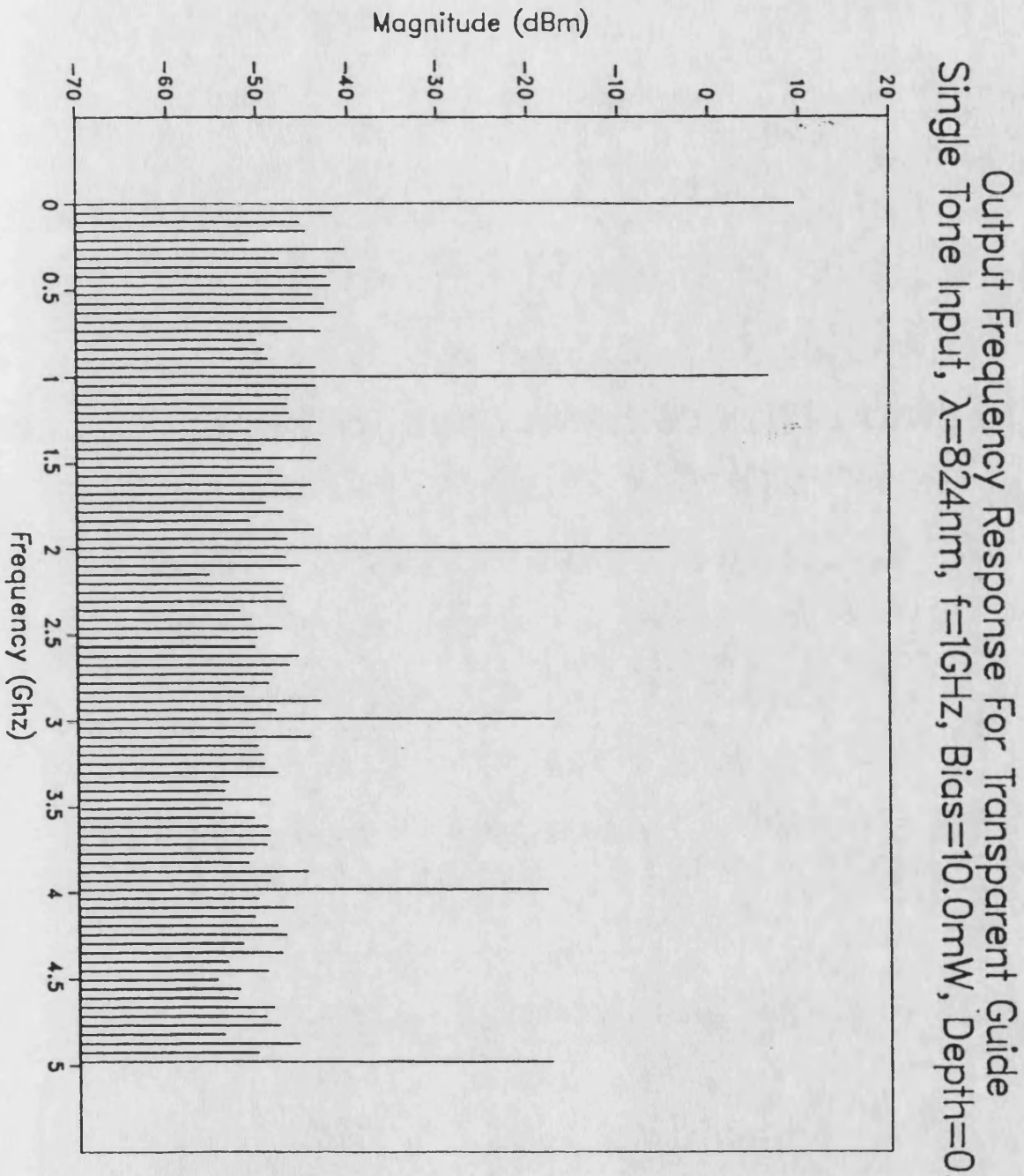

Figure 8.5 : Discrete frequency, optical output power spectrum, for a guide biased to transparency, to a single tone optical input signal, 1 GHz frequency, 10 mW bias power, 824 nm wavelength.

8.4.2 Step Response and Pulse Response

The great advantage of a large signal model is that it is very easy to consider inputs other than sinusoids without having to reformulate the continuity equations. It is also of great benefit to consider the basic step response of the guide. Firstly, the step response can give insight into the basic behaviour of the guide and the time constants associated with the continuity equations. In addition it can be used to provide a comparison between the static and large signal models. If the time dependent model is allowed to run for sufficient time with a constant input power, the solution will settle towards the value given by the steady state model.

Figure 8.6 shows the case when the input is either held at the steady state value of 1 mW or stepped to 2 mW at t=0. There is a slight drift when the input is held constant, this is mainly due to a slight rounding error introduced when loading the steady state boundary values. The step response is similar to that calculated by Otsuka [7] for a TWLA, and the final value of 1.41 mW for the 2 mW input is identical to that given by the steady state model (see figure 6.10). Initially the leading edge will see an identical gain to the steady state signal, ie 0dB. However, due to the increase stimulated recombination there is an imbalance in the carrier continuity equation (8.3), hence the output signal decays to a new steady value. Plotting the relative overshoot of the output from the final value, figure 8.7, it is clear that the decay is basically exponential. The slope of figure 8.7 gives a dominant decay time constant τ = 2.24 ns, for this case. This corresponds closely to the reciprocal of the 'natural frequency' of equation (8.3),

$$B_r N(N+p_o) - \sum_{i=1}^{i=u} g_i \cdot \left(\tilde{P}_i + \tilde{Q}_i\right) \qquad (8.35)$$

which has a value of 4.7×10^8 s^{-1}, giving τ_n = 2.13 ns, using the values and approximations of the small signal analysis.

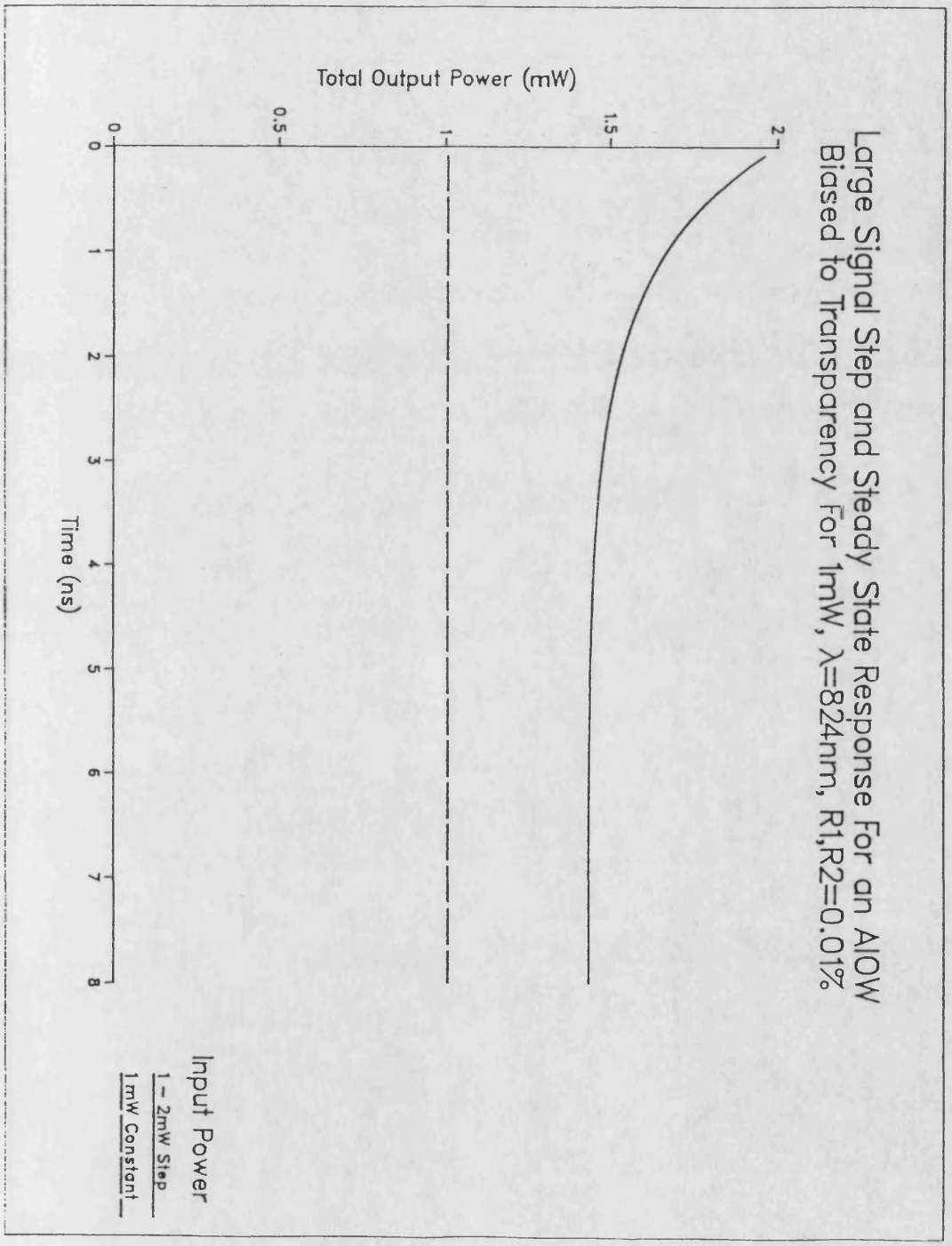

Figure 8.6 : Step response, for guide biased to transparency to a 1 mW optical bias power, 824 nm wavelength.

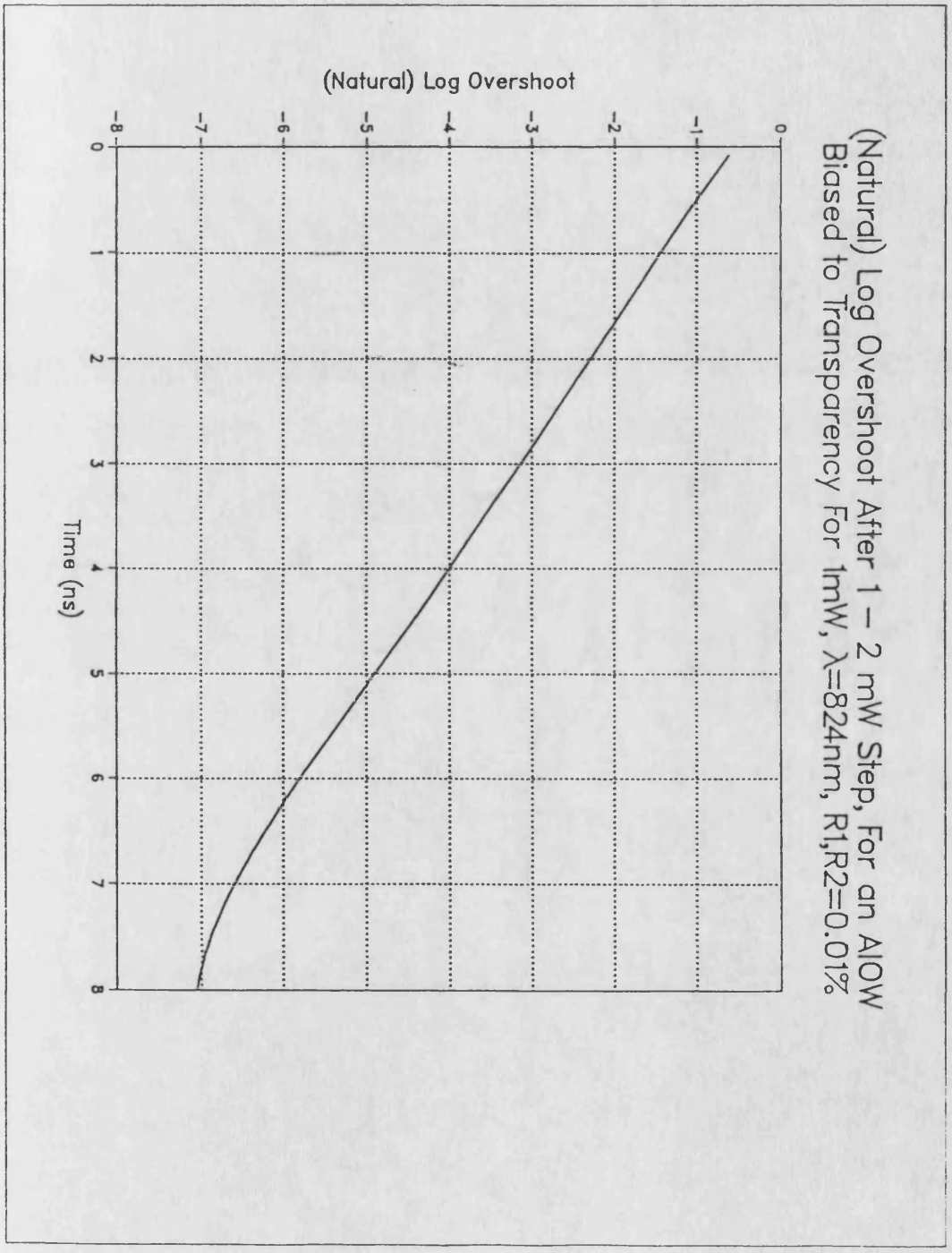

Figure 8.7 : Step response overshoot as function of time, for a 1 - 2 mW step applied at t = 0, to a guide biased to transparency to a 1 mW optical bias power, 824 nm wavelength.

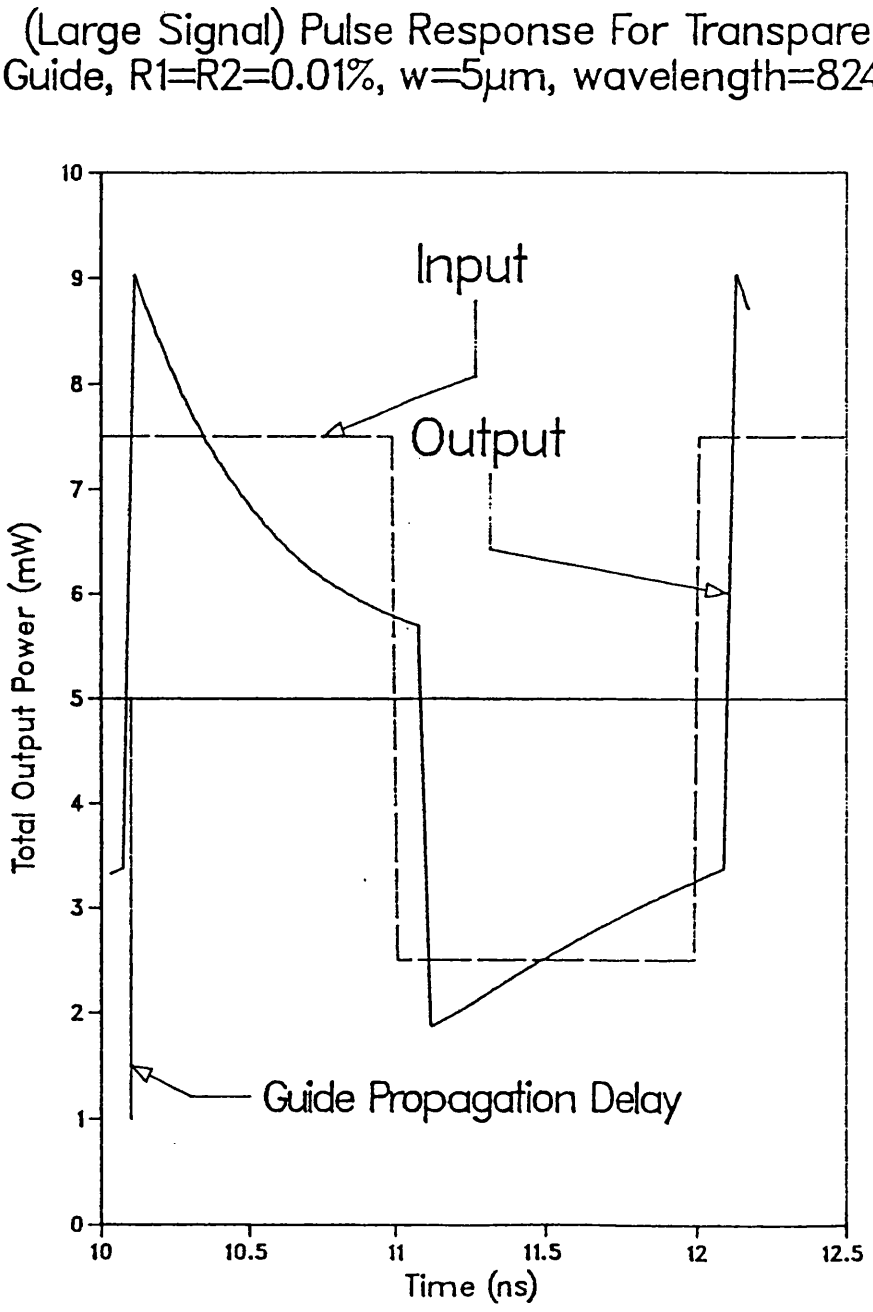

Figure 8.8 : Large signal pulse response, for a guide biased to transparency to a 5 mW optical bias power, 824 nm wavelength.

Figure 8.8 shows the response of the guide to a train of pulses. The input is varied between 2.5 and 7.5 mW whilst the guide is electrically biased to transparency to a 5 mW steady state signal. In this case there is a significant amount of pulse distortion. For much smaller inputs (< 0.1 mW) the pulse distortion is limited.

On the rising edge of the pulse the guide has excess gain and the output signal overshoots the input power. However, the increased stimulated recombination depletes the carriers and hence the gain. As a consequence the output falls in a similar manner to that described for the step response. This fall in the output power, to below the input power indicates that there is net loss on the pulse falling edge. Thus the output falls to below the input power. The imbalance in the carrier continuity equation is now opposite to that considered above and the carrier density increases until there is net gain before the rising edge.

There are two further comments to be made regarding figure 8.8. Firstly, from equation (8.35) it is clear that the stimulated recombination term controls the rate of change of carrier density and hence gain. Therefore, the rate of decay when the pulse is high will be greater than when the input is low because all three controlling factors, N, g_i and $(\tilde{P}_i + \tilde{Q}_i)$ are greater. Secondly, the asymmetrical output function will lead to a shift in the dc value of flux and hence the guide will drift away from net transparency.

8.4.3 Frequency Response

Figures 8.9 to 8.12 show the frequency response of the guide when biased to transparency to 0.1, 1, 5 and 10 mW optical bias powers respectively. In addition, to the fundamental and dc components, the higher harmonics distinguishable from the noise floor are shown. Although the large scale in these figures tends to flatten the response, the step predicted by the small signal analysis is apparent in the 100 MHz region.

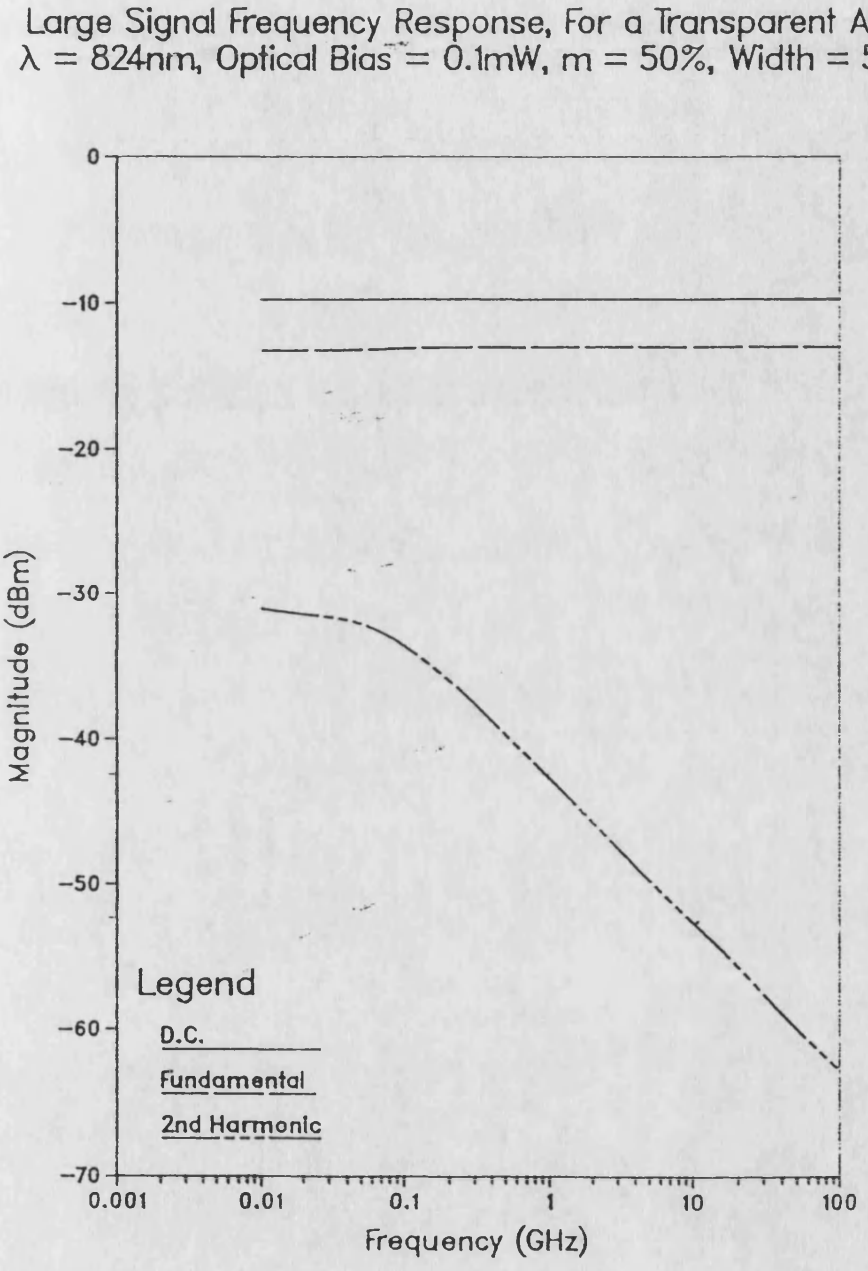

Figure 8.9 : Large signal, harmonic output power, frequency response, for 50% modulation, for a guide biased to transparency to a 0.1 mW optical bias.

Table 8.1 shows the fundamental gain compression terms compared with those calculated from the small signal analysis (from table 7.3).

Input Bias Power (mW)	Large Signal Compression (dB)	Small Signal Compression (dB)
0.1	0.25	0.31
1.0	2.23	2.45
5.0	7.10	7.50
10.0	9.50	10.10

Table 8.1 : Fundamental Component Gain Compression Term, $W_{out}[\infty] / W_{out}[dc]$, for Large and Small Signal Models.

In all cases the gain compression term is slightly below that predicted by the SSA. This is because the SSA ignores the harmonic power which can be significant.

A striking feature of the frequency response is the roll-off of the higher harmonics above the break region, for all input powers. Intuitively one may imagine the process in the following way. As the interaction between the flux and carrier density decreases with frequency (see section 7.2.3 and equation (7.15)), the change in gain and non-linearity in the transmission characteristics will also decrease. As was seen in chapter 6, as the non-linearity decreases then the harmonics also decline. This roll-off is quite regular at 10 dB/decade for the 2nd harmonic, 20 dB/decade for the 3rd and so on for the other harmonics. The key to the form of the frequency response can be found in the SSA.

In section 7.2.2 several Δ^2 terms were neglected on the grounds that they are small, it is these terms which lead to the higher harmonic powers as,

$$\left(n \cdot e^{j\omega t}\right) \cdot \left(p \cdot e^{j\omega t}\right) = n \cdot p \cdot e^{j2\omega t} . \qquad (8.36)$$

As has been shown in the previous two chapters, by far the most significant effect is the change in net effective gain with carrier density. This change is dependent on the

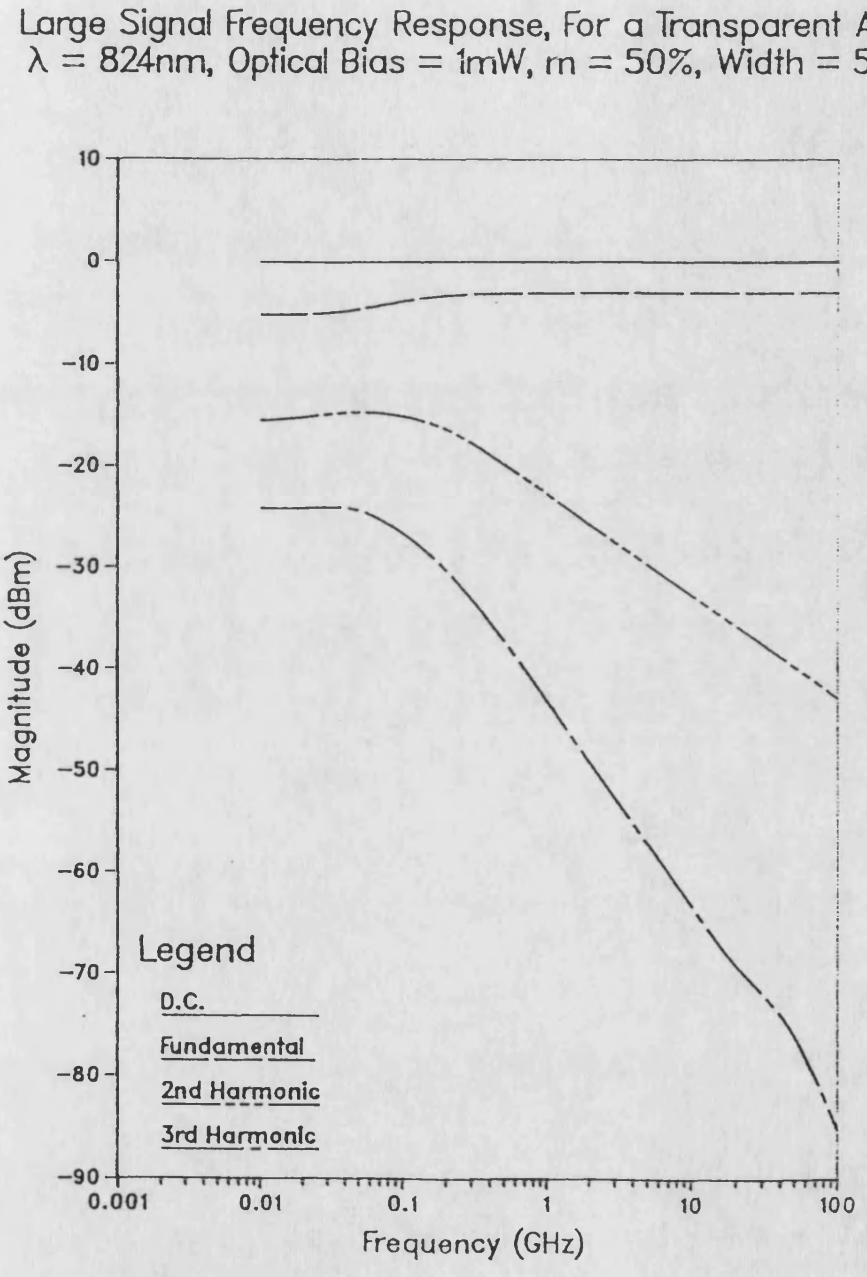

Figure 8.10 : Large signal, harmonic output power, frequency response, for 50% modulation, for a guide biased to transparency to a 1 mW optical bias.

gain polynomial and in the small signal analysis presented in chapter 7, a Taylor expansion was used to give the variation in gain as,

$$g\left[\hat{N}+n\cdot e^{j\omega t}\right] = g\left[\hat{N}\right] + n\cdot e^{j\omega t}\cdot \frac{dg\left[\hat{N}\right]}{dN} + n^2\cdot e^{j2\omega t}\cdot \frac{d^2g\left[\hat{N}\right]}{dN^2} + \text{etc} \quad (8.37)$$

The fundamental component is dominated by an expression of the from,

$$\frac{dp_1}{dz} = G\cdot p_1 + \frac{dG}{dN}\, n\cdot \hat{P} \quad (8.38)$$

where the 1 subscript refers to the fundamental component, and the backward travelling flux and spontaneous emission have been ignored. Using the SSA to substitute for n in (8.38) yields,

$$\frac{dp_1}{dz} = \left(G - \frac{g\cdot \frac{dG}{dN}\,\hat{P}}{\omega_n\left(1 + \frac{j\omega}{\omega_n}\right)} \right) p_1 \quad (8.39)$$

Thus, at high frequencies the dynamic variation in carrier density becomes negligible compared with the steady state value and (8.39) becomes,

$$\frac{dp_1}{dz} \approx G\cdot p_1 \quad (8.40)$$

ie, the fundamental component is independent of frequency above the break region, and sees the same gain as the optical bias power.

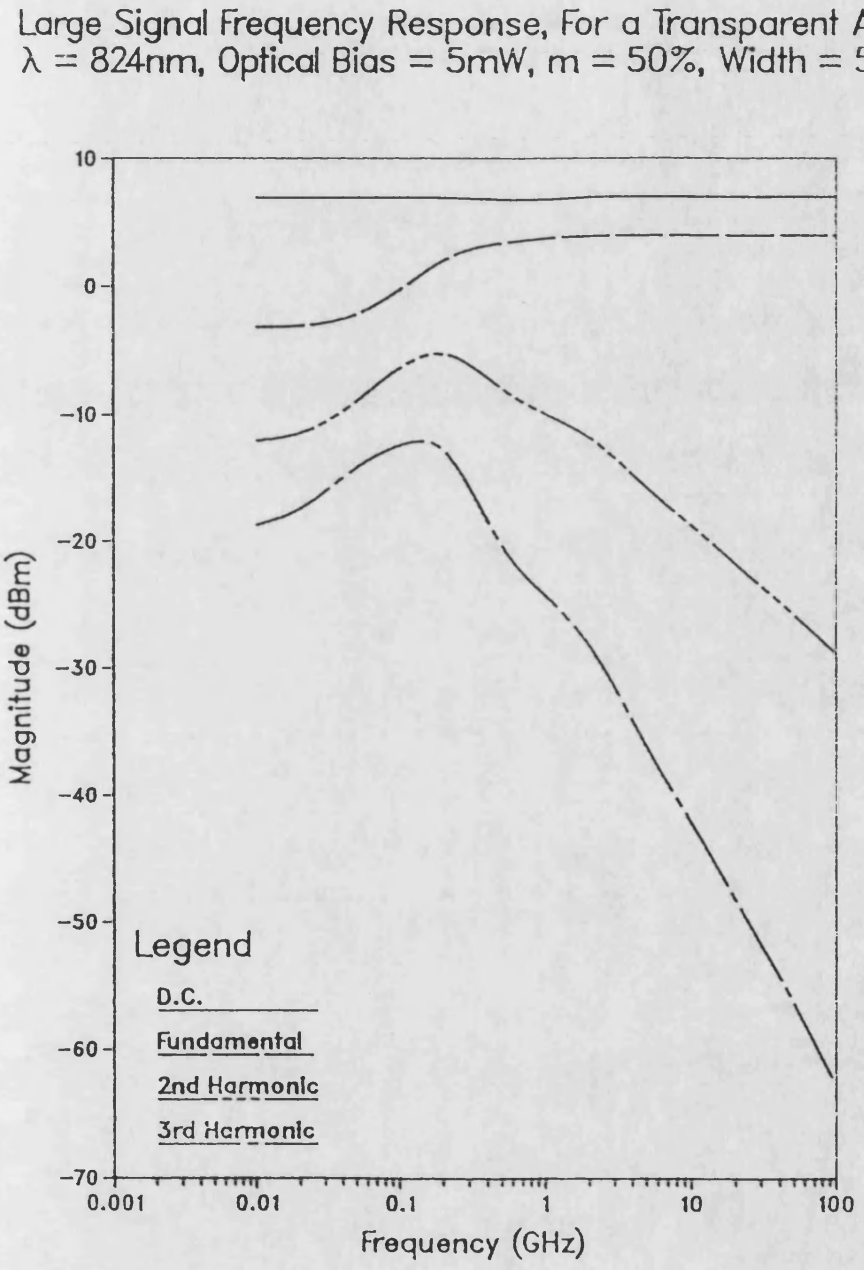

Figure 8.11 : Large signal, harmonic output power, frequency response, for 50% modulation, for a guide biased to transparency to a 5 mW optical bias.

From equations (8.37) and (8.38) the second harmonic flux is determined by,

$$\frac{dp_2}{dz} = n \cdot \frac{dG}{dN} p_1 \qquad (8.41)$$

$$= \frac{-g}{\omega_n\left(1 + \frac{j\omega}{\omega_n}\right)} \frac{dG}{dN} p_1^2 \ .$$

At frequencies above the break region p_1 has a constant value, therefore the right hand side of (8.40) will roll-off at 10 dB/decade. It is relatively easy to show that the second harmonic power will also roll-off at the same rate. The analysis can now be extended to the higher harmonics, in the general case (8.41) becomes,

$$\frac{dP_n}{dz} = \frac{-g \cdot p_1}{\omega_n\left(1 + \frac{j\omega}{\omega_n}\right)} \frac{dG}{dN} p_{n-1} \ . \qquad (8.42)$$

Thus, above the break region the n^{th} harmonic will roll of at 10 dB/decade faster than the $n\text{-}1^{th}$ harmonic, ie at $(n-1)\cdot 10$ dB/decade. [2]

The final effect that must be addressed is the shape of the harmonic components around the natural frequency of carrier density variation. Firstly, there is a rise in harmonic power as the fundamental power increases, according to (8.42). However, the carrier density roll-off then begins to dominate and eventually a smooth characteristic is seen. The rise in harmonic power (or the reduced rate of roll-off in the case of figure 8.9) is determined by the optical bias power and the fundamental output power.

---

[2]Note : this analysis is only approximate and holds for frequencies greater than the upper break frequency discussed in chapter 7, $\omega_u = \omega_n \cdot \sqrt{(\gamma L - \ln 2) / \ln 2}$

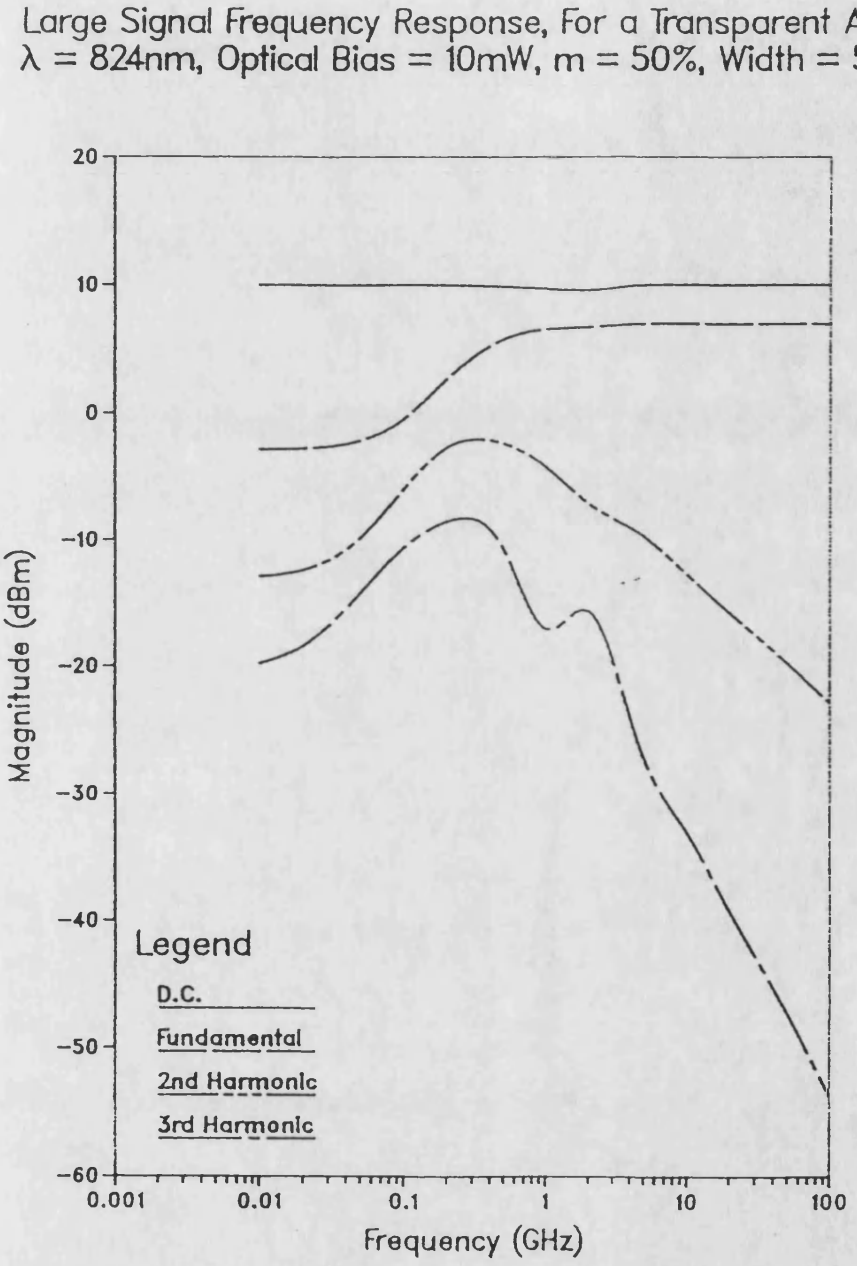

Figure 8.12 : Large signal, harmonic output power, frequency response, for 50% modulation, for a guide biased to transparency to a 10 mW optical bias.

8.4.4 Modulation Response with Bias Power and Frequency

Figures 8.13 to 8.24 represent the bulk of the work done using the large signal analysis. Indeed each figure represents approximately 50 hours CPU time on the ICL 3580. Each figure has two parts, the modulation response (a) which shows the dc, fundamental and higher harmonic components; and the modulation distortion (b) which shows the higher harmonics relative to the fundamental power. Using the terminology in chapter 6, the (a) part shows the variation of the B coefficients with modulation depth,

$$W_{out} = B_0 + B_1 \cdot \cos(\omega_m t) + B_2 \cdot \cos(\omega_m t) + \text{etc} . \qquad (8.43)$$

whilst the (b) part shows the variation of the D coefficients,

$$D_n = \left| \frac{B_n}{B_1} \right| = W_n\big|_{dBm} - W_1\big|_{dBm} \qquad (8.44)$$

where $W_1\big|_{dBm}$ and $W_n\big|_{dBm}$ are the magnitude in dBm of the fundamental and n^{th} harmonic respectively. When examining these figures it is essential to remember that there is a noise floor in the region of -50 to -70 dBm, depending on the bias and frequency. Thus harmonic components in this region are no longer governed by a continuous relationship, as shown in equation (8.42) and become unpredictable in their nature.

Twelve two part figures are rather indigestible on their own, so four summary tables are presented. Table 8.2 shows the compression of the fundamental output component from that expected if the guide was perfectly transparent, whilst tables 8.3 and 8.4 summarise the 2^{nd} harmonic magnitude and distortion respectively. Table 8.5 details the ratio, in dB of the 3^{rd} to 2^{nd} and 4^{th} to 3^{rd} harmonics.

Bias Power	0.1mW		1mW		10mW	
Modulation Index	0.1	1.0	0.1	1.0	0.1	1.0
f = 10 MHz	0.3	0.2	2.4	1.8	10	7
f = 100 MHz	≈0	0	1	0.5	7.8	5.7
f = 1 GHz	0	0	0	0	0.5	1
f = 10 GHz	0	0	0	0	0	0

Table 8.2 : Fundamental Component Compression (dB) (W_{out}/W_{trans})

For 3 Bias Powers and Decade Frequency Spacing.

Bias Power	0.1mW		1mW		10mW	
Modulation Index	0.1	1.0	0.1	1.0	0.1	1.0
f = 10 MHz	-45	-25	-29	-9	-27	0
f = 100 MHz	-47	-27	-29	-9	-22	-5
f = 1 GHz	-57	-37	-37	-17	-17	1
f = 10 GHz	-62	-47	-47	-27	-27	-9

Table 8.3 : Second Harmonic Magnitude (dBm), For 3 Bias Powers

and Decade Frequency Spacing.

Bias Power	0.1mW		1mW		10mW	
Modulation Index	0.1	1.0	0.1	1.0	0.1	1.0
f = 10 MHz	-24.5	-15	-18	-7	-17.5	-3
f = 100 MHz	-27	-17	-18	-8	-13.5	-0.5
f = 1 GHz	-37	-27	-27	-17	-17	-8
f = 10 GHz	-42	-37	-37	-27	-27	-17

Table 8.4 : Second Harmonic Distortion (dB), For 3 Bias Powers

and Decade Frequency Spacing.

Bias Power	0.1mW		1mW		10mW	
Ratio	3/2	4/3	3/2	4/3	3/2	4/3
f = 10 MHz	-19	-18	-6	-5	-2	-1
f = 100 MHz	-18	-16	-8	-7.5	-1	-1
f = 1 GHz	-28	-7.5	-17	-18	-11	-1.4
f = 10 GHz	-38	-14.5	-27	-18	-17	-18

Table 8.5 : Ratio of Higher Harmonic Magnitudes (dB), with a

modulation index of 1.

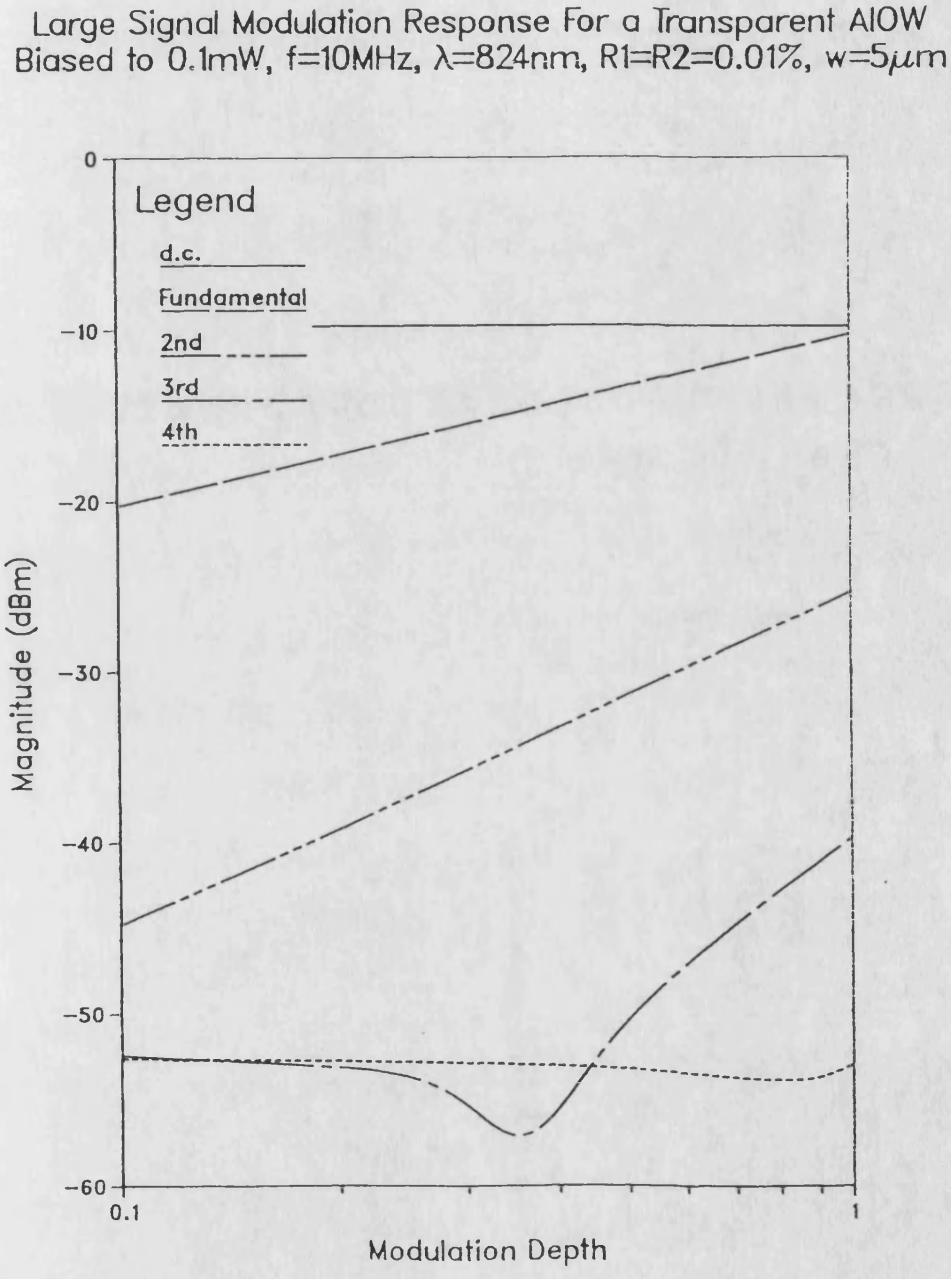

Figure 8.13a Large signal, harmonic output power, modulation response, at 10 MHz, for a guide biased to transparency to a 0.1 mW optical bias.

(a) Modulation response,

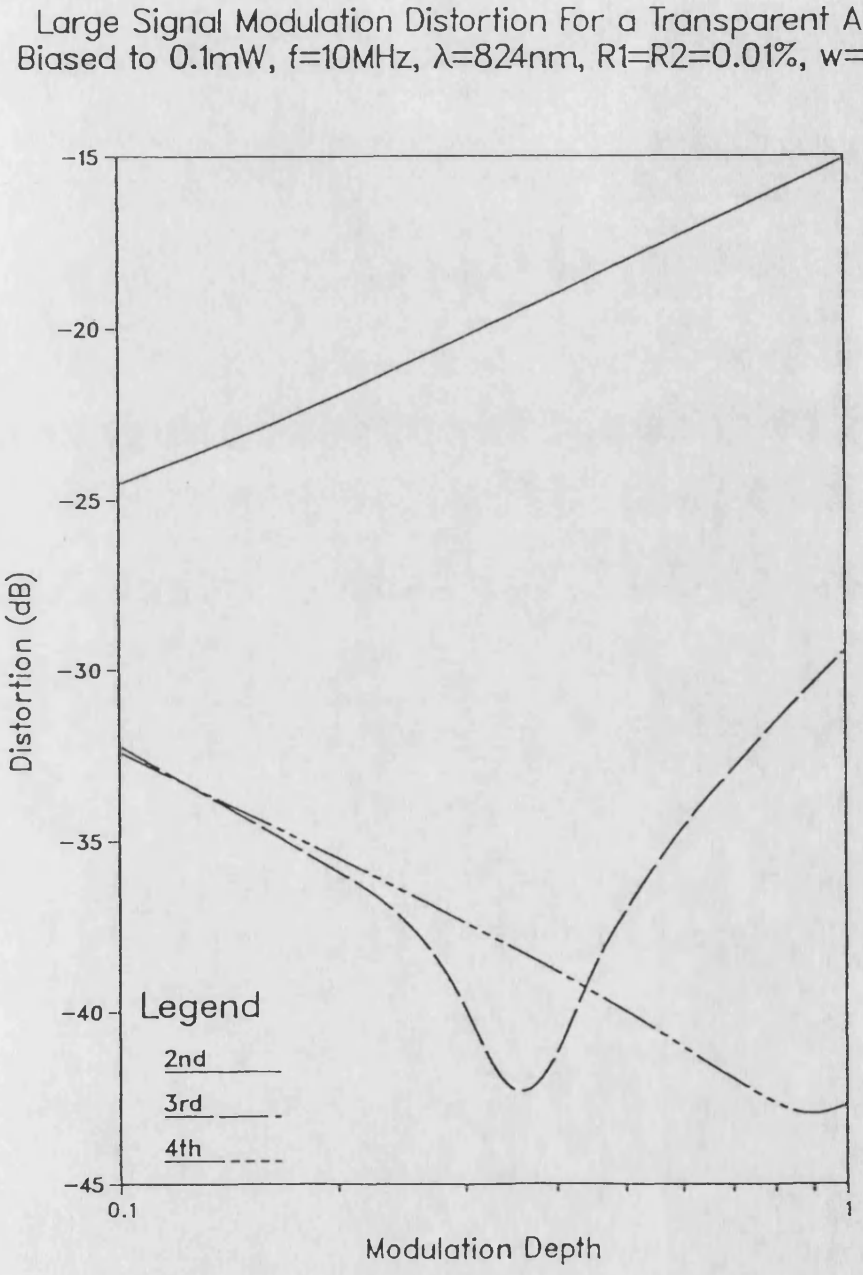

Figure 8.13 b Large signal, harmonic output power, modulation response, at 10 MHz, for a guide biased to transparency to a 0.1 mW optical bias. (b) Modulation distortion.

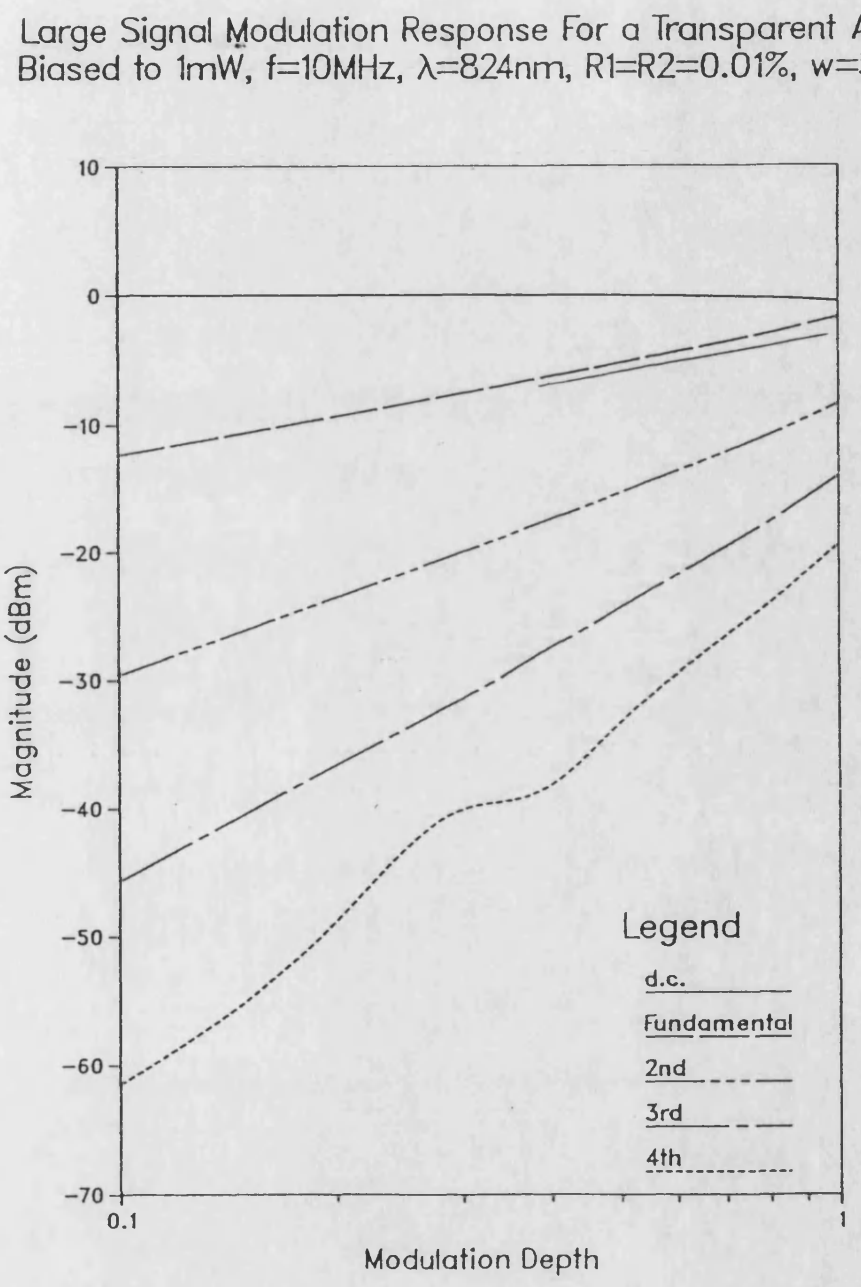

Figure 8.14*a* Large signal, harmonic output power, modulation response, at 10 MHz, for a guide biased to transparency to a 1 mW optical bias. (a) Modulation response,

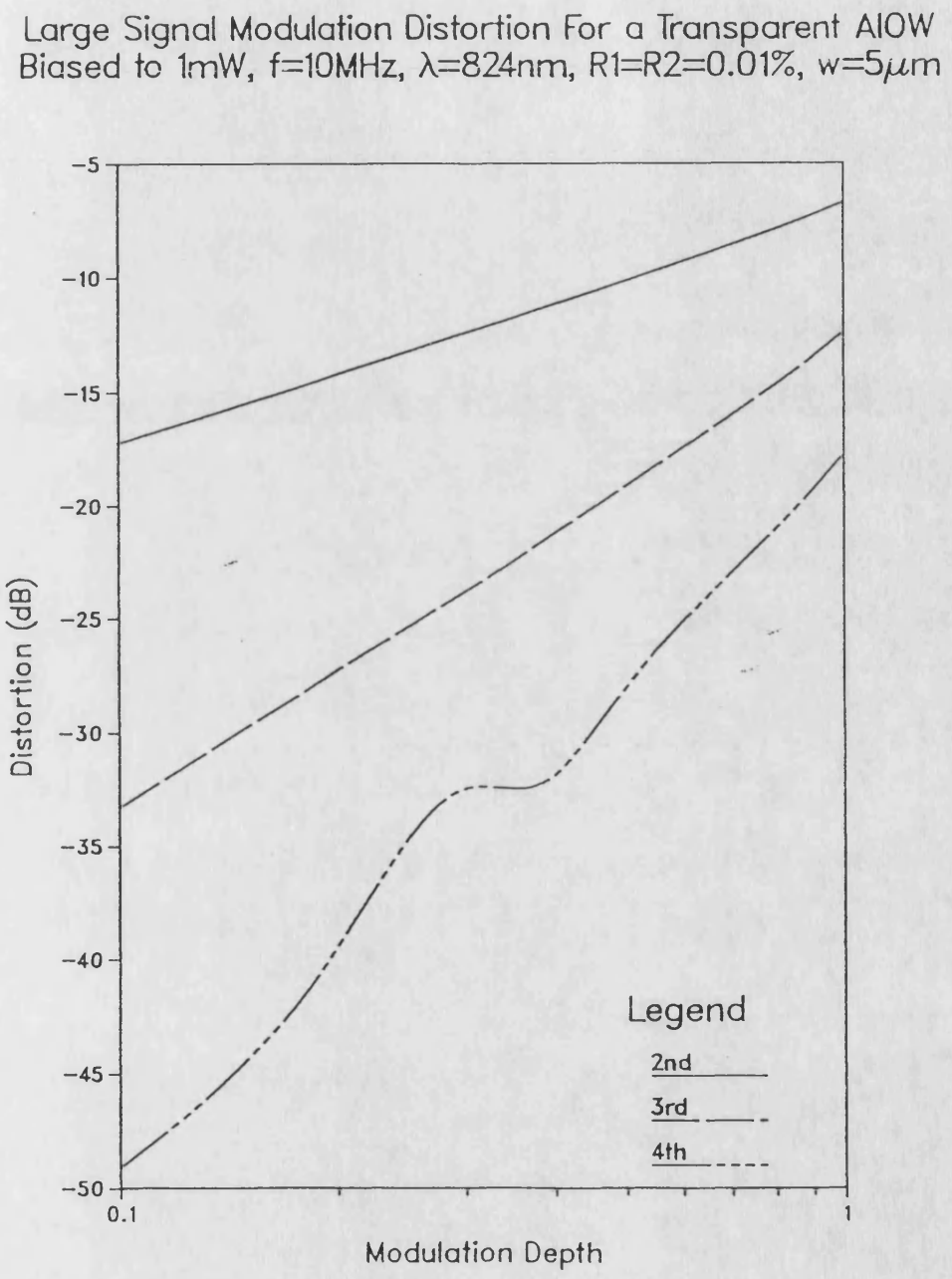

Figure 8.14b Large signal, harmonic output power, modulation response, at 10 MHz, for a guide biased to transparency to a 1 mW optical bias. (b) Modulation distortion.

From figures 8.13 to 8.24 it is possible to make some general observations regarding the modulation response of the guide. Firstly, there is a small but perceptible drift in the dc component towards lower values which becomes negligible at high frequencies.[3] Clearly any drift in the bias point is undesirable but for the transparent guide with a symmetrical input, this drift is seen to be small or negligible.

As the modulation depth and optical input power increase, the number of significant harmonics also increases, in the manner observed in section 8.4.1. However, there is a corresponding decrease with frequency. Clearly the power of all the components is dependent on the optical bias power, the modulation depth and the frequency. In addition, as the characteristics are seen to be basically linear on the log/log scale used, there must be some kind of power law relationship between the magnitude of each component and the modulation depth.

Figures 8.13 to 8.15 are very similar to those presented in chapter 6 for the quasi-static analysis (figures 6.19 to 6.21), confirming the results of the small signal investigation that well below the break region the characteristics will be constant. When the modulation frequency is well below the break frequency, then the ω_n/ω terms in equations (7.15) and (8.39) become negligible and the carrier density follows the flux exactly. The changes in flux are then so slow that the dynamic solution becomes identical to the steady state solution.

Using tables 8.2 to 8.5 it is possible to quantify some of these general observations. From table 8.2 it can be seen that not only does the gain compression decrease with frequency but also with modulation depth. The decrease with frequency has been described elsewhere and is simply due to the step in the fundamental component frequency response. The decrease with modulation depth is slightly more puzzling.

---

[3]Despite the appearance of figures 8.22(a) - 8.24(a) where the apparent fall is an optical illusion caused by the approach of the fundamental component.

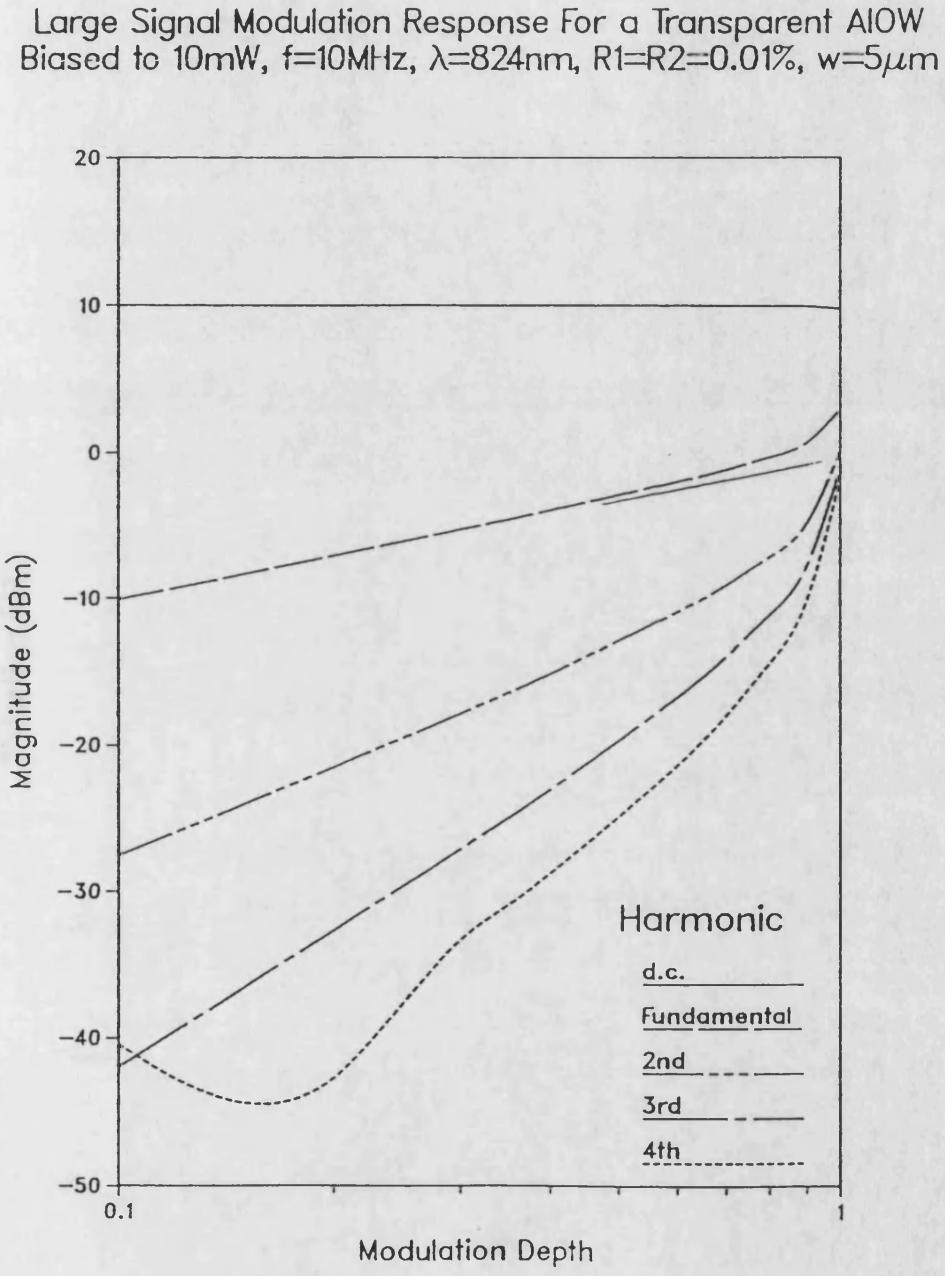

Figure 8.15*a* Large signal, harmonic output power, modulation response, at 10 MHz, for a guide biased to transparency to a 10 mW optical bias. (a) Modulation response,

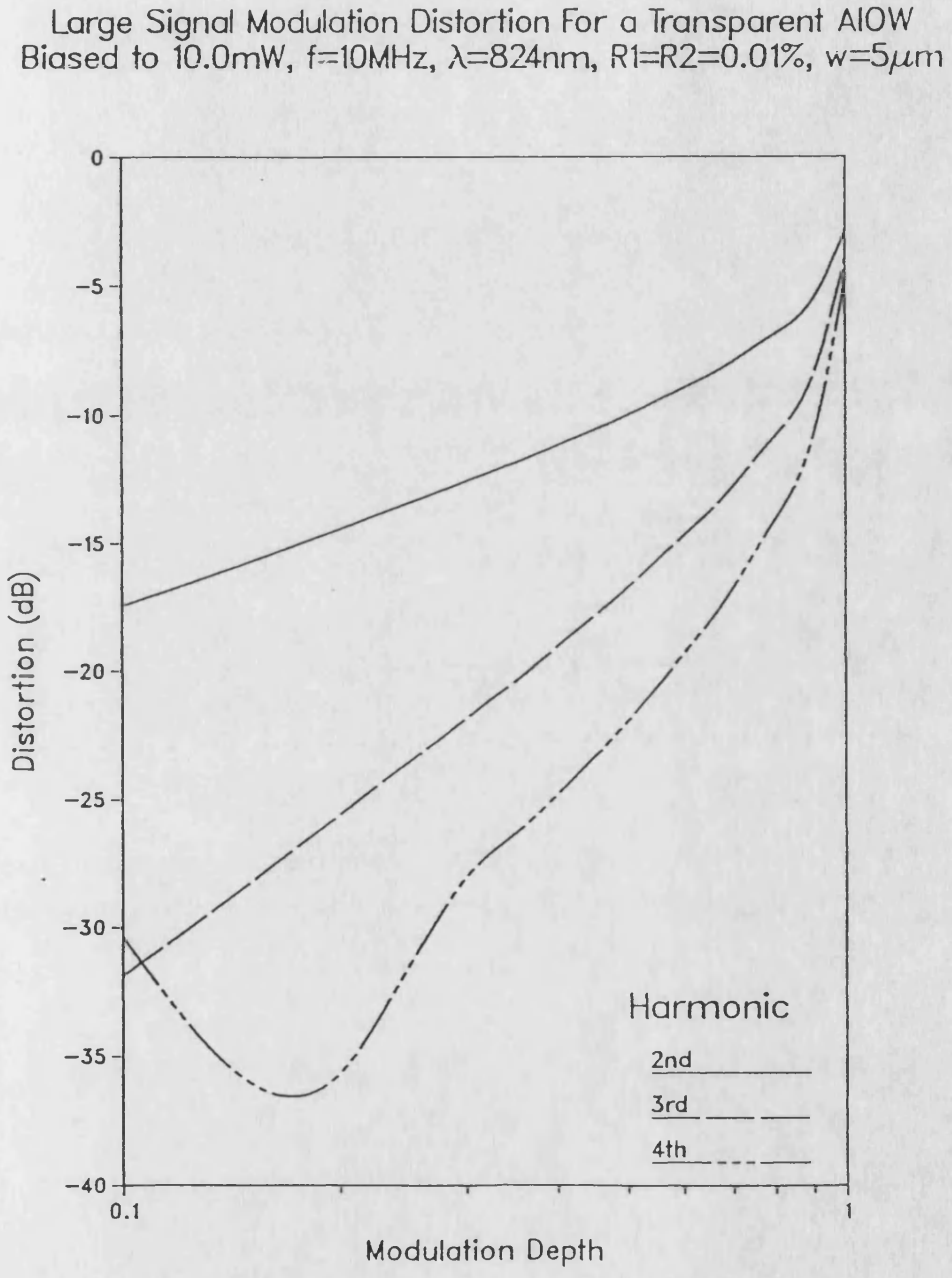

Figure 8.15 b Large signal, harmonic output power, modulation response, at 10 MHz, for a guide biased to transparency to a 10 mW optical bias. (b) Modulation distortion.

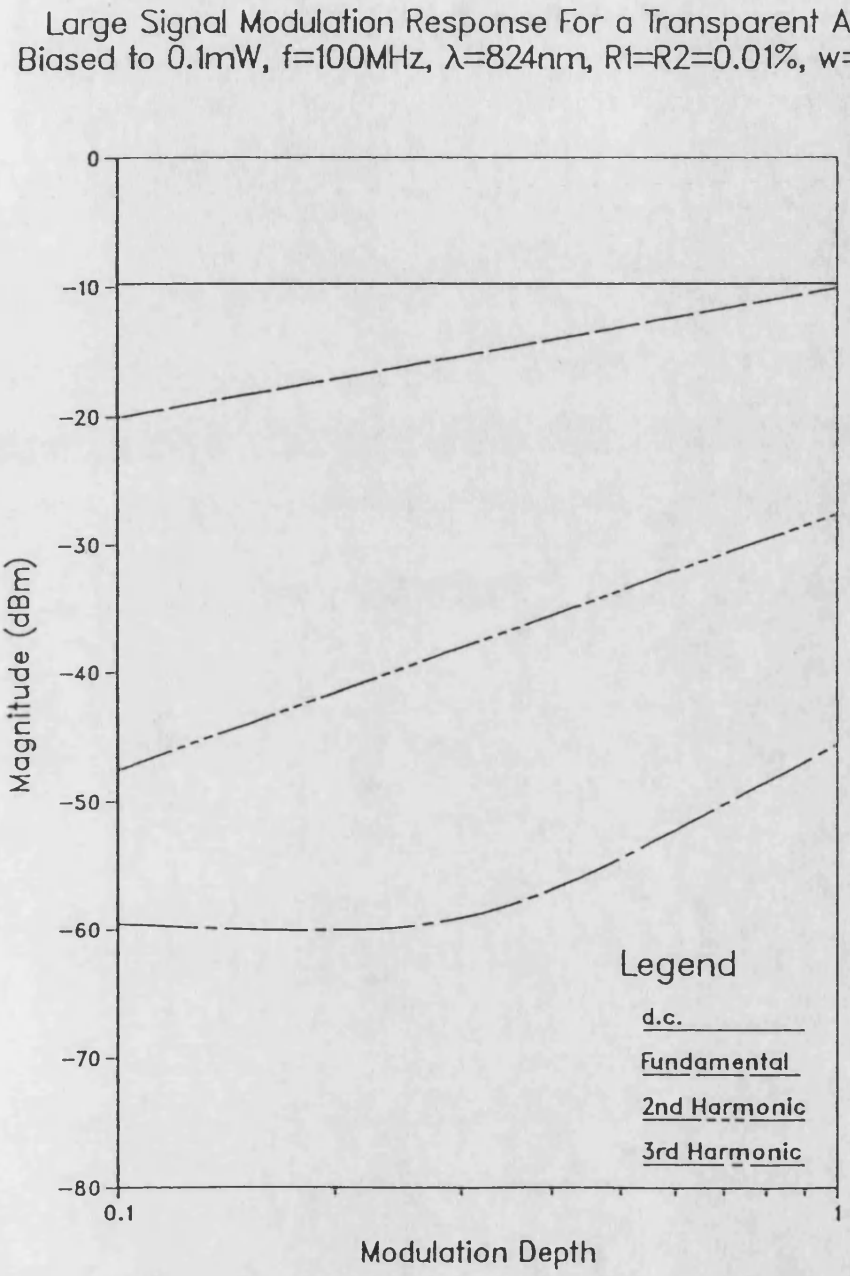

Figure 8.16a Large signal, harmonic output power, modulation response, at 100 MHz, for a guide biased to transparency to a 0.1 mW optical bias.

(a) Modulation response,

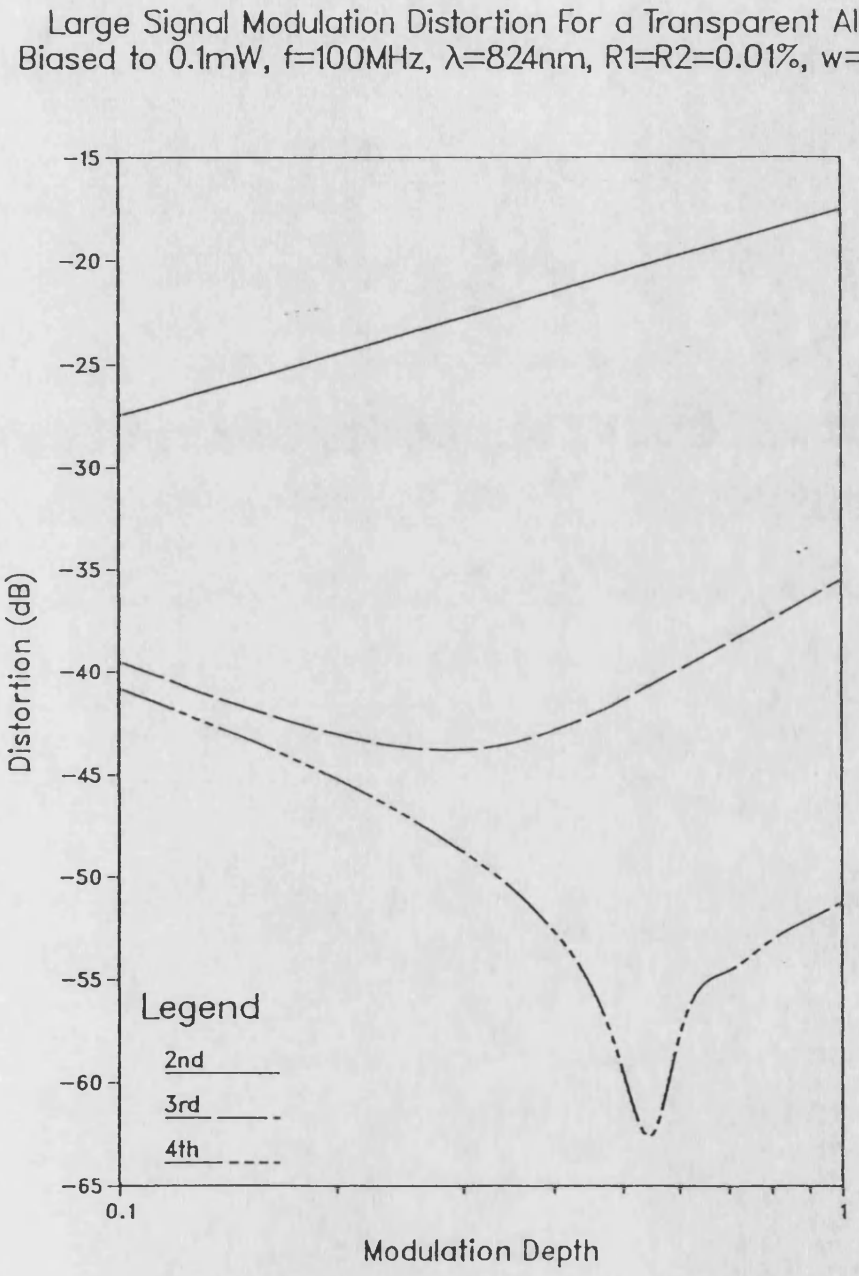

Figure 8.16b Large signal, harmonic output power, modulation response, at 100 MHz, for a guide biased to transparency to a 0.1 mW optical bias. (b) Modulation distortion.

From chapter 6, it is known that the input-output curve is non-linear and in the most extreme case can be approximated to two linear regions which join at a knee well below the bias point. Thus, as the modulation depth increases the fundamental power will rise due to the shape of the input-curve to above that predicted by the small signal analysis. For moderate bias powers the rise is smooth, eg figure 8.14(a) where a construction line has been included to show the deviation. At high biases the change is quite abrupt, as shown is figure 8.15(a) for 10 mW.

From the lower diagonal half of table 8.2 and by inspection of figures 8.13(a) to 8.24(b) it can been seen that there is no gain compression when there is little or no interaction between the flux and carriers in the guide, ie for low bias and/or high frequency. In these cases the fundamental output power from the guide is equal to the fundamental input (when the guide is transparent),

$$W_{out,1} = W_{in,1} = m \cdot \hat{W}_{in} . \qquad (8.45)$$

Thus the fundamental power is directly proportional to the modulation depth and will show a growth of 10 dB/decade.

Using tables 8.3 and 8.4 and the associated figures it is possible to determine the power law relationship which governs the harmonic powers. If the rows of table 8.3 are examined, for the non-compressed cases (lower diagonal half)[4], it is seen that the 2nd harmonic power is identical when the modulation depth - optical bias power product is the same. Thus,

$$W_{out,2} \propto \left(m \cdot \hat{W}_{in}\right)^2 \qquad (8.46)$$

---

[4]The anomaly for 0.1 mW at 10 GHz is because the 2nd harmonic becomes lost in the noise floor.

Theoretically this may be deduced by extending the analysis presented in the previous section. In equation (8.40) the 2nd harmonic power was shown to be proportional to the fundamental flux squared. As the fundamental output power and hence the fundamental flux, is proportional to $m\cdot \hat{W}_{in}$, thus the 2nd harmonic power must be proportional to $(m\cdot \hat{W}_{in})^2$. Further, equation (8.42) shows that the n^{th} harmonic power is proportional to the product of the $(n-1)^{th}$ harmonic and the fundamental, ie

$$W_{out,n} \propto \left(m\cdot \hat{W}_{in}\right)^n \quad . \tag{8.47}$$

Equation (8.42) may also be used to estimated the harmonic distortion. Integrating from z = 0 to L, assuming that the quantities do not vary in z, gives

$$W_{out,n} = \left(\frac{-gL\cdot \frac{dG}{dN}\, \hat{W}_{in,1} P(W)}{\omega_n \left(1 + \frac{j\omega}{\omega_n}\right)} \right) W_{out,n-1} \quad , \tag{8.48}$$

where P(W) is the term relating flux to optical power (equation 6.16). From equations (8.47) and (8.48) the harmonic distortion variation is given by,

$$D_n = \frac{|B_n|}{|B_1|} \propto \left(m\cdot \hat{W}_{in}\right)^{n-1} \quad . \tag{8.49}$$

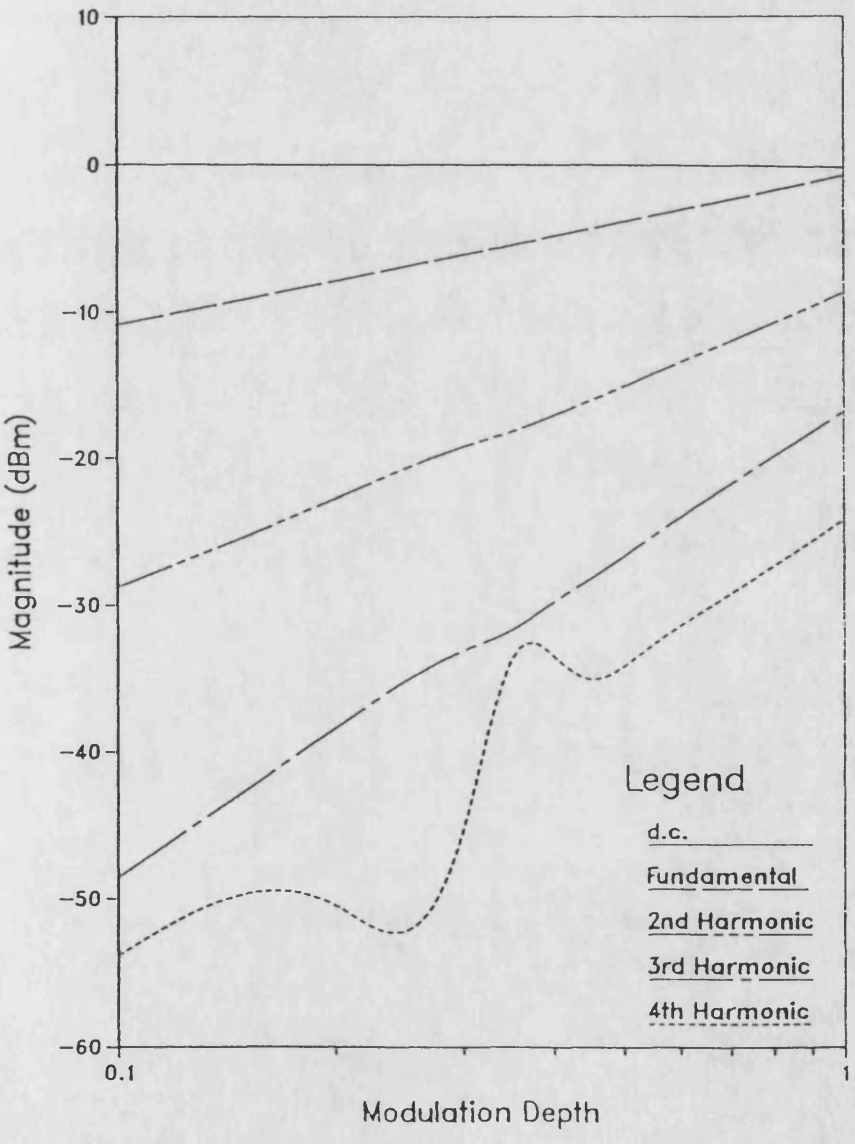

Figure 8.17a Large signal, harmonic output power, modulation response, at 100 MHz, for a guide biased to transparency to a 1 mW optical bias.

(a) Modulation response,

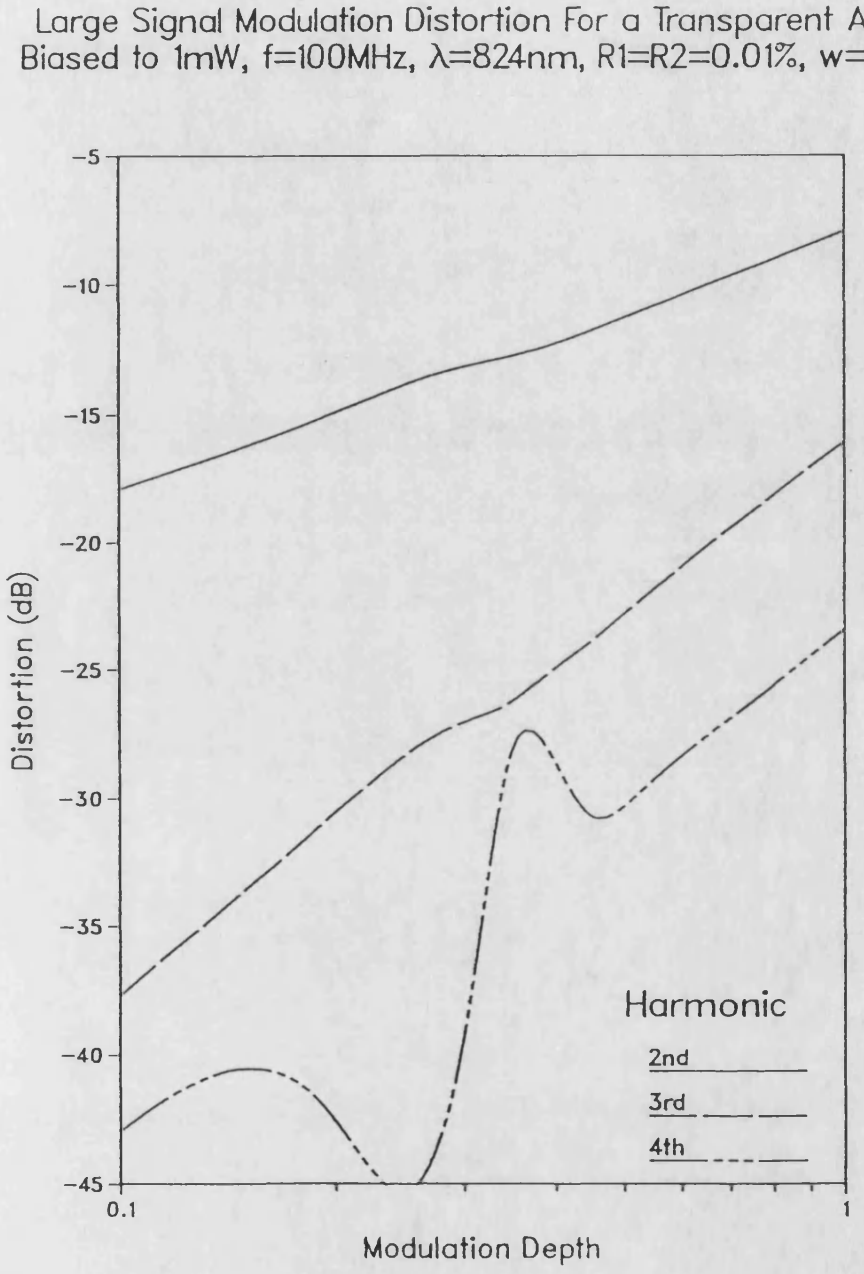

Figure 8.17(b) Large signal, harmonic output power, modulation response, at 100 MHz, for a guide biased to transparency to a 1 mW optical bias. (b) Modulation distortion.

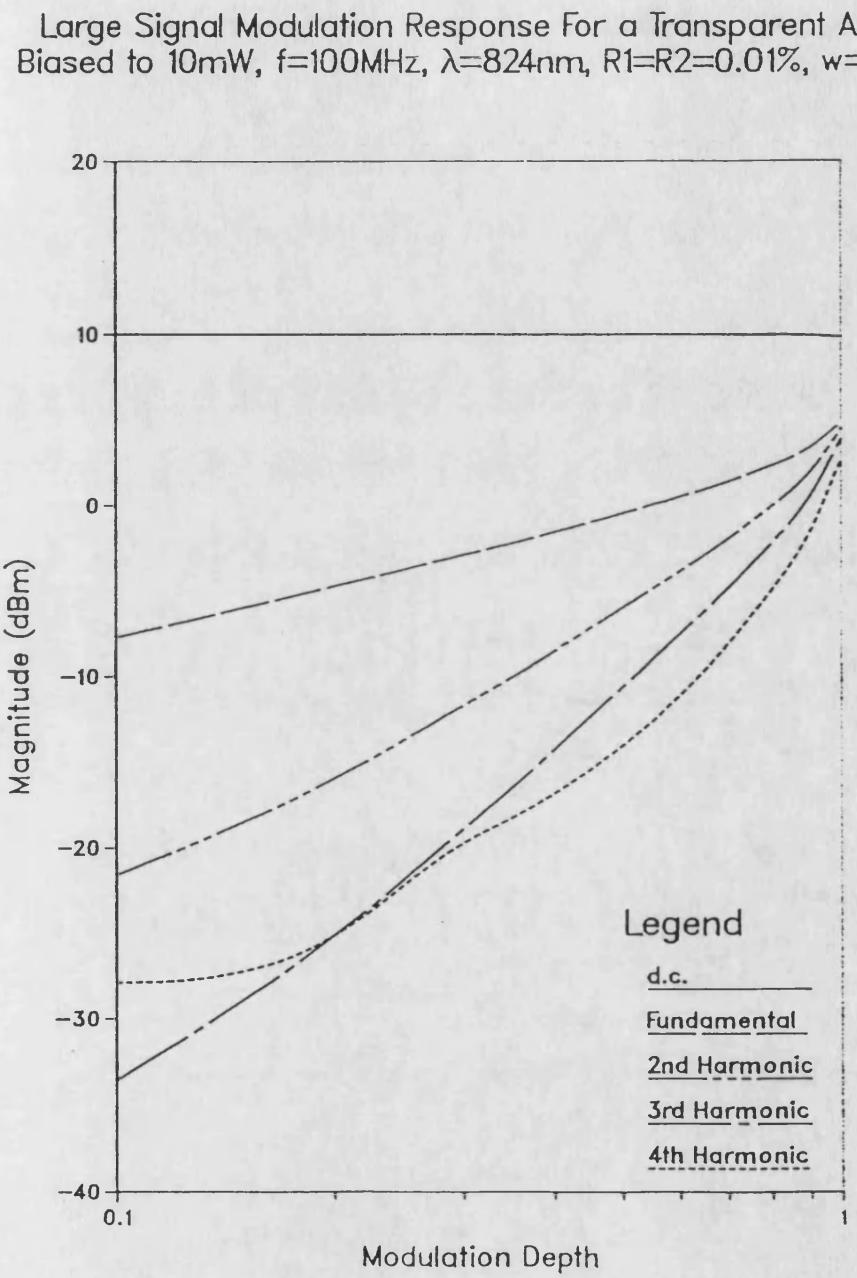

Figure 8.18 a Large signal, harmonic output power, modulation response, at 100 MHz, for a guide biased to transparency to a 10 mW optical bias.

(a) Modulation response,

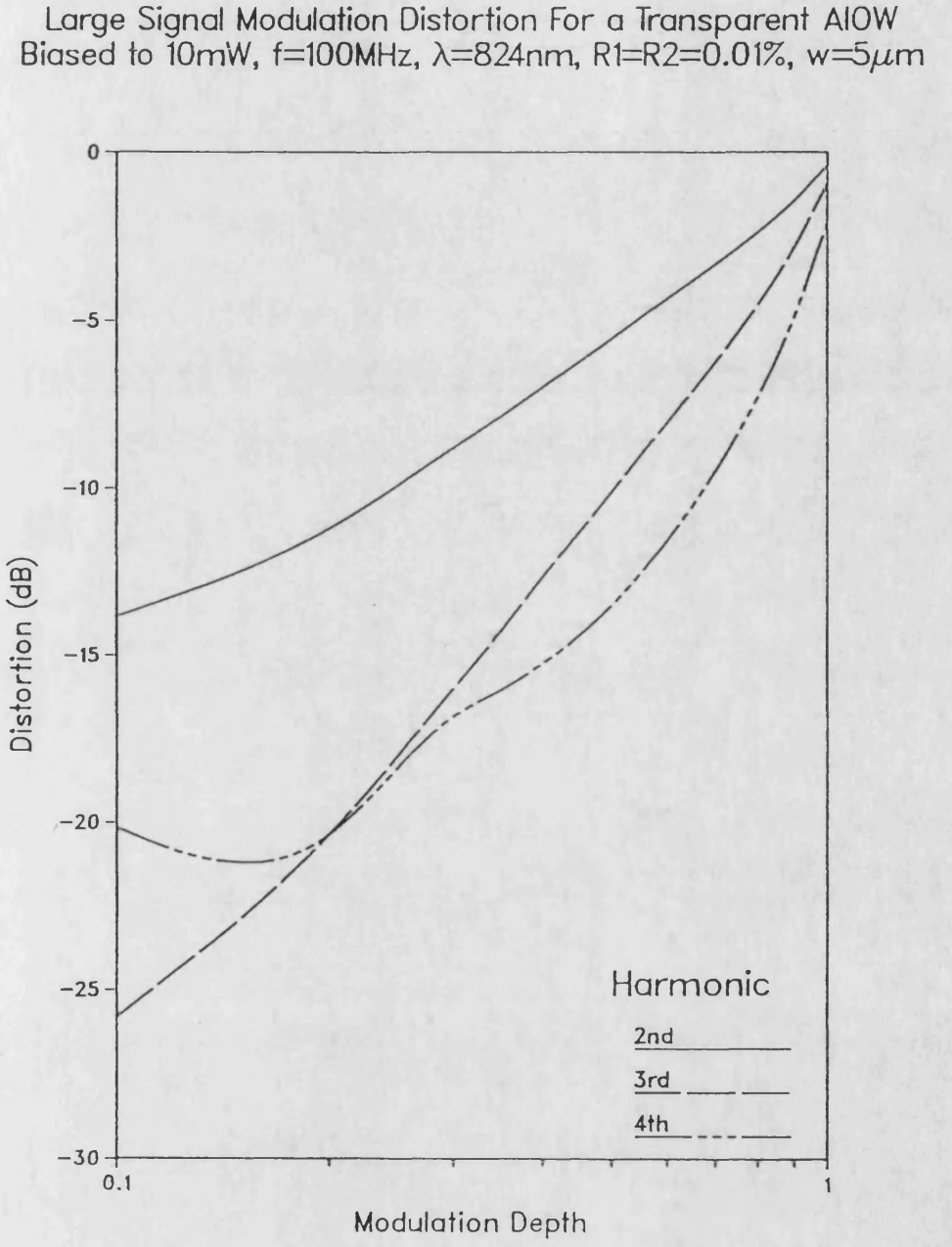

Figure 8.18b Large signal, harmonic output power, modulation response, at 100 MHz, for a guide biased to transparency to a 10 mW optical bias. (b) Modulation distortion.

Equation (8.48) also shows that there is a constant ratio between one harmonic component and the next, this ratio is given by,

$$\frac{|B_n|}{|B_{n-1}|} = \frac{gL\cdot\frac{dG}{dN}}{\omega_n\sqrt{1+\left(\frac{\omega}{\omega_n}\right)^2}}\hat{W}_{in}P(W)\ , \qquad (8.50)$$

$$= C + 10\log\left\{m\cdot\hat{W}_{in}\right\} - 10\log\left\{\sqrt{1+\left(\frac{\omega}{\omega_n}\right)^2}\right\}\ (dB)$$

where C is a constant dependent on the bias power ≈ 20 dB for a 0.1 mW optical bias power. It is clear from equation (8.50) that the ratio of harmonic powers is constant and increases at 10 dB/decade with modulation index, and rolls-off at the same rate with frequency. Table 8.5 shows the ratio in dB of the 3rd to 2nd and 4th to 3rd harmonics of a modulation index of 1. The trends in table 8.5 are not totally clear because the lower harmonics are often lost in the noise floor. However, when the fundamental compression is negligible, the ratios are seen to behave as predicted in equation (8.50) and are equal to the 2nd harmonic distortion terms in table 8.4.

Now that the behaviour of the higher harmonics in the linear regions has been quantified, the behaviour around the break frequency must be addressed. Figure 8.17, 8.18 and 8.21 are quite unlike those produced in the quasi-static analysis. In figure 8.17 there is a kink in the harmonic components at 0.4 modulation index, even for those components well above the noise floor. In fig 8.18 the 4th harmonic component is greater than the 3rd for low modulation. In fig 8.21, the 4th harmonic rises at approximately 80 dB/decade, until it is equal to the 3rd harmonic. As the modulation index increases the 3rd and 4th harmonic powers are seen to oscillate about -20 dBm and the 2nd harmonic does not rise at the expected 20 dB/decade.

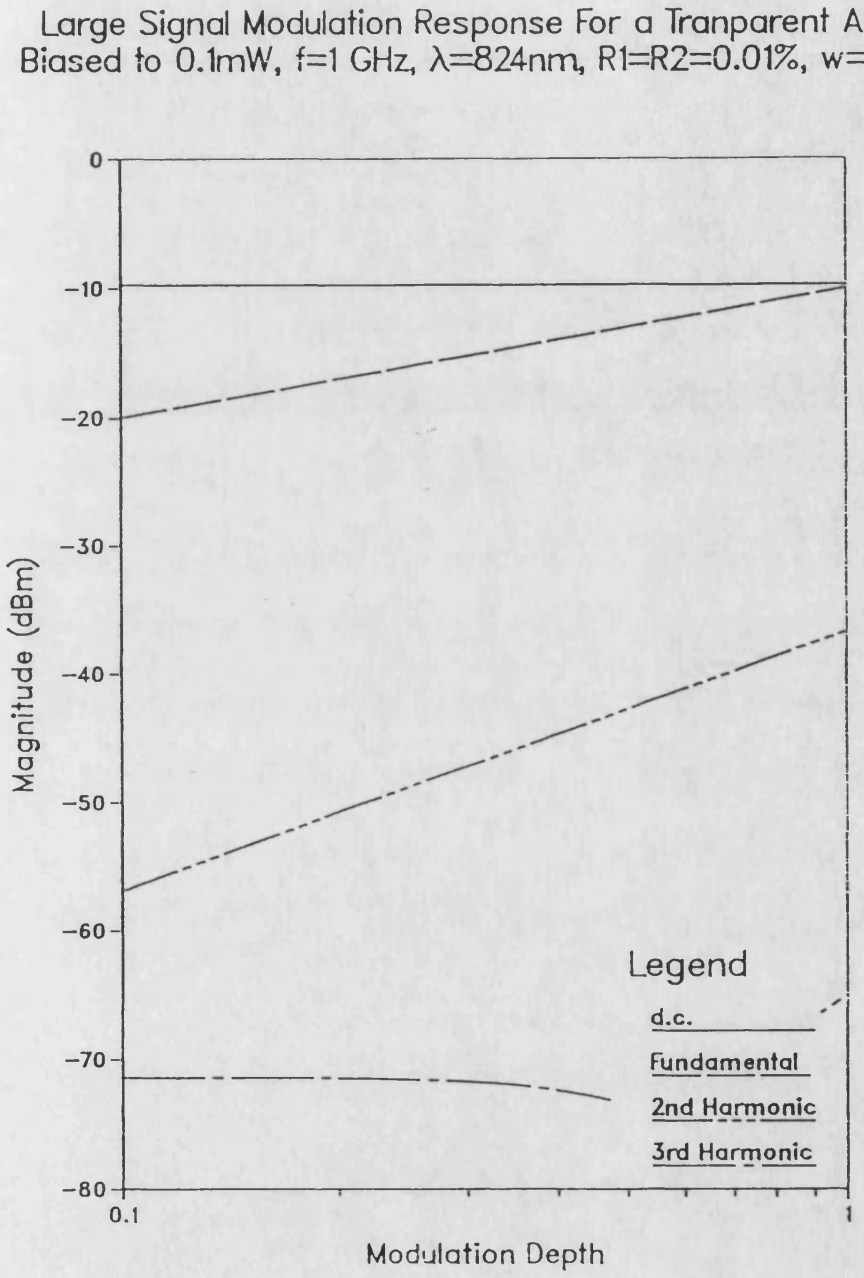

Figure 8.19 Large signal, harmonic output power, modulation response, at 1 GHz, for a guide biased to transparency to a 0.1 mW optical bias.

(a) Modulation response,

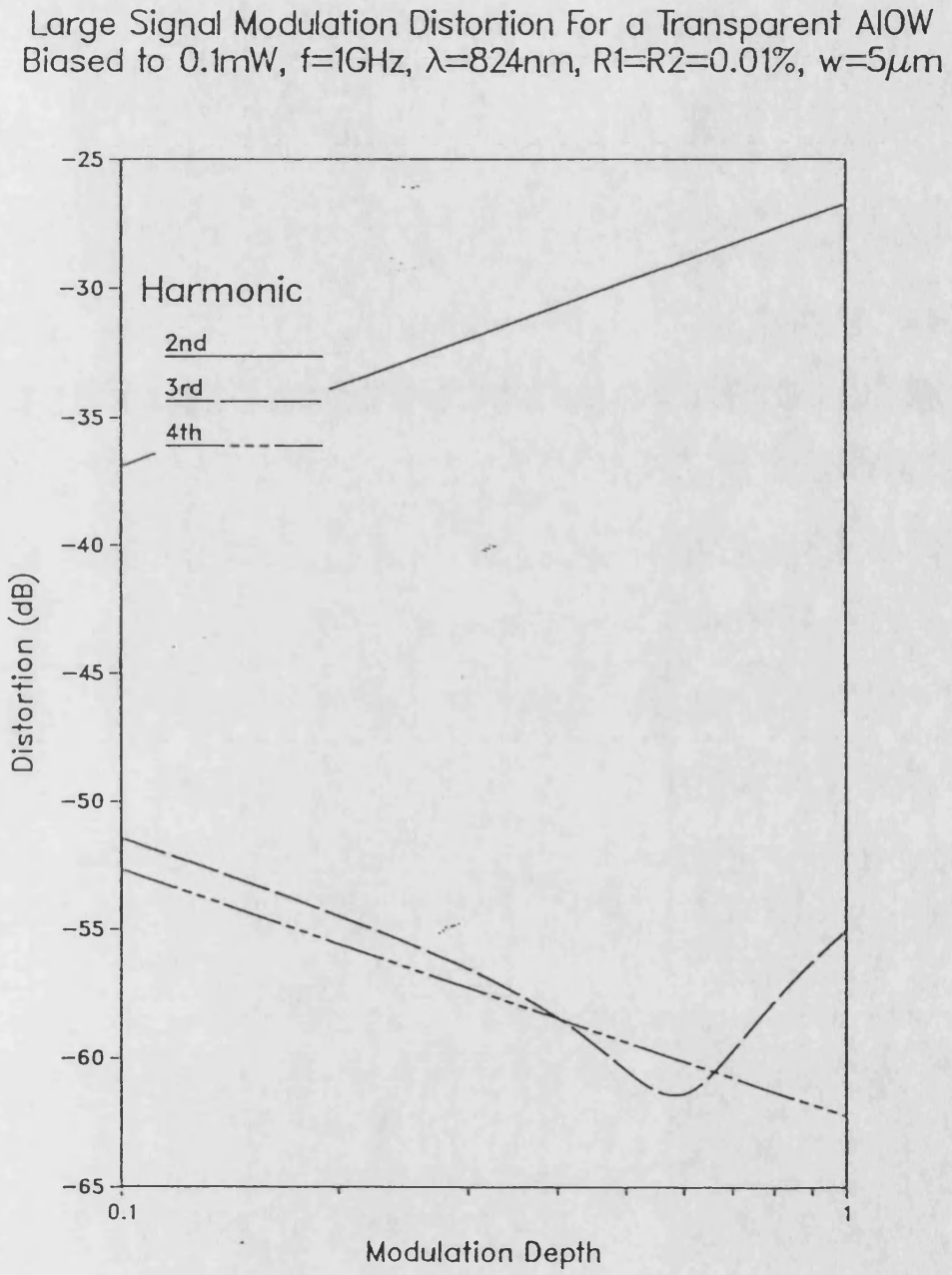

Figure 8.19 b Large signal, harmonic output power, modulation response, at 1 GHz, for a guide biased to transparency to a 0.1 mW optical bias. (b) Modulation distortion.

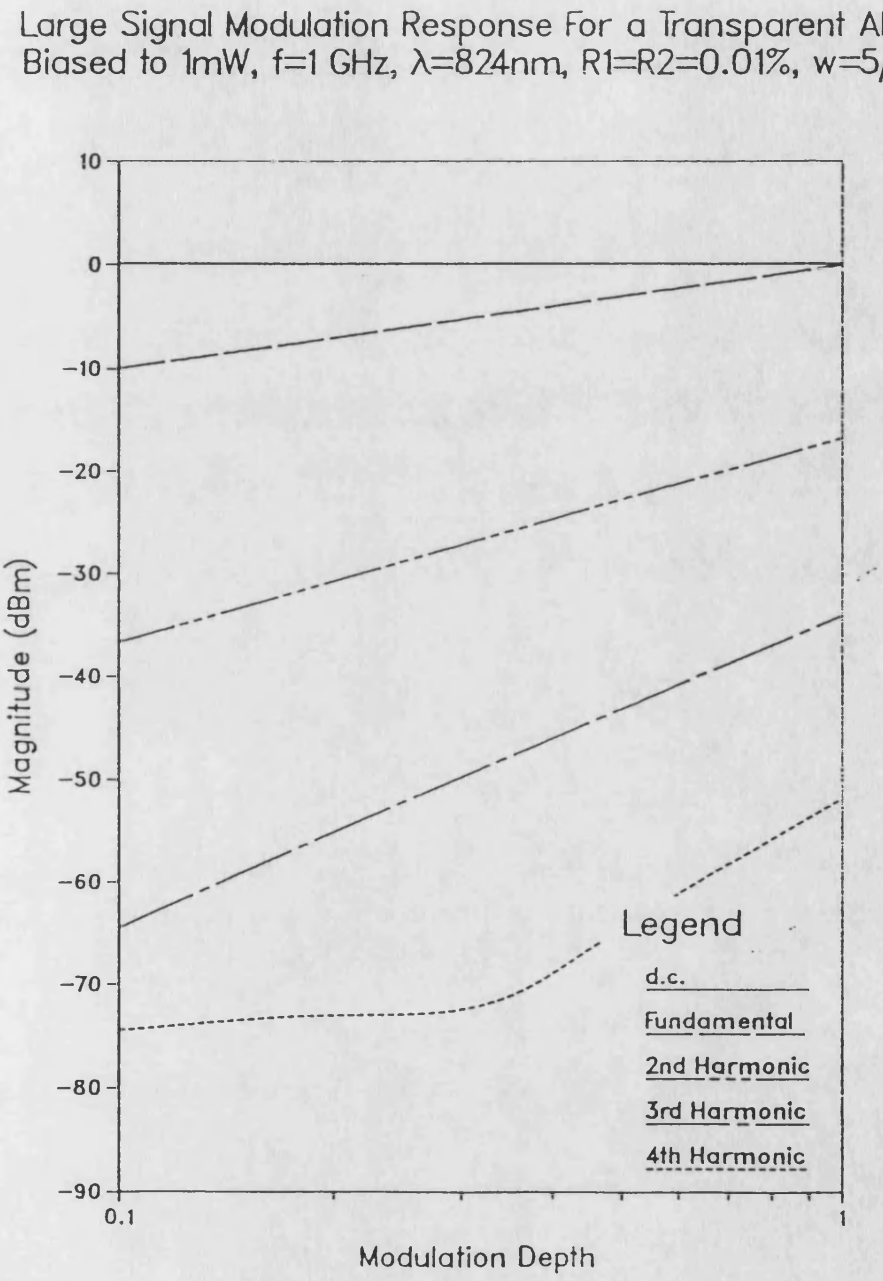

Figure 8.20a Large signal, harmonic output power, modulation response, at 1 GHz, for a guide biased to transparency to a 1 mW optical bias.

(a) Modulation response,

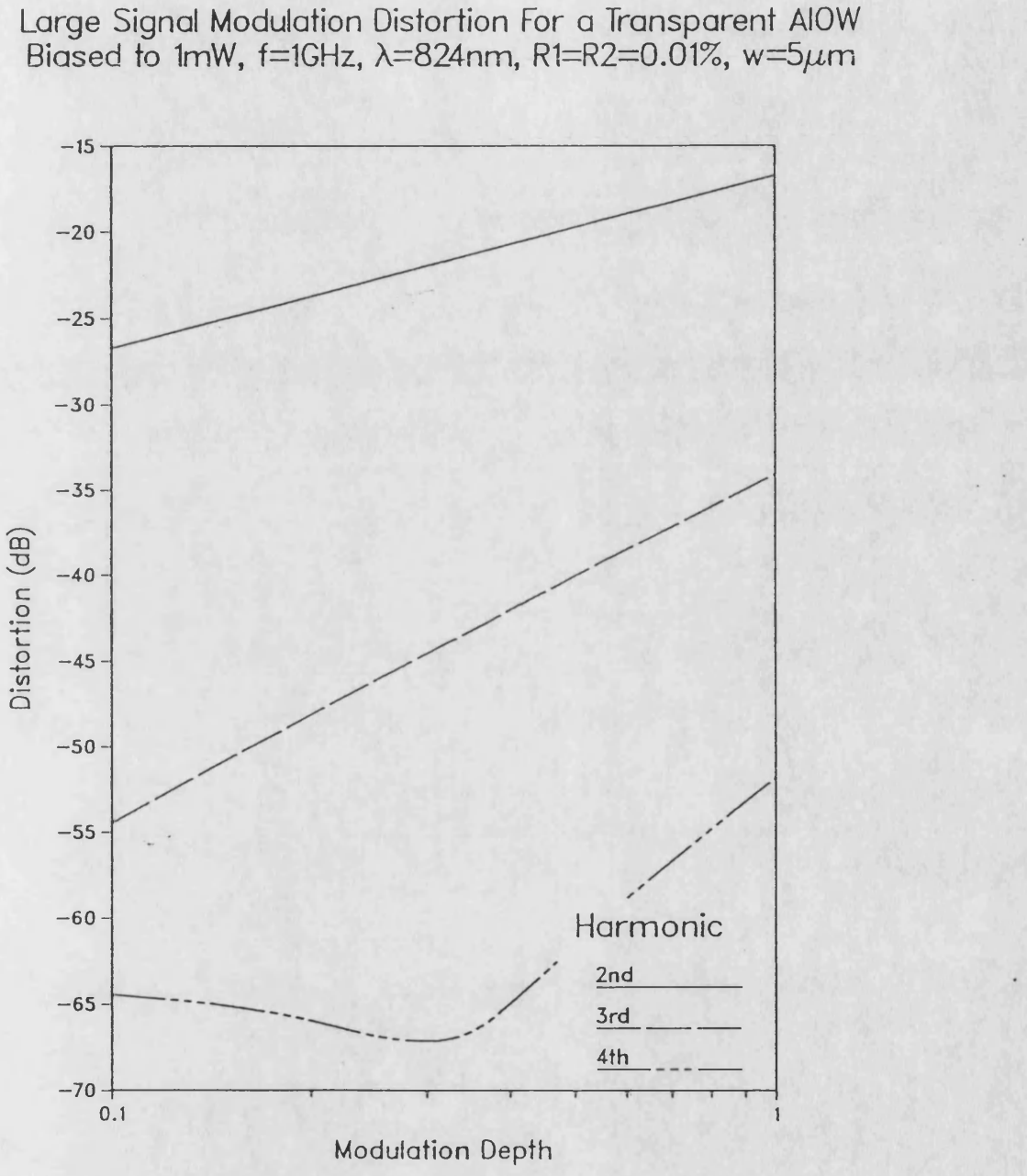

Figure 8.20b Large signal, harmonic output power, modulation response, at 1 GHz, for a guide biased to transparency to a 1 mW optical bias. (b) Modulation distortion.

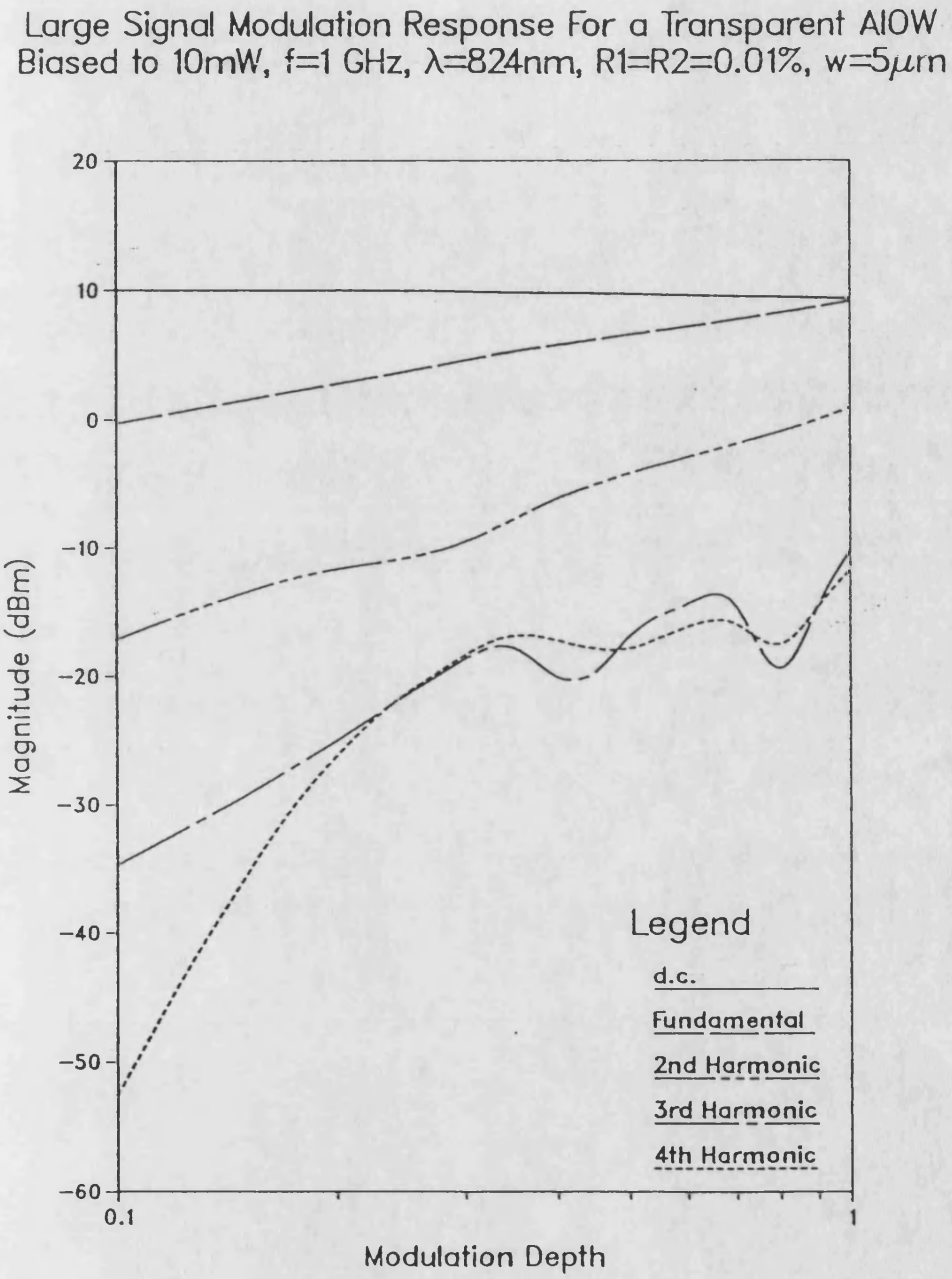

Figure 8.21 a Large signal, harmonic output power, modulation response, at 1 GHz, for a guide biased to transparency to a 10 mW optical bias.

(a) Modulation response,

Such effects can only be ascribed to the lag between the gain and flux variations described in the previous section. From equations (8.39) and (8.41) it is known that the fundamental and harmonic components are determined by the variations in net effective gain, which can be approximated to,

$$\frac{-g\cdot\frac{dG}{dN}\cdot\left(p_1+q_1\right)}{\omega_n\left(1+\frac{j\omega}{\omega_n}\right)} \quad . \tag{8.51}$$

Equation (8.51) shows that at low frequency the net effective gain variations are in anti-phase to the flux variations, ie the gain goes down when the flux increases! In this case, the anti-phase component in the fundamental manifests itself as the gain compression term, whilst the higher harmonics are shifted by π radians. Thus the even harmonics are in phase with the main fundamental component, whilst the odd harmonics are in anti-phase. As the frequency is increased this relationship breaks down and the phase difference between the harmonics is described by,

$$\phi \quad = \quad -\pi - \arctan\left(\frac{\omega}{\omega_n}\right) \quad . \tag{8.52}$$

Thus ϕ will lie in the range $-\pi$ to $-3\pi/2$ and as the frequency rises the modulus of (8.51) will eventually roll-off at 10 dB/decade.

In the linearised environment of the small signal analysis, the higher harmonics calculated in this manner would show a regular behaviour. However, in the large signal case the terms in equations (8.51) and (8.52) will all be dependent on the modulation depth, giving rise to the unpredictable behaviour seen in figures 8.17, 8.18 and 8.21. Clearly, these highly non-linear effects will only occur when the magnitude of (8.51) is relatively large and ϕ is changing, ie for high bias powers around the break region.

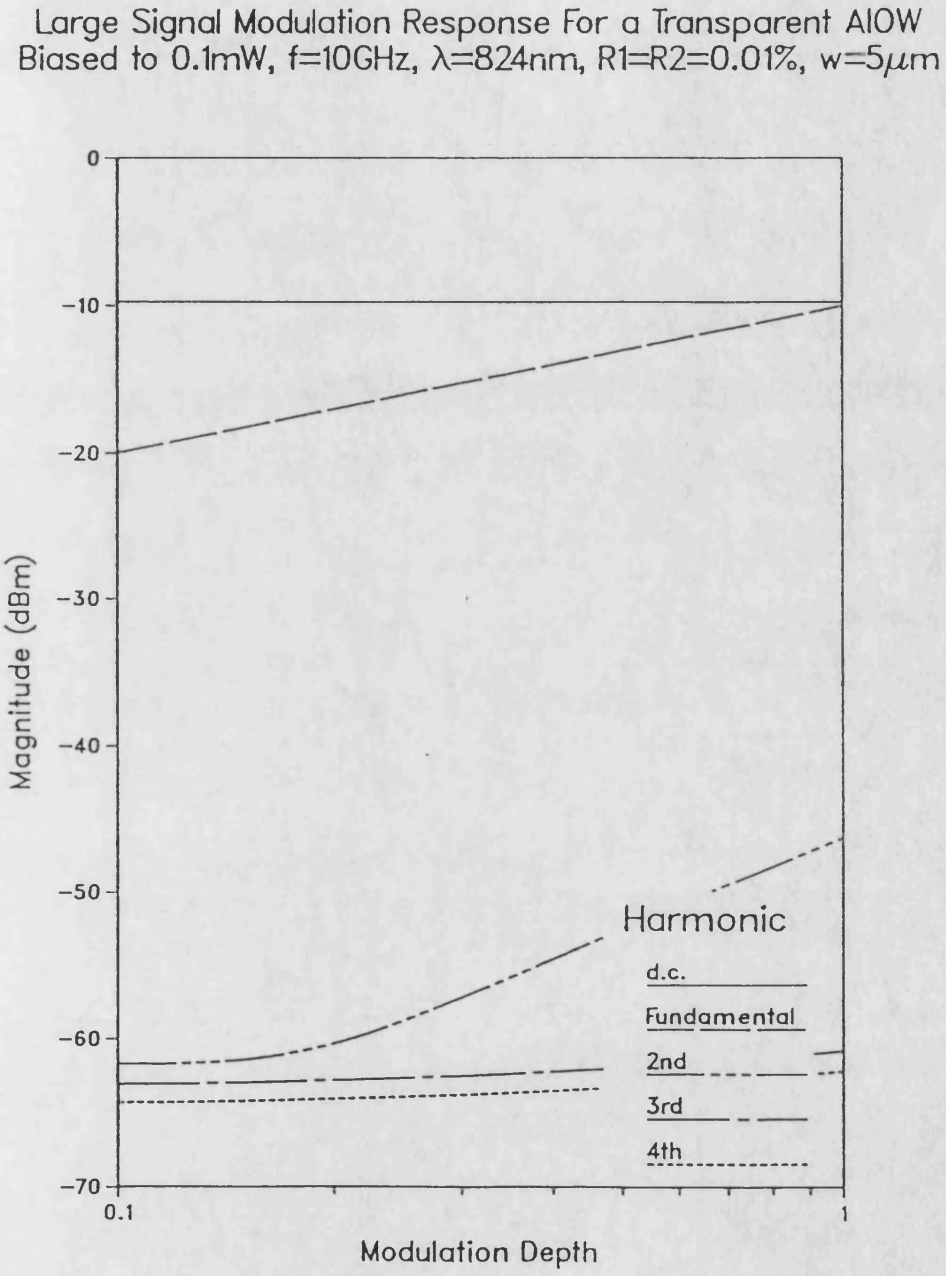

Figure 8.22a Large signal, harmonic output power, modulation response, at 10 GHz, for a guide biased to transparency to a 0.1 mW optical bias.

(a) Modulation response,

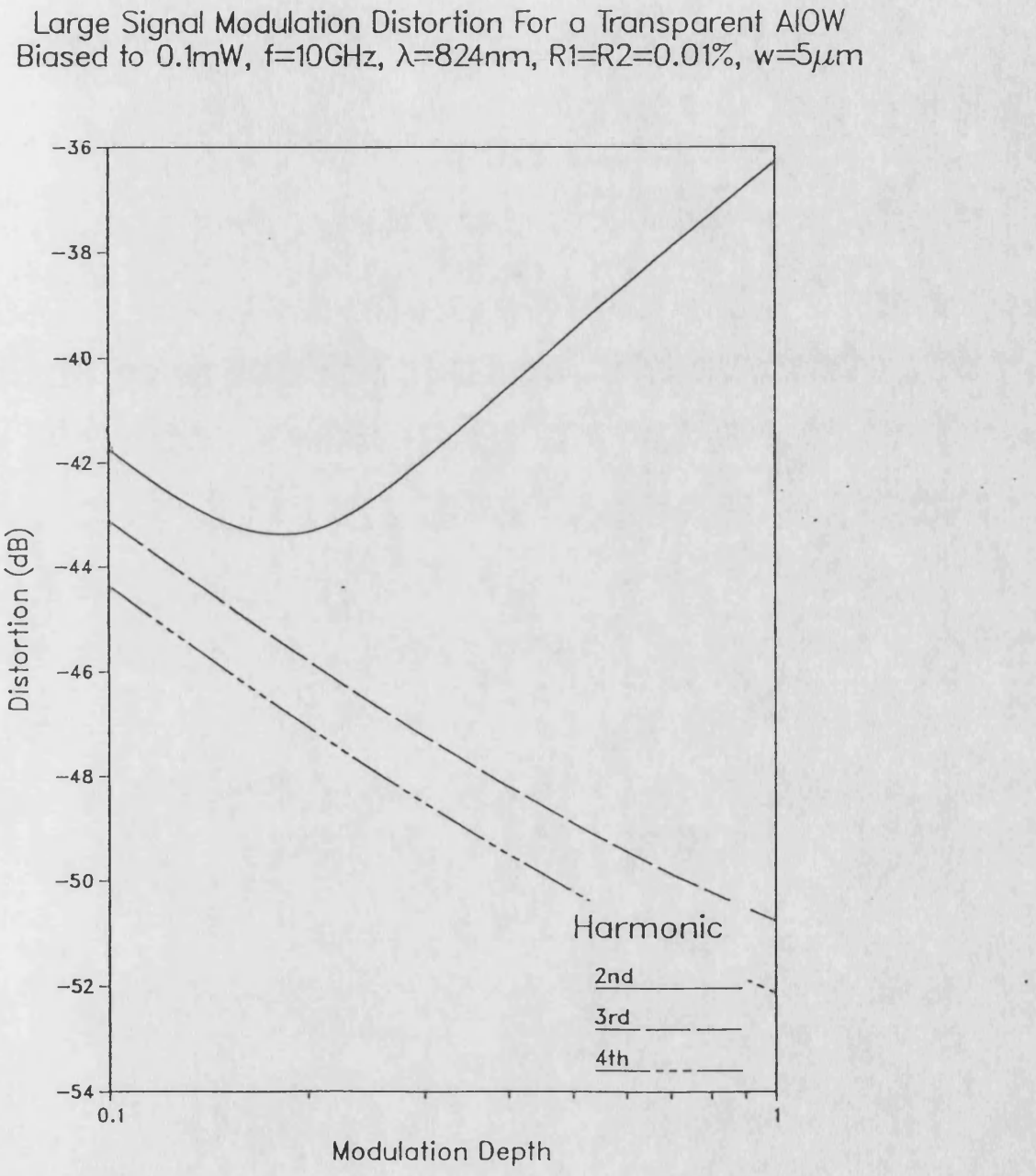

Figure 8.22b Large signal, harmonic output power, modulation response, at 10 GHz, for a guide biased to transparency to a 0.1 mW optical bias. (b) Modulation distortion.

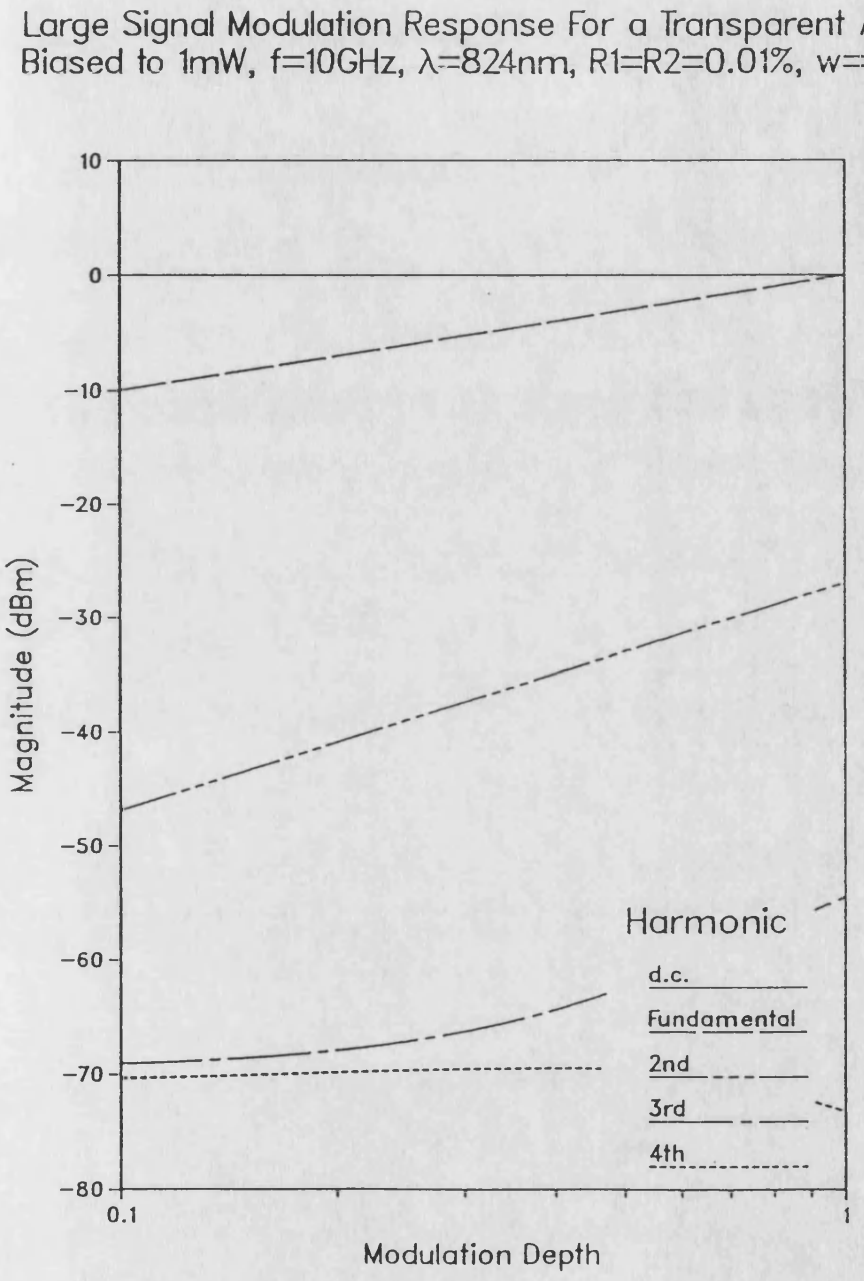

Figure 8.23 a Large signal, harmonic output power, modulation response, at 10 GHz, for a guide biased to transparency to a 1 mW optical bias. (a) Modulation response,

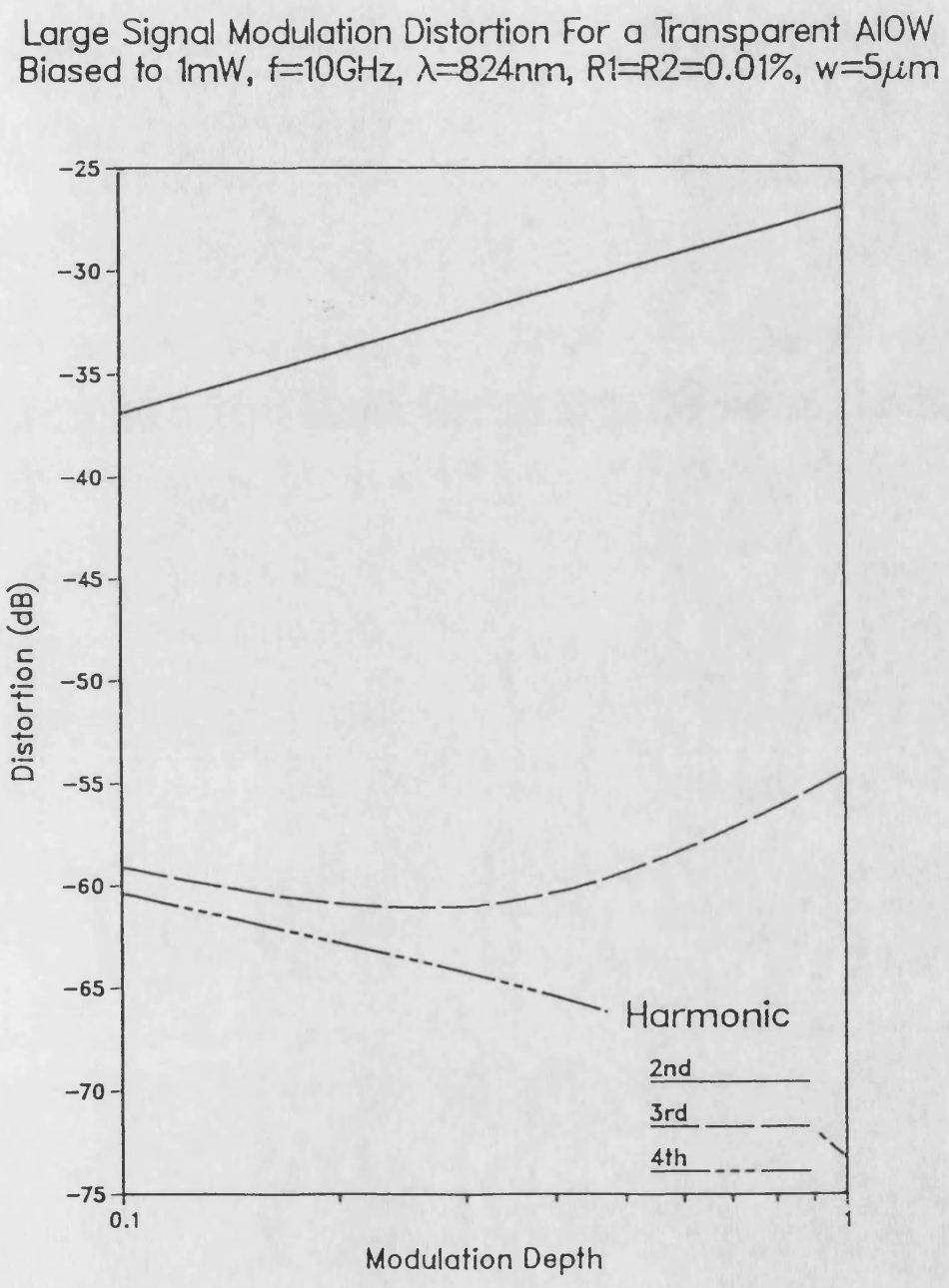

Figure 8.23b Large signal, harmonic output power, modulation response, at 10 GHz, for a guide biased to transparency to a 1 mW optical bias. (b) Modulation distortion.

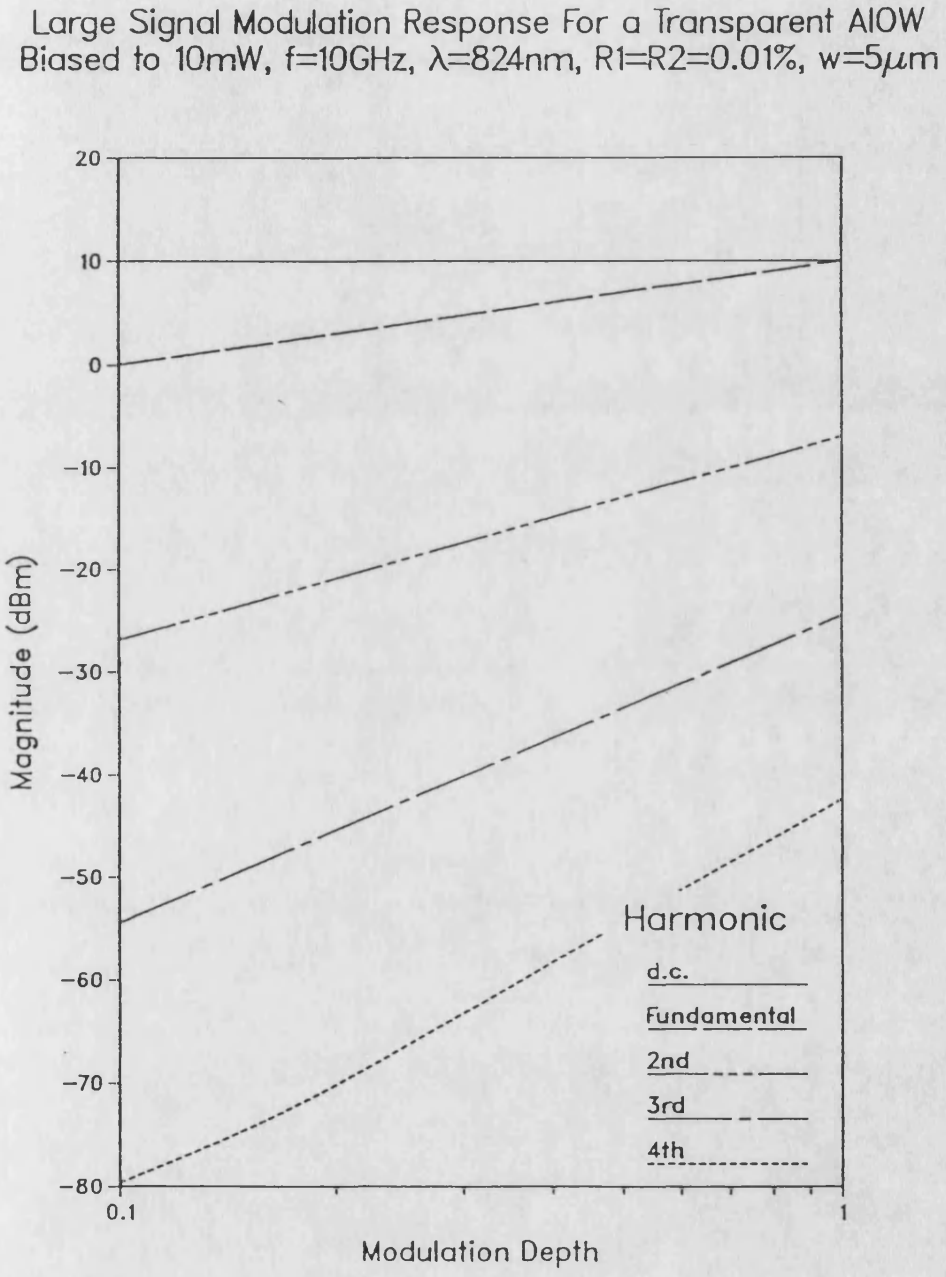

Figure 8.24a Large signal, harmonic output power, modulation response, at 10 GHz, for a guide biased to transparency to a 10 mW optical bias.

(a) Modulation response,

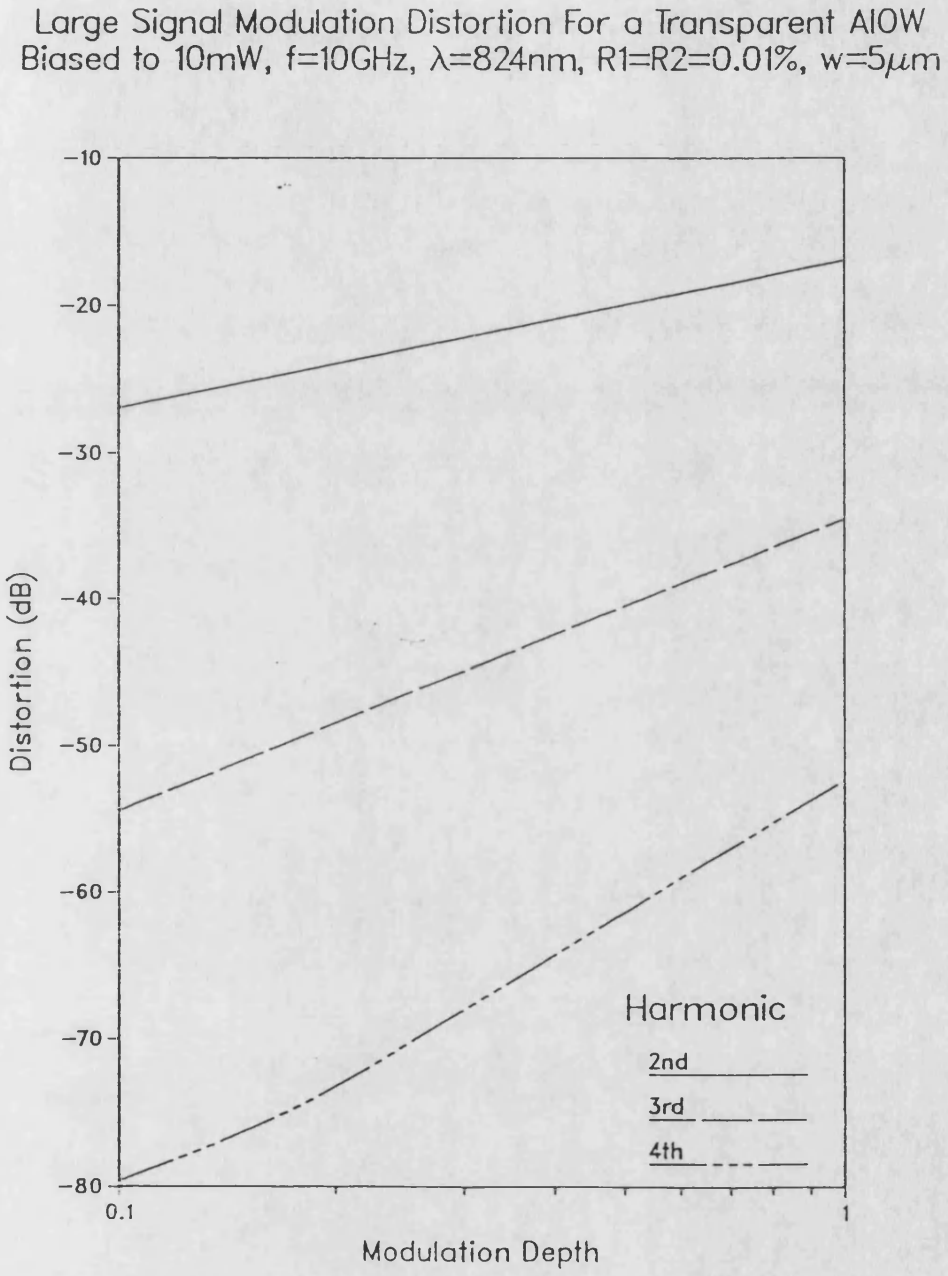

Figure 8.24b Large signal, harmonic output power, modulation response, at 10 GHz, for a guide biased to transparency to a 10 mW optical bias. (b) Modulation distortion.

8.4.5 Total Harmonic Distortion with Bias Power and Frequency

In sections 6.4.6.3 and 6.4.6.4 the Total Harmonic Distortion was examined for the quasi-static case. Figures 8.25 to 8.28 show the THD characteristics at 0.1, 1, 5 and 10 mW for the four spot frequencies used in the previous section, 0.01, 0.1, 1 and 10 GHz. These figures are a condensation of the harmonic distortion results in figures 8.13(b) to 8.24(b). In all cases the dominant slope of the THD is approximately 10 dB/decade, indicating that the 2^{nd} harmonic term dominates the modulation response. This is to be expected as the next harmonic is between 10 and 20 dB below the 2^{nd}.

Figure 8.25 is virtually identical to figure 6.22 generated from the quasi-static analysis. Again confirming the assertion that for frequencies below 10 MHz, the quasi-static approach is valid.To recap, as the optical bias power increases the THD also rises At 10 mW the flattening effect pulls the distortion down at low modulation but for indices above 0.8 the THD rises rapidly.

The form of figure 8.26 is similar to 8.25 but the characteristics become more distinct. In both figures the THD becomes greater than 0 dB for high modulation depth and bias Therefore, there is more power in the higher harmonics than the fundamental. In this case there are many high power harmonics rather than the a single harmonic which is greater than the fundamental. In figures 8.27 and 8.28 it is seen that for increasing frequency the characteristics at all powers become more linear, as the gain compression is removed. At 10 GHz the THD is directly proportional to the modulation depth and the optical bias power. The THD is therefore totally dominated by the 2^{nd} harmonic distortion and the guide is virtually linear in its response.

Figures 8.29 to 8.31 shows the alternative situation where the THD characteristics for the four spot frequencies are plotted at three bias powers 0.1, 1 and 10 mW. At 0.1 and 1.0 mW the THD tails off regularly with frequency and is smooth across the modulation range. At 0.1 mW the THD flattens or becomes raised at low modulation. At 10 MHz this is due to the 3^{rd} and 4^{th} harmonics becoming significant, whilst at 10 GHz all the harmonics become lost in the noise floor.

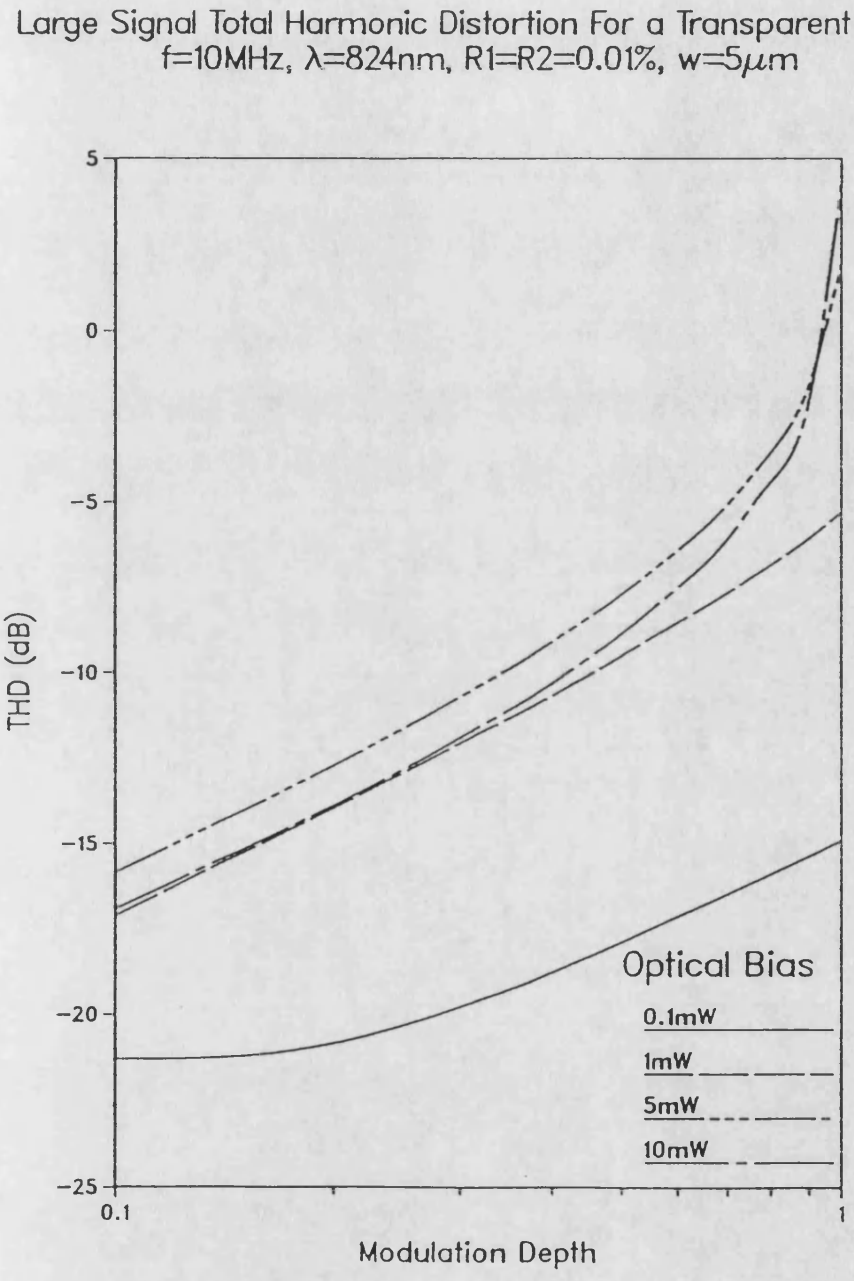

Figure 8.25 : Variation of large signal, total harmonic distortion with modulation depth, as a function of optical bias power at 10 MHz, for a transparent guide.

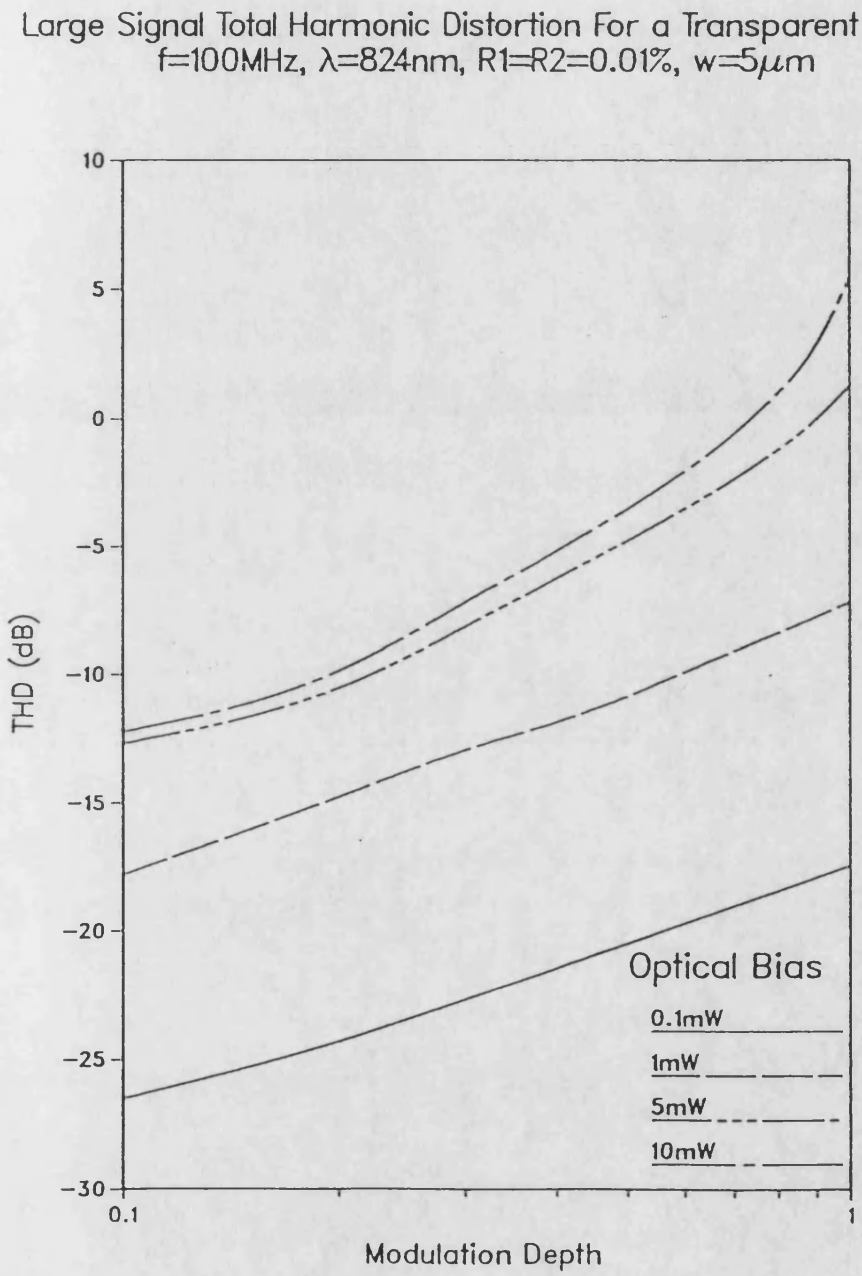

Figure 8.26 : Variation of large signal, total harmonic distortion with modulation depth, as a function of optical bias power at 100 MHz, for a transparent guide.

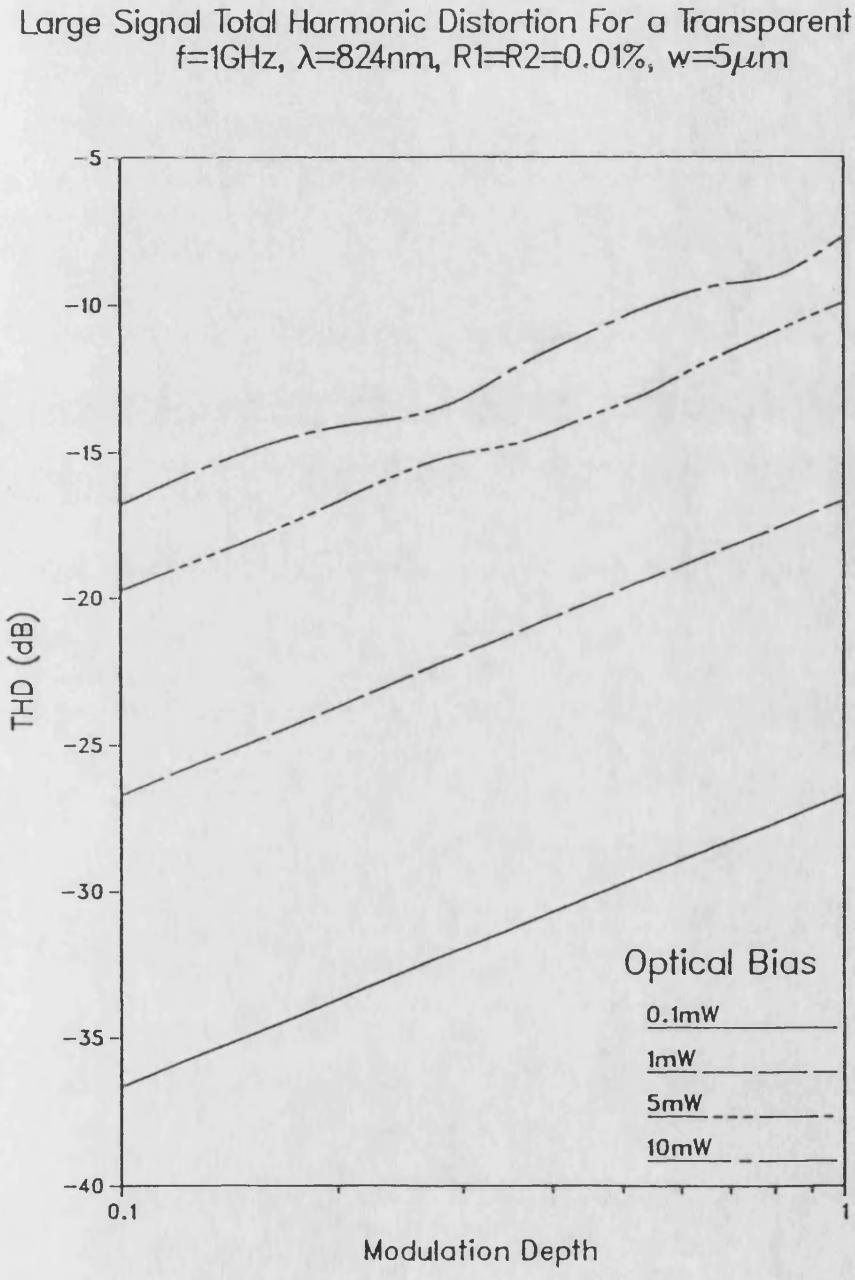

Figure 8.27 : Variation of large signal, total harmonic distortion with modulation depth, as a function of optical bias power at 1 GHz, for a transparent guide.

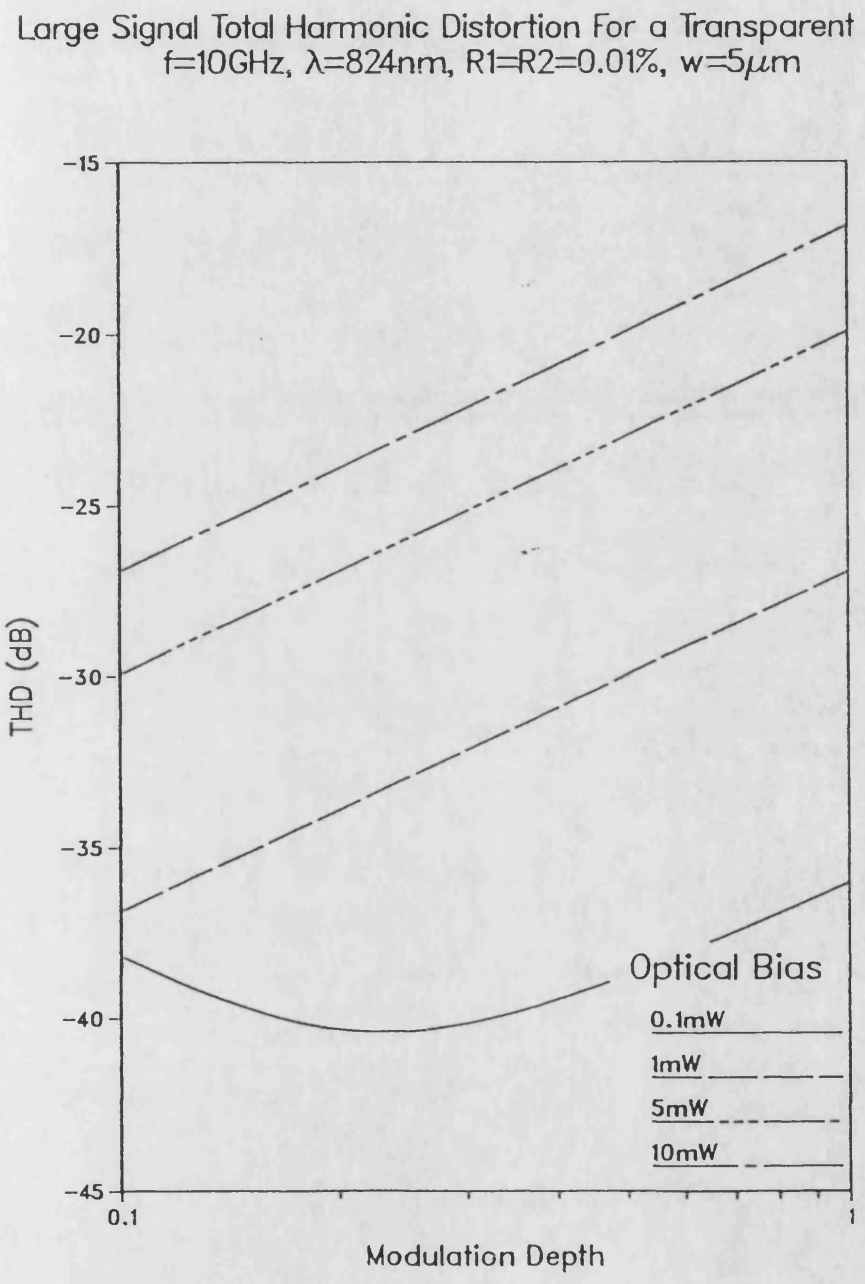

Figure 8.28 : Variation of large signal, total harmonic distortion with modulation depth, as a function of optical bias power at 10 GHz, for a transparent guide.

At 10 mW the situation is quite different. The total harmonic distortion rises between 10 and 100 MHz. From figures 8.12 it was seen that the fundamental magnitude also increases over this range, therefore there is a great increase in the harmonic powers at all modulation depths. It can be seen that at 1 GHz the THD is as bad as at 10 MHz for low modulation. Eventually the 10 dB/decade roll-off with frequency begins to dominate the response and well above the break frequency the THD begins to reduce to an acceptable value. This type of response has significant implications for the use of the guide in the manner suggested in chapter 7, where the input is modulated at above 1 GHz to achieve high power linear operation. At all modulation depths at 1 GHz it is seen that there is considerable distortion when a 10 mW bias is used. Therefore, the modulation depth will probably have to be restricted to 0.1 and below to achieve this 'linear' operation.

In addition, harmonic distortion has an impact on multi-channel systems utilising (modulation) frequency division multiplexing (FDM) techniques. In FDM the channels are separated by using a different modulation frequency and filtering the output. Clearly if the harmonic, in particular the 2^{nd} harmonic, of one channel lies in the bandwidth of a higher frequency channel then there will be significant distortion. This distortion will depend on the modulation depth of the applied signals and the frequencies involved. In the next chapter intermodulation and crosstalk effects will be examined.

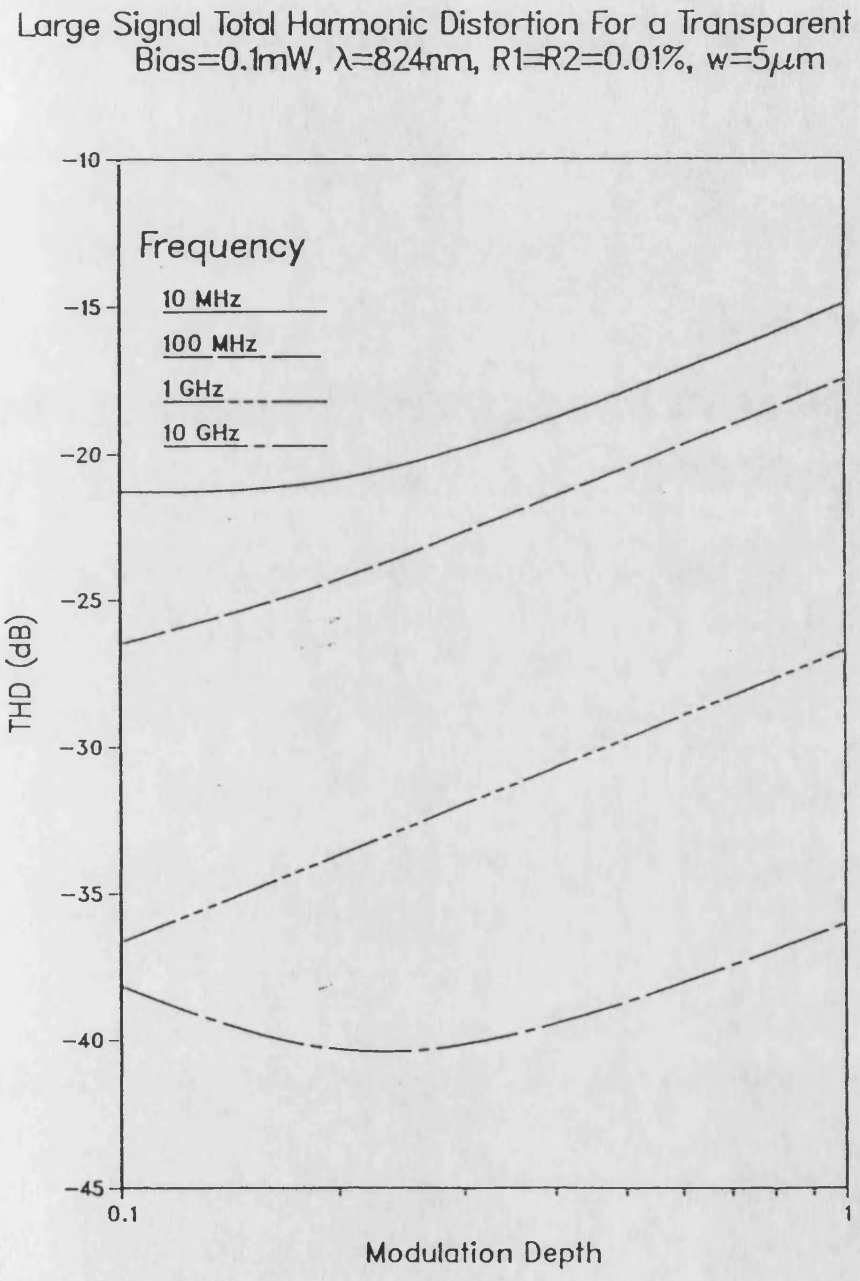

Figure 8.29 : Variation of large signal, total harmonic distortion with modulation depth, as a function of optical input frequency with an optical bias power of 0.1 mW, for a transparent guide.

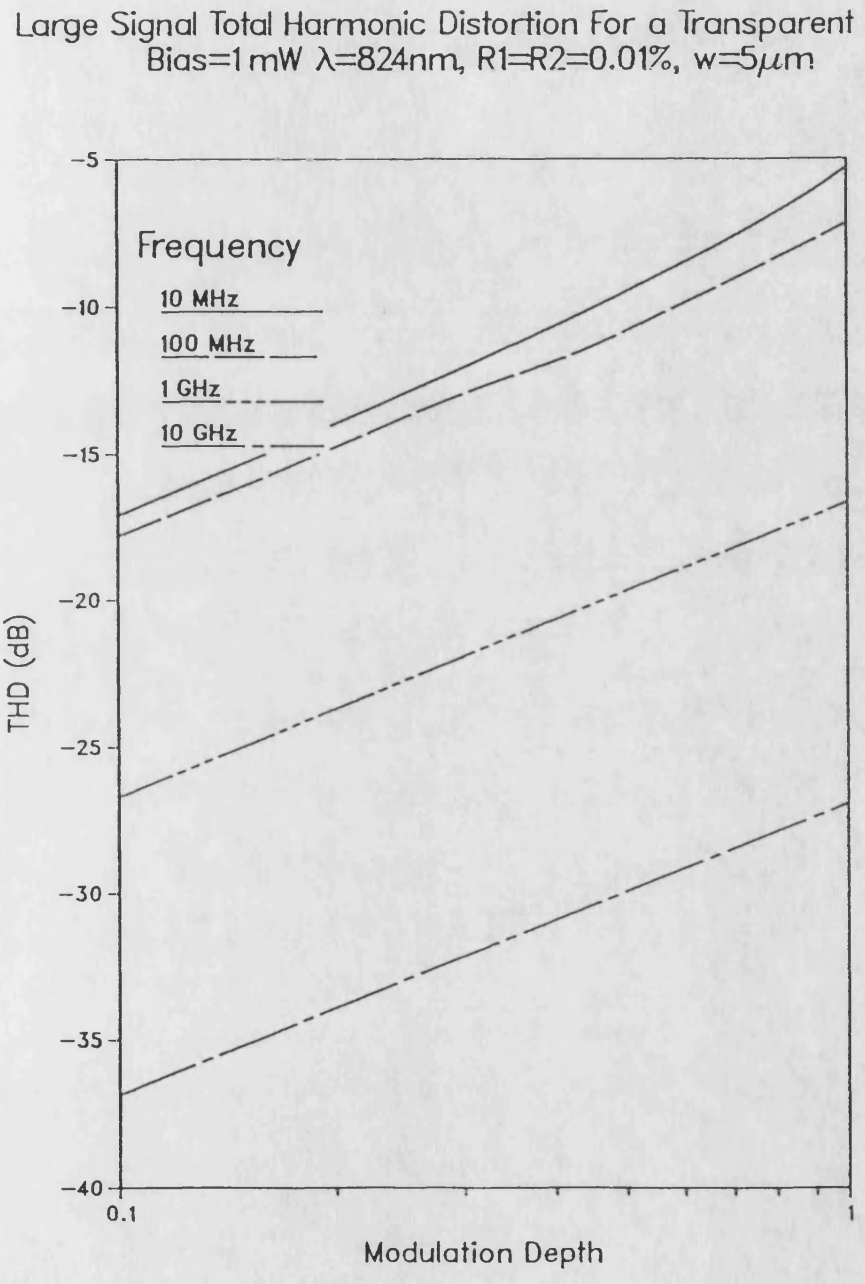

Figure 8.30 : Variation of large signal, total harmonic distortion with modulation depth, as a function of optical input frequency with an optical bias power of 1 mW, for a transparent guide.

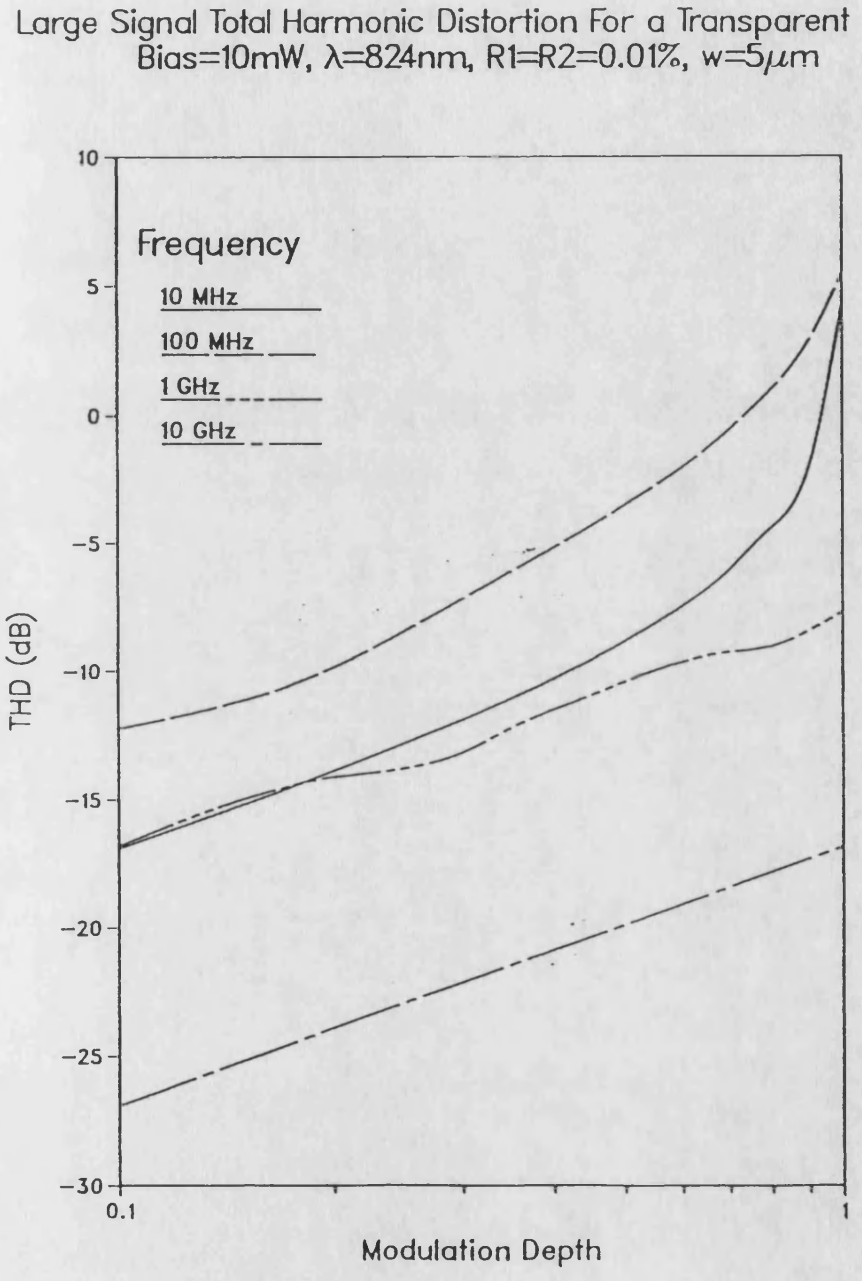

Figure 8.31 : Variation of large signal, total harmonic distortion with modulation depth, as a function of optical input frequency with an optical bias power of 10 mW, for a transparent guide.

8.5 Conclusions

In this chapter the large signal steady state model has been extended to the time domain to produce a full large signal, travelling flux time dependent model. Working from initial conditions at the t=0 boundary, usually generated by the static model, small steps in time are taken. For each step the forward and backward fluxes are allowed to 'walk' along the guide, calculated according to a relatively simple analytic expression which incorporates spontaneous emission (noise) as well as stimulated gain. The method allows the use of a fairly coarse mesh in the longitudinal dimension, c 10-50 μm, compared to those which are employed for finite difference and finite element techniques. Using this model on the SWURCC : ICL 3580 it is possible to examine pico second effects over a time scale of at least 100 ns in a single run, and as long as required in multiple runs.

In contrast to the SSA presented in chapter 7, this model is multi-dimensional as the gross optical gain and spontaneous emission terms can be considered over a range of (optical) wavelength slots. In addition, the formulation of the solution to the continuity equations does not rely on the form of the optical input. Therefore, different forms of input may be easily considered: such as, step, pulsed, sinusoidal or multi-channel inputs. In this chapter only 'perfect' input signals are considered but it would be relatively easy to provide the model with realistic inputs, from the laser diode model in chapter 5, using an 'inline' approach [7].

Using this dynamic large signal model the modulation response estimated in chapter 6 and the frequency response estimated in chapter 7 have been fully examined, for the case of a transparent guide with low input and output port reflectances (10^{-4}). The relationship between the input signal and the output (modulation) spectrum has been considered. By recourse to the SSA suitable analytic expression have been derived to describe the behaviour of the output harmonics.

Specifically, it has been shown that for near linear operation, the power in each harmonically related component is proportional to $\left(m \cdot \hat{W}_{in}\right)^2$, where m is the

modulation index or depth and $\hat{W}_{in}$ is the optical bias power. Above the break region the fundamental output power becomes independent of frequency, whilst the higher harmonics roll-off at (n-1)· 1 0 dB/decade. In this region of operation and for low input powers it is seen that the ratio of the harmonic power to the next harmonic is a frequency dependent 'constant'. Hence the dBm spacing between harmonics will be identical at a particular frequency.

As well as examining this linear region, attention has also been given to the non-linear behaviour that can only be modelled using this type of dynamic model. When large fluctuations in signal are considered the linearising assumptions of the small signal model break down. In this case several effects are observed, mainly :

- The dc or bias conditions drift due to the asymmetric variation in flux.
- The gain compression is reduced.
- Many significant harmonics become apparent, causing signal distortion.

In the break region, the harmonic behaviour exhibits quite unpredictable behaviour, due to there being a significant time varying gain component which lags the flux variations. This time varying component is seen to be dependent on the optical bias power, the modulation index and the modulation frequency.

Using the large signal model, the quasi-static analysis for low modulation frequencies has been confirmed and its range of validity, estimated by the SSA, has been established. The only deviation between the quasi-static and large signal analyses is the treatment of the noise. In the former case the noise cannot be truly estimated as its temporal behaviour is not known, whilst in the latter, the spontaneous terms are included at each time step. This gives rise to a frequency dependent noise floor, the nature of which is determined by the large signal variations in the carrier density which controls both the spontaneous emission and the stimulated gain terms.

The fundamental frequency response, predicted in chapter 7 has also been confirmed. In contrast to the Fabry-Perot Laser Amplifier [7], the fundamental gain is seen to increase with frequency above ω_n. The forward pass gain for the fundamental output tends towards the steady state bias gain, as the anti-phase component which

leads to the gain compression decays to a negligible amount. Thus, it has been established that to achieve linear or near-linear performance from the waveguide the input bias power and modulation index product must be kept to below 1 mW, or the modulation frequency must be above the upper break frequency, ω_u. In the former case, linear operation is ensured as the stimulated recombination is negligible whilst in the latter the flux and carrier density become decoupled.

Finally, it has been seen that for all cases, higher harmonic components are generated due to the interaction between the flux and carrier density. This type of effect has significant implications for multi-channel WDM or FDM systems, as it leads to inter-channel crosstalk, intermodulation distortion [10,11] and other wave-mixing effects. In many cases the THD is as significant or more significant than the broadband Amplified Spontaneous Emission (ASE). Clearly, any multi-dimensional dynamic model has a heavy computing overhead to, say, a small signal analysis. However, such a model has been shown to be essential if the full behaviour of an active waveguide is to examined.

References, chapter 8

1 WAY, W.I., : 'Large signal non-linear distortion prediction for a single-mode laser diode under microwave intensity modulation',

*IEE J. Lightwave Tech., 1987, **LT-5**, (3), pp305-315.*

2 BUUS, J., 'Principles of semiconductor laser modelling',

*IEE Proc. J, 1985, **132**, (1), pp42-51.*

3 LAU, K.Y., URY, I. and BAR-CHAIM, N., 'Superluminescent damping of relaxation resonance in the modulation response of GaAs lasers',

*Appl. Phys. Lett., 1983, **4**, (4), pp329-331.*

4 PERKINS, M.C.J. and ORMONDROYD, R.F., 'Transient analysis of optical bistability in inhomogeneously pumped lasers',

*IEE Proc. J, 1988, **135**, (2), pp133-145.*

5. OTSUKA, K., 'Proposals and analysis on laser amplifier based integrated optical circuits',

*IEEE J. Quantum Electron., 1981, **QE-17**, (1), pp23-28.*

6. ADAMS, M.J., 'Time dependent analysis of active and passive optical bistability in semiconductors.'

*IEE Proc. J, 1985, **132**, (6), pp343-348.*

7. LOWERY, A.J., 'New inline wideband dynamic semiconductor laser amplifier model',

*IEE Proc. J, 1988, **135**, (3), pp242-250.*

8. MUKAI, T. and YAMAMOTO, Y., 'Gain, frequency bandwidth and saturation output power of AlGaAs DH laser amplifiers',

*IEEE J. Quantum Electron., 1981, **QE-17**, (6), pp1028-1034.*

9. YAMAMOTO, Y., 'Characteristics of AlGaAs Fabry-Perot cavity type laser amplifiers',

*IEEE J. Quantum Electron., 1980, **QE-16**, (10), pp1047-1052.*

10. ÖBERG, M.G., and OLISSON, N.A., 'Crosstalk between intensity modulated wavelength division multiplexed signals in a semiconductor laser amplifier',
IEEE J. Quantum Electron, 1988, QE-24, (1), pp52-59.

11. DARCIE, T.E., and JOPSON, R.M., 'Non linear interation in optical amplifiers for multi-frequency lightwave systems',
Electron. Letts., 1988, 24, (10), pp638-640.

12. AGRAWAL, G.P., 'Population pulsations and non-degenerate four wave mixing in semiconductor lasers and amplifiers',
J. Opt. Soc, America, B , 1988, 5, (1- Special issue on wave mixing and phase conjugation), pp147-159.

13. TUMA, J.J., 'Engineering Mathematics Handbook' - 2nd Edition,
McGraw-Hill, 1979.

9 CROSSTALK AND INTERMODULATION

9.1 Introduction

In a practical optical communications systems, optical signals of different optical wavelength and modulation frequency will be routed through the same optical waveguide. Indeed such systems have been proposed for long time [1] and a practical example of such a system is the integrated twin DBR lasers fed into a single pumped waveguide, recently presented by Garrett et al [2] and reproduced in schematic form in figure 9.1.

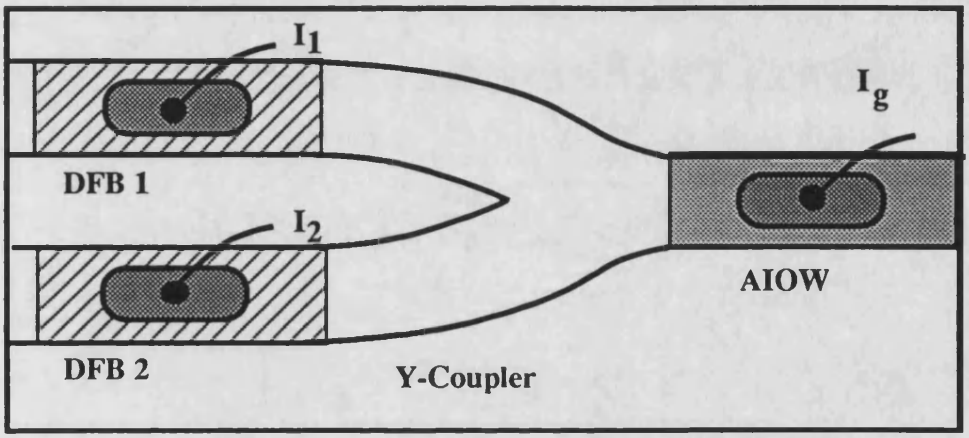

Figure 9.1, Schematic Diagram of Two DFB Lasers 'Y'
coupled to an Active Integrated Optic Waveguide (after [2]).

One of the main advantages of the active waveguide is that it is possible to use a wavelength division multiplexing (WDM) scheme; where signals with identical frequencies, but separate wavelengths, can be processed in one circuit element and still be kept separate [3]. As was stated in the conclusions to chapter 8, the presence of two optical signals of different frequencies, in an active waveguide, will lead to intermodulation products. This is due to the modulated carrier density interacting with the optical flux. It is the aim of this chapter to examine the behaviour of these intermodulation products and to quantify the nature of signal cross talk in an active

waveguide. In this case, crosstalk is taken to mean the interference between two signals at **different** optical wavelengths.

There is no significant new theory to present in this chapter, as the model used is the large signal time dependent model presented in chapter 8. The only modification required for that model is to the input signal 'generator' which is now used to produce multi frequency, multi wavelength input signals. However, a short discussion on the production of intermodulation and crosstalk products is presented, based on the small signal analysis of chapter 7. It should be pointed out that the cross talk discussed in this chapter is a dynamic phenomenon, as opposed to the static analyses presented by other authors for TWLAs (see for example [3] and the references therein).

9.2 Theoretical Discussion

In this chapter, two distinct cases are considered. Firstly, intermodulation where two input signals are applied at the same optical wavelength but with different modulation frequencies. Secondly, crosstalk where two input signals are applied at different wavelengths and with different modulation frequencies.

9.2.1 Intermodulation Distortion

For the case of intermodulation distortion, the optical flux input to the waveguide can be written as,

$$P_{in}(\lambda_k) = \hat{P}_{in}\left(1 + m_1 \cdot \cos(\omega_1 t) + m_2 \cdot \cos(\omega_2 t + \psi)\right) \cdot \qquad (9.1)$$

Equation (9.1) clearly shows that the input signal is restricted to one wavelength slot, λ_k, with a mean power of $\hat{P}_{in}$ and two modulation components, (ω_1, m_1) and (ω_2, m_2). The ψ term in the second modulation component indicates that the two components may also have a phase shift between them at t = 0. For convenience this phase shift is ignored in the analysis presented below. From equations (9.1) it can be deduced that the major time varying components of flux and carrier density will occur at ω_1 and ω_2, giving the following for P, Q and N,

$$\begin{aligned} P &= \hat{P} + p_1 \cdot \cos(\omega_1 t) + p_2 \cdot \cos(\omega_2 t) \quad (a) \\ Q &= \hat{Q} + q_1 \cdot \cos(\omega_1 t) + q_2 \cdot \cos(\omega_2 t) \quad (b) \qquad (9.2) \\ N &= \hat{N} + n_1 \cdot \cos(\omega_1 t) + n_2 \cdot \cos(\omega_2 t) \quad (c). \end{aligned}$$

The full solution of the small signal rate equations using the quantities in (9.2) is tedious and unnecessary for this analysis as the components that are of specific interest, the intermodulation products, are ignored by the small signal analysis. Instead

a condensed discussion is presented to demonstrate the generation of the intermodulation products, concentrating on the interaction of the gain and optical flux.

If the carrier density has the form shown in equation (9.2 c) then the net optical gain, G[N], will also have the same form but equation (8.52) in section 8.4.4 shows that there is a phase shift, ϕ of between $-\pi$ and $-3\pi/2$ between the flux and carrier density variations. If the effect of spontaneous emission is ignored, the variation of the forward travelling flux may be expressed as,

$$\frac{1}{v}\frac{\partial P}{\partial t} + \frac{\partial P}{\partial z} = G \cdot P . \qquad (9.3)$$

The product of the forward travelling flux and the net effective gain can be expressed as,

$$G \cdot P = \left(\hat{G} + g_1 \cdot \cos(\omega_1 t - \phi) + g_2 \cdot \cos(\omega_2 t - \phi)\right) \cdot \left(\hat{P} + p_1 \cdot \cos(\omega_1 t) + p_2 \cdot \cos(\omega_2 t)\right) . \qquad (9.4)$$

Basic trigonometry shows that the resulting flux will have components at,

$$\cos((\omega_1 - \omega_2)t), \cos(\omega_1 t), \cos(\omega_2 t), \cos((\omega_2 + \omega_1)t), \cos(2\omega_1 t), \cos(2\omega_2 t), \qquad (9.5)$$

where $\omega_1 > \omega_2$ and the constant phase shift term ϕ has been omitted for convenience. These are the primary intermodulation products and it follows from the analysis presented in section 8.4.3 that there will also be secondary intermodulation products at $\cos(\omega_1)$, $\cos(\omega_2)$, $\cos((2\omega_1 - \omega_2)t)$ and $\cos((2\omega_2 - \omega_1)t)$. These secondary intermods are of particular importance, as they will give rises to co-channel interference between the two input signals. It should be noted that the secondary intermods at $\cos(\omega_1)$ and $\cos(\omega_2)$ will not necessarily be in phase with the fundamental components.

9.2.2 Crosstalk

For the case of crosstalk, the input signal to the waveguide can be written as,

$$P_{in} = \hat{P}_{in,j}(\lambda_j)\left(1 + m_1 \cdot \cos(\omega_1 t)\right) + \hat{P}_{in,k}(\lambda_k)\left(1 + m_2 \cdot \cos(\omega_2 t)\right). \quad (9.7)$$

clearly showing that the input signal has two frequency components, ω_1 and ω_2, at separate wavelengths, λ_j and λ_k. In a similar manner to the discussion of the intermodulation products, it can be deduced that the major components of flux and carrier density are,

$$\begin{aligned}
P(\lambda_j) &= \hat{P}(\lambda_j) + p_1(\lambda_j) \cdot \cos(\omega_1 t) \quad (a) \\
P(\lambda_k) &= \hat{P}(\lambda_k) + p_2(\lambda_k) \cdot \cos(\omega_2 t) \quad (b) \\
Q(\lambda_j) &= \hat{Q}(\lambda_j) + q_1(\lambda_j) \cdot \cos(\omega_1 t) \quad (c) \qquad (9.8) \\
Q(\lambda_k) &= \hat{Q}(\lambda_k) + q_2(\lambda_k) \cdot \cos(\omega_2 t) \quad (d) \\
N &= \hat{N} + n_1 \cdot \cos(\omega_1 t) + n_2 \cdot \cos(\omega_2 t) \quad (e)
\end{aligned}$$

It should be noted that the carrier density is independent of wavelength and contains components of both modulation frequencies. The calculation of the flux at each wavelength involves solving,

$$\frac{1}{v}\frac{\partial P_i}{\partial t} + \frac{\partial P_i}{\partial z} = G_i \cdot P_i . \quad (9.8)$$

for each slot, where i is the slot index. In equation (9.9) the net effective gain in each wavelength slot, $G_i(N)$, is a function of N and will therefore contain components at both ω_1 and ω_2, ie

$$G_i(N) = \left(\hat{G}_i + g_{i,1} \cdot \cos(\omega_1 t - \phi) + g_{i,2} \cdot \cos(\omega_2 t - \phi)\right) . \quad (9.10)$$

Therefore, the gain flux product for the component of flux at λ_j, for example, will give rise to major components at,

$$\begin{aligned} &\cos((\omega_1 - \omega_2)t), \\ &\cos(\omega_1 t), \cos(\omega_2 t), \\ &\cos((\omega_2 + \omega_1)t), \\ &\cos(2\omega_1 t), \qquad\qquad \omega_1 > \omega_2 \end{aligned} \tag{9.11}$$

with secondary intermodulation products at, $\cos(\omega_1)$, $\cos((2\omega_2)t)$, $\cos((2\omega_1 - \omega_2)t)$ and $\cos((2\omega_2 - \omega_1)t)$. It is of the upmost importance to note that although the two signal have separate wavelengths, the coupling via the carrier density gives rise to crosstalk between the signals, ie there is a component of frequency ω_2 in the output signal at λ_j.

It should also be noted that the crosstalk effect is purely due to the coupling of the flux and carrier density in the active waveguide. The model does not take into account any optical - optical interactions due to polarization changes [4] and four-wave mixing [5]. However, the model does incorporate the longitudinal variations of carrier density and gain where the analyses of [3] and [4] assume spatially averaged behaviour.

9.3 Results

Unless otherwise stated the parameter values used are the same as for table 6.1. For convenience the Hertzian frequency rather than the radian frequency is used in this section ($f = \omega/2\pi$).

9.3.1 Intermodulation Output Spectra

In figures 9.2 - 9.4 the intermodulation output spectra are given for three optical input bias powers, 0.1 mW, 1 mW and 10 mW. In each case the guide is biased to transparency to the given bias power. As well as the input bias, two modulation components are present, input 1 has a modulation frequency of f_1 = 1 GHz whilst input 2 has a modulation frequency of f_2 = 0.95 GHz. For each input modulation component, the modulation index is 0.5 (50% modulation). Each figure represents an increasing level of bias and hence pumping current and flux / carrier density interaction.

Figure 9.2 represents the case for low input powers. The primary intermodulation products predicted in section 9.2.1 are present above a noise floor at around 65 dBm. The secondary products are completely swamped by the spontaneous noise, indicating the low interaction present. In order from dc, the major components are at, dc, f_2, f_1, $2f_2$, f_2+f_1, $2f_1$. The output noise spectrum is seen to be very similar to those obtained for the single tone input (figure 8.3).

The output spectrum for a 1 mW bias shown in figure 9.3, may be considered to be a 'perfect' intermodulation spectrum for a two tone input. The response clearly contains significant components at the harmonic frequencies (2f, 3f, 4f, etc), primary intermods (at $f_1 - f_2$ and $f_1 + f_2$) and secondary intermods (at $2f_2 - f_1$, etc). Each major group of intermods and harmonics is seen to be symmetrical about a central frequency, which is a multiple of $(f_1 + f_2) / 2$.

As the bias power is raised to very high values, the output spectrum becomes quite cluttered, figure 9.4. There is considerable interaction between the optical flux and carrier density. This gives rise to many significant noise components across the

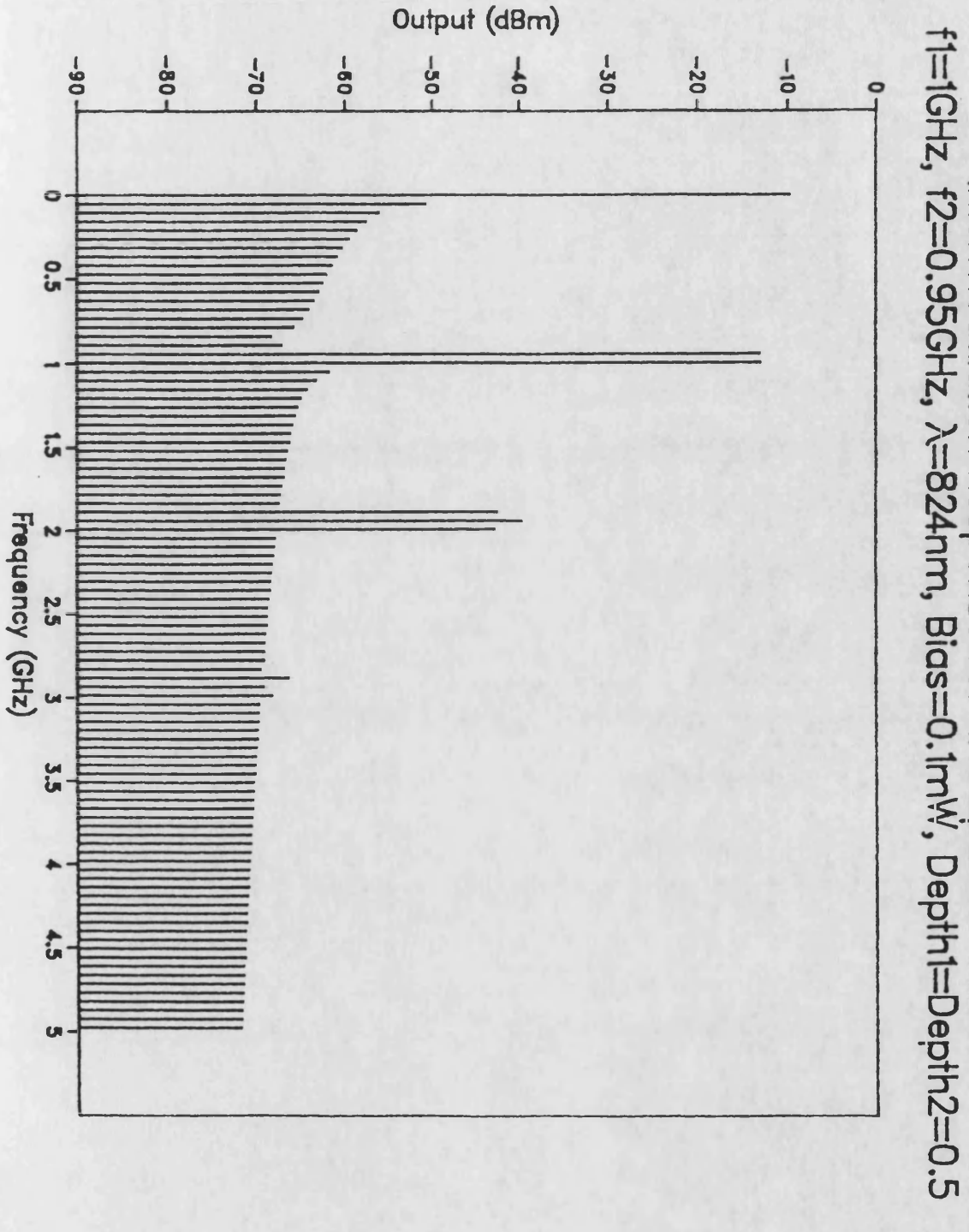

Figure 9.2 : Intermodulation spectrum response for a two tone optical input signal. Optical bias power = 0.1 mW, input wavelength = 824 nm, f_1 = 1 GHz, m_1 = 0.5, f_2 = 0.95 GHz, m_2 = 0.5.

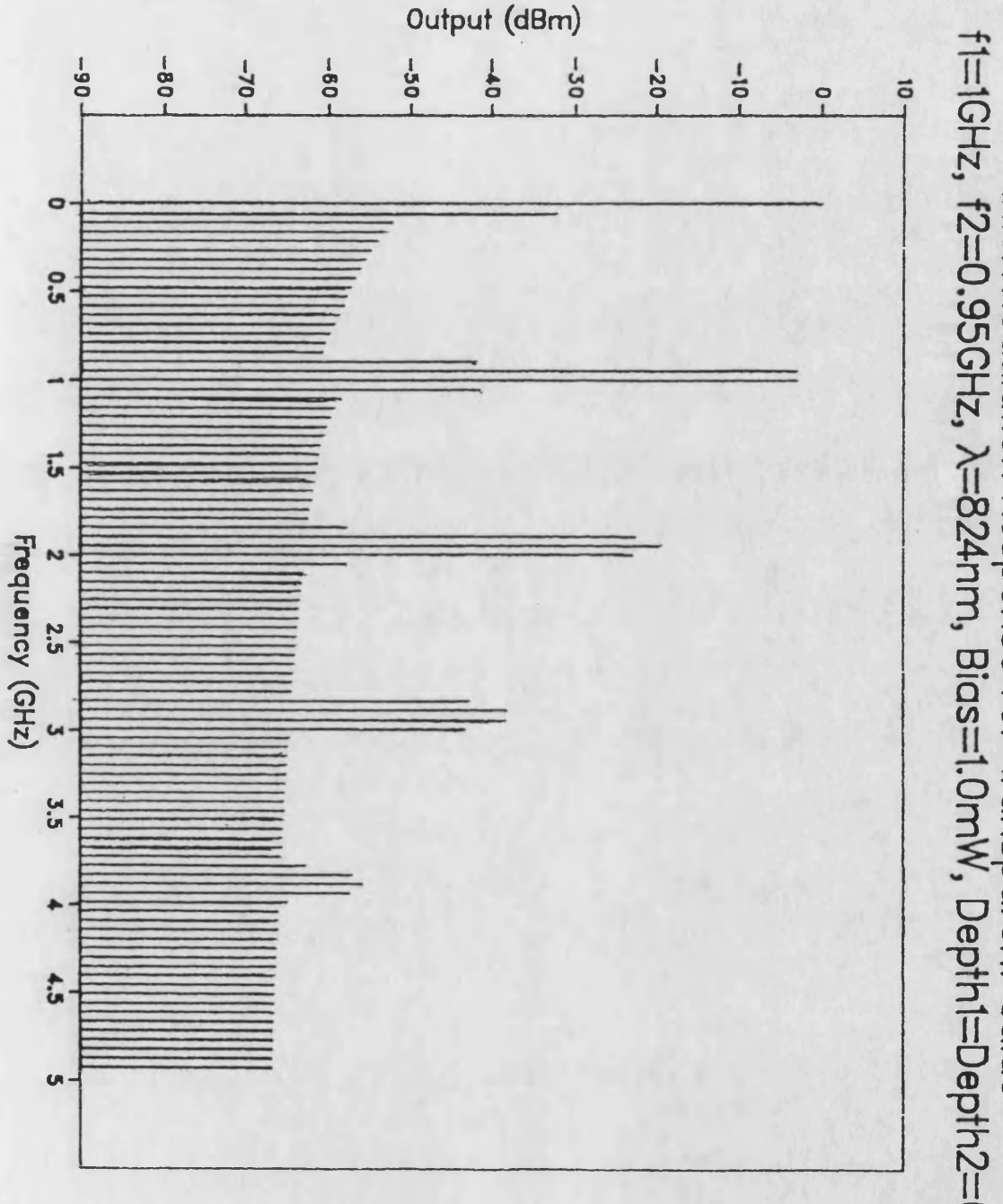

Figure 9.3 : Intermodulation spectrum response for a two tone optical input signal. Optical bias power = 1 mW, input wavelength = 824 nm, f_1 = 1 GHz, m_1 = 0.5, f_2 = 0.95 GHz, m_2 = 0.5.

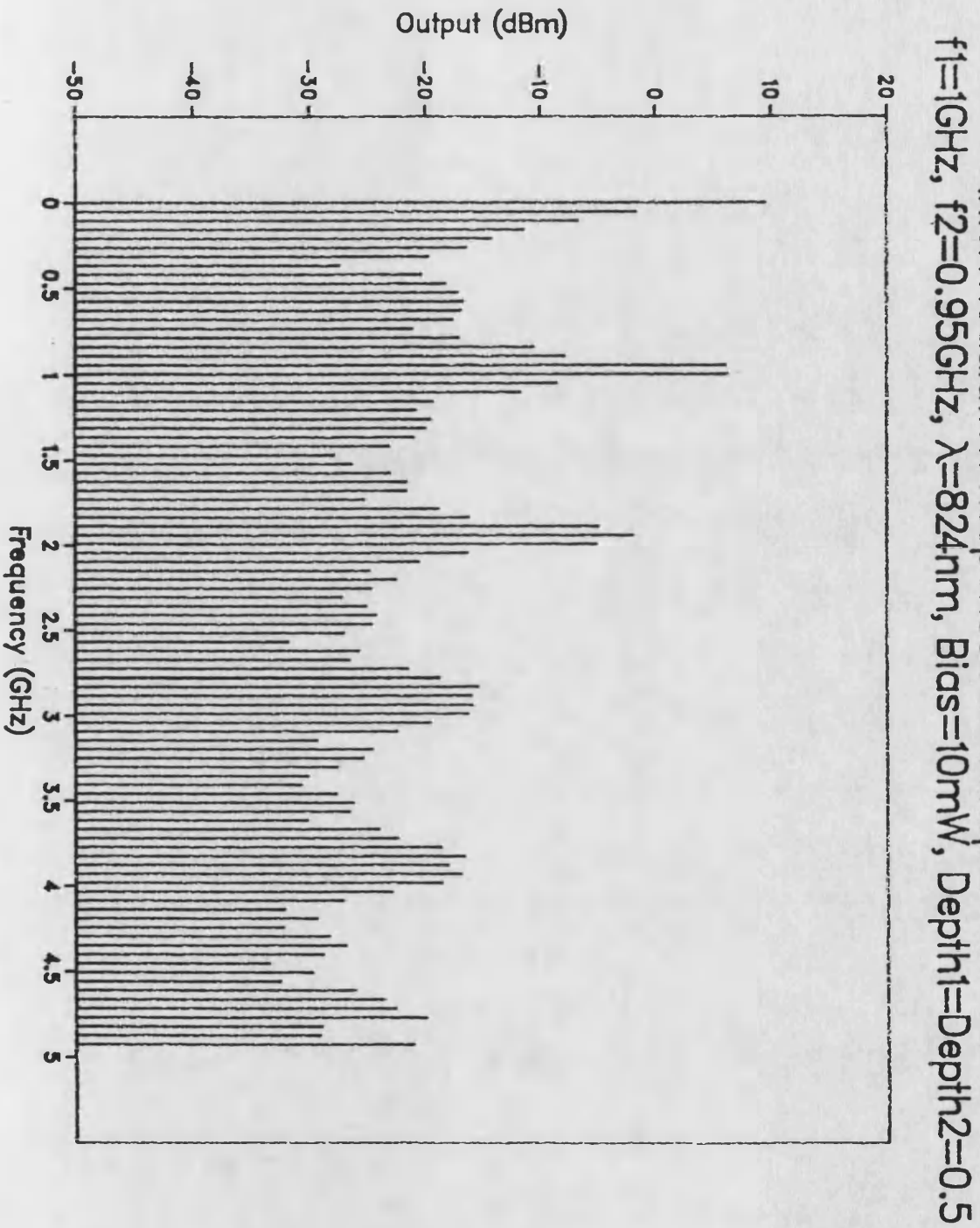

Figure 9.4 : Intermodulation spectrum response for a two tone optical input signal. Optical bias power = 10 mW, input wavelength = 824 nm, f_1 = 1 GHz, m_1 = 0.5, f_2 = 0.95 GHz, m_2 = 0.5.

frequency spectrum. The groups of harmonics and intermods are seen to be basically symmetrical at lower frequencies, but as the frequency rises the symmetry begins to be distorted by the noise floor.

9.3.2 Crosstalk Output Spectra

In this case two (optically) separate input signals are applied. Input signal 1 has an optical bias power $\hat{P}_{in,1}$ = 0.5 mW, a modulation frequency f_1 = 1.0 GHz, an optical wavelength λ_1 = 824 nm, and a modulation index of 0.5. Input signal 2 has an optical bias power $\hat{P}_{in,2}$ = 0.5 mW, a modulation frequency f_1 = 0.95 GHz, an optical wavelength λ_1 = 826 nm, and a modulation index of 0.5. The guide is biased so that the net dc output power is $\hat{P}_{in,1} + \hat{P}_{in,2}$ under the steady state input optical bias condition, ie a nominal transparency. It should be noted that as the gain varies with wavelength, for a particular value of carrier density in the guide, input 1 will 'see' a guide with net loss whilst input 2 will 'see' a guide with net gain.

The resulting output spectrum shown in figure 9.5 is shown in three ways. In figure 9.5(a) the total output power from the guide is shown. This would be the detected spectrum if a broadband optical detector were used. In figures 9.5(b) and 9.5(c) the output spectra shown are for the wavelength slots centred on 824 nm and 826 nm respectively. This is the output power which would be detected by narrow band optical detectors with a width of 0.4 nm. The narrow band spectra clearly show the co-channel crosstalk in the guide.

Some general observations can be made from figure 9.5(a) for the total output power from the guide. The two fundamental components are at, f_1, and f_2. As explained above, the two signals see different gains in the guide. Hence the output power is different for each signal, in contrast to the two-tone intermodulation case where the output power is identical for both signals. Clearly, there are intermodulation and harmonic components present in the output. One striking feature of this group of figures (9.5) is that the output spectra are very cluttered for a moderately pumped guide. This is due to the different gain for each signal leading to higher interaction.

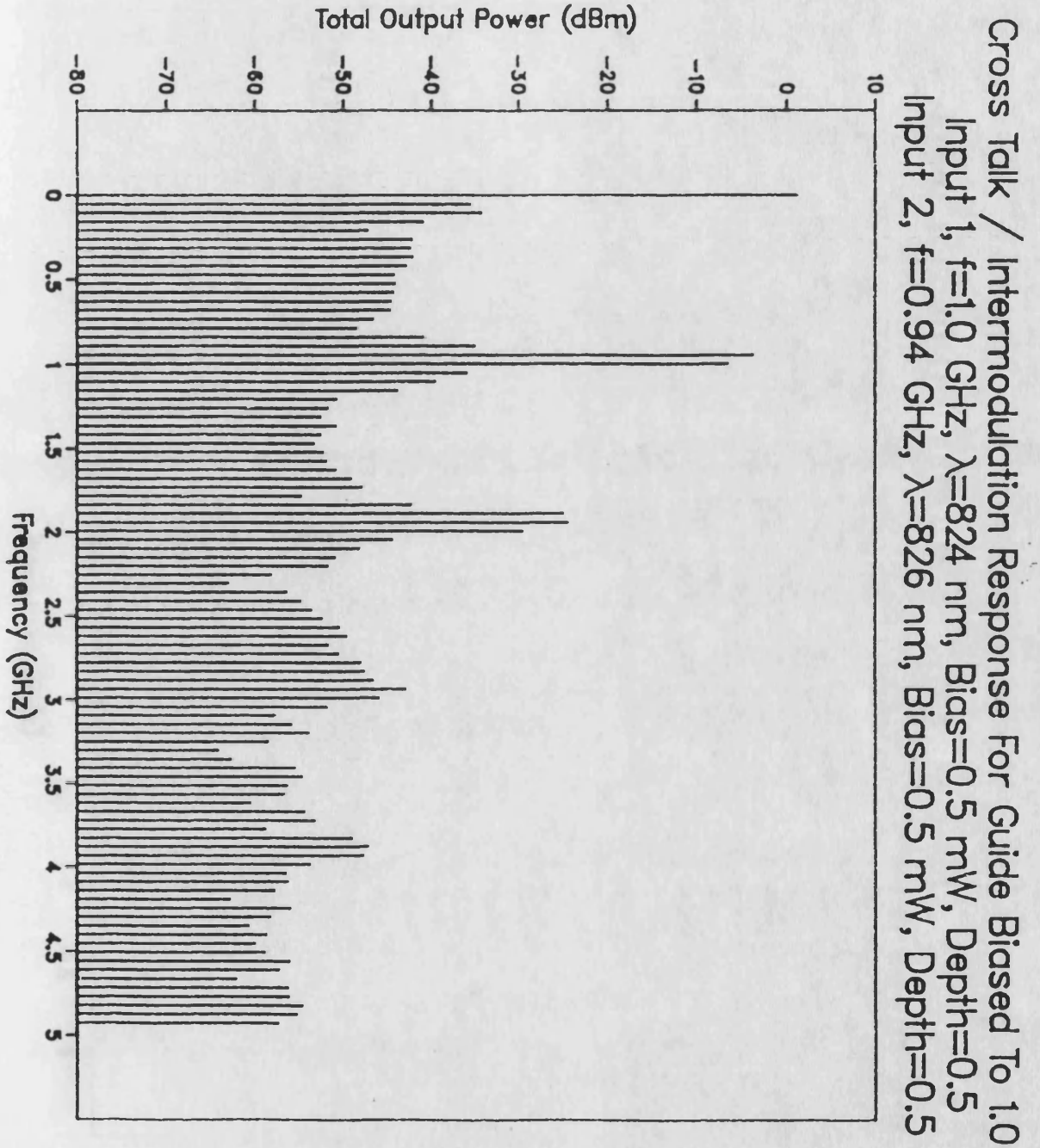

Figure 9.5a Crosstalk / Intermodulation spectrum response for a two tone optical input signal.

Input 1, P_{in} = 0.5 mW, λ_1 = 824 nm, f_1 = 1 GHz, m_1 = 0.5,

Input 2, P_{in} = 0.5 mW, λ_2 = 826 nm, f_2 = 0.95 GHz, m_2 = 0.5.

(a) Total Output Power,

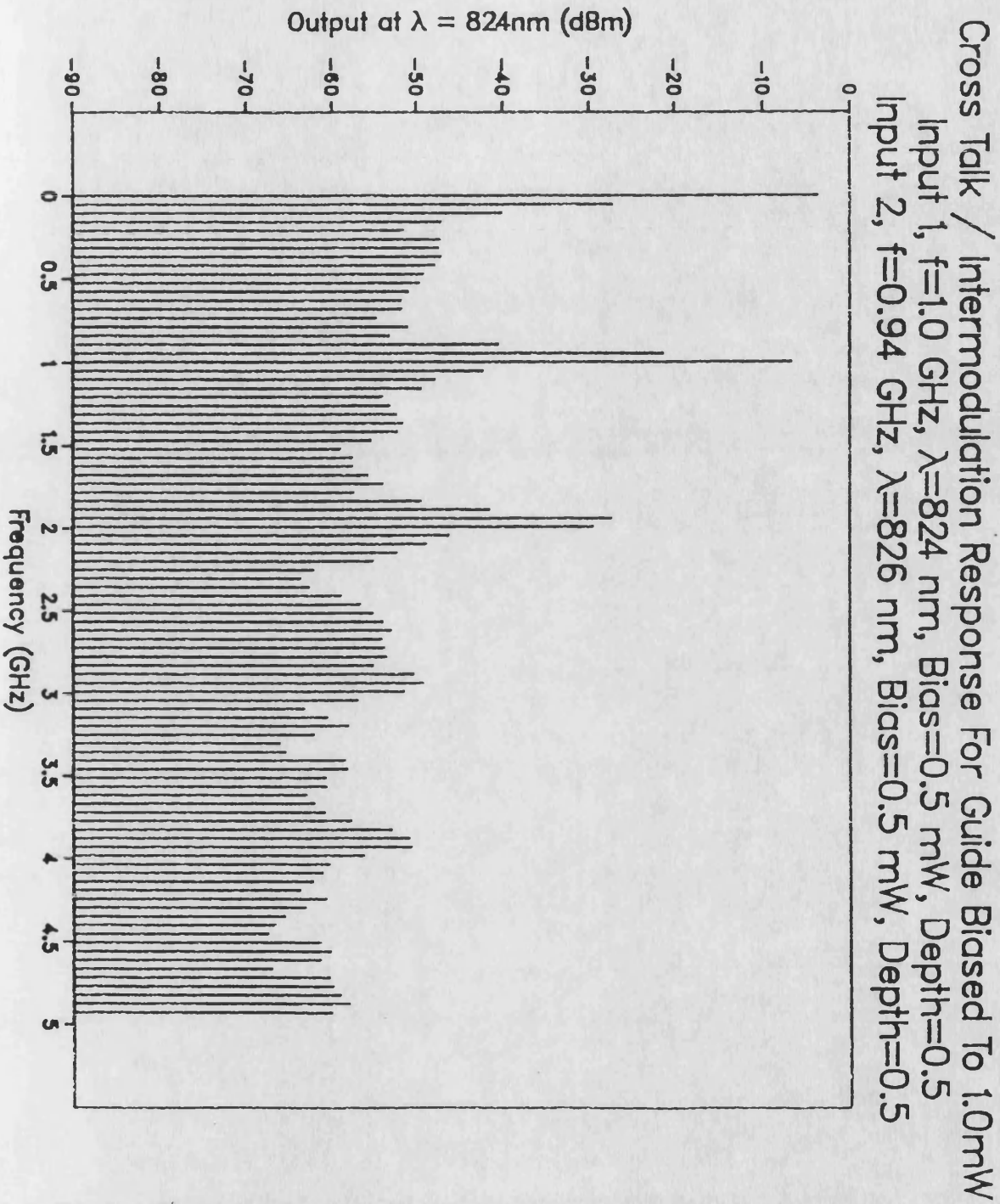

Figure 9.5b Crosstalk / Intermodulation spectrum response for a two tone optical input signal.

Input 1, P_{in} = 0.5 mW, λ_1 = 824 nm, f_1 = 1 GHz, m_1 = 0.5,

Input 2, P_{in} = 0.5 mW, λ_2 = 826 nm, f_2 = 0.95 GHz, m_2 = 0.5.

(b) Output at 824 nm,

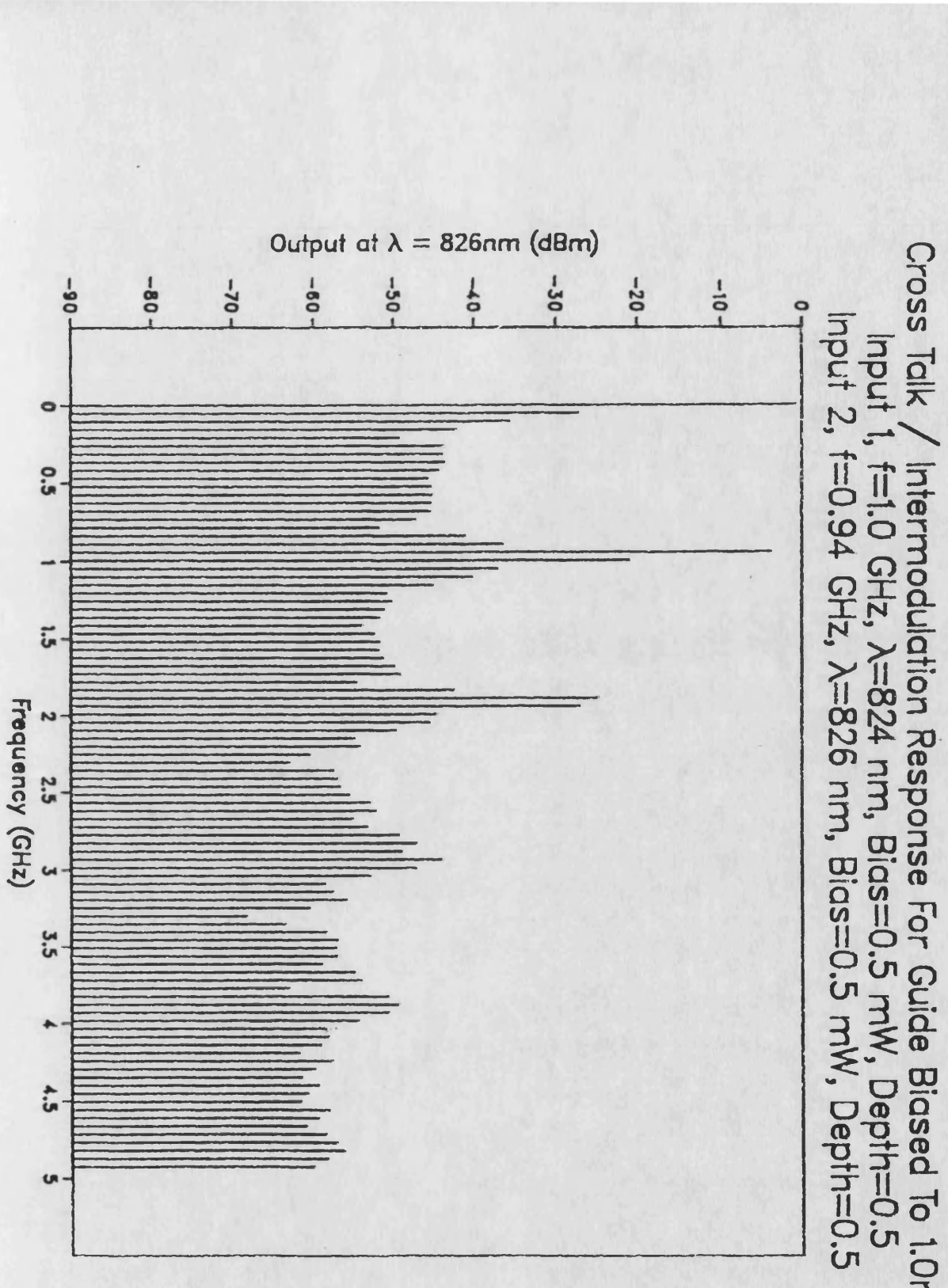

Figure 9.5c Crosstalk / Intermodulation spectrum response for a two tone optical input signal.

Input 1, P_{in} = 0.5 mW, λ_1 = 824 nm, f_1 = 1 GHz, m_1 = 0.5,

Input 2, P_{in} = 0.5 mW, λ_2 = 826 nm, f_2 = 0.95 GHz, m_2 = 0.5.

(c) Output at 826 nm.

Figures 9.5(b) and 9.5(c) show the co-channel crosstalk which arises through the interaction between the optical flux and the carrier density, as outlined in section 9.2.2. In this chapter the co-channel crosstalk is defined as the ratio of the component at particular frequency in the minor and major channels, eg.

$$X_{2,1} = \frac{P_{out}(f_1, \lambda_2)}{P_{out}(f_1, \lambda_1)} \quad , \tag{9.11}$$

which is referred to as the crosstalk in signal 2 from signal 1 or, where the context is clear, as the co-channel crosstalk.

From figure 9.5(b) the crosstalk in signal 1 from signal 2, $X_{1,2}$ = -18 dB whilst from figure 9.6(c), $X_{2,1}$ = -14 dB. The disparity between the two values is due to the different gains seen by each signal.

9.3.3 Variation of Crosstalk with Modulation Depth

In this set of results the input signal 1 is held constant with a modulation depth of 0.5 (50 % modulation) whilst input signal 2 is varied, from a modulation depth of 0.1 to 1.0 (10 - 100 % modulation). For each optical bias case, three groups of characteristics are shown: the total output power (a), the output power in the slot centred at 824 nm (b), and the output power in the slot centred at 826 nm (c). From the discussion in section 9.2.2 it is clear that there are many significant components in the output signal which may be of interest. In this section and the next, six output components are shown: the dc output bias power, the input frequency components (f_1 = 1 GHz, f_2 = 0.95 GHz), the intermodulation product at (f_1 - f_2) = 0.05 GHz, and the two secondary intermodulation products either side of the input components ($2f_2$ - f_1) = 0.90 GHz and ($2f_1$ - f_2) = 1.05 GHz.

Figure 9.6 shows the output characteristics for a guide biased to a nominal transparency for input bias powers of 0.05 and 0.05 mW. In this case there is a relatively low interaction between the flux and the carrier density, and hence the

intermodulation products tend to be lost in the spontaneous emission noise floor. The total output power characteristics in figure 9.6(a) clearly show the fixed output power at f_1 and the linearly rising component at f_2. The behaviour of the intermods is not clear, and do not shown any trend as the modulation depth increases.

In figure 9.6(b) the co-channel crosstalk is seen to rise linearly with modulation depth at 10 dB/decade, ie directly proportional to the input power of signal 2, and has a virtually constant value of $X_{1,2} \approx$ -28 dB. The rise in the crosstalk component has no perceptible effect on the dc component and the fundamental component at f_1. In contrast to the total output power characteristics, the primary intermodulation product at $f_1 - f_2$ is seen to rise at 10 dB/decade after overcoming the noise floor. In addition the secondary intermodulation products do not show the same behaviour that is shown in the total output power. These apparent discrepancies will be addressed later.

In figure 9.6(c) the co-channel crosstalk is flat across the modulation range, ie is unaffected by the change in signal 2. Therfore, the crosstalk is seen to be directly proportional to the optical input power of source signal (in this case, signal 1 and $X_{2,1}$ = -23 dB). For figure 9.6(c) the primary and secondary intermodulation products rise with modulation depths above 0.2.

It should be noted that intermodulation products will arise between all components across the frequency and wavelength spectra, as they interact via the carrier density. Therefore there will be more components in the total output power than just those shown in figure 9.6(b) and (c). However, this does not explain why the component at 0.05 GHz ($f_1 - f_2$) is less in the total output power characteristic than the sum of the two components at 824 and 826 nm. This can only occur if these components are in anti-phase which leads to a subtraction of the separate magnitudes. The phase shift, ϕ between the flux and carrier density components leads to this anti-phase component.

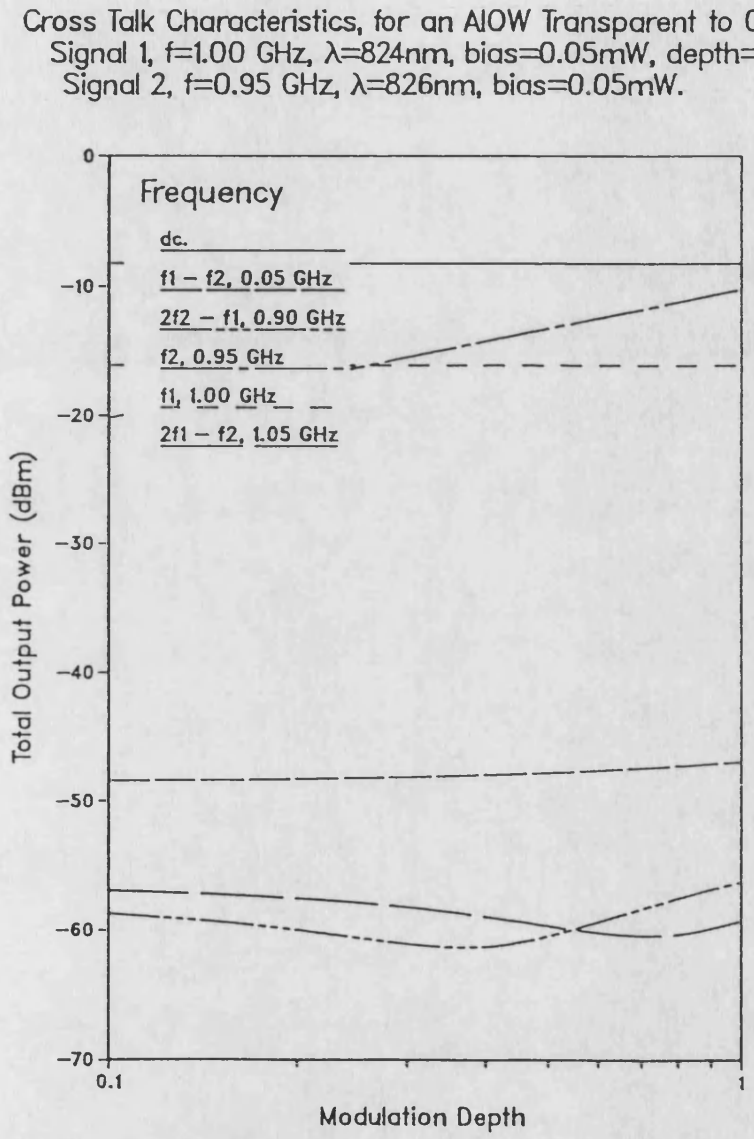

Figure 9.6a Crosstalk / Intermodulation modulation response, as a function of input modulation depth, for a two tone optical input signal.

Input 1, P_{in} = 0.05 mW, λ_1 = 824 nm, f_1 = 1 GHz, m_1 = 0.5,

Input 2, P_{in} = 0.05 mW, λ_2 = 826 nm, f_2 = 0.95 GHz, m_2 = varied.

(a) Total Output Power,

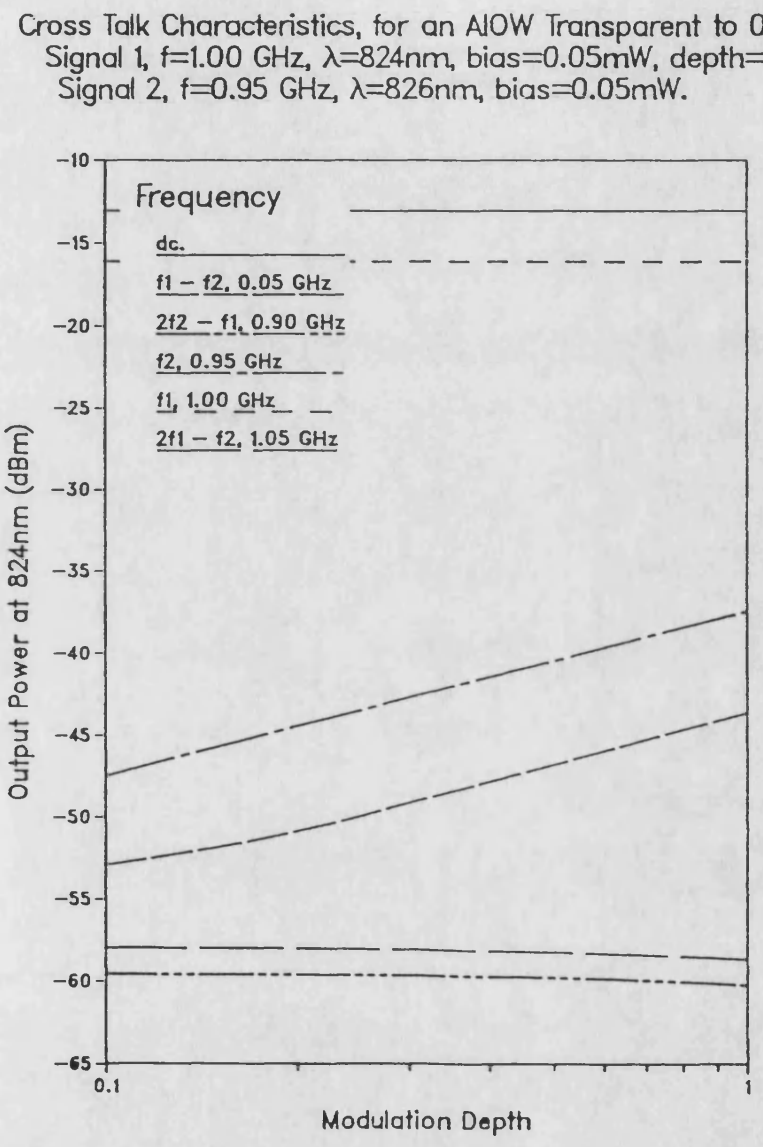

Figure 9.6b Crosstalk / Intermodulation modulation response, as a function of input modulation depth, for a two tone optical input signal.

Input 1, P_{in} = 0.05 mW, λ_1 = 824 nm, f_1 = 1 GHz, m_1 = 0.5,

Input 2, P_{in} = 0.05 mW, λ_2 = 826 nm, f_2 = 0.95 GHz, m_2 = varied.

(b) Output at 824 nm,

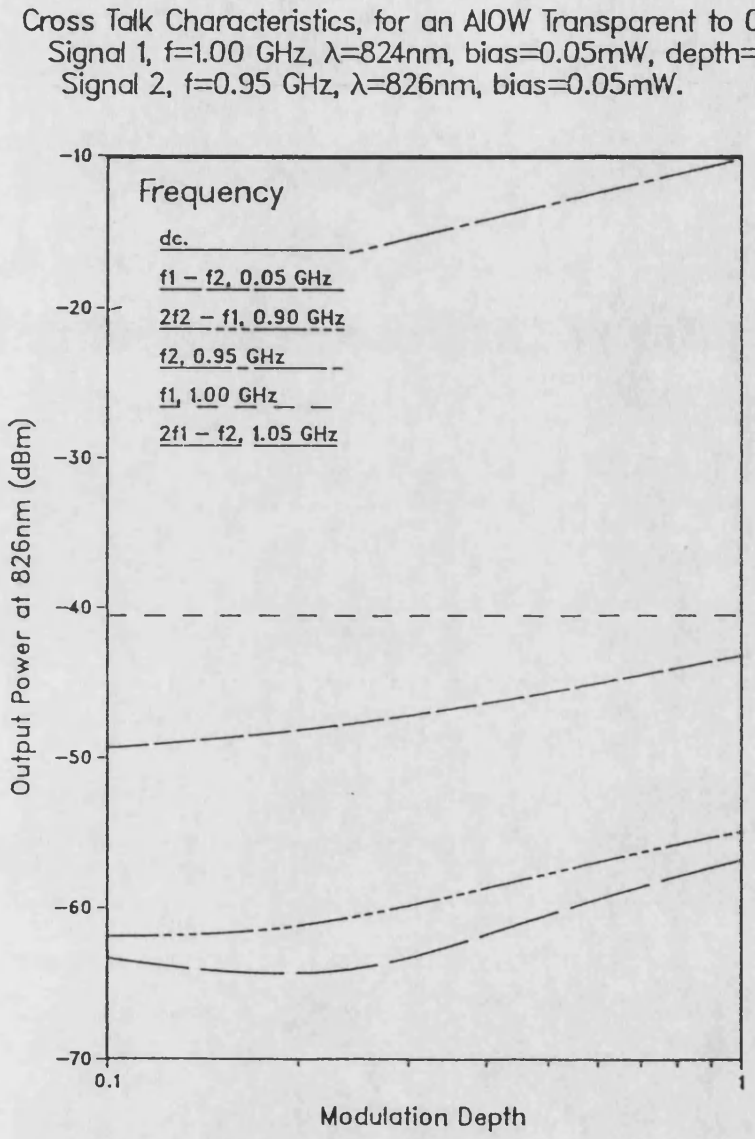

Figure 9.6c Crosstalk / Intermodulation modulation response, as a function of input modulation depth, for a two tone optical input signal.

Input 1, P_{in} = 0.05 mW, λ_1 = 824 nm, f_1 = 1 GHz, m_1 = 0.5,

Input 2, P_{in} = 0.05 mW, λ_2 = 826 nm, f_2 = 0.95 GHz, m_2 = varied.

(c) Output at 826 nm.

If the generation of the output component at 0.05 GHz is examined, there are two main components caused by the interaction of the carrier density variations with each input signal. From the interaction with signal 1 the following component arises,

$$g_{1,2} \cdot \cos\big((\omega_2 - \omega_1)t - \phi\big) \quad , \tag{9.12}$$

whilst the interaction with signal 2

$$g_{2,1} \cdot \cos\big((\omega_1 - \omega_2)t - \phi\big) \quad , \tag{9.13}$$

or

$$g_{2,1} \cdot \cos\big((\omega_2 - \omega_1)t + \phi\big) \quad , \tag{9.14}$$

from the identity $\cos(\theta) = \cos(-\theta)$, and where $\omega_1 > \omega_2$. Thus the phase shift between the two components is 2ϕ radians. From section 8.4.4 it is known that ϕ varies between $-\pi$ and $-3\pi/2$ as the modulation frequency varies from 0 to ∞. When the modulation frequency is equal to the natural frequency of carrier density variations, $f_n \approx 60$ MHz for this level of pumping (see table 7.2, in section 7.2.3), the value of phase shift is $\phi = -5\pi/4$. As the modulation frequencies in this case are much greater than ω_n then the phase shift, $\phi = -3\pi/2$ and the phase difference between the two major components will be -3π, ie in anti-phase. In this case the magnitude of the total output power component at $f_1 - f_2$ will be given by $g_{1,2} - g_{2,1}$ which is constant with modulation depth.

Figures 9.7 and 9.8 show the three groups of output characteristics as the input bias power is increased to 0.5 & 0.5 and 5 & 5 mW respectively. The trends noted above are apparent in both groups of figures but the characteristics for $f_1 - f_2$ are not constant with modulation depth, in the total output power case. Two main factors contribute to this discrepancy: Firstly, the natural frequency of carrier density variations increases with bias power / pumping. Thus the two major components of this intermod will no longer be in anti-phase. Secondly, the increased interaction at higher bias power leads to higher cross talk and spontaneous noise.

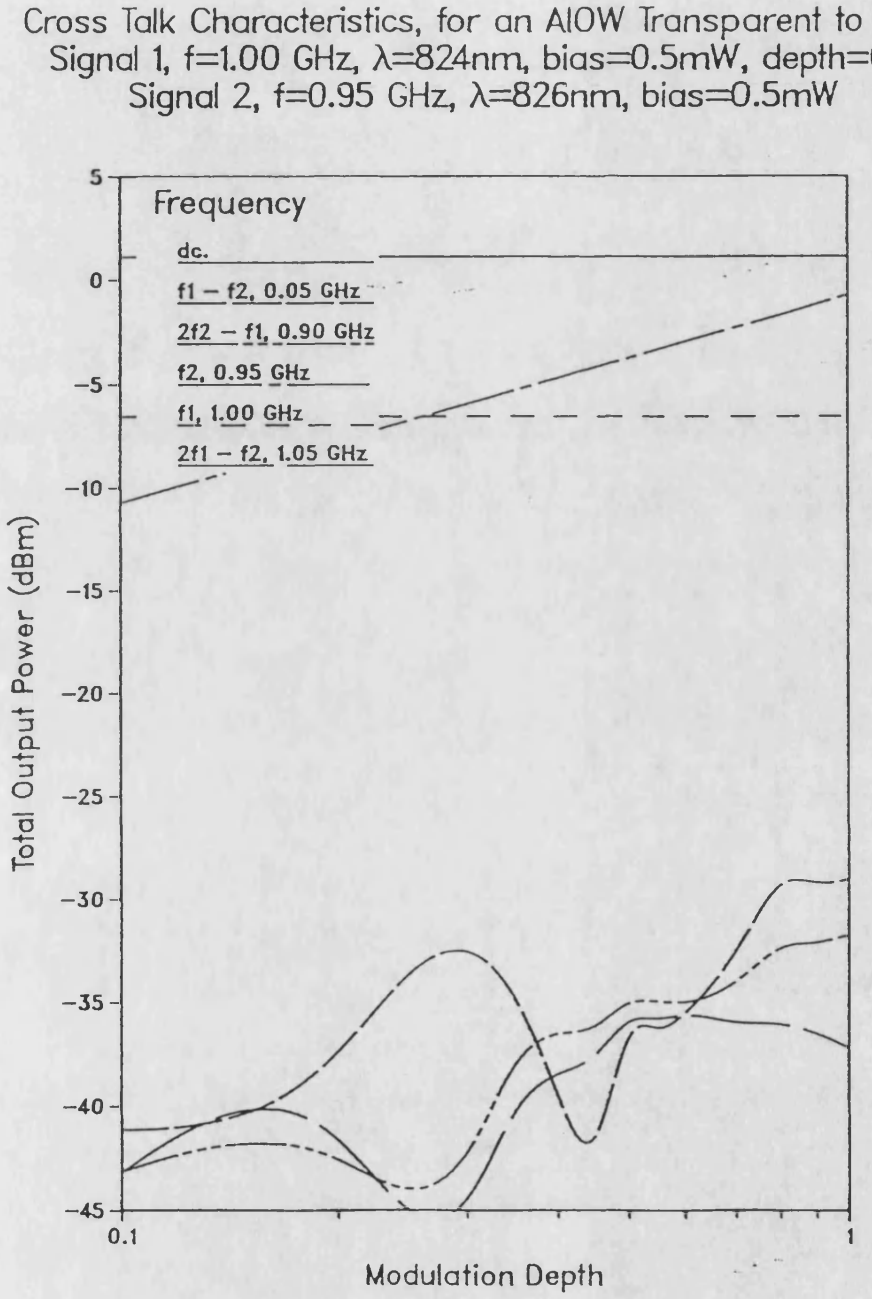

Figure 9.7 Crosstalk / Intermodulation modulation response, as a function of input modulation depth, for a two tone optical input signal.

Input 1, P_{in} = 0.5 mW, λ_1 = 824 nm, f_1 = 1 GHz, m_1 = 0.5,

Input 2, P_{in} = 0.5 mW, λ_2 = 826 nm, f_2 = 0.95 GHz, m_2 = varied.

(a) Total Output Power,

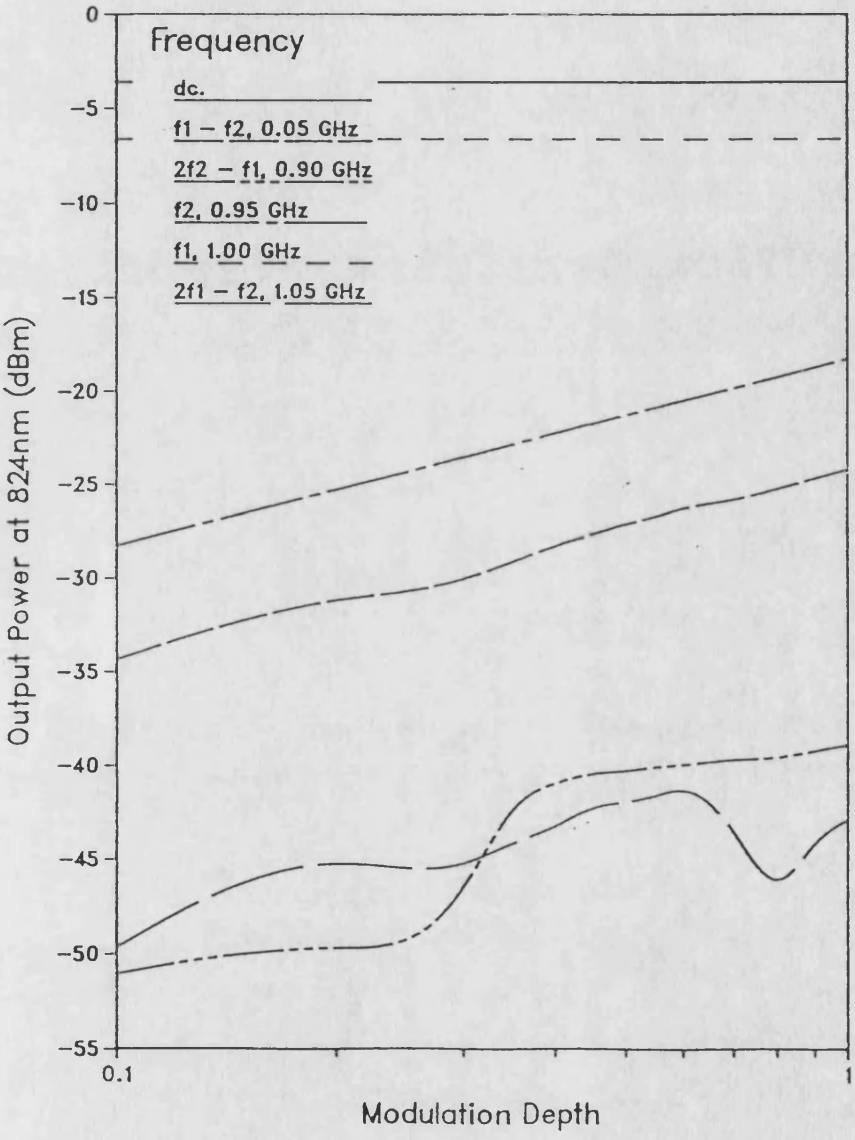

Figure 9.7b Crosstalk / Intermodulation modulation response, as a function of input modulation depth, for a two tone optical input signal.

Input 1, P_{in} = 0.5 mW, λ_1 = 824 nm, f_1 = 1 GHz, m_1 = 0.5,

Input 2, P_{in} = 0.5 mW, λ_2 = 826 nm, f_2 = 0.95 GHz, m_2 = varied.

(b) Output at 824 nm,

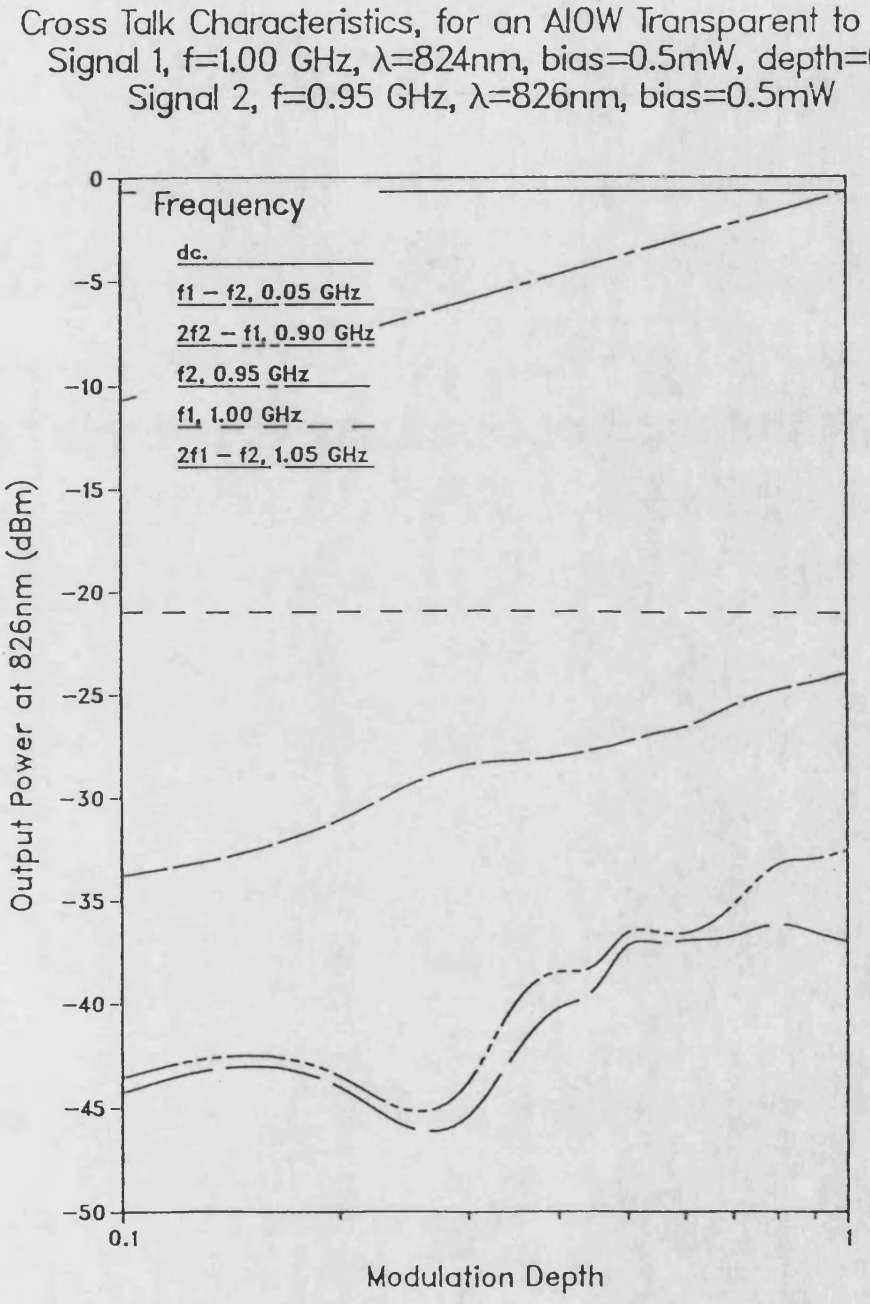

Figure 9.7c Crosstalk / Intermodulation modulation response, as a function of input modulation depth, for a two tone optical input signal.

Input 1, P_{in} = 0.5 mW, λ_1 = 824 nm, f_1 = 1 GHz, m_1 = 0.5,

Input 2, P_{in} = 0.5 mW, λ_2 = 826 nm, f_2 = 0.95 GHz, m_2 = varied.

(c) Output at 826 nm.

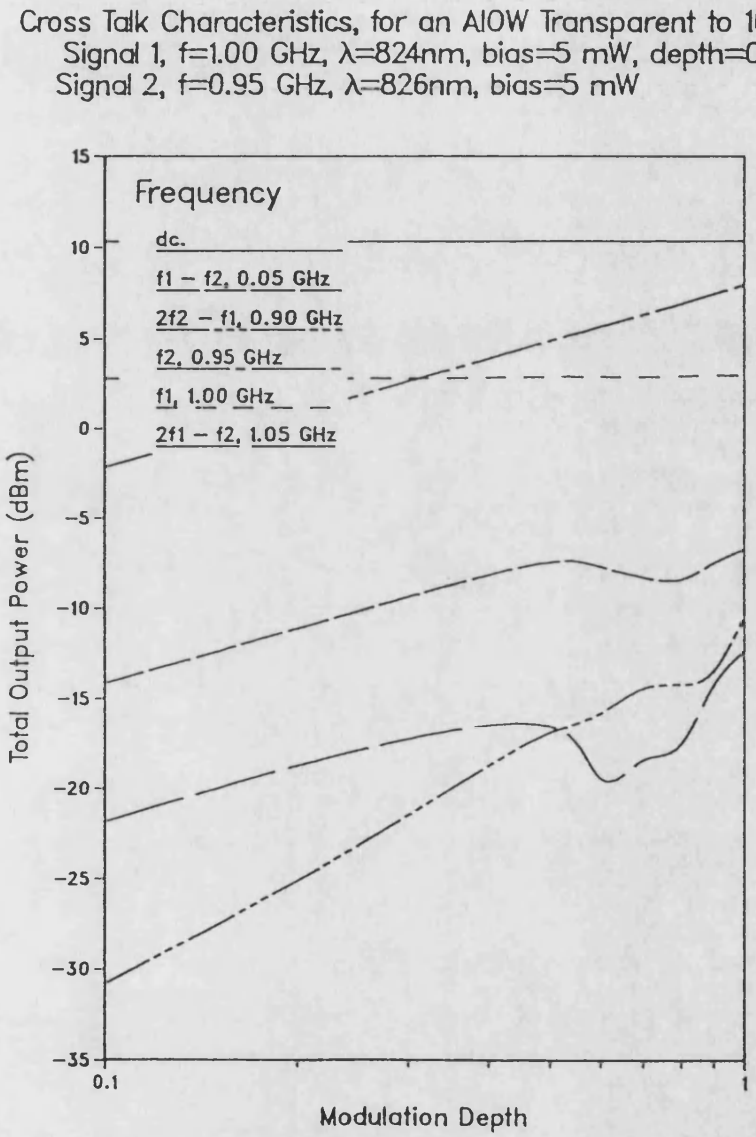

Figure 9.8a Crosstalk / Intermodulation modulation response, as a function of input modulation depth, for a two tone optical input signal.

Input 1, P_{in} = 5 mW, λ_1 = 824 nm, f_1 = 1 GHz, m_1 = 0.5,

Input 2, P_{in} = 5 mW, λ_2 = 826 nm, f_2 = 0.95 GHz, m_2 = varied.

(a) Total Output Power,

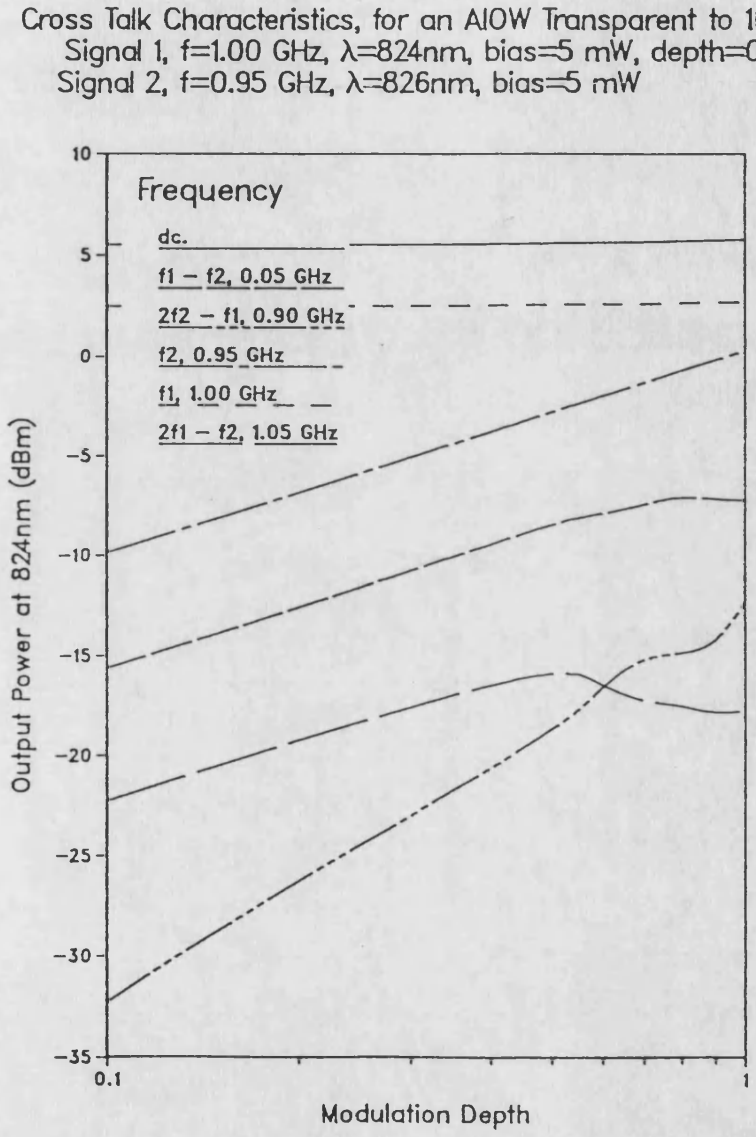

Figure 9.8b Crosstalk / Intermodulation modulation response, as a function of input modulation depth, for a two tone optical input signal.

Input 1, P_{in} = 5 mW, λ_1 = 824 nm, f_1 = 1 GHz, m_1 = 0.5,

Input 2, P_{in} = 5 mW, λ_2 = 826 nm, f_2 = 0.95 GHz, m_2 = varied.

(b) Output at 824 nm,

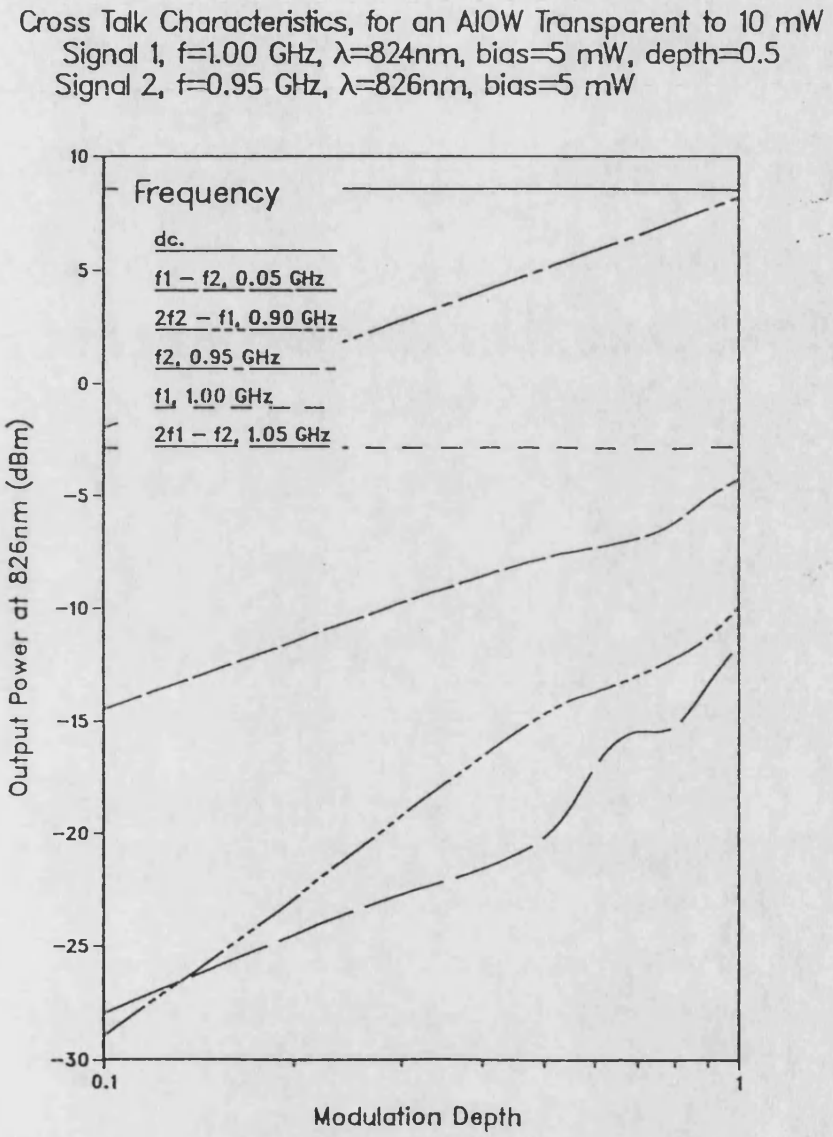

Figure 9.8c Crosstalk / Intermodulation modulation response, as a function of input modulation depth, for a two tone optical input signal.

Input 1, P_{in} = 5 mW, λ_1 = 824 nm, f_1 = 1 GHz, m_1 = 0.5,

Input 2, P_{in} = 5 mW, λ_2 = 826 nm, f_2 = 0.95 GHz, m_2 = varied.

(c) Output at 826 nm.

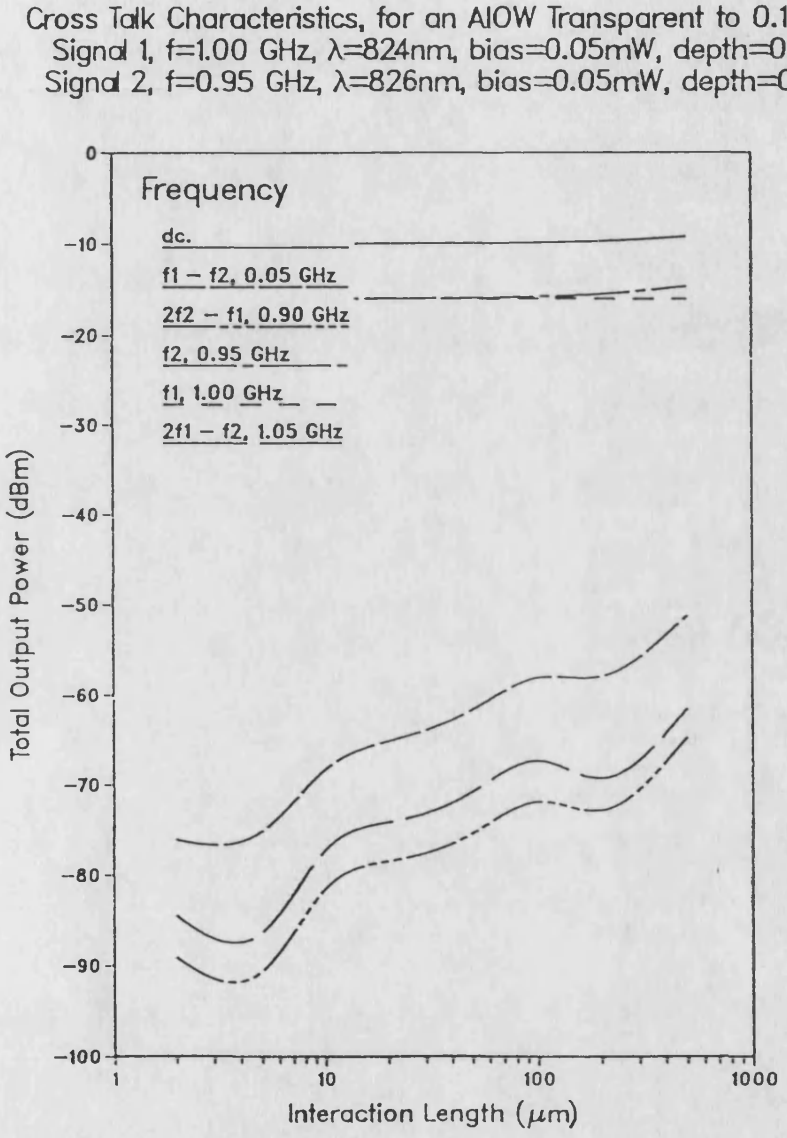

Figure 9.9*a* Crosstalk / Intermodulation modulation response, as a function of interaction length, for a two tone optical input signal.

Input 1, P_{in} = 0.05 mW, λ_1 = 824 nm, f_1 = 1 GHz, m_1 = 0.5,

Input 2, P_{in} = 0.05 mW, λ_2 = 826 nm, f_2 = 0.95 GHz, m_2 = varied.

(a) Total Output Power,

The values for co-channel cross talk for the three bias cases are summarised in table 9.1.

Input Bias (mW)	$X_{2,1}$ (dB)	$X_{1,2}$ (dB)
0.05, 0.05	-28	-23
0.5, 0.5	-18	-15
5.0, 5.0	-8	-6

Table 9.1 : Co-Channel Cross Talk variation with Input Bias Power

These values for the co-channel cross talk are seen to be independent of modulation depth in figure 9.6 - 9.8.

9.4.4 Variation of Cross Talk with Interaction Length

In this section a new view of the cross talk behaviour is presented where the effect of varying the length of the active waveguide section of (say) the tail of the 'Y' coupler shown in figure 9.1, is examined. As the interaction (waveguide) length is increased, then the cross talk and the intermodulation in the guide should change. A range of lengths from 3 to 500 μm were chosen in a logarithmic progression. The same six characteristics chosen for the previous section are used here, plotted on a dB vs log interaction length scale. Again, three graphs are presented: the total output power, the narrow band output across the wavelength slot at 824 nm, and the narrow band output across the wavelength slot at 826 nm.

It should be noted that the transparency condition is recalculated for each value of guide length, rather than maintaining a fixed value of current density across the interaction length variation. This may lead to minor discrepancies between the nominal transparencies obtained and may have an unpredictable effect on the characteristics. In addition as the interaction length is altered, there is an inevitable alteration in the step length which again may have an unpredictable effect.

Figure 9.9 shows the case for low input flux, (0.05 & 0.05 mW) with the guide biased to a nominal transparency. Several key trends are observed for rising interaction length. Firstly, the coupling or interaction between the two signals is

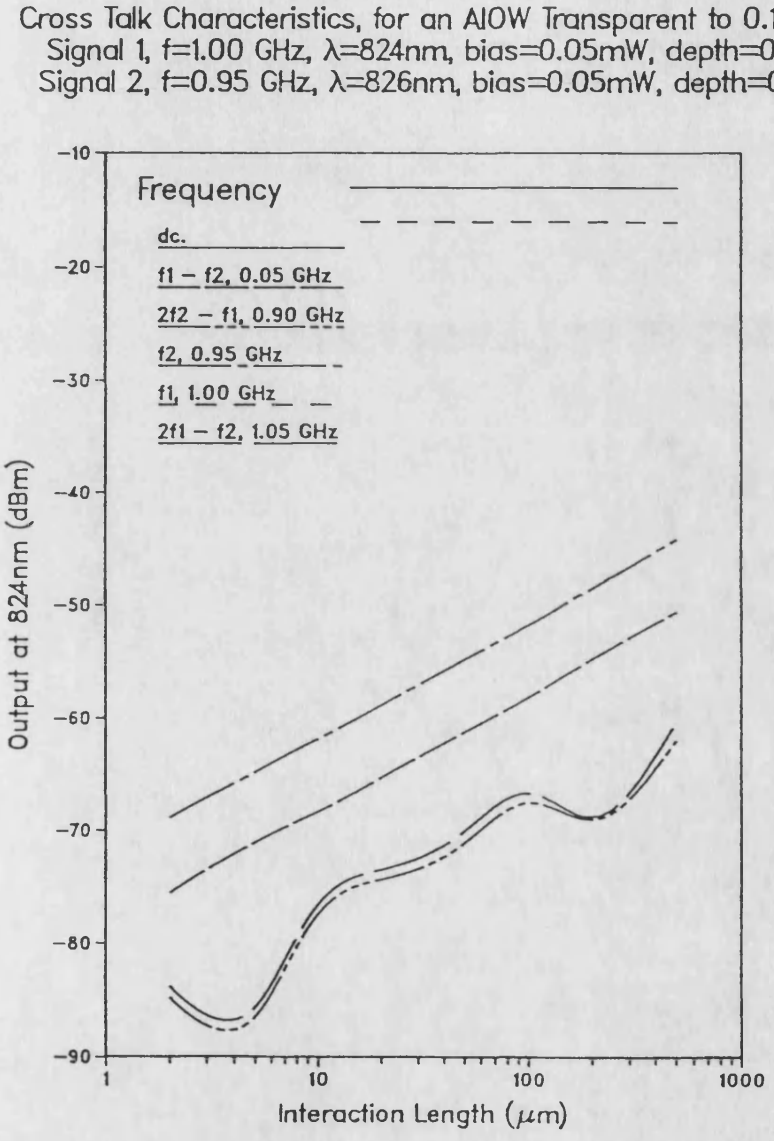

Figure 9.9b Crosstalk / Intermodulation modulation response, as a function of interaction length, for a two tone optical input signal.

Input 1, P_{in} = 0.05 mW, λ_1 = 824 nm, f_1 = 1 GHz, m_1 = 0.5,

Input 2, P_{in} = 0.05 mW, λ_2 = 826 nm, f_2 = 0.95 GHz, m_2 = varied.

(b) Output at 824 nm,

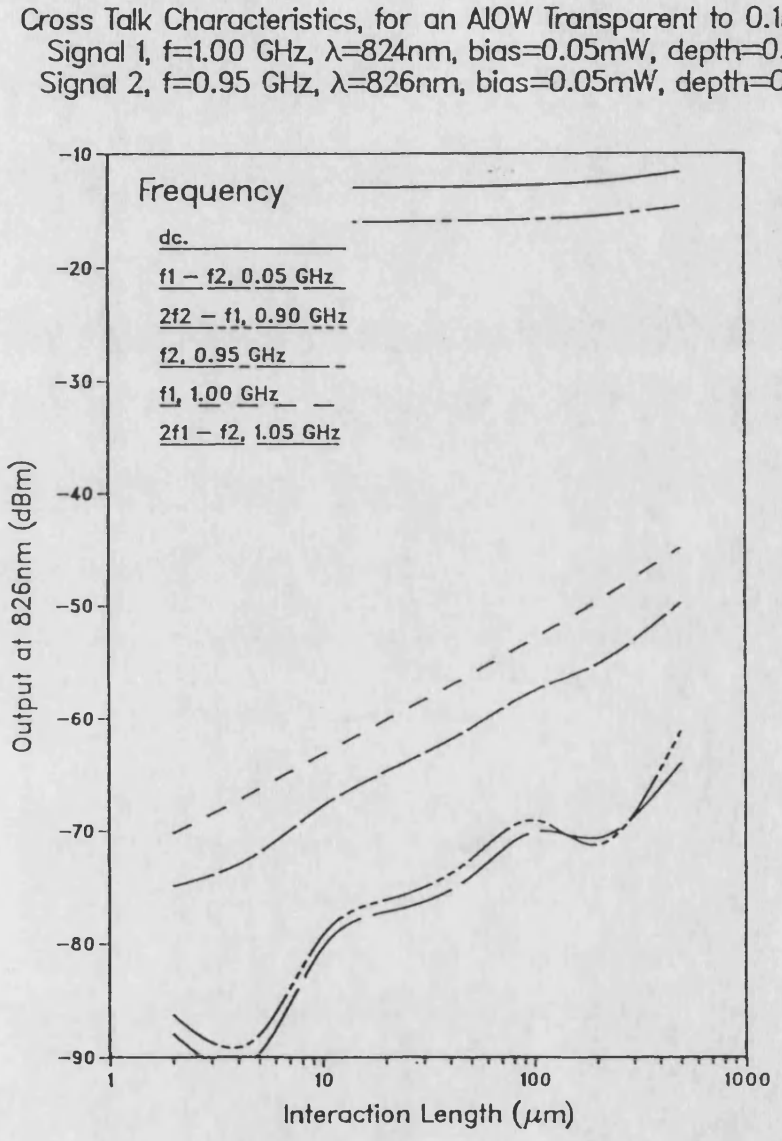

Figure 9.9c Crosstalk / Intermodulation modulation response, as a function of interaction length, for a two tone optical input signal.

Input 1, P_{in} = 0.05 mW, λ_1 = 824 nm, f_1 = 1 GHz, m_1 = 0.5,

Input 2, P_{in} = 0.05 mW, λ_2 = 826 nm, f_2 = 0.95 GHz, m_2 = varied.

(c) Output at 826 nm.

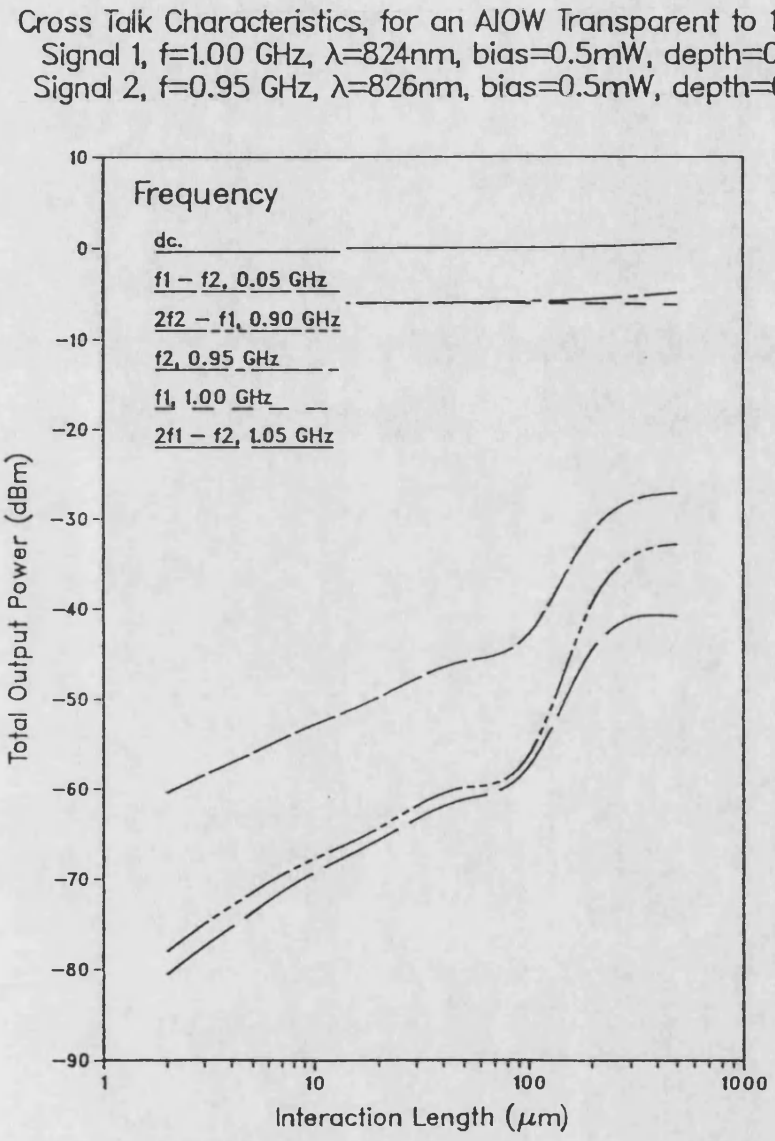

Figure 9.10a Crosstalk / Intermodulation modulation response, as a function of interaction length, for a two tone optical input signal.

Input 1, P_{in} = 0.5 mW, λ_1 = 824 nm, f_1 = 1 GHz, m_1 = 0.5,

Input 2, P_{in} = 0.5 mW, λ_2 = 826 nm, f_2 = 0.95 GHz, m_2 = varied.

(a) Total Output Power,

proportional to the interaction length. Both the primary and secondary intermodulation products in figures 9.9(a) - (c) increase with length. In figure 9.9(a), as the length increases the guide is seen to diverge from the nominal transparency ie, the total output power at the two fundamental frequencies diverges as the gain difference in the two wavelength slot become significant.

Figures 9.9(b) and 9.9(c) show a basic 10 dB/Decade rise in the cross talk and primary intermod components with interaction length. Clearly showing that the cross talk is directly proportional to the length. Again some anti-phase is present between the two channels as the total output power at $f_1 - f_2$ is less than the sum of the two components. It should be noted that for lengths less than 300 μm the cross talk $X_{1,2}$ is greater than $X_{2,1}$ but this situation is reversed for lengths above this value. Clearly, the gain or loss experienced by the fundamental signals at these higher lengths is smoothed out by the carrier density coupling.

A transition in characteristics at approximately 200 - 300 μm is seen for these three sets of figures. In figure 9.10, there is a sudden rise in the primary intermod in the output at λ_2 and the rise of secondary intermods in both channels is dramatic for all three parts, whilst in figure 9.11 similar characteristics to figure 9.9 are observed. An interaction length of 300 μm can be conveniently considered to be the dividing line (in these circumstances) between short and medium length guides, in terms of their characteristics. As observed in the previous section, as the input optical bias power is increased, the cross talk between the channels also increases.

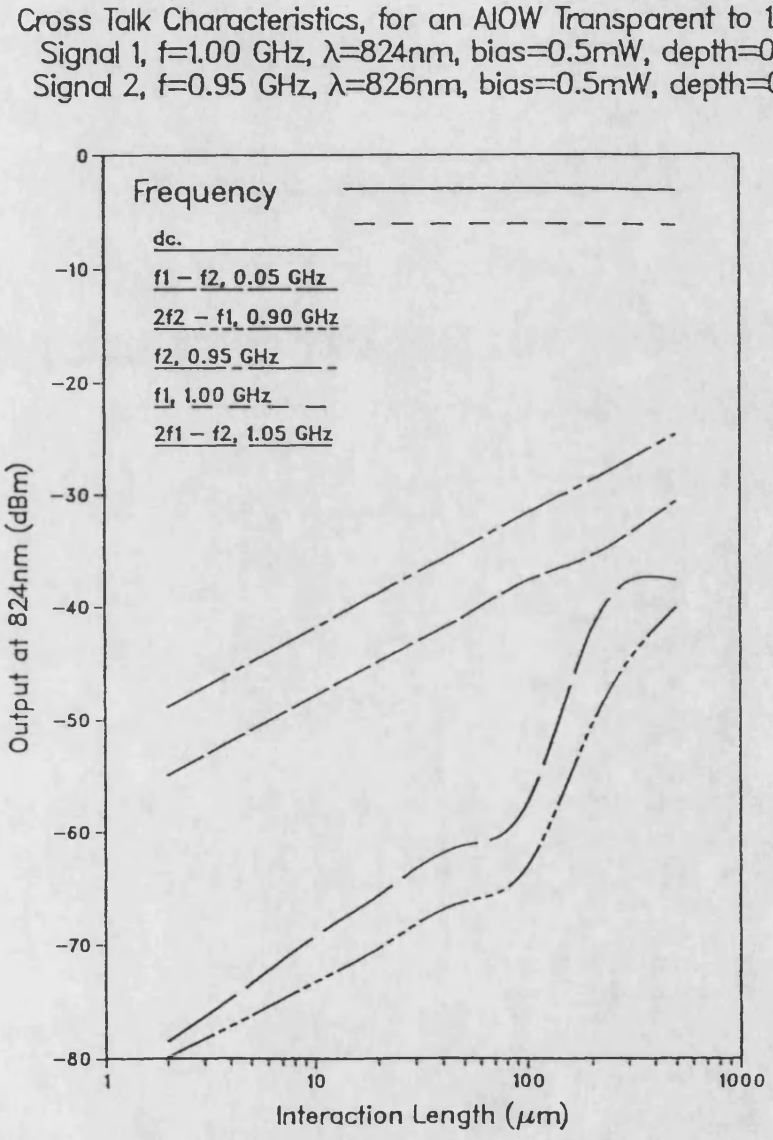

Figure 9.10 b Crosstalk / Intermodulation modulation response, as a function of interaction length, for a two tone optical input signal.

Input 1, P_{in} = 0.5 mW, λ_1 = 824 nm, f_1 = 1 GHz, m_1 = 0.5,

Input 2, P_{in} = 0.5 mW, λ_2 = 826 nm, f_2 = 0.95 GHz, m_2 = varied.

(b) Output at 824 nm,

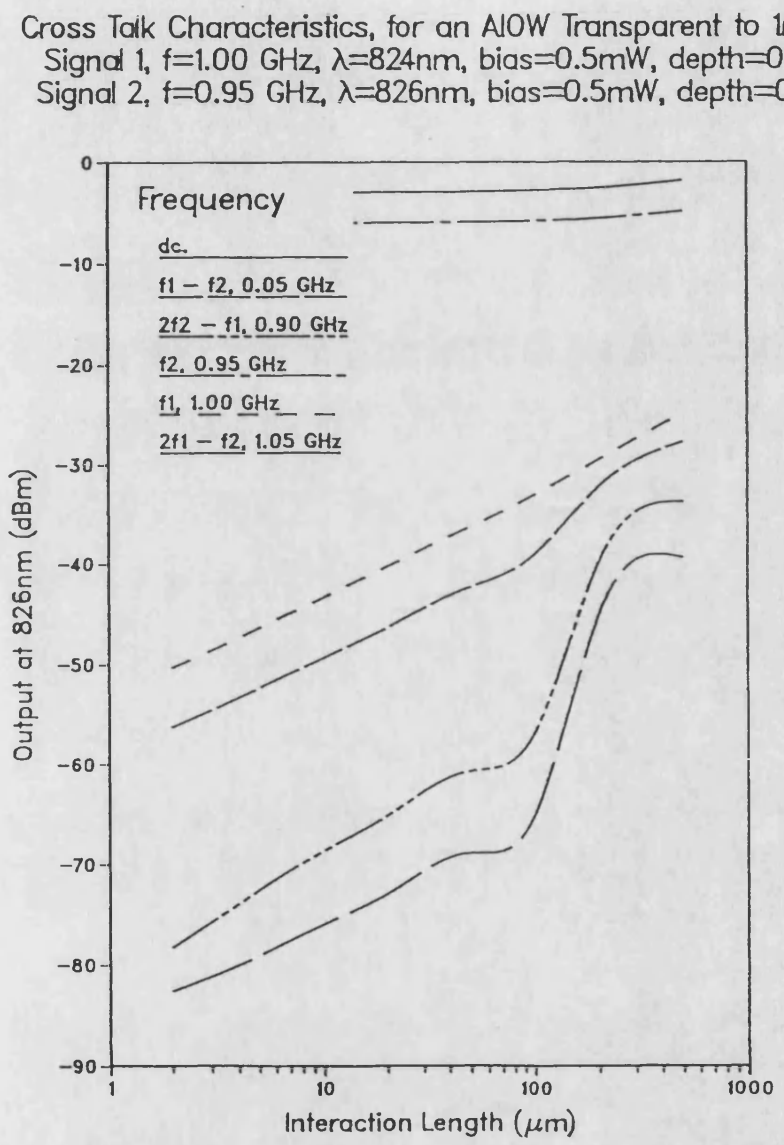

Figure 9.10c Crosstalk / Intermodulation modulation response, as a function of interaction length, for a two tone optical input signal.

Input 1, P_{in} = 0.5 mW, λ_1 = 824 nm, f_1 = 1 GHz, m_1 = 0.5,

Input 2, P_{in} = 0.5 mW, λ_2 = 826 nm, f_2 = 0.95 GHz, m_2 = varied.

(c) Output at 826 nm.

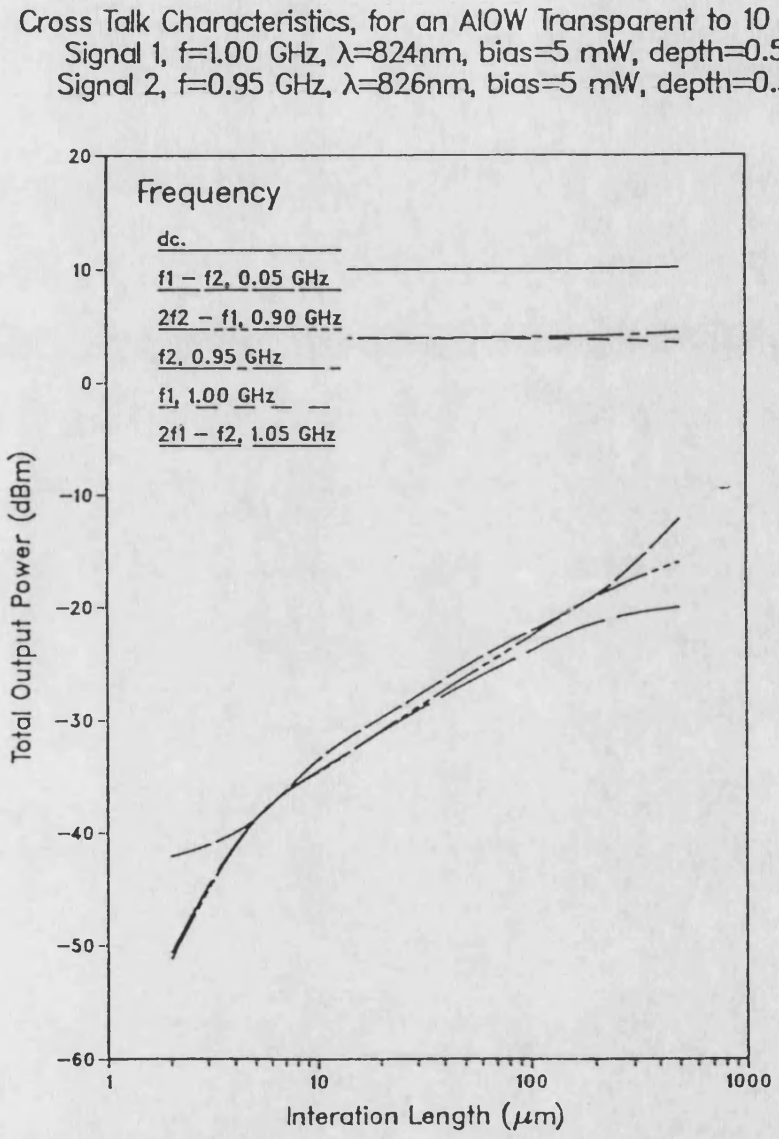

Figure 9.11a Crosstalk / Intermodulation modulation response, as a function of interaction length, for a two tone optical input signal.

Input 1, P_{in} = 5 mW, λ_1 = 824 nm, f_1 = 1 GHz, m_1 = 0.5,

Input 2, P_{in} = 5 mW, λ_2 = 826 nm, f_2 = 0.95 GHz, m_2 = varied.

(a) Total Output Power,

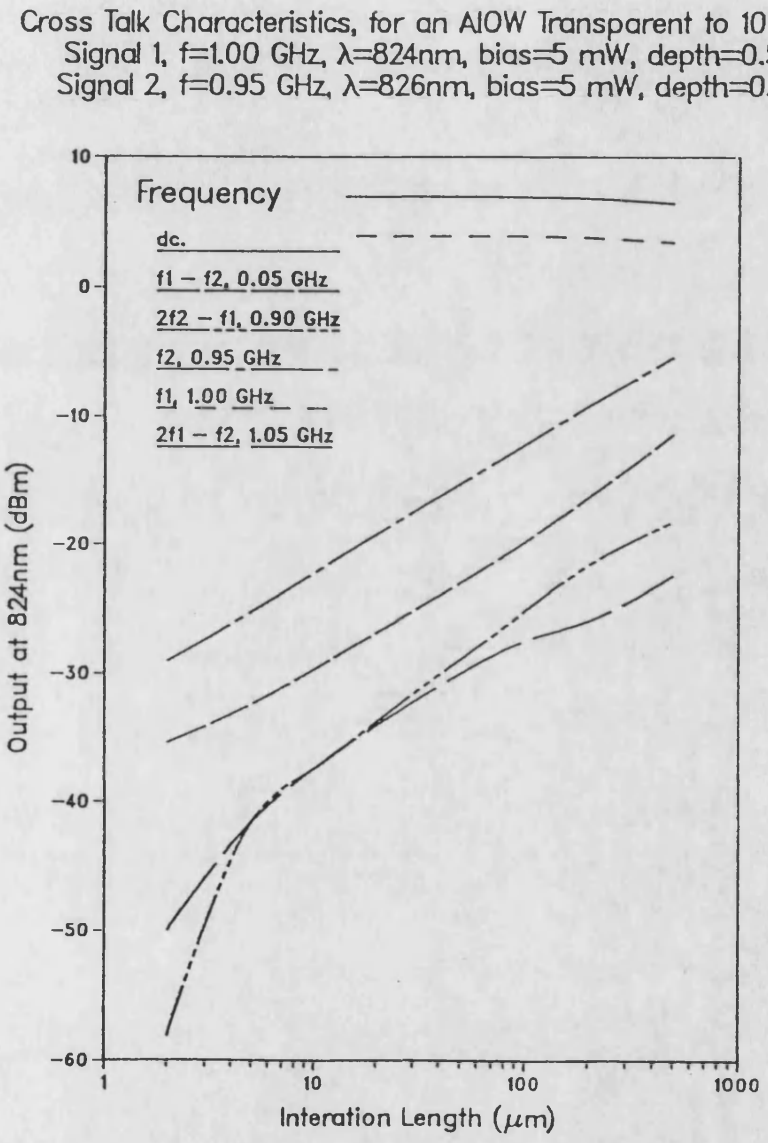

Figure 9.11 bCrosstalk / Intermodulation modulation response, as a function of interaction length, for a two tone optical input signal.

Input 1, P_{in} = 5 mW, λ_1 = 824 nm, f_1 = 1 GHz, m_1 = 0.5,

Input 2, P_{in} = 5 mW, λ_2 = 826 nm, f_2 = 0.95 GHz, m_2 = varied.

(b) Output at 824 nm,

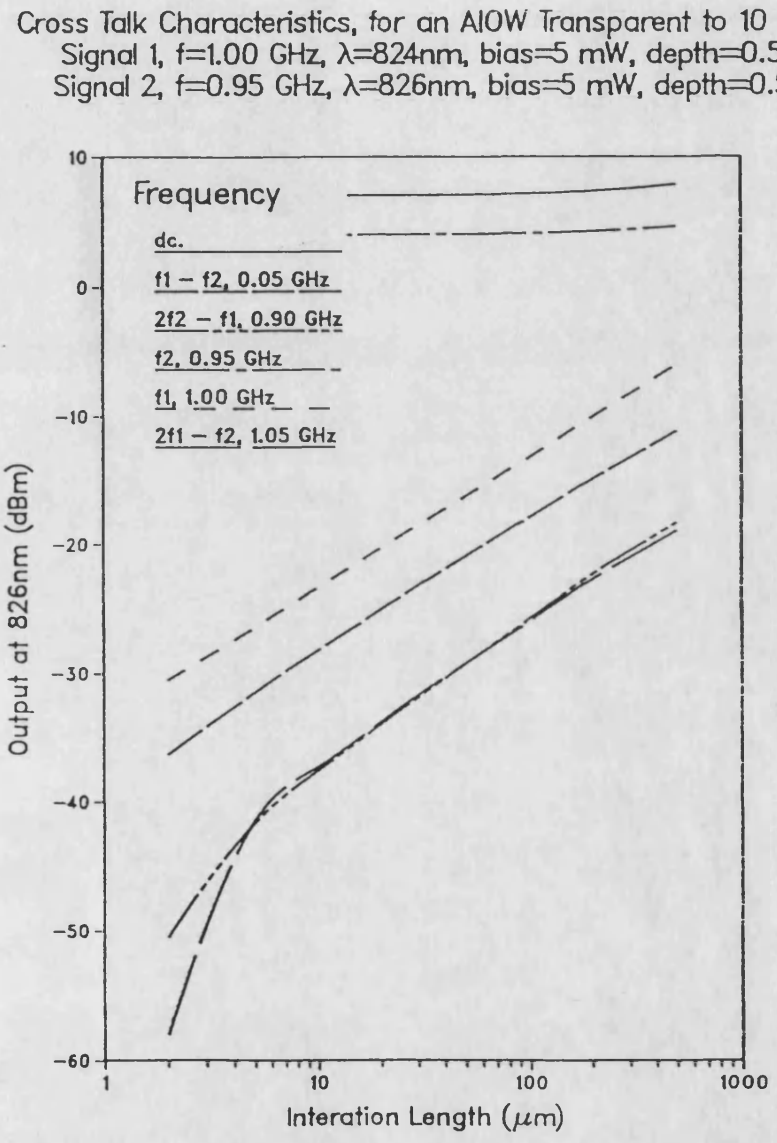

Figure 9.11c Crosstalk / Intermodulation modulation response, as a function of interaction length, for a two tone optical input signal.

Input 1, P_{in} = 5 mW, λ_1 = 824 nm, f_1 = 1 GHz, m_1 = 0.5,

Input 2, P_{in} = 5 mW, λ_2 = 826 nm, f_2 = 0.95 GHz, m_2 = varied.

(c) Output at 826 nm.

9.4 Conclusions

The presence of cross talk and intermodulation products is an undesirable by-product of the interaction between two optical input signals via the carrier density. It has been shown in this chapter that these phenomena are as significant as the effects of amplified spontaneous emission and harmonic distortion discussed at length in chapters 6 and chapter 8 respectively. However, whereas the effects of ASE and harmonic distortion can be ameliorated by use of optical and electrical filtering, intermodulation and (especially) cross talk are much more difficult to counteract.

The fundamental problem is that the intermodulation products occur at frequencies other than the harmonics. Thus unwanted signals can appear at the same wavelength or frequency as the wanted signals. This problem is quite clear for the group of figure for the cross talk results (9.5 - 9.11), where there is break through between wavelength slots. In addition, for strong interaction there are secondary intermodulation products which lie in the frequency channels of the two fundamental input components.

Some very important observations can be made from the results presented in this chapter. As one would expect the degree of (pure two-tone) intermodulation distortion and cross talk, is dependent on the interaction between the optical input flux and the carrier density. In the case of cross talk, the interaction is increased due to one input seeing net loss and the other input seeing net gain (for the nominal transparency, as defined in section 9.3.2) when compared with the intermodulation results. In addition the phase shift between the flux and gain variations leads to a phase shift between the frequency components in the various wavelength slots.

The co-channel cross talk (X) is seen to be virtually independent of modulation depth (ie the magnitude of the cross talk component rises linearly with modulation depth). However, it is critically dependent on the bias conditions and the interaction length. Clearly, there must be some limit on the linear growth of co-channel cross talk with interaction length, as a saturating effect will occur. However, it has not been

encountered by this set of results. The co-channel cross talk, along with the effect of amplified spontaneous emission, may ultimately determine the maximum length of guide that can be tolerated for a particular bias condition.

In practical optical communications systems there will be many components of input frequency rather than just the näive pure two-tone inputs considered here. In this chapter it has been shown that for an AIOW there will be significant cross talk between signals, even for low input powers. However, this disadvantage may be tolerated for the potential advantages of multi wavelength, multi frequency operation.

References, Chapter 9

1. HUNSPERGER, R.G., 'Integrated Optics : Theory and Technology' 2nd Edition. *Springer-Verlang, Heidelburg, 1984.*

2. GARRETT, B., MOULE, D.J., ARMISTEAD, C.J., BOURNE, W.O., CHAMPELOVIER, J., BAULCOMB, R.S., and COLLAR, A.J., : 'A monolithically integrated two wavelength DFB laser source for WDM optical communications systems',
Presented at SIOE '89, Paper No.25, Cardiff 20-21, March 1989.

3. ÖBERG, M.G., and OLISSON, N.A., 'Crosstalk between intensity modulated wavelength division multiplexed signals in a semiconductor laser amplifier',
IEEE J. Quantum Electron, 1988, QE-24, (1), pp52-59.

4. DARCIE, T.E., and JOPSON, R.M., 'Non linear interaction in optical amplifiers for multi-frequency lightwave systems',
Electron. Letts., 1988, 24, (10), pp638-640.

5. AGRAWAL, G.P., 'Population pulsations and non-degenerate four wave mixing in semiconductor lasers and amplifiers',
J. Opt. Soc, America, B , 1988, 5, (1- Special issue on wave mixing and phase conjugation), pp147-159.

10 CONCLUSIONS AND RECOMMENDATIONS

10.1 Review of Objectives

In the introduction, the objectives for the thesis were presented:

- To consider in detail the behaviour of a pumped AIOW in response to an ideal laser source, and its suitability as a circuit element for routing optical signals, in both the static and dynamic contexts.
- To investigate the feasibility of coupling the light from a Fabry-Perot laser source into a pumped AIOW across a simple etched or milled gap, including the efficiency of the coupling and the detuning effect on the laser source.
- Throughout the thesis an engineering perspective has been taken and the behaviour examined from a systems point of view.

10.2 Conclusions

In chapter 5 the optical coupling between a simple Fabry-Perot laser and an AIOW across a simple etched or milled gap is examined, drawing on hybrid integrated optics theory. It is seen that the coupling efficiency from the laser to the waveguide is critically dependent on the gap dimensions. The tolerances required to manufacture a predictable gap coupling are totally beyond current fabrication technology. In addition, the use of a gap coupling geometry leads to considerable detuning of the laser source.

Such effects dictate that the gap coupling geometry would not be used for an integrated laser/waveguide system. Rather, DFB or DBR lasers will be chosen as the integrated source. Although manufacturing the periodic grating required for such devices on the monolithic substrate presents some problems, the technical feasibility of the technique has been demonstrated (see chapters 2 and 9). This use of DFB or DBR lasers has particular attractions, as they have good wavelength stability and the pumped AIOW simply becomes a continuation of the active layer of the laser.

In chapters 6 to 9 the behaviour of the pumped AIOW in a variety of situations is considered in some detail. To fully model the waveguide behaviour, three new computer numerical models are presented: The Steady State Model, the Small Signal Dynamic Model, and the Large Signal Dynamic Model. In each case a travelling flux model which takes into account longitudinal variations in the flux and carrier density has been developed. Each model uses as its starting point the multi-dimensional conservation equations derived in chapter 4. In addition, there is a consistency between the models which allows cross-verification of the results obtained. These models may be applied to a variety of geometries and conditions and are not restricted to the case of an AIOW examined here.

In chapter 6 the static characteristics of an AIOW are examined in depth, in particular the effect of the guide inputs on key systems parameters. One parameter of utmost importance is the electrical current (density) required to achieve transparency. The transparency current varies with optical input power and wavelength. However, for optical input powers < 0.5 mW the current is independent of the input, and of a reasonable value compared to laser threshold. Thus, a waveguide biased to transparency at 0.5 mW will be near transparency for all inputs from 0 - 1 mW. As the transparency condition varies with wavelength, there must be a degree of tuning between the source and the guide. This makes the prospect of using a DFB laser more attractive.

One of the major problems of using a pumped AIOW is that the amplified spontaneous emission (ASE) in the guide gives rise to an undesirable noise signal. For low input powers, the ASE power is also independent of the input. Any pumped AIOW will therefore have a noise output even when no input signal is applied and will consequently draw power from the electrical pumping source at all times. Also low power input signals will become lost in the broadband ASE spectrum. The effect of ASE noise can be ameliorated by reducing the guide dimensions with a consequent reduction in the optical confinement factor, Γ and the spontaneous emission factor, δ.

Such a reduction has the side-effect of limiting the power handling capacity of the waveguide.

The underlying non-linearity of the AIOW is highlighted by the four port to port characteristics examined using the steady state model: The input/output linearity, the coherent forward pass gain, the total output noise power, and the output signal to noise ratio. The basic mechanism is the coupling between the flux and carrier densities governed by the stimulated gain and spontaneous emission parameters, which both vary with carrier density. At low input powers, the coupling is limited and the guide behaviour is basically linear. As the input power rises the coupling and the non-linearity become more pronounced. At very high input powers, saturation of the guide parameters leads to a second region of linear operation, but with a greatly compressed output power and range.

A non-linear input/output characteristic inevitably leads to distortion of optical input signals. Using the steady state model it is possible to estimate the harmonic distortion that will be experience by low frequency inputs by using a quasi-static analysis. Two methods were used in chapter 6, a polynomial fit to the input/output characteristic and an FFT of the output pseudo time series. In general, the harmonic distortion rises with both optical bias power and modulation depth. In extreme cases the non-linearity leads to generation of output harmonics with more power than the output fundamental power.

From the steady state mode, the behaviour of the guide with input power can be divided into three major regions: low interaction, moderate interaction, and high interaction. For the geometry chosen for the majority of the study, the input powers 0.1, 1.0 and 10.0 mW can be considered to be typical for each region. These three spot values are used throughout the thesis to examine the guide characteristics.

In chapter 7 a conventional small signal analysis (SSA) is applied to the pumped AIOW. However, the technique is applied to the case of a modulated optical, rather than electrical, input. In addition, longitudinal variations of both steady state and small signal quantities are permitted. In terms of the conditions where the model can be

applied and the type of results that can be obtained, the small signal model is limited in its scope. For instance, without significant mathematical manipulation it is not feasible to consider inputs other than single wavelength, single frequency, sinusoidal inputs. The model does however provide expressions to predict and describe the temporal behaviour of the waveguide and the results obtained from the large signal model.

Using the SSA technique the compression of port to port gain observed in chapter 6 is seen to be dependent on frequency as well as input power. The degree of gain compression, Δ, is determined by the optical input power and the physical parameters δ and Γ. Thus guides with a lower cross-sectional area will show a lower gain compression for a given value of optical input **flux**.

The frequency response of the fundamental small signal output power is predicted to have two invariant sections joined by a step region, centred on the natural frequency of the carrier density variations, ω_n. The nature of the break region is determined by the degree of gain compression. The results obtained for the small signal model show that the quasi-static analysis of chapter 6 has an upper frequency limit of $\approx$ 10 MHz. Above this value, a large signal analysis is required to describe the modulation response.

The large signal model described in chapter 8 is an extension of the steady state model into the time domain. A similar technique is used to solve the propagating flux continuity equations over regions of constant carrier density. However, allowing the guide quantities to vary over small steps in time, requires the additional restriction that all guide regions must be of an identical length. For the case of a pumped AIOW this is not of great importance but it does preclude the modelling of dispersive effects.

Using the large signal model, the type of inputs that can be considered is limited only by the temporal resolution which is controlled by the region length. In chapter 8, pulse and step inputs, as well as single tone sinusoidal inputs are considered. The response of guide to pulse and step inputs is of particular interest. The leading edge of a step or pulse is seen to pass through the guide virtually unchanged. As the carrier density in the guide is redistributed in response to the new input conditions, the output

power then shows a predominantly first order fall (or rise for a falling pulse edge) to a new steady state value. The time constant of the fall is determined by the carrier continuity equation.

The distortion of sinusoidal modulated inputs has been examined in great detail. For low interaction cases, the power in each harmonically related component is proportional to $(m \cdot \hat{W}_{in})^n$, where m is the modulation index or depth, $\hat{W}_{in}$ is the optical bias power and n is the harmonic index. There is also a constant ratio between the power in adjacent harmonics (ie $3^{rd}/2^{nd} = 4^{th}/3^{rd}$, etc). As the modulation frequency rises, power is transferred from the higher harmonics to the fundamental component. The fundamental forward pass gain is seen to increase with frequency above ω_n, as the gain compression decays. At high frequencies, the fundamental output power becomes constant, whilst the higher harmonics roll-off at $(n-1) \cdot 10$ dlB/dec.

By recourse to the small signal analysis it has been shown that the fundamenal time varying component of carrier density, and hence the stimulated gain, lags the variations in flux density by at least π radians. This lag increases with frequency to a maximum value of $3\pi/2$ radians. For low frequency (and steady state) behaviour this simply means that the gain falls as the input power rises. This anti-phase between the gain and flux leads to the gain compression observed in the output power frequency response. As the input frequency increases, the lag between the gain variations and the flux increases, leading to a highly non-linear and unpredictalble response.

It has been established that to achieve linear or near-llinear performance from the waveguide, the input bias power and modulation index product must be kept to below 1 mW, or the modulation frequency must be above 1–5 GHz (depending on the bias power). In the former case, linear operation is ensured as the stimulated recombination is negligible whilst in the latter, the flux and carrier density become decoupled.

For all cases of sinusoidal modulated input, higher harmonic components are generated due to the interaction between the flux and carrier density. This type of effect has significant implications for multi-channel (modulation)) FDM and (optical) WDM systems, as it leads to co-channel cross talk and intermodullation distortion. In chaper

9, these effects are examined using two tone inputs. In the case of pure intermodulation distortion the two tones are at the same input wavelength. Whilst for cross talk distortion the two tones are at different wavelengths.

The degree of (pure two-tone) intermodulation distortion and cross talk, is dependent on the interaction between the optical input flux and the carrier density. In the case of cross talk, the interaction is increased due to one input seeing net loss and the other input seeing net gain (for the nominal transparency, as defined in section 9.3.2) when compared to the intermodulation results. In addition, the phase shift between the flux and gain variations leads to a phase shift between the frequency components in the various wavelength slots.

The co-channel cross talk is virtually independent of modulation depth (ie the magnitude of the cross talk component rises linearly with modulation depth). However, it is critically dependent on the bias conditions and the interaction length. For high interaction the co-channel cross talk can be as high as -8 dB but it is of greater concern that for low interaction the cross talk only falls to around -28 dB for a 1000 μm long guide. Ultimately, this kind of cross talk may be of greater importance in setting limits on the guide length and input power than the ASE or harmonic distortion.

To summarise, the results presented in this thesis demonstrate the feasibility of using active waveguides to route signals in optical integrated circuits. The pumping requirements for moderate input powers (< 1 mW) are not excessive in comparison to laser threshold. The distortion of input signals is determined by the gain compression, which is dependent on frequency and bias power. For near-linear operation, a low input power or a high frequency (> 5 GHz) must be used. The dynamic distortion and cross talk in an AIOW are critically dependent on the interaction length, and these parameters will limit the length of guide which may be used.

The choice of guide dimensions (including the length) will be determined by the required operating conditions. For high power operation, a large cross-sectional area is required, which gives rise to a higher ASE noise power and a deterioration of the signal

to noise performance. For low input powers, a smaller cross-sectional area can be tolerated with a consequent performance improvement.

A pumped AIOW will not be the ideal solution for all routing situations. In particular, for very long cases, a guide which does not give rise to ASE and cross talk distortion would be preferred. However, for linking closely packed active optical devices, as part of an monolithic optical integrated circuit, the AIOW presents an attractive, cheap solution to the routing problem.

10.3 Recommendations For Further Work

When undertaking any period of research one is conscious of the paths that were not pursued, the limiting assumptions made and the situations not examined because of time constraints. Some of these areas may be considered for further work.

The modelling of the transverse and lateral behaviour of the waveguide is relatively simple. The waveguide need not necessarily be a buried heterostructure of *dh* rib guide, indeed other structures may be more appropriate. It is possible to consider the behaviour of the optical field in lateral, transverse and longitudinal directions using (say) the Beam Propagation Method [1]. Such a model may be used to study any variations in lateral and transverse stability over the length of the guide. AIOWs which do not rely on strong index guiding could also be examined.

Over the past decade, devices based on Indium Phosphide (InP) have become of increasing significance and may ultimately supplant GaAs as the first choice material for active integrated optic devices. To enable the models presented to consider InP devices, stimulated gain and spontaneous emission data in a suitable form is required. This could be provide by modifying the GaAs model used in this thesis. In addition, there are several additional parameters which would have to be including in the conservation equations to take account of spectral hole-burning, (optical) gain saturation and Auger effects [2]. The influence of these three effects are of greater

significance in InP devices, compared with GaAs, and their effect on the waveguide performance would have to be examined in detail.

The limitations of the large signal dynamic model have been discussed in some detail in chapter 8. The choice of travelling flux models, whilst appropriate for the cases considered in this thesis, does limit the situations that can be considered. For instance, as phase information is not considered the models cannot be used for cases where there is a high cavity feedback (determined by the product of forward pass gain and reflectivity). For such cases, an optical field model which includes phase and magnitude variations would be more appropriate.

Notwithstanding these short comings, there are still many aspects of the AIOW which can be explored in greater detail with the models developed. Throughout the thesis the main emphasis has been on the examination of analogue signals in a guide biased to transparency for a given optical input power. In the great majority of cases examined it is assumed that the input current is trimmed to achieve transparency at the particular optical input bias power. Greater consideration could have been given to the alternative situation where a constant input current is used, with a value determined by the average input bias power expected. From a systems point of view it would be of benefit to examine the guide response to a range of digital signals, which are of equal importance to analogue signals. In chapter 9, a rudimentary analysis and examination of cross talk was presented. An examination of the maximum number of multiplexed FDM and WDM channels that a pumped guide can support would be of interest.

In the literature, it is frequently assumed that the types of models used to describe the behaviour of laser diodes can be extended to other devices. In this thesis three new models have been developed which can be applied to situations where the assumptions inherent in laser diode models do not apply. The models incorporate longitudinal and wavelength variations in the guide quantities (in the case of the steady state and large signal dynamic models). The behaviour of laser amplifiers, SLED, detectors and other devices where the spectral and longitudinal effects are significant may be examined using these models.

References, chapter 10.

1 VAN ROEY, J., VAN DER DONK, J. and LAGASSE, P.E., 'Beam-propagation method: analysis and assessment',
J. Opt. Soc. Am., 1981, 71, pp803-810.

2 AGRAWAL, G.P. and DUTTA, N.K., 'Long wavelength semiconductor lasers',
Van Nostrand Reinholt, 1986.

11 ACKNOWLEDGEMENTS

There are several organisations and individuals the author would like to thank for their help and assistance over the period of research. Primarily, I would like to express my gratitude to my supervisor Dr Richard Ormondroyd for his expert guidance and support throughout this project. I would also like to thank Professor T.E. Rozzi for arranging the initial financing of the research and providing me with the opportunity to pursue this exciting area of research.

The period of research was financed jointly by the Science and Engineering Research Council (SERC), Swindon, Wiltshire and British Aerospace, Filton, Bristol, under the Co-operative Awards in Science and Engineering (CASE) scheme. The research and computing facilities were provided by the University of Bath and the South West Universities Regional Computing Centre (SWURCC). The document production facilities for this thesis were kindly provide by the Praxis Computing Facility (PCF).

There are several colleagues with whom I have had interesting and stimulating discussions during the course of the project: Paul Morton, Mike Perkins David Buckley, Paul Lambkin, John Kot, Ian Middlemast and Rob Norcross. All of whom have made a significant contribution to my understanding of the subject. I would especially like to thank Mike Perkins for the use of his SLED model which formed the basis of the Steady State model presented here and Bill Liddell for his model of stimulated gain and spontaneous emission in GaAs.

Finally, I would like to thank my wife, Jackie for her unerring support during this particular labour of love.